2007

CHARACTERIZATION AND FLOW PHYSICS OF PLASMA SYNTHETIC JET ACTUATORS

Arvind Santhanakrishnan
University of Kentucky, asant0@engr.uky.edu

ABSTRACT OF DISSERTATION

Arvind Santhanakrishnan

The Graduate School

University of Kentucky

2007

CHARACTERIZATION AND FLOW PHYSICS OF PLASMA SYNTHETIC JET ACTUATORS

ABSTRACT OF DISSERTATION

A dissertation submitted in partial fulfillment of the
requirements for the degree of Doctor of Philosophy in
Mechanical Engineering in the College of Engineering
at the University of Kentucky

By

Arvind Santhanakrishnan

Lexington, Kentucky

Director: Dr. Jamey D. Jacob, Associate Professor of Mechanical and Aerospace Engineering

Oklahoma State University, Stillwater, Oklahoma

2007

ABSTRACT OF DISSERTATION

CHARACTERIZATION AND FLOW PHYSICS OF PLASMA SYNTHETIC JET ACTUATORS

Plasma synthetic jet actuators are investigated experimentally, in which the geometrical design of single dielectric barrier discharge (SDBD) plasma actuators is modified to produce zero-mass flux jets similar to those created by mechanical devices. The SDBD plasma actuator consists of two rectangular electrodes oriented asymmetrically and separated by a layer of dielectric material. Under an input of high voltage, high frequency AC or pulsed DC, a region of plasma is created in the interfacial air gap on account of electrical breakdown of the ambient air. A coupling between the electric field in the plasma and the neutral air near the actuator is introduced, such that the latter experiences a net force which results in a horizontal wall jet. This effect of the actuator has been demonstrated to be useful in mitigating boundary layer separation in aerodynamic flows. To increase the impact that a plasma actuator may have on the flow field, this research investigates the development and characterization of a novel flow control device, the plasma synthetic jet actuator, which tailors the residual air in the form of a vertical jet resembling conventional continuous and synthetic jets. This jet can be either three dimensional using annular electrode arrays, or nearly two dimensional using two rectangular strip exposed electrodes and one embedded electrode. Detailed measurements on the isolated plasma synthetic jet reveal that pulsed operation of the actuator results in the formation of multiple counter-rotating vortical structures in the flow field. The output jet velocity and momentum are found to be higher for unsteady pulsing as compared to steady operation. In the case of flow over a flat plate, the actuator is observed to create a localized interaction region within which the baseline flow direction and boundary layer characteristics are modified. The efficiency of the actuator in coupling momentum to the neutral air is found to be related

to the plasma morphology, pulsing frequency, actuator dimension, and input power. An analytical scaling model is proposed to describe the effects of varying the above variables on the output jet characteristics and actuator efficiency, and the experimental data is used for model validation.

KEYWORDS: Active Flow Control, Plasma Actuators, Synthetic Jets, Particle Image Velocimetry, Jet Flows.

Arvind Santhanakrishnan

August 31, 2007

CHARACTERIZATION AND FLOW PHYSICS OF PLASMA SYNTHETIC JET ACTUATORS

By

Arvind Santhanakrishnan

Dr. Jamey D. Jacob
(Director of Dissertation)

Dr. L. S. Stephens
(Director of Graduate Studies)

August 31, 2007
(Date)

RULES FOR THE USE OF DISSERTATIONS

Unpublished dissertations submitted for the Doctor's degree and deposited in the University of Kentucky Library are as a rule open for inspection, but are to be used only with due regard to the rights of the authors. Bibliographical references may be noted, but quotations or summaries of parts may be published only with the permission of the author, and with the usual scholarly acknowledgments.

Extensive copying or publication of the dissertation in whole or in part requires also the consent of the Dean of The Graduate School of the University of Kentucky.

A library which borrows this dissertation for use by its patrons is expected to secure the signature of each user.

Name	Date

DISSERTATION

Arvind Santhanakrishnan

The Graduate School

University of Kentucky

2007

CHARACTERIZATION AND FLOW PHYSICS OF PLASMA SYNTHETIC JET ACTUATORS

DISSERTATION

A dissertation submitted in partial fulfillment of the
requirements for the degree of Doctor of Philosophy in
Mechanical Engineering in the College of Engineering
at the University of Kentucky

By

Arvind Santhanakrishnan

Lexington, Kentucky

Director: Dr. Jamey D. Jacob, Associate Professor of Mechanical and Aerospace Engineering

Oklahoma State University, Stillwater, Oklahoma

2007

This dissertation is dedicated to the loving memory of my grandparents, Lakshmi and Parthasarathy. Thank you for always watching over me.

ACKNOWLEDGEMENTS

It is not always the end result, but the path taken in a journey that often makes it an unforgettable one. At the completion of this academic endeavor that I embarked on several years ago, I am indebted to many people across two different parts of the world for making the course of my graduate education enjoyable. My special thanks to everyone in my family in India for supporting me with their love, affection, constant encouragement, and understanding the lifestyle of a graduate student. It would have been impossible to come this far without each and everyone of them.

Rare is the occasion when a student finds a mentor who not only guides him toward achieving a goal successfully, but also leaves an indelible impression that the student can live up to. I have had the pleasure of working under such a mentor, Prof. Jamey Jacob. Thank you very much for everything—for all your words of wisdom, for your support, and for inspiring me.

I would like to thank Prof. Raymond LeBeau, Prof. James McDonough, Prof. Suzanne Smith, Prof. Todd Hastings, and Prof. Keith MacAdam for serving on my advisory committee and providing valuable inputs to this work. My sincere thanks go to Prof. LeBeau for his guidance and help with my research and teaching throughout my graduate education. I would like to thank Prof. McDonough for his insightful recommendations on improving the mathematical rigor of this dissertation, and for all the informative discussions on turbulence and CFD. Many thanks go to Prof. Smith for her encouragement and words of advice.

I would like to thank my current and former lab-mates Andrew Simpson, Nan Jou Pern, Karthik Ramakumar, and Hubert Rojas for all their help with my research. I would also like to thank Daniel Reasor for his help with the formatting of this dissertation.

My last five years definitely would not have been the same without all my friends here in America. I would like to thank Mark, Kylie, and Madison for being my home away from home. Many thanks to Rick and Connie for their warm hospitality, in spite of me showing up quite often and staying too long at their place. I could not thank Christine enough for showing me what life was, helping me with all kinds of things (that I could not possibly even list), and for knowing me before I myself did. A note of thanks goes to Macavity for showing me times when I had to put off work. And thanks to Kathy for the great hospitality.

This research was supported in part by a grant from Kentucky NASA EPSCoR under the direction of Drs. Richard and Karen Hackney. I thank them for their support of this research. I am grateful to Dr. David Ashpis of NASA GRC, Prof. Ari Glezer of Georgia Tech, and Dr. Tom McLaughlin of USAFA for their advice.

TABLE OF CONTENTS

LIST OF TABLES

LIST OF FILES

santhanakrishnandissertation.pdf: 12.5 MB PDF file.

psja2-0020.avi: 4.3 MB AVI file movie with Schilieren flow visualization of a plasma synthetic jet in an initially quiescent medium.

video5.avi: 17.7 MB AVI file movie showing formation of the plasma synthetic jet with increasing time in actuator duty cycle.

plasma-0615.mov: 7.28 MB Quicktime movie showing plasma morphology.

NOMENCLATURE

r_o: exposed/outer electrode radius of annular PSJA

d_o: exposed/outer electrode diameter of annular PSJA

w_e: width of exposed electrode of the linear PSJA

r_i: embedded/inner electrode radius of annular/linear PSJA

d_i: embedded/inner electrode diameter (or width) of annular (or linear) PSJA

w: gap between the asymmetric placement of exposed and embedded electrodes of annular/linear PSJA

r: radial coordinate of annular PSJA in quiescent flow

x: wall-normal/axial coordinate of annular PSJA in quiescent flow

U: mean component of axial direction jet velocity for actuator in quiescent flow

U_{max}: mean component of local maximum jet velocity in axial direction for actuator in quiescent flow

U_p (or U_{peak}): peak jet velocity in axial direction for actuator in quiescent flow

u': RMS component of axial direction jet velocity for actuator in quiescent flow

V: mean component of radial direction jet velocity for actuator in quiescent flow

v': RMS component of radial direction jet velocity for actuator in quiescent flow

F: average hydrodynamic force output of jet in quiescent flow

F_{max}: maximum hydrodynamic force output of jet in quiescent flow

L: distance from leading edge of flat plate to center of the actuator

V_{AC}: actuator input AC waveform voltage amplitude (or potential)

T_{act}: actuator input AC waveform time period

f_{AC}: actuator input AC waveform frequency

T_p: actuator pulsing time period

f_p: actuator pulsing frequency

t: time along actuator pulsing duty cycle for phase-locked PIV measurements

U_∞: magnitude of free stream velocity

U_{js}: peak axial direction velocity for steady operation of actuator in quiescent flow

U_{jp}: peak axial direction velocity for 10 Hz pulsed operation of actuator in quiescent flow

Re_L: Reynolds number based on distance from leading edge of flat plate to center of plasma actuator

x: horizontal/streamwise coordinate of annular/linear PSJA in cross flow

y: vertical/cross-stream coordinate of annular/linear PSJA in cross flow

u: mean component of horizontal velocity for actuator in cross flow

v: mean component of vertical velocity for actuator in cross flow

δ^*: displacement thickness of flat plate boundary layer, actuator in cross flow

$\delta_1{}^*$: displacement thickness of flat plate boundary layer at 2Δ upstream of actuator center, actuator in cross flow

θ: momentum thickness of flat plate boundary layer, actuator in cross flow

θ_1: momentum thickness of flat plate boundary layer at 2Δ upstream of actuator center, actuator in cross flow

x_C: wall-normal/axial coordinate location of starting vortex center induced by pulsing of annular PSJA in quiescent flow

r_C: radial coordinate location of starting vortex center induced by pulsing of annular PSJA in quiescent flow

u': RMS component of horizontal velocity

v': RMS component of vertical velocity

Δt: time between successive pulses of Nd:YAG laser used for PIV measurements

P_{in}: average input electrical power to actuator per cycle of AC waveform

D: diameter of circular cylinder

f^+: nondimensional pulsing frequency for actuator applied to flow over a circular cylinder

η: actuator efficiency

η_{max}: peak value of actuator efficiency

E_{out}: mechanical energy output of plasma induced jet

E_{in}: electrical energy input of PSJA

I: pixel brightness (arbitrary units) of plasma morphology image

I_{median}: median value of pixel brightness (arbitrary units) of plasma morphology image

$\overline{u}_i$: average plasma induced jet velocity (of entrained flow in quiescent conditions)

$\overline{u}_j$: average plasma synthetic jet velocity in quiescent flow

h: incoming entrained flow width in wall-normal direction for actuator in quiescent flow

c: actuator circumference

U_c: centerline velocity of plasma synthetic jet in quiescent flow

$U_{c,p}$: peak centerline velocity of plasma synthetic jet in quiescent flow

b: half-width of plasma synthetic jet in quiescent flow

Chapter 1

INTRODUCTION

Flow control, or the ability to actively or passively manipulate a flow field, has emerged as one of the preeminent topics of research in fluid dynamics. The performance of vehicles (such as Unmanned Aerial Vehicles—UAVs and Micro Aerial Vehicles—MAVs) or devices (such as low pressure turbine blades and fuel injectors) that operate in low Reynolds number conditions is limited chiefly by the reduced ability of the low kinetic energy flow to smoothly negotiate an adverse pressure gradient scenario. The adverse pressure gradient is typically imposed due to a combination of both the curvature of the surface (uphill regions) and operation of the device or vehicle, such as in the high angle of attack pitch-up maneuvering of an aircraft. As a result of this tendency of low Reynolds number flow to separate from the surface when subjected to an adverse pressure gradient, the pressure drag component of the parasitic drag increases, reducing the overall efficiency. As an example of the consequences of separation, previous studies dating to 1990 have shown that a skin friction drag reduction in the order of 20% would result in an annual fuel savings of roughly $1 billion in the commercial aircraft industry, and a 6.8% increase in speed of underwater vehicles in the military sector (Gad-El-Hak *et al.* [1]). In the case of aircraft, laminar boundary layer separation may lead to problems such as separation bubble bursting and associated stall (see Lissaman [2]). The vast range of applications arising from the ability to manipulate fluid flows, beyond the obvious advantages in micro and meso aerial vehicles, in other areas such as the excitation of jet boundary layer instabilities (Peacock *et al.* [3]), combustion (De Zilwa *et al.* [4]), internal aerodynamics (low pressure turbine blades—see Bons *et al.* [5] and Rivir *et al.* [6], stator vanes—see Culley *et al.* [7], and diffusers—see Chiekh *et al.* [8]), and suppression of wind-induced vibrations in tall structures (Kubo *et al.* [9]), just to name a few, provides a strong motivation for research in the subject of flow control. This science is currently of major importance in fluid dynamics research, and several techniques to alter and manipulate a flow field have been explored (see Gad-El-Hak [10]). The work presented herein, in particular, investigates a method for flow control using weakly ionized discharge plasmas.

This first section of this introductory chapter discusses the physics of the problem of boundary layer separation, and a brief review of the science of flow control will be presented. This is followed by an introduction to plasma based flow control and the flow control device

of interest herein, the plasma synthetic jet actuator (PSJA), and the objectives of this research and organization of the dissertation are presented in the concluding portions of this chapter.

1.1 Boundary Layer Separation

The concepts of boundary layer theory and flow control were first introduced by the German mathematician and fluid physicist, Ludwig Prandtl, in his seminal address to the Third International Mathematical Congress in 1904 [11]. Prior to this work, fluid dynamics was pursued heavily by mathematicians within the confines of the inviscid, irrotational, potential flow approximation. Notwithstanding their appreciable success in various flow formulations, the theoretical results did not entirely agree with experimental observations at the time (d'Alembert's paradox, for example, is used to refer to the zero drag around a rigid body predicted from a simple potential flow model, in contrast to experimental observations that confirm a finite drag force.) Departing from the previous notion that the layer of fluid nearest to a solid wall tends to "slip" through the surface without suffering any motion retardation, Prandtl's work identified the property of viscosity (fluid friction) to actually be responsible for the discrepancies between the idealized potential flow predictions and actual behavior of a fluid flow over a surface. On account of this property, the velocity of the layer of fluid in contact with the solid flow boundary was observed to be equal to that of the surface itself. Thus, in the case of a solid wall at rest, the value of fluid velocity at the wall would have to be zero (the no slip condition in fluids parlance), while it would be equal to the free stream value well outside of it. In order to ensure that the change in velocity from the wall to the mean flow was continuous, the flow field was divided into an thin inner boundary layer region near the wall where viscous effects were important, and an outer region where the potential flow approximation was still valid. Within the boundary layer, both the free stream pressure gradient imposed on the solid surface as well as frictional force (otherwise known as wall shear) tend to lower the momentum of fluid particles such that the layer of fluid located closer to the wall suffers more deceleration than the layer further away from the wall. A sample boundary layer velocity profile on the flow over an airfoil is shown in Fig. 1.1, at the first station closest to the leading edge. Typically, the flow over a streamlined body such as an aircraft wing is dictated by the fluid pressure acting on it. The gradient of pressure across the various locations on the surface provides the necessary impetus required for fluid motion, in the form of potential energy. Thus, in a scenario wherein the pressure gradient is such that it promotes acceleration

of the flow, the available potential energy is converted into kinetic energy which sustains the flow momentum. Within the boundary layer region, this kinetic energy is depleted by the viscous resistance at the bounding surface. Flow separation occurs when the fluid has insufficient momentum to overcome both the wall shear and pressure gradient imposed by the surface. Physical observations indicate that the surface streamline nearest to the wall leaves the body at the spatial location of the separation point, as seen in Fig. 1.2. The following definition of boundary layer separation, as quoted from the review article by Brown & Stewartson [12], is useful to note at this juncture:

> *The phenomenon of separation is one of the most interesting features of the motion of an incompressible fluid past a bluff body at high Reynolds number. Here the main stream, which has hitherto been in close contact with the body, suddenly, and for no obvious reason, breaks away, and downstream a region of eddying flow, which is usually turbulent even if the flow elsewhere is laminar, is set up.*

Regardless of the nature of the free stream prior to separation, the boundary layer beyond the separation point is three-dimensional (see Panton [13] for related discussion). Consequently, the rotational flow region next to the surface thickens, normal velocity increases and the usual boundary layer approximations are no longer valid. This phenomenon is usually highly unsteady, and so some of the fluid still remains attached at the top of the boundary layer, where the velocity equals the velocity of entrainment. The separated flow forms a free shear layer that is typically highly unstable, with an increasing tendency for transition to turbulent flow. Depending on the length and velocity scales of the flow, as well as the streamwise pressure gradient, transition may occur. Following transition, the mutual interaction between the boundary layer and outer potential flow may result in the formation of a reversed flow region downstream of the separation point, an observation not fully captured in Prandtl's theory.

To understand the criteria required for boundary layer separation, consider the two dimensional (x-y), steady ($\frac{\partial(\cdot)}{\partial t}$=0), incompressible Navier–Stokes equations in differential form:

$$\frac{\partial u}{\partial x} + \frac{\partial v}{\partial y} = 0 \tag{1.1}$$

$$\rho u \frac{\partial u}{\partial x} + \rho v \frac{\partial u}{\partial y} = -\frac{\partial p}{\partial x} + \mu \left(\frac{\partial^2 u}{\partial x^2} + \frac{\partial^2 u}{\partial y^2} \right) + 2\frac{\partial \mu}{\partial x}\left(\frac{\partial u}{\partial x}\right) + \frac{\partial \mu}{\partial y}\left(\frac{\partial u}{\partial y} + \frac{\partial v}{\partial x}\right) \tag{1.2}$$

$$\rho u \frac{\partial v}{\partial x} + \rho v \frac{\partial v}{\partial y} = -\frac{\partial p}{\partial y} + \mu \left(\frac{\partial^2 v}{\partial x^2} + \frac{\partial^2 v}{\partial y^2} \right) + 2\frac{\partial \mu}{\partial y}\left(\frac{\partial v}{\partial y}\right) + \frac{\partial \mu}{\partial x}\left(\frac{\partial u}{\partial y} + \frac{\partial v}{\partial x}\right) \tag{1.3}$$

Since the discussion herein pertains to boundary layers, consider the above equations at the wall y=0, such that we have the following conditions:

$$u = 0$$

$$v = v_w$$

The first of which represents the no-slip condition, and v_w indicates velocity of the wall (through mechanisms such as suction, blowing, or surface motion). The boundary layer approximation is also considered, through which the streamwise velocity gradients ($\frac{\partial u}{\partial x}, \frac{\partial v}{\partial x}$) can be treated to be small in comparison to the cross-stream velocity gradients ($\frac{\partial u}{\partial y}, \frac{\partial v}{\partial y}$). Applying the above boundary conditions, we obtain the Navier–Stokes equations near the wall:

$$\left.\frac{\partial v}{\partial y}\right|_{y=0} = 0 \tag{1.4}$$

$$\rho v_w \left.\frac{\partial u}{\partial y}\right|_{y=0} = -\left.\frac{\partial p}{\partial x}\right|_{y=0} + \mu \left.\frac{\partial^2 u}{\partial y^2}\right|_{y=0} + \left.\frac{\partial \mu}{\partial y}\right|_{y=0} \left.\frac{\partial u}{\partial y}\right|_{y=0} \tag{1.5}$$

$$0 = -\left.\frac{\partial p}{\partial y}\right|_{y=0} + \left.\frac{\partial \mu}{\partial x}\right|_{y=0} \left.\frac{\partial u}{\partial y}\right|_{y=0} \tag{1.6}$$

It is important to note that due to the Dirichlet boundary (no slip) conditions on the solid wall, with the exception of very smooth solutions, the differential equations 1.4–1.6 are not expected to be valid in general. This is especially problematic if the solid surface is not smooth, as a result of which the above equations are satisfied only in a piecewise sense. In the simplest case of no wall velocity and constant viscosity, the momentum equations reduce to the following

$$\left.\frac{\partial p}{\partial x}\right|_{y=0} = \mu \left.\frac{\partial^2 u}{\partial y^2}\right|_{y=0} \tag{1.7}$$

$$\left.\frac{\partial p}{\partial y}\right|_{y=0} = 0 \tag{1.8}$$

The parabolic nature of the boundary layer equation 1.7 dictates that information travels in the downstream, and not in the upstream direction. Equation 1.8 suggests that the surface pressure varies only along the streamwise x direction, i.e., $p = p(x)$. The pressure distribution imposed by the free stream flow of a fluid over the surface of a body is invariant along the wall-normal direction and hence unaffected by the boundary layer. Thus, the pressure distribution can be determined through integration of the velocity distribution in the primarily inviscid, irrotational region of the flow field,

$$U \frac{dU}{dx} = -\frac{1}{\rho} \frac{dp}{dx} \quad \Rightarrow p = -\rho \int U \, dU$$

Figure 1.1 illustrates boundary layer separation on a flow over an airfoil in terms of streamlines and velocity profiles. An accelerating flow occurs when the streamwise pressure gradient at the wall is negative (or favorable), and this is present at portions near the leading edge of the airfoil. The flow streamlines start to converge before the most uphill point, and velocity increases. Downstream of this location, the pressure gradient is positive (or adverse), and flow velocity decreases. Two dimensional boundary layer separation is defined as the location where the shear stress τ at the wall, given in terms of the cross-stream gradient of horizontal velocity $\mu\frac{\partial u}{\partial y}$, is equal to zero (see Schlichting & Gersten [14]). The definition of three dimensional boundary layer separation is much more complicated, defined as the location where both the velocity at the wall and shear stress simultaneously go to zero [1]. As seen in Fig. 1.1, the velocity profile gradient is positive before separation, zero at the point of separation and negative in the reverse flow region. An examination of equation 1.7 shows that a positive (or adverse) pressure gradient, necessary for separation, means that the velocity gradient $\frac{\partial u}{\partial y}$ increases in the wall-normal direction. The second derivative of the velocity is thus required to be positive as a necessary condition for separation to occur. The velocity gradient profiles before and at separation are illustrated in Fig. 1.3. In the case of an adverse pressure gradient, the increasing wall-normal gradient $\frac{\partial u}{\partial y}$ means that that there has to exist a point in the flow where the shear stress value would reach its maximum, as by definition $\tau = 0$ at $y = \infty$. Thus the requirement of a point of inflection in the boundary layer velocity gradient profile is a sufficient condition for separation. Extensive research has been conducted on steady/unsteady, two-/three-dimensional laminar and turbulent separation, and reviews on these topics can be found elsewhere (see Brown & Stewartson [12], Williams [15], Smith [16], and Simpson [17]).

The parameter that describes the viscous character of a fluid flow is the Reynolds number, a non dimensional quantity defined as the ratio of inertial to viscous forces acting on the system

$$Re = \frac{F_{inertial}}{F_{viscous}} = \frac{\rho U^2 L^2}{\mu U L} = \frac{\rho U L}{\mu} = \frac{U L}{\nu}$$

where ρ is the density, μ is the dynamic viscosity, and ν is the kinematic viscosity of the fluid, respectively. U and L are the characteristic velocity and length scales of the flow, respectively. The Reynolds number of a flow is often perceived to be a measure of its non dimensional speed, and serves as a *control parameter* to produce the bifurcations in the solutions of the Navier–Stokes equations which govern laminar and turbulent fluid flows. The latter observation may be noted by examining the non dimensional form of the Navier–

Stokes equations (see Kundu & Cohen [18] or many others for a detailed derivation)

$$\frac{\partial U_i}{\partial t} + u\,\frac{\partial U_i}{\partial x} + v\,\frac{\partial U_i}{\partial y} = -\frac{\partial p}{\partial x_i} + \frac{1}{Re}\left[\frac{\partial^2 U_i}{\partial x^2} + \frac{\partial^2 U_i}{\partial y^2}\right] + F_{b,i}$$

where subscript i refers to components of the vector quantity, p indicates the fluid pressure, and F_b is the body force, and all quantities have been scaled with appropriate factors. In the absence of the body force term, it can be seen that the Reynolds number is the *only* independent quantity that controls the flow behavior (see McDonough [19]). The inverse relation between Re and viscosity suggests that in low speed flows, viscous forces tend to predominate. Laminar boundary layers have lower levels of energy compared to turbulent flows on account of low flow velocities. As a result, laminar boundary layers quickly separate when subject to an adverse pressure gradient. Turbulent boundary layers have better separation resistance as compared to their laminar counterparts, and correspondingly can withstand moderate adverse pressure gradients.

The mean spanwise vorticity is zero at the wall or solid surface but is very large close to it, reaching a maximum at the edge of the viscous sublayer (see Gad-El-Hak [20]). In addition, turbulence continually promotes mixing of high and low momentum fluid within the boundary layer. This prevents the deceleration of fluid within the layer by the pressure gradient, thereby postponing the occurrence of separation. In the case of laminar separation, depending on the velocity and length scales of the flow as well as the imposed pressure gradient, the increased entrainment of fluid (as turbulence develops) leads to reattachment of flow in some cases and reorganizing back to form a normal turbulent flow profile. A region of recirculating fluid is thus created when the above processes are recorded on a time-averaged basis. This forms the laminar separation bubble, otherwise known as a transitional separation bubble. Note that the flow does not reattach if the Reynolds number of the flow is very low, and hence no bubble formation occurs. The reattachment occurs only when the boundary layer can recover enough energy to traverse the adverse pressure gradient. Figure 1.4, adopted from Horton [21] illustrates the features of a laminar separation bubble, at their respective regions in an airfoil. Note that the horizontal surface is scaled to 10 times the vertical surface as the boundary layer effects are pronounced along the streamwise direction. The resultant turbulent boundary layer can handle adverse pressure gradients better without separating from the surface. For example, in a review on the flow over a circular cylinder for $Re_D < 2 \cdot 10^5$ by Roshko & Fizdon [22], transition to turbulence was observed to occur in the free shear layer downstream of the laminar separation point, followed by reattachment and turbulent separation on the back of the cylinder. The laminar separation bubble was, in particular, observed to enable the boundary layer to handle greater than the normal pressure

rise and displaced the separation point further downstream. Thus in a low speed flow over a sharp contoured surface, one way to delay or even eliminate separation, for example, is to artificially inject turbulence by means of devices such as trips, or roughness in the flow prior to the laminar separation point. In addition to this method, there exists various other possible strategies to keep the flow attached, as will be touched upon in the next section of this chapter. These kinds of schemes that attempt to control boundary layer separation are referred to as flow control methods. To highlight the importance of flow control, the detrimental effects of boundary layer separation on the aerodynamic effectiveness of low Re aircraft are presented in the following discussion as an example.

1.1.1 Effects on Aerodynamic Effectiveness

The action of an aircraft wing is merely to push the air flowing on its surface downwards, so as to generate a net aerodynamic reaction force. This force can be resolved into two components, the vertical component being the lift L and the horizontal component being the drag D, as shown in Fig. 1.5. The lifting capacity of the wing is measured in terms of its lift coefficient given by

$$C_L = \frac{L}{\frac{1}{2}\rho U^2 S} \tag{1.9}$$

where S is the surface area of the wing, which in this case, is given by $S = bc$, where b is the span and c is the chord length. From the above equation, it can be observed that the lift force is directly related to the incoming flow velocity U

$$L \propto \rho U^2 b\, c$$

Defining two Reynolds numbers using c and b as the two different length scales and U as the common velocity scale, we get

$$L \propto Re_c \cdot Re_b \tag{1.10}$$

The drag coefficient is defined in terms of drag force is given by

$$C_D = \frac{D}{\frac{1}{2}\rho U^2 S} \tag{1.11}$$

where D represents the total effect of individual contributions from the pressure (form drag), friction (skin friction drag), and lift (induced drag) forces. Similar to the lift in equation 1.10, the drag force can also be shown to be directly related to the Reynolds number of the incoming flow. Thus the wing performance efficiency η, defined in terms of its lift to drag ratio, is therefore a function of Re

$$\eta = \frac{L}{D} = f(Re) \tag{1.12}$$

The maximum lift produced by the wing is usually a linear function of the angle of attack α

$$C_L = f(\alpha)$$

Each wing design has a particular value of stall angle of attack at which the maximum possible lift force is achieved, and any further increase in the aircraft attitude results in a massive deterioration in performance, such that the vehicle lift decreases and drag increases by substantial levels. Stable flight cannot be maintained beyond the stall angle of the wing, and the aircraft is limited to operation only for angles of attack lesser than the stall value,

$$C_{L,max} = f(\alpha_{max}),\ \alpha_{max} \leq \alpha_{stall}$$

An expression that can be used to estimate the maximum angle of attack in the case of unseparated flow is given by Tuck [23],

$$\alpha_{max} = 0.818\sqrt{(r/c)}$$

where r is the nose radius of curvature of the wing.

The performance of low Re airfoils is entirely dictated by the relatively poor separation resistance of the laminar boundary layer. It is foremost important to design airfoils so as to keep the flow attached to the wing surface during the entire operating time of the aircraft. Laminar separation bubbles produced at low Re values affect the performance of the aircraft to a great extent, which can be explained as follows. As the Reynolds number of the flow increases due to higher speed or turbulence, the length of the bubble gets shortened. At high lifts and/or high angles of attack, this short bubble bursts to form a long bubble to cause stall. This process is most often irreversible, and reducing the angle of attack beyond this point would not immediately negate the stall effects. The long bubble formed on the surface of low Re airfoils usually stalls for low angles of attack and lift coefficients before the trailing edge. This leads to a massive deterioration in the airfoil efficiency. Stall causes the flow to separate and results in a sharp increase in drag forces while decreasing the lift. Short separation bubbles are formed at high Reynolds number flows, and tend to have negligible effect on the pressure distribution around the lifting surface. However, long bubbles, characteristic of very low speed flows, significantly affect the pressure distribution by effectively changing the shape over which the potential flow is developed [20]. This greatly reduces the slope of the lift curve and an increase in the pressure or form drag. The lift-to-drag ratio is higher for the airfoil with shorter bubble, and improves with increase in the Reynolds number of the flow. At large incidence angles, the short bubble breaks down to form a long bubble. Further increase of angle of attack causes the point of reattachment

to move downstream until it reaches the trailing edge—where the bubble thickness would have reached around 3% chord. Thin-airfoil stall is caused at high incidences where the flow is completely detached (see Crabtree [24]). Delaying the separation has benefits of reducing the pressure drag, enhancing circulation and hence, the lift produced. Boundary layer separation control is critical for successful aircraft design, and amounts to being a direct indicator of its performance.

1.1.2 Flow Control Methods

The importance of separation control requires research into strategies to artificially keep the flow attached over the surface during the entire time of operation. Flow control methods are used to bring about an advantageous change in the flow development with the purposes of (a) delaying or advancing transition, (b) suppressing or enhancing turbulence, and (c) preventing excessive boundary layer growth and separation (as recognized by Stanewsky [25]). For example, the useful results obtained on aircraft on successful implementation of flow control may include drag reduction and lift enhancement (e.g. Nagib *et al.* [26]). Flow control devices principally affect the energy state of the boundary layer close to the surface, and alter its behavior to be beneficial. In laminar flows the near-wall fluid layer is slowed down and has insufficient energy to overcome both the wall shear and viscous dissipation. Flow control is accomplished by active or passive control methods, a broad classification based on the requirement of external energy input for the process/device. Active flow control devices require external sources of energy and have an inherent advantage of being controllable, viz., they can be switched on and off when required, compared to passive devices that do not require additional energy for their action. Active devices can be driven either by open loop (not regulated by the output) or closed loop control with feedback. Some examples of passive flow control methods that have been used in existing literature are boundary layer trips (Lyon *et al.* [27]), roughness elements (Kerho & Bragg [28]), ejector nozzles (McQuilling & Jacob [29]), and surface perturbations (Miklosovic *et al.* [30], and Santhanakrishnan & Jacob [31, 32]). Some examples of active flow control methods include acoustic excitation as in Zaman *et al.* [33], continuous or pulsed suction and blowing (Seifert *et al.* [34, 35], and Amitay *et al.* [36]), and surface motion (Modi [37], Lee & Gerontakos [38], Santhanakrishnan *et al.* [39], and Pern *et al.* [40]). Detailed reviews of active and passive flow methods can be found elsewhere (see Gad-El-Hak [41] for example).

For the interested reader, a detailed discussion of the flow control problem with analysis of the governing equations can be found in the article by Gad-El-Hak [20]. Some important observations from this article will be merely paraphrased herein. The starting point

is the x-direction momentum conservation equation 1.5 above. To introduce the effects of heat transfer into the above equation, viscosity can be assumed to be affected by temperature ($\mu = \mu(T)$), and temperature can be made to vary in the wall-normal direction ($T = T(y)$) where the gradients are much higher than those in the streamwise direction (following boundary layer analysis). After introducing the above modifications, we obtain the momentum equation in streamwise direction with wall velocity and pressure gradient, which will be the starting point of analysis for flow control. The independent variables identified in the flow control problem are the normal wall velocity, temperature gradient and pressure gradient. The only dependent variable involved is the second derivative of velocity, which needs to be negative for the flow to remain attached. This condition can be achieved by using one or a combination of (a) negative wall velocity; wall suction ($v_w < 0$), (b) positive wall velocity; wall blowing ($v_w > 0$), (c) negative or favorable pressure gradient; streamlining the surface ($\frac{dp}{dx} < 0$), and (d) wall heating in the case of liquids ($\frac{d\mu}{dT} < 0$, $\frac{dT}{dy} < 0$) or wall cooling in the case of gases ($\frac{d\mu}{dT} > 0$, $\frac{dT}{dy} > 0$).

$$\rho v_w \left.\frac{\partial u}{\partial y}\right|_{y=0} = -\left.\frac{\partial p}{\partial x}\right|_{y=0} + \mu \left.\frac{\partial^2 u}{\partial y^2}\right|_{y=0} + \left.\frac{\partial \mu}{\partial T}\right. \left.\frac{\partial T}{\partial y}\right|_{y=0} \left.\frac{\partial u}{\partial y}\right|_{y=0} \tag{1.13}$$

An alternate classification of flow control techniques can be made on the basis of the desired objective—direct boundary layer control for drag reduction; control for lift enhancement and separation suppression (following [20]), and will be explained in more detail below.

A. Direct Boundary Layer Control

This flow control method is used for skin friction drag reduction, which is responsible for a major loss in performance of the aircraft. Transition delaying mechanisms maintaining the laminar flow that occurs over low Re airfoils. Transition control is also used for lift enhancement. Shaping the surface to provide favorable pressure gradient, providing sustained natural laminar flow by active or passive means, or a combination of both are examples of these mechanisms. Leading edge suction is employed to control the amplification of disturbances in the boundary layer. Wall cooling may be employed in tandem to increase the efficiency of the flow control process, and hence of the aircraft. Another important reason for transition is due to low free stream turbulence of the incoming flow. The flow can be accelerated and its turbulence intensity increased by having roughness elements in spanwise direction of the wing. It is most beneficial to have a real time adaptive system to provide surface changes most suited for the incoming flow; such a mechanism with pneumatic elements has been discussed in White *et al.* [42]. Transition may be promoted in

certain cases, particularly when laminar separation is inevitable. Turbulence manipulation devices are used to reduce the skin friction drag in turbulent boundary layer flow. Passive devices used for turbulence manipulation include riblets and other surface modifiers. Riblets have sharp teethed notches that act as boundary layer trips to create turbulence. The profile and spacing between the ribs may be adjusted real time to achieve adaptive control. Large Eddy Breakup Devices (LEBUs) are passive devices to break large structures in the boundary layer to reduce the turbulent skin friction. An active method for turbulence manipulation may include gas injection, polymers, surfactants and particulates in case of hydrodynamic flows; while mass injection or blowing can be used to impart low momentum air into the boundary layer in case of gaseous flows. Micro Electro Mechanical Systems (MEMS) based shear stress sensors and actuators have potential application in interactive turbulence control, and they are considered in detail in Löfdahl *et al.* [43].

B. Control for Lift Enhancement and Separation Suppression

Flow control for lift enhancement is accomplished by the use of trailing edge devices. Gurney flaps and vortex generators are examples of such devices. Flaps, in general, change the effective camber of the airfoil. The change in camber can be manipulated to control separation and thereby increase the lift. Additional increase in lift can be obtained by having tabs—small devices located close to the aft end of the flaps. They have the effect of closing the flap gap created at the joint between the wing and the flap. Consequently, the viscous drag due to separation on the flap is reduced by the flow control exerted by the lift enhancing tabs. Vortex generators (VGs) are geometric flow control devices that produce counter-rotating vortices to cancel out the separation bubbles produced during separation. However, VGs cause an increase in skin friction drag at lower lift coefficients, and are most effective when used for high lift conditions. Pneumatic devices can be used for separation suppression at higher lift coefficients. Zero-mass pulsing jets delay separation by means of excitation of the flow through periodic suction and blowing over the upper surface. In principle, these massless air jets enhance mixing between the near wall shear layer and outer flow to delay separation [25]. Reverse flow flaps are being considered as an alternate means to control separation. They are modeled on the principle of bird feathers during landing. These devices are pivoted to the trailing edge and are self-adjusting to the flow conditions. They deflect upward gradually as the flow starts to separate and control separation, as a result of which they increase maximum lift and limit drag. Although similar in construction to spoilers used in aircraft, they are considerably different in operation. Reversed flow flaps do not extend into the outer flow as in spoilers—which are actually used for the opposite

task of increasing drag and reducing lift associated with landing the aircraft. Divergent trailing edges have similar functionality as Gurney flaps, but are found to produce lesser drag at equal lift coefficients and correspondingly higher L/D values. It is preferable to use Gurney flaps when maximum lift is desired—while divergent trailing edges can be used when efficiency is the main concern. Streamlining the surface of the body reduces the pressure gradient and helps to control separation. Oscillatory excitation of camber has beneficial effects on separation control. Pitch oscillation at various frequencies produces an increase in maximum lift, the effect of which may be related to a delay in vortex bursting (Soltani *et al.* [44]). The oscillation trips the boundary layer and increases the freestream turbulence to delay the separation. Piezo electric material based oscillation of the upper surface has shown positive effects in separation control (e.g. Munday *et al.* [45] and Pern *et al.* [40]). Some of the boundary layer and flow control devices reviewed in this section are illustrated in Fig. 1.6.

1.2 Flow Control with Plasma

Plasma actuators refer to a broad class of devices based on using electrical discharges. The class of discharges may include corona discharges, dielectric barrier discharges (DBDs), glow discharges (such as the OAUGDP$^{\mathrm{TM}}$, one atmosphere uniform glow discharge plasma, see Roth *et al.* [46], and Roth & Dai [47]) and arc discharges. Figure 1.7(a) shows a commonly used construction of an aerodynamic plasma actuator consisting of an asymmetric arrangement of two rectangular-strip electrodes, one exposed to the atmosphere and the other embedded on the surface where it is applied, separated by dielectric material. Under input of a high voltage, high frequency AC or pulsed DC, a region of plasma (in this design, a DBD) is created in the interfacial air gap starting from the region of highest electric field (usually around the electrode edges), due to the electron avalanche breakdown process. This plasma region introduces a coupling between the applied electric field and the ambient air, and for the asymmetric design shown in Fig. 1.7(a), the residual fluid is found to be tailored in the form of a horizontal wall jet synthesized from the working fluid (Fig. 1.7(a)). The input voltage and current controls the nature, type, and intensity of the discharge, hence the induced flow velocity. For instance, the filamentary discharge typically produced in DBD actuators (Fig. 1.7(b)) results in lower induced velocities as compared to the OAUGDP$^{\mathrm{TM}}$ which produces a uniform discharge [47]. Plasma actuators can be readily employed as active flow control devices, and have been shown to control boundary layer separation through their impact on (but not necessarily addition of) near-wall flow

momentum (as suggested by List *et al.* [48], and Jacob *et al.* [49]).

1.3 The Plasma Synthetic Jet Actuator (PSJA)

Conventional plasma actuators, hereon referred to as linear actuators (Fig. 1.7), while useful, are limiting in flow control applications. Essentially, these actuators, whether single or multiple phased arrays, affect primarily the boundary layer flow on a scale of $\mathcal{O}$(1 cm) as shown by the results presented below. Figure 1.8 shows vorticity contours overlaid with streamlines obtained from time-averaged PIV measurements for steady operation of the linear actuator in quiescent flow. The upstream influence of the linear actuator is moderate, and the flow at x=1.2 cm (location of the actuator interface at x=1.4 cm) resembles a potential sink. The thickness or width of the wall jet induced downstream of the plasma is about 0.4 cm. Figure 1.9 shows the horizontal and vertical mean velocity profiles developed by a linear DBD plasma actuator in quiescent flow. The profiles are plotted for 2 stations upstream of the actuator, at the actuator interface (near the region of densest plasma), and 4 stations downstream of the actuator. For this case, the plasma region was generated using a square wave with a frequency of 1.8 kHz and an amplitude of approximately 5 kV. An examination of the vertical velocity profiles reveal that the flow is being drawn into the plasma region, with the highest fluid entrainment occurring at the location of the actuator interface ($x = 0$). The horizontal velocity at the interface is relatively small, and the magnitude at this point is largely due to the vertical downward component. As we proceed further downstream, the velocity increases on account of the wall jet induced by the plasma actuator, and reaches a maximum of roughly 100 cm/s located 1.6 cm away from the interface within the FOV of the experimental observation. The width (or in this case, height) of the jet is confined to less than 1 cm away from the wall. The momentum within this jet is non-negligible, however. Essentially, these actuators, whether single or multiple phased arrays, affect primarily the boundary layer flow on a scale of $\mathcal{O}$(1 cm) as shown by the results above.

To increase the impact that the plasma actuators can have on the flow field, this research proposes to investigate geometric variants of the DBD plasma actuator, so as to leverage the plasma induced jet to create flow fields with a much greater impact. The actuators can be readily arranged such that complex flow structures are created. To enhance the flow control effects obtained on using the conventional linear actuator, a novel design consisting of annular electrode arrays (Fig. 1.10(a)) was investigated, hereafter referred to as the plasma synthetic jet actuator (PSJA). This particular actuator construction tailors

the plasma induced flow in the form of a zero-net-mass-flux (ZNMF) jet, and unlike synthetic jets, these can be easily reversed to act as suction devices by merely inverting the electrode arrangement. Figure 1.10(b) shows the creation of a plasma induced synthetic jet by using such an annular plasma actuator. These can be pulsed to create vortex rings or run continuously to create a steady "synthetic jet." Like synthetic jets, these may be pulsed at any frequency, but unlike synthetic jets, they can easily be reversed to act as suction devices. By modifying the actuator geometry, the plasma induced jets can be arranged such that they create an upward synthetic jet structure or an inverted jet with a downward—then—outward flow. Pulsing the actuator, as shown in phase-locked PIV measurements of a plasma synthetic jet actuator pulsed at 1 Hz in Fig. 1.11, creates two counter-rotating vortex rings that develop into a jet in the steady state, which can be used for either flow control or thrust generation. Pulsing the actuator at a critical frequency allows the continuous development of high strength vortex rings, similar to a pulsed jet.

Likewise, due to their nature, it is theoretically straightforward to modify the actuator geometry to produce three-dimensional structures. Linear actuators acting at angles to one another should produce vortical structures through entrainment of the surrounding flow by the plasma induced jets. Such an example is shown in Fig. 1.12(a), where a chevron actuator is used to generate cross-stream vortices. By varying the angle with respect to the cross-stream flow, the actuator will generate either a co-rotating or counter-rotating vortex pair at the chevron apex. By utilizing the combined effects of synthetic jet like flows of the annular array and vortex generator jet like flows of the chevron pattern, hybrid arrangements can be constructed where the detailed flow field can be controlled as desired. This offers the potential to create complex structures that synthetic jets cannot.

1.3.1 Research Objectives

The purpose of the present work is to develop novel plasma actuator geometries and investigate the detailed structure of the induced flow generated by these novel plasma synthetic jet actuators (PSJA), particularly turbulent characteristics, and demonstrate how this can be leveraged to alter the flow field either directly or indirectly through flow control. Tasks of specific interest to this research are: a thorough examination of the PSJA induced flow physics, and comparison of PSJA laminar/turbulent jet characteristics with conventional mass flux and synthetic (zero-net-mass-flux) jets. For this purpose, detailed measurements of the flow field structure are conducted, both locally and globally, around actuators with varying geometric and input parameters. Input parameters include actuator geometry, input power, and pulsing frequency of jet. The end goals will include verification

of the numerical models and optimization of the actuator output. Some questions that will be addressed in this dissertation include:

- What are the various flow field characteristics of the plasma synthetic jet, such as the maximum jet velocity and momentum?
- How do the PSJA induced flow field characteristics compare to those of conventional linear plasma actuators?
- How do the different observed flow field structures form and evolve?
- How does the plasma interact with the near actuator fluid?
- How does the plasma induced jet interact with a cross flow?
- How do the actuator outputs scale with respect to the various system inputs?

1.3.2 Impact and Importance of Research

The main deliverable from this study is an overall application methodology for plasma flow control applications. The individual items are: (i) an experimental database for plasma actuators, (ii) novel geometries for enhanced plasma actuator flow control, (iii) a set of well documented experiments specifically designed for testing actuator configurations and numerical simulation techniques, and (iv) an improved understanding of plasma actuator behavior. This research will have a broad impact in fundamental understanding, design, development, and application of plasma actuators and associated control systems for various fluid flow applications. Although the use of plasma actuators to control boundary layer and flow separation has received limited attention in recent years, the subject on how to design an effective system for the plasma actuator control devices has received only limited consideration. Once a better understanding of actuator behavior is obtained, this approach can be implemented in numerical simulations (CFD) to optimize the designs and this allows new control strategies to be tested before the devices are fabricated.

1.4 Organization of Dissertation

This dissertation is divided into nine chapters. Detailed reviews of the state-of-the-art of two specific flow control methods related to this research, plasma actuators and synthetic jet actuators, are provided in Chapter 2. Some preliminary results from experiments conducted on the plasma synthetic jet actuator are presented in Chapter 3 to serve as a

background for the reader. The description of the experimental setup, wind tunnel used for the study, actuator construction and diagnostic methods used for this research are presented in Chapter 4. The characteristics of plasma synthetic jets induced in an initially quiescent medium are discussed in Chapter 5, while Chapter 6 examines the interaction of the jet with an external flow. The effects of plasma morphology on the flow field are presented in Chapter 7. Scaling arguments for plasma synthetic jet actuators are discussed in Chapter 8. Finally, the various conclusions of this study, along with suggestions for future work are presented in Chapter 9.

1.5 Tables and Figures

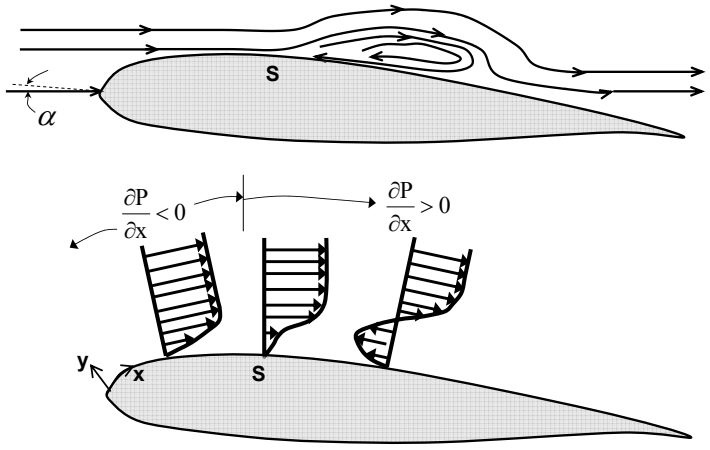

Figure 1.1: Cartoon showing the occurrence of boundary layer separation and reattachment of flow over an airfoil. Streamlines of the flow are shown on the top half, while the x-direction velocity profiles are shown in the bottom half; α is the angle of attack, P is the surface pressure, and S indicates point of separation.

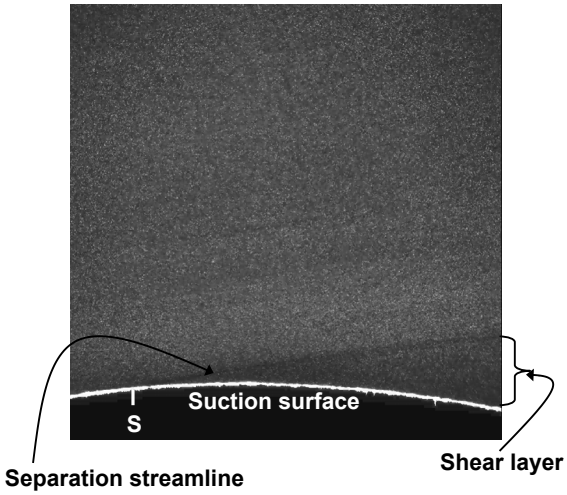

Figure 1.2: Experimental visualization of flow separation on the suction (upper) surface of an Eppler 398 airfoil. Chord length $c = 0.128$ m, $Re_c = 36 \cdot 10^3$, $\alpha = 10°$, S indicates separation point, flow direction is from left to right, and field of view corresponds to $0.22c$–$0.48c$ (from Santhanakrishnan & Jacob [31]).

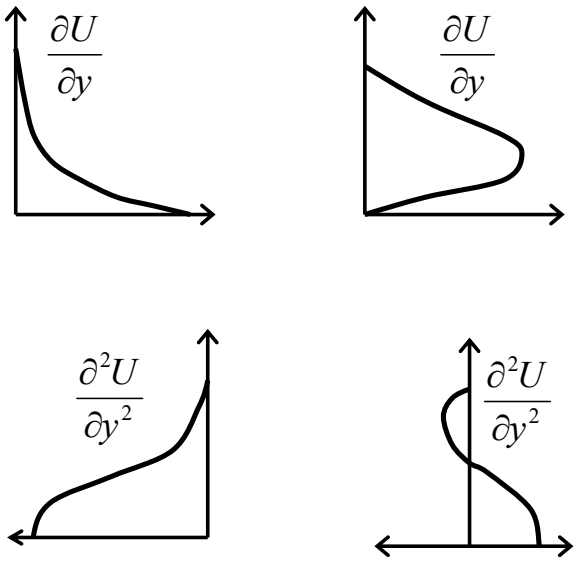

Figure 1.3: Velocity profile gradients of unseparated flow (left half), and at laminar separation (right half).

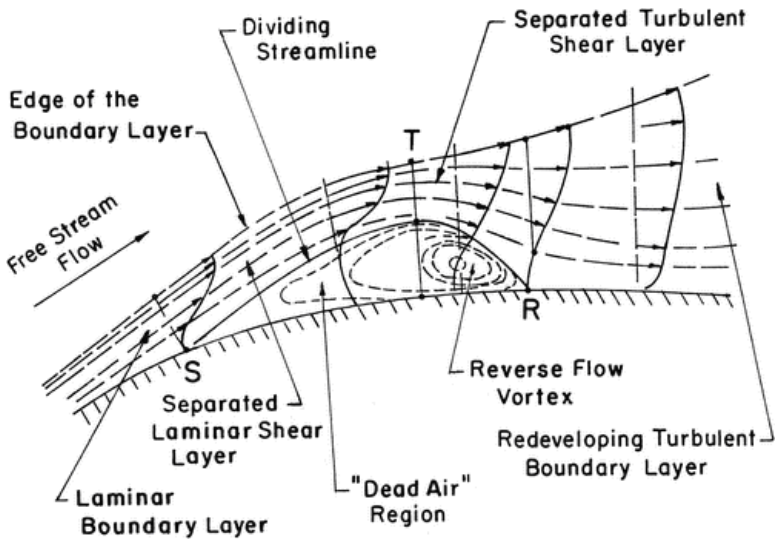

Figure 1.4: Time-averaged features of a low Re transition bubble (from Horton [21]).

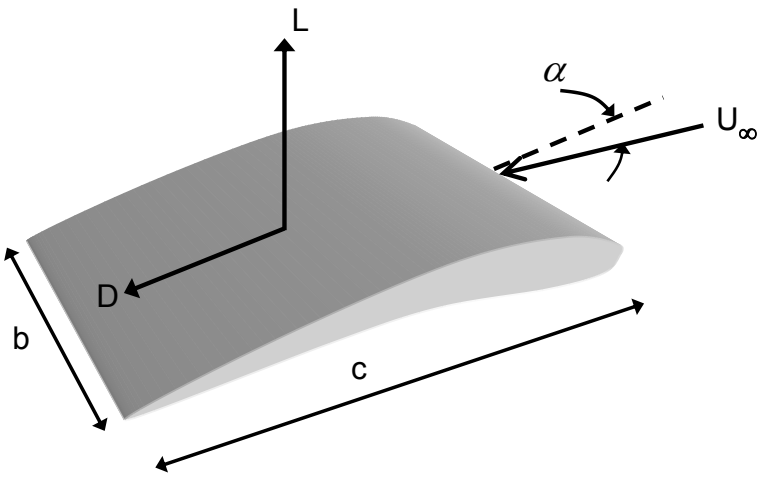

Figure 1.5: Rectangular wing geometry showing aerodynamic loads. α is the angle of attack, U is the free stream velocity, c is the chord, and b is the span.

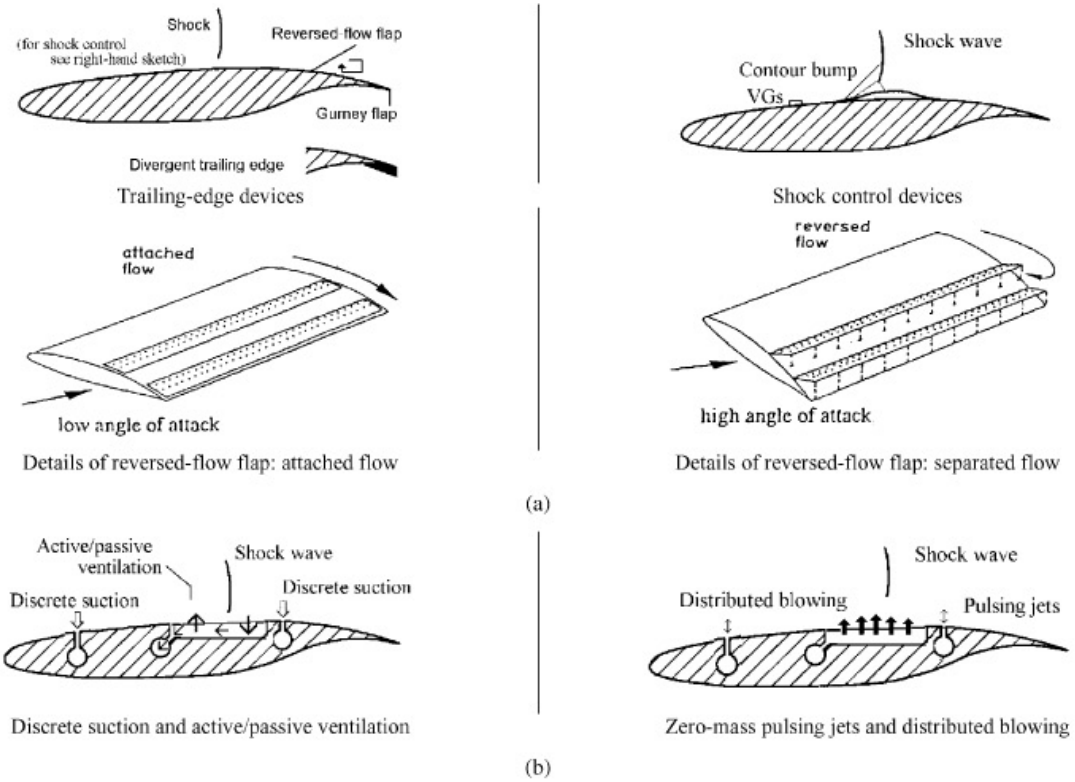

Figure 1.6: Examples of boundary layer and flow control devices on an aircraft wing: (a) Geometric devices, and (b) Pneumatic devices (from Stanewsky [25]).

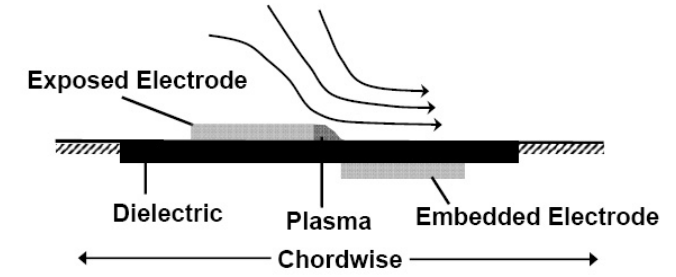

(a)

(b)

Figure 1.7: The linear plasma actuator: (a) cross section (direction of induced flow is shown), and (b) plasma structure in the spanwise direction, image has been inverted for clarity.

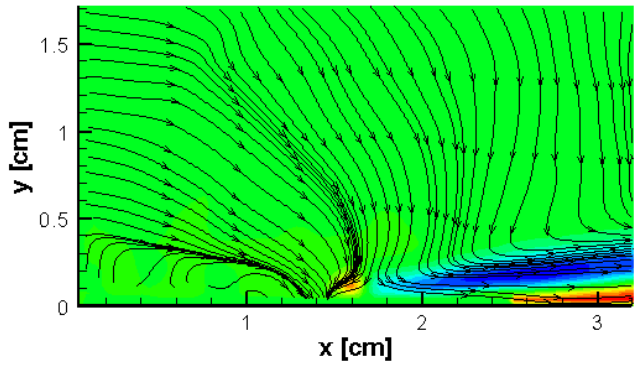

Figure 1.8: Averaged PIV results showing vorticity contours overlaid with streamlines for steady operation of actuator in quiescent flow. Actuator interface is located at x=1.4 cm in the figure.

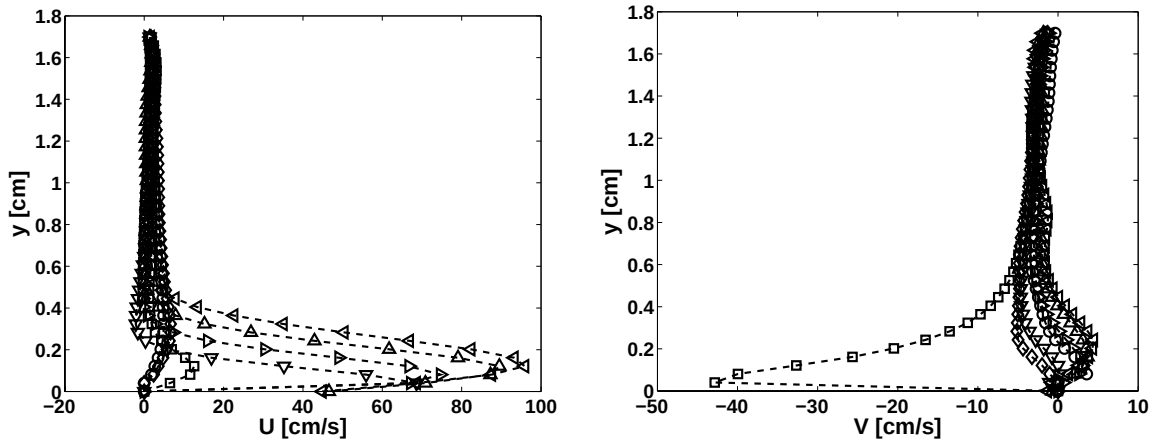

(a) Horizontal velocity U.

(b) Vertical velocity V.

Figure 1.9: Velocity profiles near a linear actuator in quiescent flow. $\circ$, x=0.8 cm upstream; $\diamond$, x=0.4 cm upstream; $\square$, x=0 (at interface); ∇, x=0.4 cm downstream; $\triangleright$, x=0.8 cm downstream; $\triangle$, x=1.2 cm downstream; $\triangleleft$, x=1.6 cm downstream.

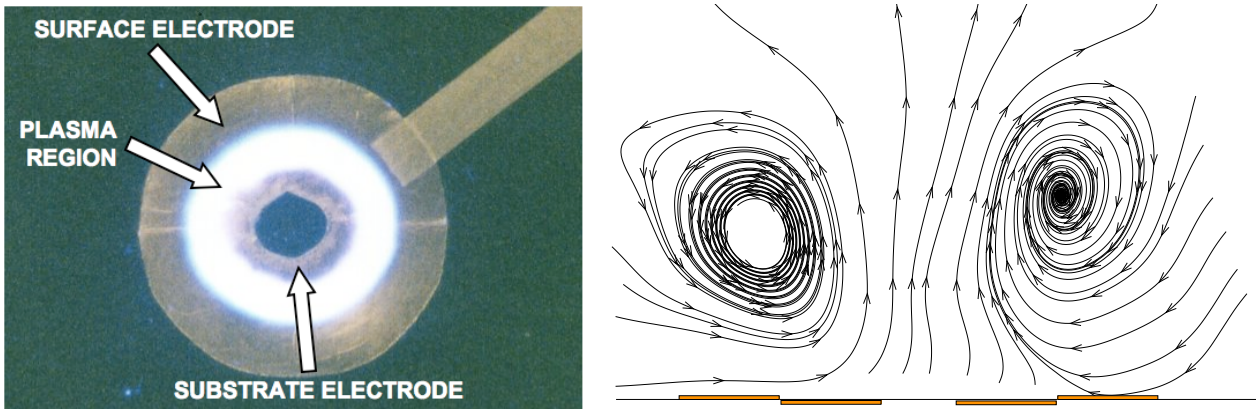

Figure 1.10: (a) Plasma ring created by annular actuator. (b) Cross-stream of vortex created by pulsing an annular plasma actuator.

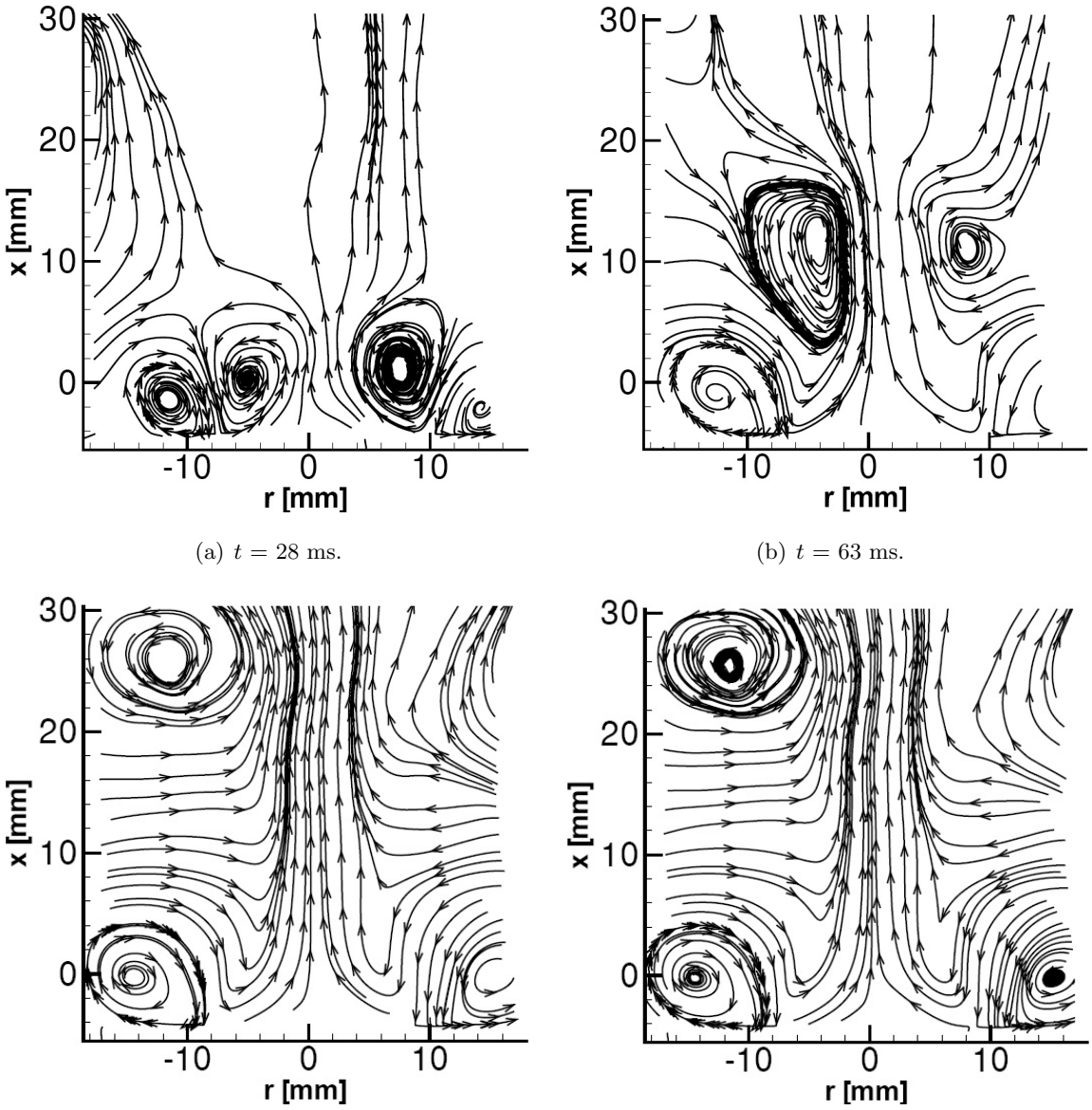

(a) $t = 28$ ms.

(b) $t = 63$ ms.

(c) $t = 153$ ms.

(d) $t = 300$ ms.

Figure 1.11: Streamlines of flow induced by annular plasma synthetic jet actuator pulsed at 1 Hz in quiescent flow obtained from phase-locked PIV measurements, t indicates time of the actuator pulsing duty cycle.

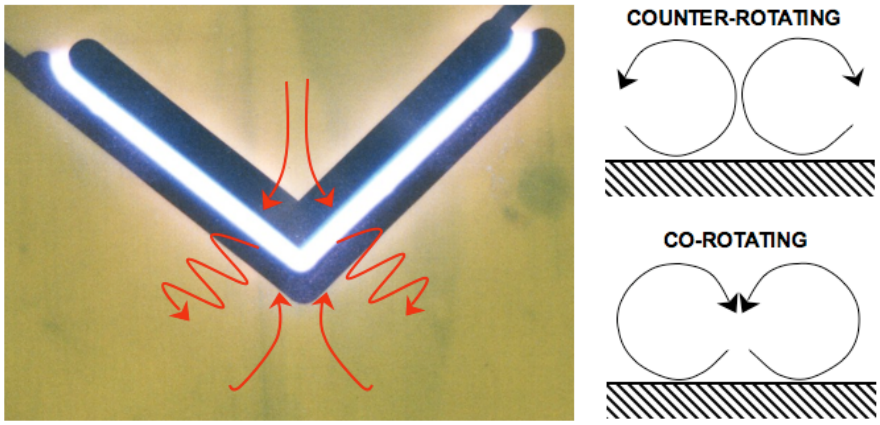

Figure 1.12: (a) Vortices induced by chevron actuator. (b) Cross-stream vortex structures.

Chapter 2

BACKGROUND

2.1 The Physics of Plasmas—Basics

Plasmas are the most common form of matter in the universe. The sun and most other stars, as well as substantial portions of the interstellar medium are in the plasma state. Simply stated, a plasma is an *ionized gas* containing free charges created as a result of the disassociation of its constituent atoms into an approximately equal number of positive ions and negative electrons (Fig. 2.1(a)). Plasmas are often referred to as the "fourth state of matter" in order to distinguish their behavior compared to the other common states. In the case of an ordinary fluid, intra-molecular collisions dominate and determine the resultant motion of the flow. The interactions between individual particles occur within extremely small distances in both fluids and solids. In the case of a plasma, the *charged particles* are relatively free to move, and collisions are not as important a predictor of motion. The motion of the free charges result in setting up electric and magnetic fields on account of spatially localized charge concentrations and induced currents, and the effects of these fields are percieved in a rather "global" sense across a large spatial domain in the plasma. Thus, long-range forces between large numbers of particles are important in a plasma (often referenced to as "collective" behavior, see Chen [50], Gurnett & Bhattacharjee [51]), in direct contrast to the short-range forces between individual particles in both solids and fluids.

2.1.1 Formation Criteria

The simplest method to produce a plasma is to elevate the temperature of a gas to a level where the electrons in a nominally bound state are excited sufficiently to disassociate from the nuclei of the respective atoms. The energy required for this process can be supplied externally through direct heating or by means of an applied electric field. Plasmas generated in this manner are also known as discharge plasmas and are of specific interest to the research presented in this dissertation (see Fig. 2.1(b)). Depending on its composition, the temperature required to create such a "breakdown" of a gas may vary widely. For instance, the temperature required for ionization of pure cesium is around 4000 K (see Lieberman & Lichtenberg [52]), while that for air at atmospheric pressure is approximately 2000 K (see Kruger *et al.* [53]). The density of a discharge plasma is usually a small fraction of the

neutral gas density. Depending on the fractional ionization coefficient given by,

$$x_{iz} = \frac{n_i}{n_g + n_i}$$

plasmas can be categorized into fully ionized ($x_{iz} \approx 1$) and weakly ionized ($x_{iz} << 1$) plasmas, where n_i and n_g are the number densities of ions and neutral gas, respectively. [52] However, any ionized gas cannot be considered a plasma, and a set of criteria required for plasma formation can be identified. In this regard, a slightly rigorous definition of a plasma by F. F. Chen from *Introduction to Plasma Physics and Controlled Fusion* [50] is worth noting:

> *A plasma is a quasineutral gas of charged and neutral particles which exhibits collective behavior*

The collective behavior of plasmas was discussed earlier in this section, and the other important requirements suggested by the above definition are now examined. As the name suggests, *quasineutrality* is used to refer to the fact that the number density of positively charged ions is approximately equal to the number density of negatively charged electrons. However, in order to respond to applied electric fields, such as in the case of electrical discharge plasmas, a net charge imbalance is required. Unlike electrically conductive gases, plasmas respond to an applied external field through the displacement of its free charges in an independent manner, rendering it a complex problem for analysis. With the exception of a cold plasma (such as in the interstellar medium), thermal losses and motions are primarily responsible for creating charge imbalances within most other plasmas (such as the weakly-ionized discharges of interest here). The electrons have higher mobility than ions on account of their lower masses ($m_e/m_i << 1$). The mobility difference directly translates to increased thermal velocities of electrons as compared to ions. At the beginning stages of formation of an electrical discharge plasma (Fig. 2.1(b)), the *applied potential* heats all the particles within the plasma evenly, resulting in a net charge density given by

$$\rho = e\,(n_i - n_e) = 0$$

which represents a perfectly neutral plasma with zero electric potential and field strength. After a small fraction of time has elapsed, thermal motions of charged species are initiated near the edges of the plasma, where the electric potential is weaker than the bulk region. This is mostly on account of the absence of any confining field in the neutral plasma, which allows the lighter and fast-moving electrons to impinge on and be absorbed by the grounded electrode surface, resulting in a decrease in their number density such that $n_e << n_i$. A thin

cloud or *sheath* with a net positive charge is thus formed near the edges of the plasma. It is important to note that the length of the plasma sheath is much less than the characteristic length scale of the system, say the electrode dimensions. Due to the charge imbalance set up within the edges of the plasma, the applied external potential drops to zero along the plasma edges, which can be explained as follows, starting from the Maxwell's equations in vacuum

$$\epsilon_0 \nabla \cdot E = \rho \tag{2.1}$$

$$\nabla \times E = -\frac{\partial B}{\partial t} \tag{2.2}$$

$$\nabla \cdot B = 0 \tag{2.3}$$

$$\nabla \times B = \mu_0 \left(J + \epsilon_0 \frac{\partial E}{\partial t} \right) \tag{2.4}$$

$$B = \mu_0 H$$

where E is the electric field, B is the magnetic induction, H is the magnetic field, J is the total current density, ρ is the total charge density (ions and electrons), μ_0 is the magnetic permeability and ϵ_0 is the electrical permittivity of free space. For a time invariant electric and magnetic field, the curl of electric field strength E is zero from equation 2.2, as a result of which E can be defined as the negative gradient of a scalar potential ϕ

$$E = -\nabla \phi,$$

Substituting this expression in the relation between applied field and charge density ρ given by equation 2.1, we obtain

$$\epsilon_0 \nabla \cdot (-\nabla \phi) = \rho \tag{2.5}$$

$$-\epsilon_0 \nabla^2 \phi = e\,(n_i - n_e) \;\; \Rightarrow \nabla^2 \phi = \frac{e}{\epsilon_0}\,(n_e - n_i)$$

As $n_e << n_i$ within the sheath region, the right hand side of $\nabla^2 \phi$ is rendered negative, resulting in a decrease in the electric potential along the edges of plasma. The electric field within the plasma is directed outwards from the bulk central region toward the sheath. The force acting on the electrons, given by $-eE$, is directed inwards to the plasma, due to which electrons near the wall are deflected back into the bulk portion. Similarly, the ions are directed away from the plasma into the sheath region. Large charge imbalances leading to local changes in electric potential are hence shielded out within the sheath region, leaving the rest of the plasma quasineutral, viz., $n_i \approx n_e$, wherein time-averaged and instantaneous potentials (and electric fields) are sufficiently low [52]. The characteristic dimension of this sheath region is termed *Debye length* λ_D, and this represents the length scale over which charge density imbalances can exist. For lengths greater than λ_D, the plasma shields out

external electric potentials applied to it. To obtain an expression for λ_D, it is useful to start with the Boltzmann relation relating number density of charges with the corresponding temperature (see [50] for details)

$$n_s = n_0\, exp\left(\pm\frac{e\phi}{KT_s}\right)$$

where s indicates the type of species, K is Boltzmann's constant, n_0 is the background density in the unperturbed state (when $\phi \to 0$), and the exponential function is positive for electrons and negative for ions (Enloe *et al.* [54]). The net charge density therefore becomes

$$\rho = e\left(n_i - n_e\right) \approx -e^2 n_0 \phi\left[\frac{1}{KT_i} + \frac{1}{KT_e}\right].$$

The left hand side of the above equation can be written in terms of potential as

$$-\epsilon_o \nabla^2\phi = -e^2 n_0 \phi\left[\frac{1}{KT_i} + \frac{1}{KT_e}\right].$$

A minor rearrangement of terms results in a second order differential equation containing a quantity having the units of length, and can be solved to obtain electric potential in the plasma

$$\nabla^2\phi = \underbrace{\left(\frac{e^2 n_0}{\epsilon_0}\left[\frac{1}{KT_i} + \frac{1}{KT_e}\right]\right)}_{\propto\, length^{-2}}\phi. \tag{2.6}$$

The Debye length can be defined as the inverse square root of the quantity noted above

$$\lambda_D = \sqrt{\left[\frac{e^2 n_0}{\epsilon_0}\left(\frac{1}{KT_i} + \frac{1}{KT_e}\right)\right]^{-1}}. \tag{2.7}$$

For an electron densities of 10^{12} cm^{-3}, typical values of λ_D are $\mathcal{O}(10\,\mu m)$ [52]. For length scales of the fluidic system L much greater than λ_D, the plasma remains quasineutral. Thus, a condition for a weakly ionized gas to behave as a plasma is

$$\lambda_D << L$$

The concept of electrostatic shielding will be valid only if there are sufficient number of particles within the sheath region to arrive at reasonable averages. If the plasma sheath region is approximately spherical (for illustration), then the number of particles N is given by

$$N = n_0\left(\frac{4}{3}\pi{\lambda_D}^3\right)$$

To behave in a collective manner defined in the earlier part of this chapter, we have the next criterion required for plasma formation

$$N >> 1$$

The final requirement is related to the rate of collisions within the plasma. Particles in ionized gases (that do not qualify as a plasma), in general, exhibit a tendency to collide frequently with neutral atoms such that they exchange momentum through hydrodynamic forces. The motion of particles within a plasma, however, is controlled primarily by electromagnetic forces. If ω is the frequency of plasma oscillations and τ is the mean time between collisions, then $\omega\tau > 1$ is required to be satisfied by a weakly ionized gas to be a plasma [50].

2.1.2 Modeling

Due to the high density of particles in a fluid, the motions of individual molecules can be safely neglected within the confines of the continuum hypothesis. The density of particles in a plasma is $\mathcal{O}(10^{12})$ ion-electron pairs per cm^3, which is in between that for typical fluids and extremely low-density devices. In addition, the effects of collisions in a plasma are not as important as in a fluid, but are still non-negligible. Consequently, plasmas tend to sometimes behave like fluids and like a set of individual particles during other times, rendering their behavior inherently difficult to analyze. Depending on the kind of behavior that the plasma exhibits, two different modeling approaches are commonly employed to describe the plasma state.

Kinetic theory based models are employed for detailed plasma characterization, in which the location, velocity and electric potential distribution of each individual particle in the plasma are calculated as a function of both space and time. An example of this approach may be seen in the *particle-in-cell* (PIC) method (see Li and Dhali [55] for example), where the effect of many thousands or millions of individual particles are grouped together into a single computational particle. The spatial trajectory, velocity distribution, electric and magnetic fields of thousands or millions of these computational particles are computed in a time-varying manner. The charge distribution in the plasma is computed from the positions of the particles, and is used for the calculation of electric potential by solving the Poisson's equation. The local electric fields are then calculated as the gradient of the electric potential. The local magnetic fields are computed similarly based on the particle positions. The electromagnetic force experienced by each particle is determined from the above electric and magnetic fields. This force is used to update the velocity and particle positions for the next step in time, where the above set of steps are again repeated. Essentially, the motion of the charges are influenced by the applied electric and magnetic fields, as well as contribute to them. As expected, this method of describing a plasma is computationally intensive, but is necessary in the case of low-density, "collisionless" plasmas.

Fluid theory based models are employed in the case of high-density or weakly ionized plasmas, in which the plasma behavior is approximated to be similar to a fluid containing electrical charges. The effects of collisions between the individual particles are therefore neglected, and the plasma is described in terms of global continuous variations in density, velocity, etc., similar to the Eulerian description of a fluid flow field. The approach herein is to first compute the electric and magnetic fields for a given state of plasma using Maxwell's equations in vacuum, presented above in equations 2.1–2.4. The charge and current densities can be related to the number density n, particle charge q and *average* drift velocity u of the respective charge species (i for ions and e for electrons) as

$$\rho = n_i q_i + n_e q_e \tag{2.8}$$

$$J = n_i q_i u_i + n_e q_e u_e \tag{2.9}$$

The complexity of the kinetic model is reduced herein by assuming a distribution function for the particle positions and velocities. The *macroscopic* characteristics of the plasma are then described by averaged quantities such as charge density, drift velocity and energy. In the fluid model, the plasma is considered to consist of two or more *interpenetrating* fluids [50], which reduce to ions and electrons in the simplest case. The fluid equations of motion (mass and momentum) are then solved for each species separately. Since this model is usually applied for *weakly ionized* plasmas, another equation for the neutral or background gas is also required. The conservation of mass requires that total number of charged particles of any particular species s (e.g. s=i for ion) in a given volume of plasma remains constant, and is given by

$$\frac{\partial n_s}{\partial t} + \nabla \cdot (n_s u_s) = n_{s,C} - n_{s,D} \tag{2.10}$$

where $n_{s,C}$ is the number of particles created and $n_{s,D}$ is the number of particles destroyed (per unit volume) due to chemical reactions such as ionization or recombination that occur during collisions. The average drift velocity u is obtained by solving the fluid dynamic equations for each species of particles contained in the plasma. The effects of electric and magnetic fields determined from the Maxwell's equations are included in the fluid dynamic equations through the Lorentz force term given below

$$f_s = F_s n_s = q_s n_s \left[E + u_s \times B\right] \tag{2.11}$$

where f_s is the Lorentz force F_s per unit volume of charge species s. The conservation of fluid momentum per unit volume can then be written as

$$mn\frac{du}{dt} = f_s$$

Employing the definition of the advective derivative from standard fluid mechanics literature, we can reduce the above equation to

$$m_s n_s \left[\frac{\partial u_s}{\partial t} + (u_s \cdot \nabla) u_s \right] = f_s$$

Note that in the above momentum equation, the effects of collisions and thermal motions, if any, have been neglected. The effect of random temperature driven motions is typically described by a pressure gradient term ∇P. It must be noted herein that collisions become important when considering weakly ionized plasmas. The ions and electrons interact with each other through the electric and magnetic fields they generate. Each of these species interacts with the neutral gas (without any charges) only through collisions. If the collision frequency is denoted by ν_s and the velocity of the neutral fluid is U, then the collisional force per unit volume is given by

$$f_{s,c} = m_s \nu_s (U - u_s)$$

The overall conservation of momentum for each "fluid" within the plasma, which includes charged species plus neutral gas, is therefore given by

$$m_s n_s \left[\frac{\partial u_s}{\partial t} + (u_s \cdot \nabla) u_s \right] = q_s n_s [E + (u_s \times B)] - \nabla P + m_s \nu_s (U - u_s) \tag{2.12}$$

The pressure field in the above equation is unknown, and is determined from a thermodynamic equation of state. One such commonly employed treatment considers an isothermal relation for an assumed *Maxwellian* velocity distribution

$$P_s = n_s K T_s \tag{2.13}$$

where K is the Boltzmann constant, and T_s is the average temperature of the particular charged species. Equations 2.1–2.13 represent the total set of equations that must be solved as a self-consistent problem in order to fully describe a plasma using the fluid model.

2.2 Plasma Actuators

A brief review of the existent research on plasma actuators, with some recent developments in the state-of-the-art is presented in this section. The articles by Rivir *et al.* [56], Suchomel *et al.* [57], Corke & Post [58], and Moreau [59] present detailed reviews of the developments in plasma flow control, and can be referred to for further information. The early efforts that examined modulation of a fluid flow in the presence of electrostatic fields employed corona discharges. These discharges are created typically with DC excitation

and the voltage inputs required are lower than those of DBDs. Harney [60] first examined the effect of a corona discharge introduced on the inner walls of a cylindrical tube under both quiescent conditions and with (internal) cross flow velocities as high as 60 m/s. A one dimensional theoretical model of the interaction of the electric field of the discharge with the surrounding atmospheric pressure air was proposed, where only a single charged species was considered. The effect of the electric field of the discharge was conjectured to introduce a pressure gradient in the flow, which was in turn expressed as a function of the applied current density and a constant ion mobility. Peak induced velocities of approximately 4 m/s was reported for voltage inputs in the order of 12 kV and 9 μA current input. The model predictions compared within 1% of experimental measurements of the pressure difference across the discharge. Malik *et al.* [61] used DC corona discharge (which occurs at lower voltage and current inputs than DBDs) to manipulate flat plate boundary layers with a drag reduction in the order of 20% for freestream velocities up to 30 m/s and 15 kV applied voltage. They concluded that drag reduction was largely voltage-dependent and that it would be necessary to use multiple discharges to obtain higher efficiencies. Numerical investigations of corona discharge induced drag reduction in flat plates at low Re (see for example Rosendale *et al.* [62], and El-Khabiry & Colver [63]) show that the "ion wind" strongly affected the skin friction distribution, and the drag reduction diminished with increasing freestream velocity and decreasing potential difference between the wire electrodes. Other experiments (such as Artana *et al.* [64] and Moreau *et al.* [65]) have also used corona discharge to modify the flow over a flat plate at flow velocities up to 25 m/s, and they observed non-negligible near wall flow accelaration that was uniform in the spanwise direction. Roth *et al.* [66] used glow discharge surface plasma to control boundary layer flow on flat plates and observed that asymmetric spanwise electrode strip configurations produced thrust, while symmetric spanwise electrode strip configurations increased drag. They attributed these effects to be the result of a combination of mass transport and vortical structures induced by electrohydrodynamic body forces. The literature reviewed hereon pertains primarily to the asymmetric DBD plasma actuator configuration presented in chapter 1.

The application of plasma actuators to flow control in low pressure turbine (LPT) blades has been investigated by several groups. Rivir *et al.* [56] investigated the use of high frequency AC and pulsed DC sources of excitation. Uniform AC atmospheric glow discharges were obtained for a number of parameters while uniform pulsed DC glow discharges were obtained for pulse widths from 22 ns to 2 s with input voltages up to 11 kV. List *et al.* [48] examined the use of a plasma actuator in a LPT cascade for separation

control over a range of Re from 30,000 to approximately 200,000. They used a triangular waveform as the excitation signal and measurements were made using thermal tufts and wake surveys. The measurements indicated that the plasma actuator added momentum to the flow, eliminating the separation bubble. Hultgren & Ashpis [67] investigated the use of plasma flow control (PFC) on a flat plate under an adverse pressure gradient simulating the conditions of LPT loading over the Re range from 30,000 to 300,000 and low (0.2%) and high (2.5%) FSTI conditions. The plasma actuator was a spanwise-oriented—phased-plasma-array device. Hot-wire and pressure measurements indicated the ability to control separation, particularly in the low turbulence, low Re regime. Extensive experimental investigations using hot-wire anemometry (see Huang *et al.* [68]) and particle image velocimetry (see Ramakumar [69]) suggest that the actuators would have to be placed slightly upstream of the separation location, for control to be most effective. Huang *et al.* [70] observed that an optimum forcing frequency was found to exist for unsteady operation of plasma actuators, such that the Strouhal number based on separated flow length and local freestream velocity was unity.

In the area of flow control applications, Corke *et al.* [71] used weakly-ionized plasma actuators for lift enhancement on a NACA 0009 airfoil. While lift was increased during actuation, drag was also increased, providing only minor improvement. The drag increase was eliminated by using actuators in series. PIV measurements of Post [72] showed that a jet was formed immediately downstream of the actuator. Discussions do not form a firm conclusion as to the physical mechanism of the lift enhancement, though the drag increase is explained using PIV and DNS information. Asghar & Jumper [73] examined the use of PFC for phase synchronization of the KVS from multiple cylinders. They were effectively able to modify the natural out-of-phase vortex shedding and force an in-phase vortex shedding behavior for a pair of cylinders. McLaughlin *et al.* [74] used plasma actuators to control the structure of the Karman vortex street by using feedback results from measurements of the shedding frequency to drive the actuator frequency. Likewise, Siegenthaler *et al.* [75] investigated the use of a single PFC actuator to control the coherent structures in a planar, weakly compressible, free shear layer.

Corke *et al.* [76] demonstrated the use of plasma actuators as virtual flaps and slats for airfoil flow control. Actuators located at the leading edge can control separation while actuators placed at the trailing edge can control lift. Post & Corke [77] showed that plasma actuators can be used to control airfoil stall in a dynamic pitching motion. While drag was not measured, there was measurable improvement in the lift over the oscillation cycle using different steady and unsteady modes of plasma actuation. Thomas *et al.* [78] investigated

the application of plasma actuators for landing gear noise reduction. Multiple actuator elements were mounted along the circumference of both upstream and downstream parts of a generic landing gear strut with cylindrical cross-section. Reduction of both drag and vortex shedding was obtained with steady actuation, and drag reduction was found to be be inversely related to Re. Alternate strategies for noise control using base blowing (to control vortex shedding) and vectoring the upstream wake were discussed. Recent results include Corke *et al.* [79] where plasma actuators were used for lift enhancement on a natural laminar flow airfoil (HSNLF(1)–0213). The actuator was located just upstream of the laminar separation point, and both experimental lift measurements and numerical simulations were used to optimize the unsteady operation for chord based Re of 215,000. The most number of plasma actuator based application studies are found in separation control at low Re (see Goksel *et al.* [80], and Sosa & Artana [81]). While most of the above applications are restricted to incompressible flows, some high speed applications such as in axisymmetric jet forcing using arc plasma based configurations have been reported (see Samimy *et al.* [82, 83]).

Enloe *et al.* [84, 54] presented numerous findings on the behavior of plasma actuators. Based on large scale integral measurements of thrust output, voltage and plasma emission measurements, and simulations, the authors make several interesting conclusions, including that the power input, P, to the plasma is nonlinear with the voltage drop, ΔV, across the dielectric, and that both the maximum induced velocity, u_{max}, and thrust, T, are proportional to input power, such that

$$T \propto u_{max} \propto P \propto \Delta V^{7/2} \tag{2.14}$$

In addition, their measurements found that the plasma has complex spatial and temporal structure, the creation of plasma occurs on both the positive and negative slopes of ΔV and is dependent upon $d\Delta V/dt$. Also, thrust is greater for a "positive" waveform as opposed to a "negative" waveform, even though the bulk plasma structure is the same. This observation implies that bulk heating is not the mechanism for thrust generation, as some researchers (such as Leonov *et al.* [85]) have previously speculated, as the "positive" waveform produced a more uniform discharge. Their final conclusion is that the plasma induces an electrostatic body force per unit volume f on the surrounding fluid that is proportional to the net charge density and the strength of the electric field. The basis of their argument stems from the Lorentz force equation 2.11, already defined above. The magnetic field effects are ignored, most ostensibly due to the low velocities of the charged particles, resulting in the expression

below

$$\vec{\mathbf{f}} = q_s n_s E = \rho E. \tag{2.15}$$

The net charge density can be expressed as a function of the electric potential, starting with equation 2.5 above

$$\rho = -\epsilon_o \nabla^2 \phi.$$

The Laplacian of electric potential is given by equation 2.6, which in turn is in terms of Debye length defined in equation 2.7. Combining all the above, we obtain

$$\rho = -(\epsilon_o / \lambda_D^2)\phi.$$

The body force per unit volume of plasma is thus given by substituting the above relation for charge density in equation 2.15:

$$\vec{f} = -(\epsilon_o / \lambda_D^2)\phi E. \tag{2.16}$$

Presently, this model serves as the basis for much of the current plasma actuator development. They observed that the direction of the plasma induced flow can be tailored by the electrode arrangement, which is important to the current study. Experimental measurements of the induced velocity by Forte *et al.* [86] at the start and stop of the discharge reveal that the ionic wind in a DBD actuator is actually generated in a periodic manner, showing that the actuator does not behave the same in positive and negative portions of the input AC cycle.

Several factors including input power, input voltage, input frequency, electrode geometry, actuator orientation, dielectric material, dielectric thickness, free stream Re, pressure gradient, plasma chemistry and air humidity have been shown to affect the behavior of a plasma actuator. Baughn *et al.* [87] measured velocity profiles at several locations upstream and downstream of a plasma actuator, and calculated the body force using a control volume momentum balance approach. They observed that the force was not affected in the presence of an imposed cross flow (for free stream velocities in the order few meters per second), and the extent of the force was limited to well within the boundary layer. Also, the body force production decreased with input AC frequency (between 5 kHz and 20 kHz) for nearly constant input power. Porter *et al.* [88] measured the body force produced on steady operation of a plasma actuator, and examined the effects of individually varying input AC voltage and frequency. They conclude that the time-averaged body force is: (a) linearly proportional to input AC frequency between 5 kHz and 20 kHz (for constant input voltage), and (b) non-linear with the input voltage (for constant frequency). Further, they

observed that the actuator "pushes" (with higher magnitude) and "pulls" (with lower magnitude) the fluid in opposing directions during each cycle. Balcer *et al.* [89] used plasma actuators on a flat surface with adverse pressure gradient resembling the suction surface of a low pressure turbine blade, and the exposed electrode was oriented sixty degrees to free stream direction. While an increase in near-wall velocities was observed on actuation, the skewed electrode orientation did not introduce any substantial longitudinal vorticity in the boundary layer.

Roth & Dai [47] present detailed investigations on the effects of changing dielectric material, electrode geometry, input frequency and input voltage on the flow velocity induced by the OAUGDP$^{\mathrm{TM}}$ actuator. It was observed that the choice of dielectric material affects plasma volume, distribution of electric field lines (dictated by the dielectric constant value), and dielectric heating power loss (which in turn, is proportional to input AC frequency and electrode area). In general, a material combining all these properties was recommended, higher dielectric constant value (e.g., alumina), higher dielectric strength (e.g., Kapton) and lower heating loss factor (e.g., quartz and Teflon). Compared to quartz, Teflon was found to generate a higher value of induced flow velocity for lower power input and was used as the dielectric material for their remaining parametric studies. The width of the embedded electrode was found to have negligible effect on both the maximum induced velocity and input power per unit length of the actuator. The separation distance between the edge of the exposed and embedded electrodes was adjusted to have variable gap, zero gap, and overlap between electrodes, with all other parameters being the same. This variation had a significant effect on the induced velocity, and a 1–2 mm gap width was found to be optimum for their actuator. The maximum induced velocity was found to increase with input voltage (at constant frequency) and input frequency (at constant voltage) to a certain level, after which it reached a constant value and later started to drop with any increase. VanDyken *et al.* [90] observed that a thicker dielectric would be able to handle higher input voltage, and an optimum input AC frequency (to obtain maximum body force) existed for a specific dielectric. Enloe *et al.* [91] speculated that the lifetime of the plasma was related to the presence of negative oxygen ions in the air. Anderson & Roy [92] showed that the skin friction coefficient produced by a plasma actuator mounted on a flat plate varied with the relative humidity of air. Forte *et al.* [93] conducted a detailed parametric study on the DBD plasma actuator with the objective of maximizing the plasma induced jet velocity. They examined the effects of variation in electrode gap, embedded electrode width, dielectric material thickness, input AC frequency, input voltage, substrate material and multiple actuator arrays on the maximum plasma induced jet velocity. A non zero

value of electrode gap was found to exist for maximum velocity, while the maximum velocity varied asymptotically with the embedded electrode width, input voltage and frequency. The dielectric material thickness was found to affect the breakdown voltage and consequently, the nature of the discharge. A filamentary discharge arising from a thinner dielectric, while increasing the maximum induced velocity, was found to damage the material. To have a more uniform discharge, increasing dielectric thickness was recommended.

While a vast majority of plasma flow control literature is primarily experimental in nature, several methodologies for numerical modeling of plasma actuators have been investigated. Most of the current models typically use an electrohydrodynamic (EHD) body force term to simulate the effect of a plasma actuator on the external flow. Shyy *et al.* [94] considered a linear approximation for the electric field distribution within a plasma region consisting of a triangular area located above the embedded electrode. The time-averaged electrostatic body force acting on the fluid was computed and then added to the 2-D steady, incompressible, Navier–Stokes equations to solve for the entire flow field. A similar approach of specifying the charge distribution and spatial distribution of electric field has been used recently by Visbal & Gaitonde [95] to investigate effects of both steady and unsteady plasma actuation on a 3-D flow. Hall *et al.* [96] adopted a potential flow approach to model the behavior of a plasma actuator, where a doublet element was used to mimic the actuator-induced velocity field. Orlov & Corke [97, 98] used the body force expression developed by Enloe *et al.* [54], and a lumped electric circuit model was used to compute the electric potential and volume of plasma. Boeuf & Pitchford [99] conducted a numerical study of the electrohydrodynamic force exerted by a dielectric barrier discharge in a neutral fluid. They observed that the force acting on the flow was significant only within distances very close to the plasma region. Suzen *et al.* [100, 101] computed the body force as the product of net charge density and electric field as observed earlier by Roth [102], and this was introduced as a source term in the Navier–Stokes equations. The electric field was obtained from Maxwell's equations as the gradient of scalar electric potential, and another equation for charge density was solved. In contrast to the simplified treatment used in the above models, some researchers have used a more elaborate particle physics and plasma chemistry based approach. Font *et al.* [103, 104, 105] used a particle-in-cell direct-simulation-Monte-Carlo (PIC—DSMC) method to model the interaction between various ionic species, and numerically solve for electric potential. The model developed by Roy *et al.* [106] solves for drift-diffusion form of equations governing dynamics of ions, electrons and fluid. Shang [107] solved the time-dependent Maxwell's equations along with particle concentration equations to compute the electromagnetic field distribution of a dielectric

barrier discharge.

Besides the beneficial attributes of ease of construction, high operational bandwidth, large control authority and excellent dynamic response, the actuator geometry can in itself be varied to create complex flow structures. This has important implications on the use of plasma actuators in flow control.

2.2.1 Plasma-Neutral Gas Interaction Mechanisms

While there is an extensive database on flow control applicability studies of these devices, specific details on the plasma-bulk fluid interaction still remain largely unclear. Amidst the volumes of research works, very few investigations have actually shed some light on the physical mechanisms with which these devices affect the near wall fluid flow. Roth *et al.* [66, 108] conjectured that the OAUGDP$^{\mathrm{TM}}$ actuator creates a charge buildup in the inter-electrode gap due to "ion-trapping" at time scales larger than the period of applied voltage. This effectively produced Lorentzian collisions between the ions and the neutral gas atoms. A paraelectric electrohydrodynamic (EHD) body force, proportional to the gradient of electric field strength, was attributed to being the reason for the observed flow field effects. No explanations were provided as to how the discharge produced by the actuator was self-sustaining. Enloe *et al.* [84] refuted the above theory on the grounds that dielectric barrier discharges occur in much smaller time scales ($\mathcal{O}(10^{-6}\mathrm{s})$) than that of the applied duty cycle, and this would therefore prevent the accumulation of ions at any particular spatial location. While they also related the flow field effect of the plasma through an EHD body force, the explanation of its origin was substantially different than the OAUGDP$^{\mathrm{TM}}$ model, as follows. The dielectric material in between the exposed and embedded electrodes acts as a virtual electrode where electrical charge deposition occurs. The nature of the input waveform alternates the electrodes from behaving as an anode or as a cathode in the plasma actuator. The inter-electrode air gap is ionized by the electrical discharge, and the highly mobile electrons created on the cathode are directed toward the anode electrode. In contrast, the ions are heavier, and therefore primarily exchange their momentum to the background air through collisions, resulting in the induced flow pattern that is commonly observed. The movement of the electrons is interrupted by the dielectric, and negative charge buildup occurs across timescales of the discharge. This action saturates the opposing potential on the electrode which acted as the electron source, thereby shutting off the discharge. When the input potential reverses in sign, a reversal of the above events occur (see Fig. 2.2 for a schematic). Thus, as long as the input potential is asymmetric and is of sufficient magnitude to create electrons near the cathode, the discharge sustains on its

own without collapsing into an arc. Forte *et al.* [93] conducted detailed steady and unsteady measurements of plasma actuators in quiescent flow, and identified some interesting features of the discharge. They observed that the plasma induced flow in a pulsating manner at nearly the same time scales as the applied voltage. Both the negative and positive half cycles of actuation were found to induce a positive ion wind, suggesting that the actuator "pushes" the fluid during both halves of the AC cycle. This "push-push" mechanism is in contrast to earlier "push-pull" observations made by Porter *et al.* [88] on the DBD actuator.

Recent experimental studies by Enloe *et al.* [109] have shown that the action of the plasma is to increase density of neutral particles near the edge of the exposed electrode, which in turn causes a pressure gradient-directed force that pulls air upstream (toward the plasma region) against the density slope, and releasing it downstream when the plasma quenches. Acoustic emission measurements by Baird *et al.* [110] on the plasma actuator suggest that compressibility effects of the air might play an important role on its momentum imparting mechanism. Enloe *et al.* [111, 112] conducted detailed temporal measurements of density perturbations in the plasma region. Their investigations showed that the effect of the actuator was entirely downstream of the exposed electrode edge, and the density increase (relatively steady with time) was not as prominent as density decrease in the region. The density depletion was observed to be balanced by neutral air filling up the region, and this action eventually reached a constant level with time (in the order of milliseconds) that was coincident with the start of large scale downstream motion of the bulk fluid. The initial phase of density depletion and air balance was dominated by diffusion, after which convection was also observed to play a substantial role, suggesting that heating affected the spatial structure of air near the actuator.

The effect of the collisions that impart momentum to the neutral fluid, which as of the moment appears to be the consensus among plasma actuator researchers, are relevant on spatial scales that are on the order of the mean free path of the gas molecules [50]. However, the observed interaction of the plasma with the neutral air extends beyond several mean free paths (for air, MFP$\approx$0.1μm). Previous studies have shown that the presence of oxygen ions in the atmosphere is important to the efficiency of the fluidic momentum coupling by the actuator (such as Gregory *et al.* [113], Abe *et al.* [114], and Enloe *et al.* [111]). To understand the contribution of collisions and its concomitant effects on the flow field, the measurements on the discharges under different atmospheric compositions is required. At the present state of research in DBDs, no experimental information is available at the nanosecond level to clearly arrive at a well-founded mechanism of plasma actuators, rendering the development of accurate predictive numerical methodologies needed toward real-time implementation of

these devices a perplexing problem.

2.3 Synthetic Jet Actuators

Synthetic jet actuators introduce a jet with non zero momentum into the fluidic system in which they are employed, similar to plasma actuators. They have been shown to be useful active flow control devices for several applications over the recent years (see Amitay *et al.* [115], Rediniotis *et al.* [116], Mittal & Rampunggoon [117], and Chiekh *et al.* [8] for example). Figure 2.3(a) shows a common method employed to create a synthetic jet through the motion of a vibrating membrane (or diaphragm) that is mounted on the bottom wall of a cavity (shown in blue). The diaphragm is usually a metal disk that is set to oscillate by means of a piezoelectric actuator embedded on its surface. The fluid surrounding the cavity fills in the volume available at static (unactuated) conditions. When the actuator is operated such that it effects a finite upward displacement of the membrane through stroke B (shown in red), a small volume of fluid is pushed out of the cavity through the orifice. When the membrane returns back to its static position through stroke S (shown in blue), fluid is entrained via the orifice into the cavity (volume of fluid entrained is nearly equal to that expelled, ignoring viscous effects). An oscillatory motion of the membrane thus results in alternating entrainment and ejection of the residual fluid surrounding the cavity through the orifice. During the ejection stage (B) of the actuator cycle, the fluid emanating from the cavity encounters a pressure drop at the sharp edges of the orifice exit, resulting in flow separation at this region. The separated shear layer rolls up into a vortex ring (or counter-rotating vortex pairs in the case of a rectangular orifice) that advects in the vertical direction under its own self-induced velocity during blowing stroke B. Multiple vortical structures of this nature can be created via operating this actuator across many cycles, and the interaction between these vortices coupled with their self-advection result in creating a vertical jet with non-negligible flow momentum. For flow control applications, this cavity unit is typically flush mounted onto the pertinent surface of interest such that the synthetic jet is injected into the mean flow field. The resulting interaction resembles that of conventional jets placed in a cross flow. However, it must be noted that synthetic jets are produced (or "synthesized") from the fluid available within the system in which they are employed, thereby eliminating the requirement of a complicated external plumbing system to supply the additional mass of fluid required to produce conventional jets. The mass flux at the orifice exit averaged over the suction and blowing cycle of a synthetic jet actuator cycle is zero, and hence these jets are otherwise deemed zero-net-mass-flux (ZNMF) jets.

It must be emphasized herein that it is not the components of the actuator in itself that define a synthetic jet. The fundamental mechanism of synthetic jet formation is through the generation and interaction of trains of vortex structures occurring at the exit of an orifice. The hydrodynamic force and mass of fluid necessary for this process to occur is provided by the actuator. In addition to diaphragm actuation discussed above, other sources such as imposing an acoustic field and vibration of a solid wall in contact with a quiescent medium can also be used to introduce streaming fluid motion. With regard to the former method, Ingard & Labate [118] employed standing acoustic waves in a circular tube to synthesize a ZNMF jet near its orifice. Several regimes of induced flow were found to occur on adjusting the sound intensity. Variations in the frequency of the applied sound wave and orifice geometry were investigated. A pulsatile jet was found to be formed at sufficiently high sound intensities in addition to multiple sets of vortex rings. Jet velocities as much as 700 cm/s were recorded, and the sound intensity levels were varied up to a maximum value of 140 dB in the tube. This type of motion induced by transmission of sound through a fluid is also referred to as *acoustic streaming*. Fluid motion associated with moving boundaries have been investigated in several works (such as Riley [119], and Riley & Wybrow [120]), especially in the context of transverse periodic oscillations of circular and elliptic cylinders. Davidson and Riley [121] employed time harmonic vibrations normal to the cylinder axis with an amplitude of 0.1 cm and frequency 45 Hz, and reported maximum steady jet velocities $\mathcal{O}(1$ cm/s). No closed streamlines were observed in their flow visualization results, indicating the absence of vortical structures, a noticeable difference from cavity driven synthetic jets. In his 1978 review lecture, Lighthill [122] attributed the mechanism of fluid motion induced by transmission of sound or the oscillation of a viscous boundary to the action of Reynolds stresses. He observed that the dissipation of the input acoustic energy as a result of sound wave attentuation created the gradients in the momentum flux (the mean value of which is the Reynolds stress) necessary for fluid motion. In the case of a moving boundary, frictional dissipation was deemed responsible for generation of Reynolds stresses. In addition to standing waves, another method to induce acoustic streaming using high intensity ultrasonic sound beams (also known as "quartz wind") can be used, and a recent review article by Riley [123] may be referred to for further information.

Based on the above comments on the mechanism of synthetic jet formation, a general set of conditions required to produce such a jet can be recognized:

a. The jet driver (diaphragm oscillation, sound waves, etc.) has to provide the necessary pressure difference for sustained generation, roll up, and advection of starting vortices.

b. The amplitude of the pressure oscillation imparted by the driver has to be large enough so as to prevent the starting vortex from being entrained along with the residual fluid during the suction portion of the actuator cycle.

c. The frequency of the jet driver has to be sufficient to promote the dynamics of vortex interactions necessary to sustain the jet.

Annular and rectangular synthetic jets generated near an orifice of a flow boundary through alternating suction and ejection of the working fluid have received considerable amount of attention in the recent years, both from a classical fluid dynamics of jets perspective (see Smith & Swift [124]) as well as practical aerodynamic flow control applications [26]. Besides their zero-net-mass-flux characteristic which eliminates the need for an elaborate fluid supply system, the ability to manufacture synthetic jet actuators at micron scales (see Edis *et al.* [125]) using Micro Electro Mechanical Systems (MEMS) based technologies (see Gad-El-Hak [126] for explanation) has motivated researchers to explore several application studies of these devices. The modification of the direction of a conventional air jet ("vectoring") by means of a synthetic jet has been investigated experimentally by Smith & Glezer [127, 128] and numerically by Guo *et al.* [129]. Compared to conventional methods of jet vectoring using mass-laden air jets (such as in Strykowski *et al.* [130]), synthetic jets do not require extended surfaces to provide the necessary deflection force. In addition, these investigations showed that synthetic jet based primary jet vectoring resulted in an increase in the small-scale motions in the flow, suggesting enhanced mixing on account of the oscillatory flow. This latter observation has been used in a study of augmentation of heat transfer using impinging synthetic jets by Travnicek & Tesar [131], and mixing enhancement using micro-scale synthetic jets such as Davis & Glezer [132], and Wang & Menon [133]. The control of flow separation using synthetic jets in both external (see [117], Parekh *et al.* [134], Vadillo *et al.* [135], and Dandois *et al.* [136] for example) and internal (see Amitay *et al.* [137], Amitay *et al.* [138], and [8] for example) aerodynamic flows has been investigated by several researchers. Recent studies have examined the active control of axisymmetric free jets (Tamburello & Amitay [139]) and sprays (Pavlova *et al.* [140]) using synthetic jets. Currently, there appears to be an increasing trend of research efforts directed to transition the aerodynamic flow control applications of these devices from the laboratory level to real time flight. Nagib *et al.* [26] applied voice coil driven rectangular synthetic jets in the wing flaps of the XV-15 tiltrotor aircraft (manufactured by Bell Helicopter Inc.) with the objective of affecting the drag induced by the downwash of the rotor over the wing during hover. From full scale flight testing results, they first demonstrated a 9 to 14% reduction in down-

wash drag through succesful application of active flow control using synthetic jet actuator technology. Other similar studies have shown the usefulness of these devices implemented on full scale UAV platforms such as the "Stingray" developed by Boeing Phantom Works Inc., in problematic areas such as flight control during takeoff and landing, and gust load alleviation (see Farnsworth *et al.* [141], Liu *et al.* [142], Amitay *et al.* [143], Washburn & Amitay [144], Parekh *et al.* [145] for example). At even smaller scales, synthetic jet based micro air vehicle (MAV) propulsion has been investigated experimentally by Whitehead & Gursul [146].

This section will present a brief review of the existing state of research in synthetic jets. The article by Glezer & Amitay [147] presents a comprehensive survey of synthetic jets, and can be referred to for further information. The first part of this section focuses on the characteristics of synthetic jets in a quiescent fluid medium. This is followed by a discussion of the interaction of synthetic jets with a cross flow. Owing to the vast amount of literature available on synthetic jets, an exhaustive review of this topic is not presented herein for the sake of brevity.

2.3.1 Isolated Synthetic Jets

James *et al.* [148] experimentally investigated an annular synthetic jet formed in quiescent water through the oscillation of a submerged brass diaphragm flush mounted on a flat plexiglass plate. A piezoelectric actuator was used to drive the diaphragm at its resonance frequency of 7 kHz to produce a displacement of 10μm. Radial and axial velocity measurements were conducted using Laser Doppler Anemometry (LDA) across varying actuator excitation levels. Jet formation was observed to occur only when the actuator input voltage exceeded a critical threshold value, and the centerline velocity increased linearly with applied voltage beyond this limit. The existence of cavitation bubbles was found to be necessary for formation of the jet. Although not verified from the experiments, two mechanisms of jet formation via the advection and interaction of vortex rings were proposed: one in which flow separation about the cavitation bubble during the negative (inward) flow of water toward the diaphragm was conjectured to create vortex rings, and an other explanation based on the possible formation of strong localized jets due to collapse of the cavitating bubbles on the plate surface resulting in the generation of primary and secondary vortex rings. The synthetic jet was found to achieve self preservation at distances sufficiently near the actuator, and the far field behavior was found to be similar to conventional turbulent jets. Similarity characteristics including jet half width, inverse of the centerline velocity, and volume flow rate were found to be linearly related to the streamwise distance. Interest-

ingly, the entrainment rate of the synthetic jet was observed to be lower than conventional turbulent jets, indicating that most of the fluid entrainment occurred within a localized region near the actuator. Furthermore, the entrainment rate was constant in the case of the synthetic jet unlike a classical round turbulent jet, and this lead the authors to conclude that the former did not have a "potential core" region.

The evolution of a cavity-membrane driven rectangular synthetic jet in quiescent air was investigated by Smith & Glezer [149]. Following the earlier work of Glezer [150], they introduced a "slug" flow model to characterize the vortex pairs (or vortex rings in a 3-D case)

$$\tau = \frac{T}{2} \tag{2.17}$$

$$L = \int_0^{\tau} u_0(t)\, dt \tag{2.18}$$

$$Re_{I_0} = \frac{I_0}{\mu h} = \frac{\rho h \int_0^{\tau} {u_0}^2(t) dt}{\mu h} \tag{2.19}$$

where τ, L and Re_{I_0} denote, respectively, the time scale, length scale and Reynolds number. In the above equations, $u_0(t)$ indicates the centerline velocity at the orifice (x-coordinate value, vertical direction in Fig. 2.3(b)), I_0 indicates the momentum imparted by the jet per unit width of the orifice, h is the characteristic orifice dimension (width in 2-D, diameter in 3-D), T is the time period of the diaphragm motion, μ is the dynamic viscosity and ρ is the working fluid density. A velocity scale based on the length and time scales defined above was thus arrived

$$U_0 = Lf = \frac{1}{T} \int_0^{T/2} u_0(t)\, dt \tag{2.20}$$

This velocity U_0 thus represents the velocity of the synthetic jet directed downstream only during the blowing portion of the actuator cycle, but averaged over the entire cycle (Note that this is strictly not any time-average of the centerline velocity $u_0(t)$.) The authors argued that the observed flow phenomena is controlled by the average of the *downstream directed* volume flux of the synthetic jet, by comparison with the traditional velocity scale U_{ave} calculated by averaging mean exit velocity at the orifice used in continuous jets. From phase-locked schlieren flow visualization images in the region near the actuator (streamwise distance $x < 9.5h$), laminar vortex pairs were observed to be formed and advected upward through small scale motions. This stage was followed by the appearance of an instability in the azimuthal (or spanwise) direction, evidenced by the formation of secondary vortical

structures trapped within the primary vortex pairs, with the result that these vortices ultimately breakdown the primary vortex core and transition to turbulence. It was conjectured that the transition process, which was observed to begin somewhere near the suction cycle, may have been initiated by the reversed entrainment flow during this actuation stage. Following transition, the turbulent vortex pair was found to have a lower propagation velocity and eventually lost coherence, and many such vortex pairs merged at this stage to form the mean synthetic jet. Several scaling relations for vortex pair centerline and propagation (celerity) velocities, as well as the spatial and temporal evolution of vortex pair trajectories were documented from the results of hot wire anemometry (HWA) measurements. Far-field cross-stream distributions of both mean and fluctuating velocity components of the synthetic jet were observed to be self-similar, resembling conventional turbulent jets. However, several differences in their self-similarity characteristics were identified:

a. The decay of the mean centerline velocity in the streamwise direction was found to be marginally higher for synthetic jets ($U_c \propto x^{-0.58}$), as compared to conventional 2-D turbulent jets ($U_c \propto x^{-0.5}$).

b. The streamwise variation of the synthetic jet spreading rate, indicated by its width b, was found to be slightly deviant ($b \propto x^{0.88}$) from the linear variation ($b \propto x$) common in conventional 2-D turbulent jets.

c. The volumetric flow rate Q, defined by the integral below (where y is the cross-stream coordinate and U is the mean jet axial velocity),

$$\int_{-\infty}^{\infty} U \, dy,$$

was found to vary streamwise as $Q \propto x^{0.33}$, once again lower than that seen in non-synthetic 2-D turbulent jets where $Q \propto x^{0.5}$.

d. Compared to conventional 2-D turbulent jets, the synthetic jet showed nearly twice an increase in the rate of streamwise increase of jet width (db/dx at x=30h) and substantially larger net volume flow rate (from $0 < x < 80h$)

The above differences were attributed to the streamwise decay of momentum flux observed in synthetic jets, compared to other self-similar 2-D jets where this quantity is invariant. This variation of momentum flux was associated with the prevalence of lower than ambient value of mean static pressure in the synthetic jet flow field, which was due to the adverse pressure gradient created near the orifice during the suction stage of the actuator cycle.

Crook & Wood [151] investigated the formation and interaction dynamics of vortex rings produced at the orifice of a cavity by an electromagnetically driven piston at 50 Hz. The effect of orifice length and input Reynolds number (based on orifice diameter and peak velocity at the orifice exit) were examined via flow visualizations (Fig. 2.4). Note that in addition to the stroke length L_0 and Reynolds number based on hydrodynamic impulse in equation 2.19, a non-dimensional formation frequency F^* of vortex rings may be defined as below (see Glezer & Amitay [147]),

$$F^* = \frac{fI_0}{\rho\nu^2}$$

This characteristic, which is the non-dimensional measure of the impulse per unit time, can be used to compare different synthetic jets based on their vortex strengths.

Béra *et al.* [152] conducted a particle image velocimetry (PIV) based investigation of a rectangular synthetic jet and compared its characteristics with two non-ZNMF jets: a steady blowing jet and a mixed pulsed jet which consisted of the above synthetic jet with an additional steady blowing component. A loudspeaker enclosed in a cavity was used as the driver for the synthetic jet. The peak velocities of the above different jets used were unequal, however. The mixed pulsed jet was driven with a peak velocity equal to the sum of the corresponding values for the synthetic and steady blowing jets. Details on the spatial flow field evolution, vortex pair trajectories, maps of fluctuating quantities and similarity characteristics were derived from these measurements. The synthetic jet flow field showed a clear inflection point where the mean streamwise velocity was zero, where the suction and blowing cycles were compensated for each other. The entrainment in the streamwise direction was found to be greater for the mixed pulsed jet. The synthetic jet showed cross-stream expansion of turbulence kinetic energy and high levels of fluctuations for a small distance from the orifice, after which the expansion was reduced. The mixed pulsed jet showed the most fluctuations, on account of its additional downstream blowing component. The half width of the synthetic jet based on local maximum mean streamwise velocity (the same quantity was calculated based on centerline velocity scale in [149]) was found to be greater than the steady or mixed pulsed jets. The streamwise variation of maximum synthetic jet velocity was found to increase from the orifice and reach a maximum near the actuator, after which it decayed nearly at the same rate as the steady jet. From an examination of similarity profiles, negative streamwise velocities were observed at large cross-stream distances from the orifice, suggesting the presence of secondary vortices effecting fluid entrainment into the mean jet. The trajectories of vortex centers were observed to be nonlinear for both the synthetic and mixed pulsed jets, with greater cross-stream dispersion in the former case.

Guy *et al.* [153] conducted hot film based velocity measurements on a 2-D synthetic jet

emanating from a slot of a cavity embedded with a flexible diaphragm, and the effects of variation in actuator input frequency and waveform signal on the jet velocity were examined. The maximum peak velocity of the jet of roughly 9 m/s was obtained when the actuator was operated at its resonance frequency (derived from theoretical mechanics based relations for a disk clamped at its edges) with a square wave input signal. For streamwise distances up to 12 slot widths from the actuator surface, large turbulent fluctuations were found to be present on account of the membrane motion, indicating non-fully developed flow. Beyond this point, the jet evolved into a fully developed state, and the decay of the mean centerline velocity was found to be similar to conventional 2-D turbulent jets.

Cater & Soria [154] conducted detailed investigations on the evolution of circular synthetic jets and compared it to equivalent continuous jets using PIV measurements. The synthetic jet was created at the exit of a circular orifice on a cylindrical cavity, and fluid motion within the cavity was triggered by alternating motion of a piston. Similar to the findings reported above, their flow visualization observations also confirmed that the width of the synthetic jet was greater than that for the equivalent continuous jet (Fig. 2.5). In contrast to the velocity scale in [149] presented in equation 2.20, the authors propose an alternate velocity scale for description of ZNMF jet flow phenomena based on the observation that while the integrated mean exit velocity of fluid through the orifice over a full cycle is zero, the hydrodynamic impulse imparted by the ZNMF jet is non-negligible. They start with the mean flow momentum flux (per unit density) integral for axisymmetric jet flow

$$I = \int_0^r u^2(r,t)\, 2\,\pi\, r\, dr$$

To obtain units of velocity, the above quantity was time-averaged over one entire oscillation period T and divided by the orifice area, and the square root of the resulting expression was taken to obtain the *momentum flow velocity scale* below

$$U_0 = \sqrt{\frac{1}{\left(\frac{\pi D^2}{4}\right) T} \int_0^T I\, dt} \tag{2.21}$$

The effects of variation in source Reynolds number (based on D and U_0) and Strouhal number based on the frequency of oscillation f (equal to $1/T$), and the above length and velocity scales were investigated, the definitions given below

$$Re = \frac{U_0\, D}{\nu}, \quad St = \frac{f\, D}{U_0} \tag{2.22}$$

While the Reynolds number was varied by changing f (so as to change U_0), the Strouhal number was altered by varying the actuator amplitude. The latter input parameter was

found to be inversely related to the Strouhal number and directly related to the Reynolds number. Departing from many earlier studies on synthetic jets, the authors examined values of operational Strouhal numbers much less than one. The flow pattern obtained was found to be highly dependent on the input Reynolds and Strouhal numbers (Fig. 2.6). Interestingly, they observed the formation of a vortex ring centered 5 diameters downstream of the orifice and roughly 4 diameters in length for a flow Reynolds number of 1000, stationary in its spatial location across all phases of the actuator cycle. This "trapped" vortex ring was unique to the synthetic jet and generated on account of the radial flow near the actuator wall, and the effect of this structure was to accelerate the entrainment of fluid toward its core (thereby contracting the jet) and thereafter decelerate the flow so as to effect rapid jet spreading via transverse diffusion. This was proposed to be the reason for the substantial increase in the jet width and radial entrainment observed in the case of synthetic jets as compared to continuous jets. Such a standing vortex had not been observed by other researchers, and the authors conjectured that operating the actuator at higher Strouhal numbers would result in its spatial advection. They attributed the near-field structures to be the reason for increased jet spreading observed in ZNMF jets, as compared to conventional continuous jets.

Smith & Swift [155, 124] compared the characteristics of rectangular synthetic and continuous jets, matched in terms of their Reynolds numbers defined using the slot width as the length scale and an appropriate velocity scale (U_0 in eqn. 2.20 for synthetic jets and U_{ave} defined in the discussion following eqn. 2.20 for continuous jets.) A wide variety of Reynolds numbers ($\mathcal{O}(10^3)$) and input stroke lengths (indicative of the "length' of fluid injected into the system during the blowing cycle, calculated as L/h, see eqn. 2.18) were investigated in the case of synthetic jets. For the same stroke length of a synthetic jet, the effect of increasing Re in the near field was to promote the generation of small-scale structures in both the starting vortex pair and the mean jet. On the other hand, for the same Re, the effect of increasing the stroke length in the near field was in altering the rollup of the starting vortex pair. No relation between Re or L_0/h was observed on the vortex pair trajectories. The far-field characteristics were found to be affected by both Re and L_0/h. Equivalent continuous and synthetic jets were compared for $Re \approx 2200$. In general, synthetic jets were observed to be wider, slower and contain more momentum than similar continuous jets. Cross-stream spreading of the synthetic jet was observed to begin much earlier upstream than the continuous jet. At the same Re, unlike the laminar continuous jet, the synthetic jet was observed to be turbulent, with transition in the latter most ostensibly being initiated on account of its oscillatory nature. In the near field, the mean centerline

velocity for synthetic jets was found to be lower than that of continuous jets, and this was suggested to be the reason for the increased width, slower velocities, and increased volume flux observed in synthetic jets.

The criteria required for synthetic jet formation has been investigated by a few researchers. As stated earlier, the advection rate of the starting vortex pair has to be sufficient enough to avoid its ingestion during the reversed motion created by the suction stroke of the actuator cycle. Smith *et al.* [156] showed through experimental measurements that the formation of an axisymmetric synthetic jet of diameter D will occur only when the input stroke length L_0/D was greater than 1. In their study of rectangular synthetic jets, Smith & Swift [155] used a potential flow approximation to derive a threshold minimum stroke length ($L_0/h = 4/\sqrt{\pi}$, where h is the slot width) condition required for jet formation. Experimental results indicated that their formation threshold was not a constant, and exhibited deviations for smaller slot widths. Holman *et al.* [157] related the strength of the starting vortex pair (and hence its self induced velocity) to be proportional to the vorticity flux at the orifice exit, and used an order of magnitude analysis to propose a different formation condition based on Reynolds (Re), Strouhal (St) and Stokes (S) numbers as

$$\frac{1}{St} = \frac{Re}{S^2} > K$$

where K was assumed to be dependent on a variety of geometric parameters of the actuator. Experiments were used to arrive at the values of K for both 2-D (K=1) and 3-D (K=0.16) synthetic jets. The same formation criterion was also arrived in a separate investigation of the axisymmetric synthetic jet by Zaman & Milanovic [158]. Interestingly, they reported a minimum stroke length of 0.5 required for formation of the synthetic jet, in disagreement with the value of 1 proposed by Smith *et al.* [156]. In addition, these authors first recognized the existence of an upper threshold limit input stroke length (L_0/D=10), after which the mean centerline velocity remained invariant, on account of the saturation of vortices produced in the flow field.

While most of the work described above is purely experimental in nature, numerical modeling of synthetic jet flows has been investigated by several researchers. Rizetta *et al.* [159] used direct numerical simulations (DNS) of the unsteady compressible Navier–Stokes equations to investigate both the characteristics of an isolated rectangular synthetic jet flow field, as well as the flow within the cavity. A sinusoidal velocity profile was provided as the boundary condition to simulate the motion of the diaphragm. The effects of Reynolds number and cavity height were investigated on two dimensional flow fields. The laminar solutions rendered a train of vortex rings that did not coalesce to form a jet. Near the jet

centerline, the time-averaged velocity distributions obtained from 2-D and 3-D simulations reasonably compared with other experimental results. Lee & Goldstein [160] conducted 2-D DNS studies on rectangular synthetic jets produced at an orifice on a cavity by motion of a piston inside it. To model the moving boundary, a localized body force term was added to the Navier–Stokes equations along specific regions in the computational domain. Both the effects of input flow conditions (Re and St) as well as geometric parameters (lip thickness, lip geometry and cavity depth) were investigated. While the flow structures inside the cavity were found to be highly sensitive to Re, the interactions of ejected vortices were found to be more influenced by St. Interestingly, the celerity (or propagation velocity) of the vortex pairs was found to be increased when the cavity was made shallower, similar to earlier observations of Rizzetta *et al.* [159]. Kotapati & Mittal [161] conducted DNS simulations of quiescent rectangular synthetic jet actuator flow fields using the 3-D, incompressible Navier–Stokes equations. A time varying sinusoidal velocity condition was provided at the bottom wall of the cavity to mimic the motion generated by the jet driver. Both the spatial evolution and temporal characteristics were presented and compared with experimental measurements. The secondary instability in the azimuthal direction identified by Smith & Glezer [149] as the reason for the vortex pair transition process was also identified in these simulations. Regardless of conditions elsewhere in the computational domain, the flow accelerating into the slot during suction and blowing strokes of the actuator cycle was observed to be laminar.

In contrast to the above DNS efforts, several researchers have employed Reynolds Averaged Navier–Stokes (RANS) equations for description of synthetic jet flow fields, ostensibly with a motivation to minimize computational time involved. Kral *et al.* [162] first conducted 2-D simulations of laminar and turbulent synthetic jets by introducing a simple harmonic velocity profile boundary condition to describe the flow at the orifice exit. A turbulence model was incorporated to mimic the dynamics of vortex interactions observed in experiments. The mean flow characteristics in the far-field compared well with experiments. The flow within the cavity was not modeled and RMS velocity components were not compared. Cui & Agarwal [163] performed three dimensional studies on isolated synthetic jets by modeling the actuator flow field using the unsteady RANS (URANS) equations. The results of URANS simulations employing several turbulence models, including the one-equation Spalart–Allmaras (ST), the two-equation shear stress transport (SST), a hybrid SA–Large Eddy Simulation (similar to a detached eddy simulation (DES) in the context of modern day turbulence modeling terminology, see Wilcox [164]), and a hybrid SST–LES model, were compared with PIV measurements available in the literature. However, no

single model showed any improvement in terms of the flow field predictions, and the authors concluded that the overall agreement of the simulations with experiments to not be satisfactory. Park *et al.* [165] investigated the importance of numerical considerations such as spatial discretization and time integration schemes on 2-D RANS based simulations of isolated rectangular synthetic jets. Of the turbulence models (SA, k–ω SST, linear k–ϵ) used for modeling the RANS eddy viscosity, the SST model compared most favorably with experiments. Bulk flow features such as the width and velocity magnitudes predicted by these simulations were is good agreement with measurement values.

The interaction of linear or annular arrays of multiple synthetic jets has been investigated by Smith *et al.* [156], and Smith & Glezer [166] in related PIV investigations. These studies examined the formation and evolution of the flow field of a pair of rectangular synthetic jets oriented adjacent to each other in quiescent medium, parallel about the long dimensions of their orifices. By varying the phase difference between the operation of the two actuators, the direction of the resultant synthetic jet was shown to be altered, as shown in Fig. 2.7. When both actuators were driven in phase, each induced the formation a counter-rotating vortex pair at the exit of their respective orifice. The resulting flow field was observed to be heavily influenced by the ensuing vortex pair interaction dynamics. The adjacently-located vortices generated by each actuator (viz., unlike signed vortices spaced closest) canceled each other, resulting in a single vortex pair with more circulation strength than the vortex pair of a single synthetic jet. Also, the vortex pair of the combined jet propagated with lower velocities than the single jet. The suction stroke entrainment was identified to be responsible for initiating the vortex pair interactions. Compared to the single synthetic jet case, an increase in the entrainment, volume flow rate and jet spreading were observed simultaneous with the vortex pair interaction process in the combined jet. Several flow field modifications such as a change in the directionality of the combined synthetic jet and formation of closed separation bubbles were introduced through an adjustment of the phase delay angle between the actuator cycles.

2.3.2 Synthetic Jets in a Cross Flow

This section of the literature review examines the interaction of synthetic jets with a cross flow, and the observations herein are presented in terms of two common test flows used by researchers to describe the jet-external flow interaction physics.

Flat Plate Boundary Layer Flows

Gordon & Soria [167] experimentally investigated the flow field characteristics of a round synthetic jet in cross flow using PIV and compared them to equivalent continuous and pulsed jets. The synthetic jet was produced at the exit of a circular orifice plate on one surface of an otherwise sealed cavity, and set to interact with the incoming flow at an angle of 90°. The oscillating pressure drop required for synthetic jet formation was introduced by the motion of a diaphragm inside the cavity through an electromagnetically driven piston. The effects of variation of three input parameters were examined: a jet Reynolds number Re defined based on the orifice diameter d and an *average momentum flow velocity* U_j (equal to the root mean square value of the measured diaphragm velocity), Strouhal number St based on the input actuator frequency f (in addition to d and U_j), and the ratio R of jet velocity (U_j) to free stream velocity (U_∞). The St values investigated were lower than other synthetic jet studies, with frequency of oscillation f varied to either a value of 5 Hz or 10 Hz. The free stream velocities in this study were lower than the jet velocity, and the resulting values of R investigated were 4.6 and 7. Details on the evolution of the streamwise vortices and volume flow rates were examined in the near-field of the jet ($<5d$ measured from the orifice plate in the direction normal to free stream). From multiple phase-locked measurements, the vortex structures introduced at the exit of the orifice were found to move in the cross-stream direction very near the actuator and eventually advect along the free stream direction with increasing distance from the wall. This resulted in the "tilting" of the vortex ring produced by the synthetic jet along the free stream direction (see Fig. 2.8). The volume flow rate in the wall-normal direction was calculated along different cross-stream distances and in general compared well with isolated synthetic jet characteristics (e.g. Smith & Glezer [149]). In spite of the availability of a higher volume of fluid in the system on account of an external flow (compared to an isolated synthetic jet), most of the entrainment of residual fluid by the actuator was still found to occur within a few diameters of the orifice. Even at a distance as close as $0.2d$ from the orifice plate, 25 to 40% of the total volume flow rate was found to be derived from the suction stroke of the actuator cycle. Downstream of the orifice, the flow streamlines were displaced by nearly three diameters in the cross-stream direction. The interaction region of the synthetic jet with the external flow was observed to extend to distances of up to 20 diameters in the cross-stream direction. Both the jet trajectory, as well as velocity decay along the trajectory of the synthetic jet were similar to those for equivalent conventional jets in cross flow.

Smith [168] investigated the interaction of a rectangular synthetic jet actuator array

with an incoming turbulent boundary layer at a free stream velocity of approximately 9.1 m/s (Re_θ=1.79×10^3). The velocity scale proposed by Smith & Glezer [149] was used to define the jet-to-free stream velocity ratio of 1.2. Two different array orientations, each consisting of three synthetic jet actuators of identical dimensions were examined: a "spanwise" configuration where the major axes of all actuator orifices were perpendicular to the free stream direction and a "streamwise" configuration with major axes parallel to the free stream direction (major axis refers to the axis in the direction of the longer dimension of the exit orifice). HWA measurements were used to infer the velocity profiles and boundary layer characteristics. In general, the orifice orientation was found to affect the development of the flow field substantially. In the spanwise configuration, the synthetic jet was observed to interact with the incoming cross flow so as to result in the formation of a localized closed reversed flow region. Similar to previous observations, the synthetic jet was bent in the direction of the incoming flow. Due to the blockage imposed by the jet, a wake region was developed downstream of the actuator array and the formation of a wall jet like flow was observed. The velocity profiles in the streamwise configuration showed a decrease in flow reversal with increasing downstream distance, in contrast to the spanwise oriented array. A wall jet like behavior was also observed in the streamwise configuration at near wall distances. The interaction scale of the synthetic jet in both configurations were comparable. However, the interaction of the streamwise configuration extended to the edge of the boundary layer, compared to the lower penetration height of the spanwise configuration. The increased area of the synthetic jet in the latter case was conjectured as the reason to why the jet in spanwise array was quickly tilted by the free stream. The synthetic jet trajectory in the spanwise configuration was found to follow the power law scaling of a conventional continuous jet in cross flow. The momentum thickness increased monotonically in both actuator array orientations, and a return to static (unactuated) values downstream of the actuator occurred only for the spanwise configuration. The displacement thickness remained nearly a constant and returned to static values downstream for the spanwise array, while it increased monotonically for the streamwise array and no return to static values were observed. Zaman & Milanovic [169] conducted HWA measurements on the flow field of a round synthetic jet introduced normal to a flat plate boundary layer flow with a velocity of 20 ft/s. The input "stroke length" (defined in the earlier parts of this section) and jet-to-free stream velocity ratio were varied. In general, the mean velocity, streamwise component of vorticity, and turbulence intensities resulting from the synthetic jet-flow field interaction resembled those of a continuous conventional jet in cross flow. The jet trajectories were found to be independent of the input stroke length and purely affected by the input velocity

ratio. The penetration depth of the synthetic jet compared well with analytically predicted values of equivalent continuous jets.

The effect of spanwise orifice orientation (yaw) angle of a rectangular synthetic jet in cross flow was investigated experimentally Bridges & Smith [170]. The velocity of the free stream was roughly 17 m/s, and the boundary layer was turbulent throughout the entire length of the plate. The synthetic jet-to-free stream velocity ratio was 0.82, and three yaw angles of 0°, 10° and 20° were studied. HWA measurements were used to examine velocity contours near the actuator and identify flow structures in the spanwise plane. For zero yaw angle, a weak stationary vortex pair was observed very close to the wall. With increase in yaw angle to 10°, the flow field resembled a skewed synthetic jet in cross flow, and a single streamwise directed vortex was formed downstream of the interaction region. At a yaw angle of 20°, the influence of the synthetic jet on the cross flow became weaker, and a horse-shoe vortex pair also directed in the streamwise direction was observed. The vortex structures (for any yaw angle) were observed to introduce a higher level of turbulent fluctuations in the boundary layer, and their positions were found to be affected by the driving actuator frequency. Milanovic & Zaman [158] investigated the effects of changing orifice geometry on the flow field of a synthetic jet discharged normal to the direction of an incoming flat plate boundary layer flow with a velocity of 20 ft/s. In addition to a circular geometry, an orifice pitched 20° relative to the wall, and a cluster of nine orifices were investigated. While the clustered and pitched orifice arrangements improved the mixing, their jet penetration was lower when compared to that of the single circular orifice. The flow field observed in the single and clustered orifices resembled a conventional jet in cross flow. The pitched orifice directed the synthetic jet at an angle, resulting in a flow field that resembled a horizontal wall jet. Interestingly, the jet trajectory from all the orifices were found to follow analytical correlations for a continuous jet in cross flow.

In addition to the above experimental investigations, Dandois *et al.* [171] recently conducted numerical simulations of synthetic jets in cross flow. The performance of using the URANS equations and LES equations to model the unsteady flow field structures were compared, and the sensitivity of the results to the computational grid, time stepping, and boundary conditions were considered. The global far-field characteristics were found to not be affected by the above parameters. However, the evolution and interaction of the counter-rotating vortices showed a strong dependency on the computational setup, particularly the grid resolution and turbulence model. It was concluded that while a URANS simulation could predict the bulk flow features and velocity profiles reasonably well, LES was the best alternative to achieve better predictions of the near field structures as well as flow

characteristics.

Flow Over a Circular Cylinder

The circular cylinder has been a simple, albeit powerful geometry revisited time and again to help in the understanding of the physics of fluid flows. Both the baseline flow and the evolution of boundary layer separation with inflow conditions have been documented extensively. Amitay *et al.* [172] conducted smoke-flow visualization of the modification of the low speed flow over a circular cylinder (Re_D=4000, where D=diameter of the cylinder). Sample results from these experiments are shown in Fig. 2.9. As can be inferred from the flow streamlines, operation of the actuator reduced the extent of separation and moved the separation point downstream. By adjusting the position of the actuators relative to the free stream flow, various flow field modifications including alterations in the wake symmetry and wake vectoring were exerted. In a related investigation, Amitay *et al.* [115] conducted HWA and pressure measurements on cylinder flow separation control using synthetic jets at higher flow speeds ($Re_{D,max}$ = 131 $\times 10^3$). An array of two rectangular synthetic jet actuators located adjacent to each other in the spanwise dimension were mounted on the top surface of the cylinder, and the effect of variation of the angle between the synthetic jet and the free stream was examined. The actuators were typically operated at near the resonance frequency to obtain maximum jet output. Excitation of the flow by the actuators rendered the velocity and vorticity profiles asymmetric about the centerline, and the velocity deficit in the near wake region was reduced. In addition, a downward displacement of the wake was observed on actuation compared to the nominally symmetric baseline case. The Reynolds stresses were actually lowered in the near-field post excitation, suggesting that the actuators did not act in a way similar to turbulators that trip a laminar or transitional boundary layer. While the actuator frequency was much higher than the vortex shedding frequency in the wake, it was also lower than the small-scale motions occurring in the wake. As a result, the actuator induced excitation was coupled to the wake, thereby enhancing dissipation and hence lowering the Reynolds stresses. Positioning the actuators upstream of the baseline separation point was not observed to affect the pressure distribution around the cylinder. The interaction of the synthetic jet with the mean flow resulted in the formation of a closed region of separation, and displaced the immediate streamlines outside to the potential flow region. Within the range of transitional Reynolds numbers investigated in this study, this recirculation bubble renders the boundary layer to better withstand adverse pressure gradients and consequently delay the occurrence of separation. The effect of actuation on the aerodynamic loading was to increase the lift by decreasing the pressure

coefficient throughout the cylinder (both upstream and downstream), and also decrease the drag through increasing the base pressure. Increasing the angle of the jet with respect to the free stream direction increased the lift coefficient and decreased the drag coefficient on the upper surface (where actuators were located), and a reversal of trends in the lower surface. In a related investigation, Honohan *et al.* [173] observed that when the actuators are operated at frequencies much larger than the wake shedding frequency of the baseline flow, the interaction of the synthetic jet with the cross flow produces a beneficial alteration of the streamwise pressure gradient so as to effect a virtual shape modification. This resulted in thinning of the boundary layer downstream of the actuator, and the ensuant delay (or complete elimination) of separation. The most interesting aspect of the synthetic jet interaction was that although the synthetic jets were operated at time scales well below the characteristic time scale of the flow, the actuation affected length scales that were several orders of magnitude of the characteristic dimension (slot width or orifice diameter) of the synthetic jets.

Rediniotis *et al.* [116] investigated the application of rectangular synthetic jets for the control of flow separation over a circular cylinder using PIV. The actuator effect in delaying separation was explained by the combined outcome of two independent mechanisms: one based on the removal of decelerated boundary layer level fluid during the suction stroke and injection of the same volume of fluid with increased energy during the ejection stroke to result in a Coanda effect based flow reattachment, and the other based on increase in flow mixing through the introduction of longitudinal vortical structures created as the result of the oscillatory blowing and associated increased shear layer receptivity. Recent results include the control of the flow over a circular cylinder using pulsed modulation of the actuation waveform by Glezer *et al.* [174]. The authors found that this form of modulation introduces coupled high and low frequency actuation so as to affect the aerodynamic loading, most ostensibly through its effect on the global instabilities prevalent in the mean flow. The circulation strength about the cylinder was examined from phase-locked HWA measurements. The wake width was found to be considerably narrower in case of the high frequency actuation, and no coherent vortices were present in the wake, in sharp contrast to low frequency actuation. From these results, lower actuation frequencies were observed to create strong oscillations in the lift and drag forces, as opposed to high frequencies which "quietened" the wake and rendered the aerodynamic loading to nearly quasi-steady values.

2.4 Summary

This chapter presented a brief background of the physics of plasmas and a literature review of research on the flow control methods of specific interest to this dissertation, including plasma actuators and synthetic jet actuators. Both these devices have to be activated through an input of energy, and their flow field effects are comparable to traditional methods employed for control of boundary layer separation through tangential blowing and mixing enhancement. Plasma actuators modify the flow momentum near the surface where the actuator is applied, mostly by means of fluid entrainment introduced as a result of an electrostatic coupling between the electric field of a single dielectric barrier discharge with the surrounding flow field. While a clear description of the reason as to why this coupling arises yet remains to be unraveled, an external body force introduced on the flow field due to the collisional transfer of momentum contained within mostly immobile ions in the discharge plasma with the neutral ambient gas molecules appears to be the current state of consensus, as far as the actuator mechanism is concerned. Numerous studies on the applications of plasma actuators toward air flow control have been investigated, and the majority of these efforts have been limited to low Re flows on laboratory scale models, however. In an initially quiescent medium, current studies have shown that the velocity induced by a single dielectric barrier discharge actuator (a function of the input power) is typically lesser than 10 m/s. The inherent advantages of these devices are the absence of moving parts, high bandwidth, low input power ($\sim \mathcal{O}(10$ W) for most laboratory scale applications), and ease of implementation on any arbitrary surface without major modifications to its internal structure.

Synthetic jet actuators introduce a rectangular or annular jet to the free stream (usually in the wall-normal direction), formed by alternating suction and ejection of the residual fluid at the orifice of a cavity embedded flush on the surface of the flow boundary. While the average mass flux integrated over an entire cycle comprising suction and ejection phases is zero, the hydrodynamic impulse of the jet is non-zero. The jet driver provides the action responsible for initiating and sustaining the oscillatory motion of near wall fluid toward and away from the cavity, and commonly used drivers include a flexible diaphragm embedded on the surface of the cavity, a piston connected to the lowermost moving surface of the cavity, and acoustic excitation. The jet is formed by the self-induced motion and interactions of trains of vortex structures generated periodically on account of separation of ejected flow at the sharp corners of the orifice and consequent roll up of the shear layer. Peak velocities as high as 100 m/s have been realized with conventional synthetic jets in

quiescent conditions, and extensive studies of the applications of these devices have been conducted across a variety of system scales ranging from a few microns to those of an actual aircraft. As impressive as the success of this device as a viable active flow control technology can be, there exists a few limitations, the most important being the requirement of a rather elaborate arrangement required to modify the flow surface so as to house a cavity. Also, the input required for formation of a synthetic jet is required to be necessarily pulsatile, whereas plasma actuators can be driven either in steady or unsteady pulsed operation. The scalability aspect of the synthetic jet actuator is outweighed by the ease of construction and implementation of plasma actuators. However, the peak velocity metric definitely restricts the applications of plasma actuators to a smaller domain than synthetic jets, and whether this barrier can be broken still remains to be determined.

With regard to the effort put forward within this dissertation, a concept for including the features of both plasma actuators and synthetic jet actuators is examined. While the intent herein is not necessarily to introduce a replacement for one or the other device, it is expected that this work would remove the limitation of plasma actuators from being merely modifiers of boundary layer level flow via tangential blowing, and therefore have an impact on their applicability. Essentially, the positive aspects of plasma actuators in terms of construction and implementation will be retained, but the flow field effect of the plasma will be tailored so as to resemble synthetic jets.

2.5 Tables and Figures

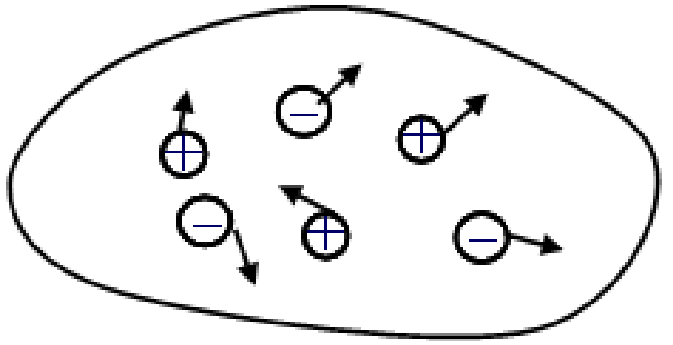

(a)

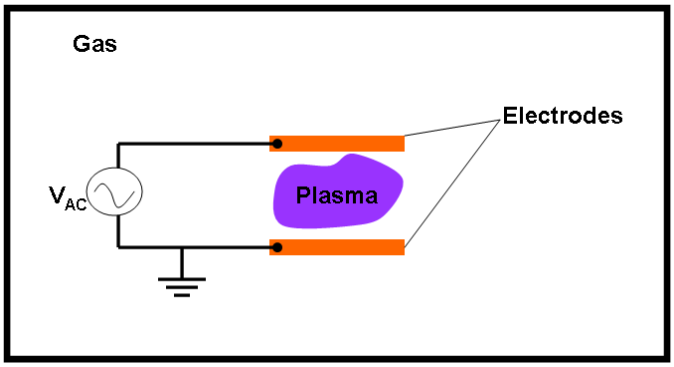

(b)

Figure 2.1: Plasmas: (a) basic description, and (b) generation via electrical discharge.

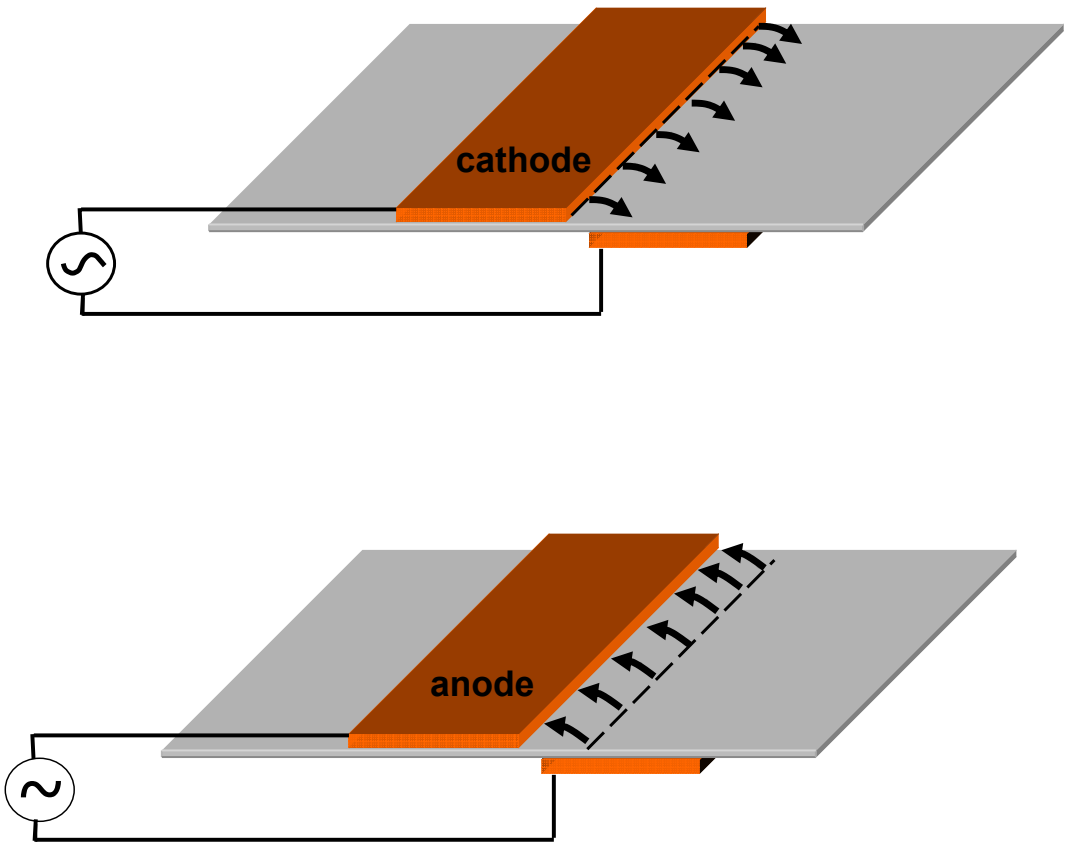

Figure 2.2: Mechanism of self sustaining nature of the DBD plasma actuator proposed by Enloe *et al.* [84]. Top and bottom halves correspond to the negative and positive portions of the input potential waveform, respectively, and arrows indicate the direction of motion of electrons (− signed).

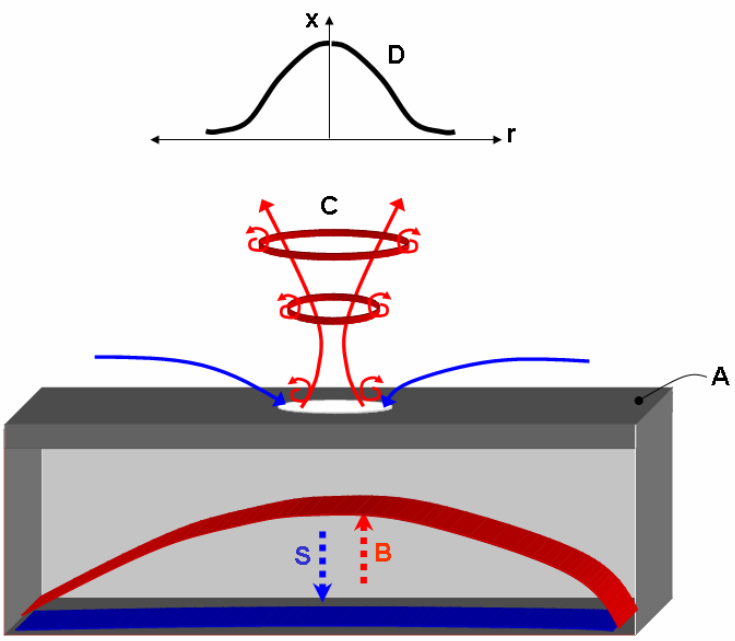

(a) Schematic.

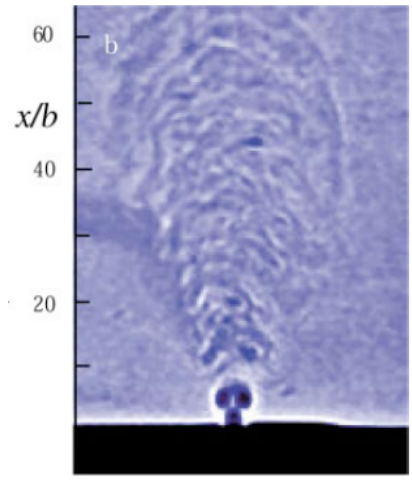

(b) Jet flow field.

Figure 2.3: Synthetic jet actuator: (a) shows a cavity-membrane motion driven concept, where A indicates the cavity, B (in red) indicates the blowing stroke and S (in blue) indicates the suction stroke of the flexible diaphragm, C indicates the jet induced by advection of vortex rings, and D: axial velocity profile. (The direction of motion induced during each portion of the cycle are shown in the respective colors) (b) shows a Schlieren flow visualization of the induced flow field (from Glezer & Amitay [147]).

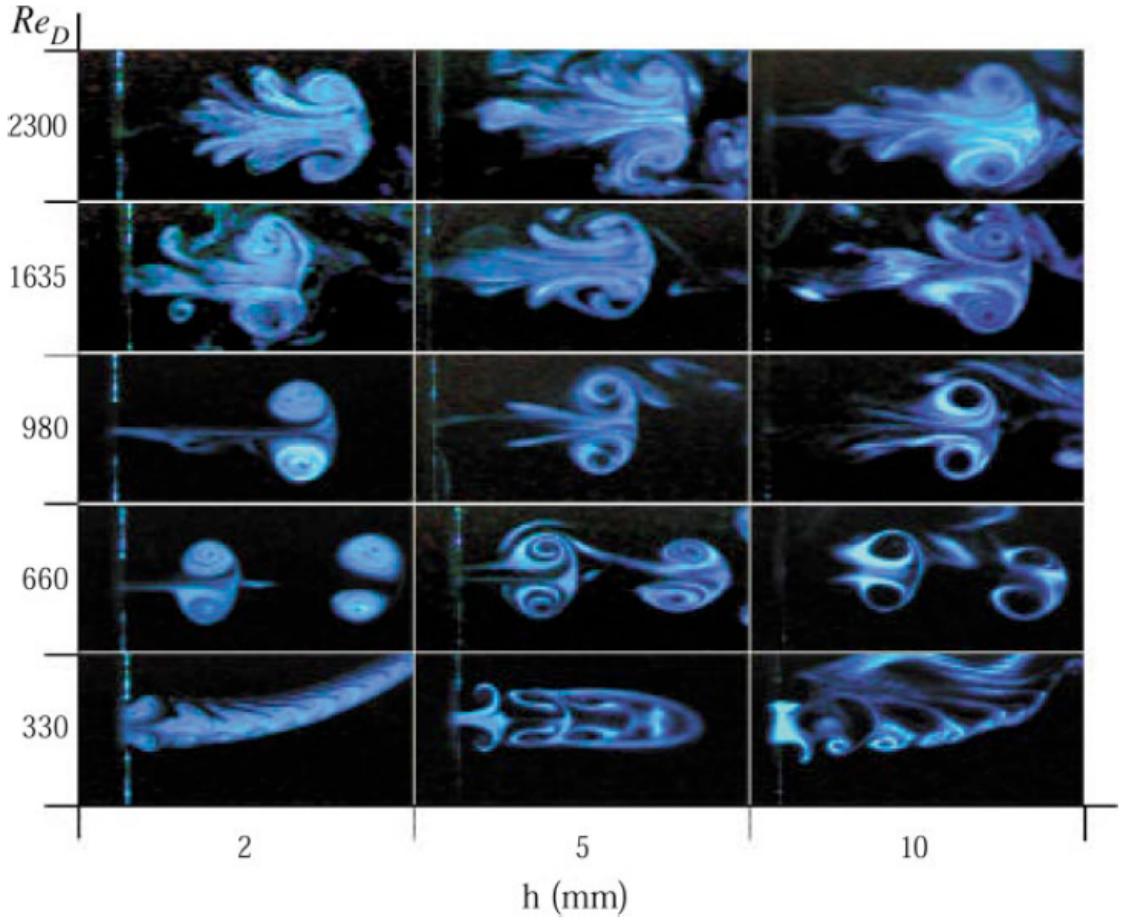

Figure 2.4: Effect of Re (based on orifice diameter D=5 mm) and orifice length on the flow field of a round synthetic jet operated at f=50 Hz (from Crook & Wood [151]).

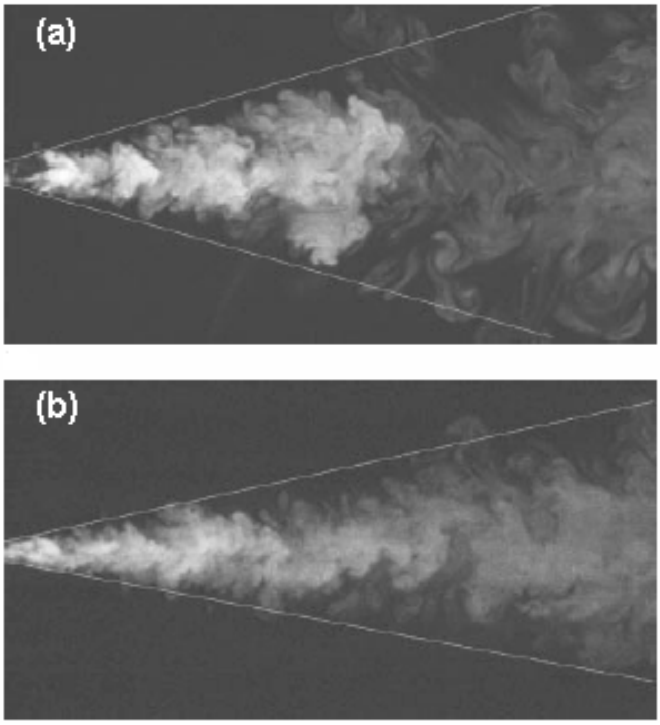

Figure 2.5: Flow visualization of a round synthetic jet (a) and equivalent continuous jet (b) (from Cater & Soria [154]). The white conical lines are drawn to indicate the relative spreading of each jet. $D = 2$ mm, $Re = 10^4$, and $St = 0.0015$ (see eqn. 2.22 for definitions).

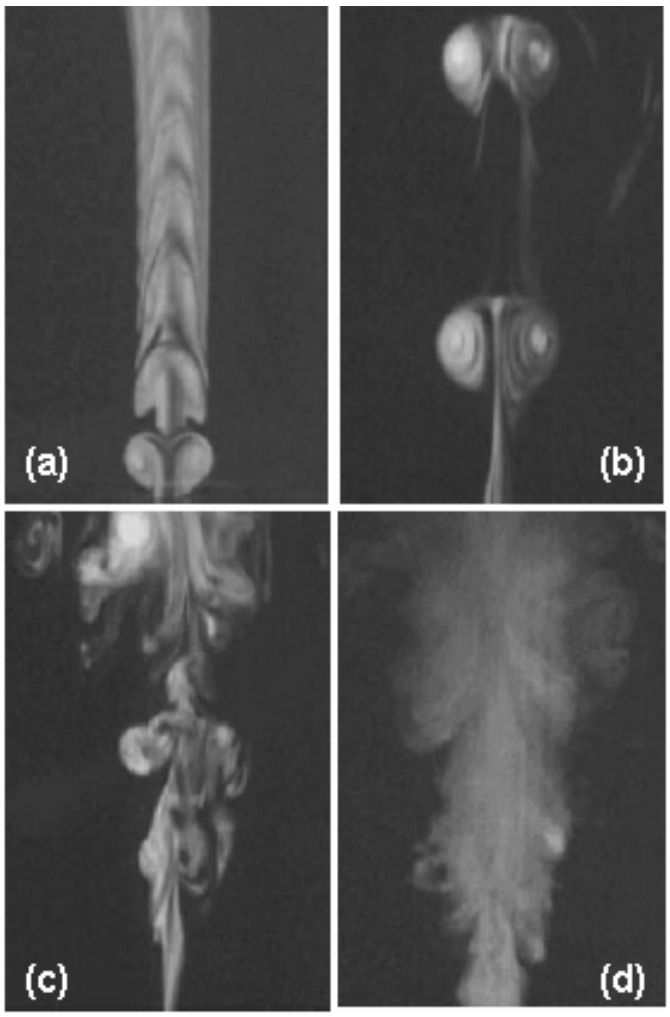

Figure 2.6: Effect of Re and St variation on the flow field of a round synthetic jet. (a) Re = 3336, St = 0.03, (b) Re = 7784, St = 0.012, (c) Re = 11,121, St = 0.009, and (d) Re = 66,961, St = 0.009 (from Cater & Soria [154]).

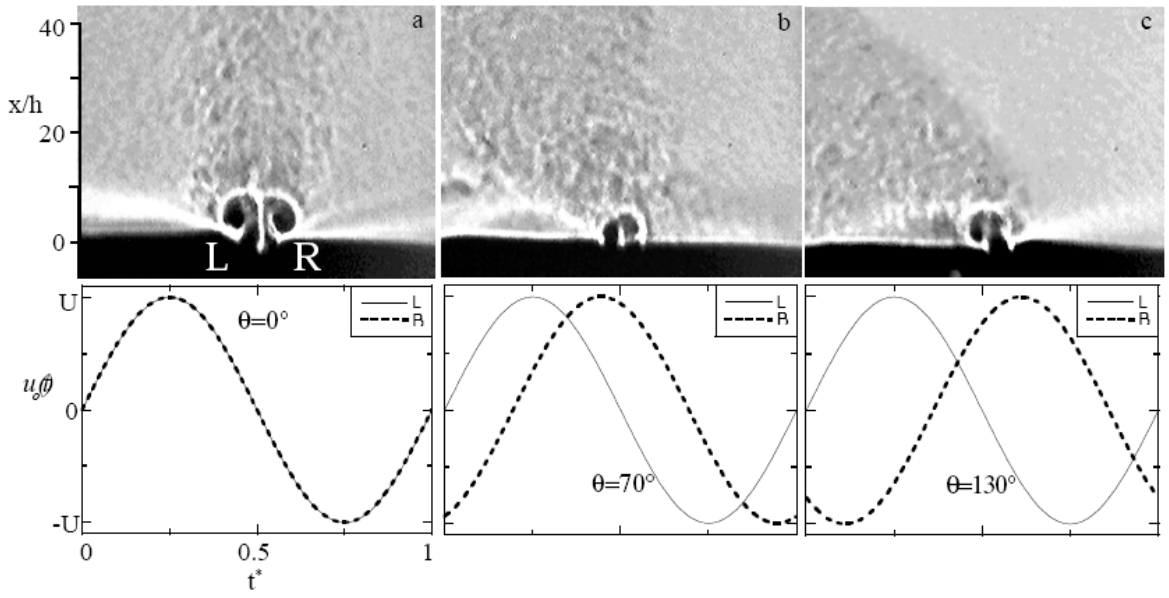

Figure 2.7: Schlieren flow visualization of the induced flow field of adjacent rectangular synthetic jets located parallel to each other. L and R indicate left-side and right-side actuators respectively, and the phase difference between the driving signals of the actuators are shown (from Smith *et al.* [156]).

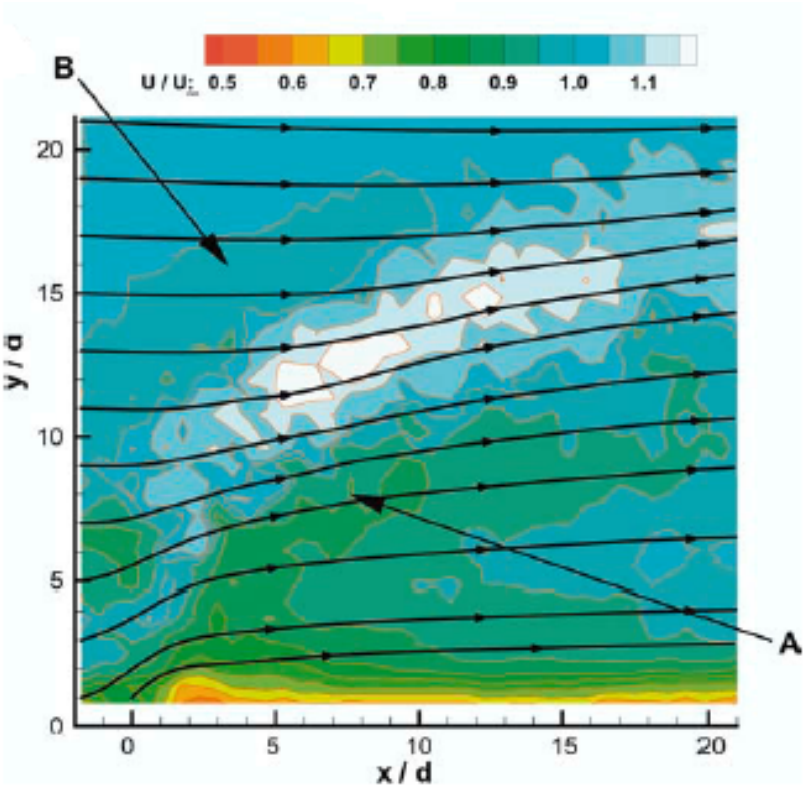

Figure 2.8: Streamwise velocity contours from averaged PIV results showing the interaction of a round synthetic jet with a flat plate boundary layer flow. A and B indicate regions of lowered velocity downstream and upstream of the jet respectively, cross flow direction is from left to right (from Gordon & Soria [167]).

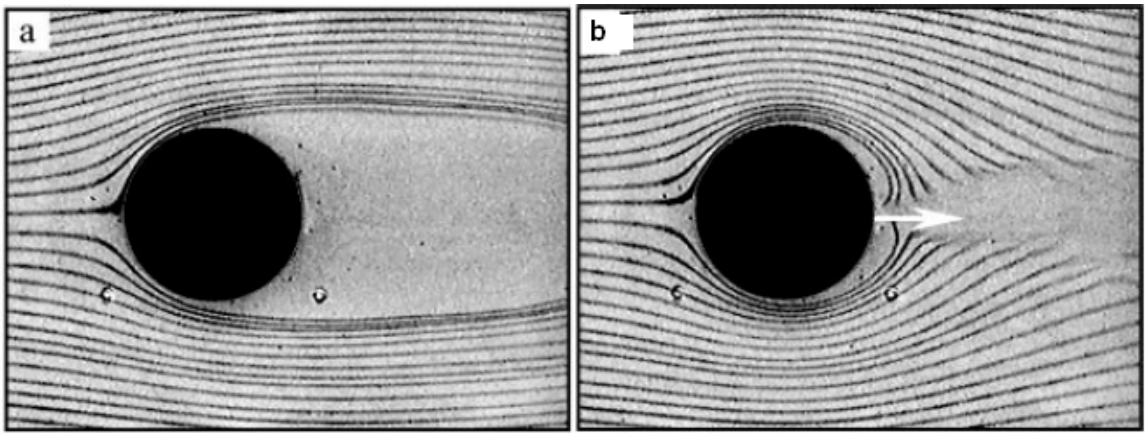

Figure 2.9: Visualization of the interaction of a synthetic jet with the flow over a circular cylinder: (a) actuator off, and (b) actuator on. Flow direction is from left to right (from Glezer & Amitay [147]).

Chapter 3

PRELIMINARY OBSERVATIONS

Toward the final section of the introductory chapter, the motivation for exploring the plasma synthetic jet actuator for active flow control applications was discussed. As a way of introduction, this chapter will examine some background work that was performed on this design. These are presented in this chapter with the intention of providing the reader with a basic idea of some of the characteristics of plasma synthetic jet actuators, before indulging in further exploratory studies provided throughout the rest of the dissertation. Figure 3.1(a) shows a schematic of the annular plasma synthetic jet actuator construction. It is observed that operation of the annular actuator results in the formation of a plasma region that is toroidal in nature, starting from the inner edge (closer to the actuator center) of the exposed electrode ring and expanding toward the center of the enclosed circular area on the dielectric surface. This arrangement is essentially a geometric variant of the linear plasma actuator design, in that annular electrodes are used instead of rectangular strips. From the earlier discussion in the first chapter, it can be noted that the single line of plasma formed on operation of the conventional plasma actuator introduces near actuator entrainment and subsequent expulsion of this volume of air in the form of a wall level jet. Obviously, the plasma is responsible for this flow field feature, and hence the jet characteristics would have to be related to plasma strength. Intuitively, the proposed annular design should also promote entrainment near the plasma region in a similar manner. In contrast to the linear plasma region, however, if the strength of the plasma was approximately equal along the circumference of the toroidal region, the flow field effects are expected to be symmetric about the vertical axis referenced from the actuator center. The action of pulling in air by the plasma towards the actuator center would thus have to result in a vertical jet on account of mass conservation. The maximum spatial extent of the plasma on the exposed surface of the annular actuator is limited by the region within which the applied electrical potential exists, and this is given by the sum of the embedded electrode dimension and the net gap (if any) between the placement of the inner edge of the exposed electrode and outer edge of the embedded electrode. Figure 3.1(b) shows a sample Schlieren flow visualization image of a vortex ring advecting downstream of the plasma induced jet, and the creation of a plasma induced synthetic jet by on/off pulsed operation of the annular plasma actuator. A motion sequence (provided separately as a movie file) obtained by

using the above visualization technique shows that pulsed operation of an annular actuator induces a jet with a "braided" structure similar to those seen in conventional synthetic jets, suggesting an interaction between the vortices generated during different portions of the actuator duty cycle. As expected, the pulsing frequency and the actuator dimension affect the formation of the flow field structures and the resultant jet, as shown from PIV based visualizations shown in Fig. 3.2(a) and (b).

To characterize the actuator, the experiments were first conducted in nearly quiescent environment, and the PSJA was mounted on a flat plate with no external flow. The flow induced by the PSJA was examined from PIV measurements phase-locked to the actuator pulsing frequency. Figure 3.3 shows vorticity contours for an annular PSJA operated at a pulsing frequency of 1 Hz, where four different times of evolution of jet are shown. These were obtained for input sine waveform signal with AC amplitude of about 5 kV and frequency of 4.2 kHz. The diameters of the exposed (d_o) and embedded (d_i) electrodes (conductive copper strips) were 5.8 cm and 3.8 cm respectively, with a gap width of 1–2 mm, and 50 micron thick Kapton was used as the dielectric material. It can be seen that pulsing the actuator creates three counter-rotating vortex rings in addition to the synthetic jet. The plasma ring created on actuation of the PSJA (see Fig. 1.10(a)) pulls in residual fluid adjacent to the surface and ejects it in the form of a jet. The primary vortex ring (Fig. 3.4) is created due to suction and turning of the fluid by the plasma, while the counter-signed secondary vortex ring would have to be created to balance the net flow field circulation in accordance with Kelvin's theorem. When the fluid is ejected out as a jet, it separates from the actuator surface. This produces a weak strength tertiary vortex ring of the same sign as the secondary. The primary vortex ring, while clearly seen near the actuator surface at t=28 ms, advects downstream ahead of the jet at t=63 ms. The primary vortex ring forms near the actuator surface (as seen in Fig. 3.3(a)) and advects downstream ahead of the jet at t=63 ms. The secondary and tertiary vortex rings remain stationary in their spatial location after t=63 ms, however. The secondary vortex ring was observed to be advected outward along the wall when the actuator was turned off. The vortex rings were characterized by defining a circulation based Reynolds number: $Re_\Gamma = \Gamma/\nu$. The starting vortex circulation based Re (at t=28 ms) and secondary vortex circulation based Re (at t=300 ms) were determined to be 135 and 160, respectively.

Figure 3.5 shows the cross-stream distribution of mean axial velocity at t=153 ms. The mean axial velocity and cross-stream distance was non-dimensionalized with local maximum mean axial velocity U_{max} and diameter of embedded electrode d_i. The jet starts to become self-similar at distances close to the actuator. At distances very near the actuator, the

entrainment of fluid by the plasma can be seen, which is is in contrast to the similarity profiles of conventional pulsed jets. A simple control volume analysis shows that there is no net mass flux injected to the flow field, as the fluid that is entrained by the plasma is ejected out as the jet. Figure 3.6 shows a velocity vector plot of the jet flow field, where the vertical lines have been additionally included to indicate the radial stations corresponding to the RMS component streamwise velocity profiles shown in Fig. 3.7 were extracted. Note that u refers to the axial velocity while v refers to the radial velocity. Each of these velocity fluctuations were normalized with the maximum value of the maximum vertical RMS velocity. The RMS velocity component in any particular direction (radial/axial) was calculated by computing the norm of the mean velocity in that direction, and dividing this quantity by the square root of the number of tensor sets (equal to the number of data points) used. For phase-locked measurements, 61 tensors were used for calculation of mean and RMS quantities, all taken at the same phase point (indicated by t) on the actuator pulsing cycle. It can be observed that both radial as well as axial fluctuations for the jet are greater than those of the secondary vortices. The distance from the wall where the peak value of both horizontal and vertical direction fluctuations appears to be very close to the actuator and nearly the same across any radial location. Within the jet field of view, the radial component of the RMS velocity reaches its baseline value very near the wall (at distances $< 0.2d_i$), while the decrease of the corresponding axial counterpart does not occur even at a cross-stream distance of $0.4d_i$. This is expected physically, as a conventional synthetic jet transports higher levels of RMS quantities in the longitudinal direction as opposed to the transverse direction. The Reynolds stress term normalized by its maximum value is also shown. A short-lived peak in this value occurs very close to the wall, and the flow field barring the jet appears to be relatively void of any comparable level of RMS components. This suggests that the jet contains higher levels of turbulent fluctuations than the rest of the flow structures, an observation that is also supported by the turbulent kinetic energy contours shown in Fig. 3.8(a), where this quantity was defined per unit mass of fluid using the expression $\sqrt{u'^2 + v'^2}$. The jet is unstable, while the secondary vortical structures in the flow field are laminar. The kinetic energy peak occurs at the center plane of the jet, and in general, decreases downstream. Interestingly, a comparison of this behavior to the turbulent kinetic energy of a conventional rectangular synthetic jet obtained from the PIV investigation by Béra *et al.* [152] shows a complete disparity between the jets, ostensibly due to the difference in mechanism of jet formation (Fig. 3.8(b)). It must be noted that no effort has been made to match the dimensionality, length, and velocity scales of the two jets compared, and the observations stated herein are merely qualitative. The energy of the

conventional synthetic jet is dominated by substantial transverse expansion, in complete opposition to the decreasing transverse expansion in the streamwise direction of the plasma synthetic jet. The fluid entrainment initiated by the jet driver in each case (acoustic field and plasma) creates increased fluctuations in the near field of both cases. The longevity of these fluctuations and its cross-stream distribution, however, are very short for the plasma synthetic jet as compared to its conventional counterpart.

Interestingly, while the net mass flux of the jet in the near-field of the actuator is zero on account of a balance between the entrained and ejected fluid, the hydrodynamic force imparted by the jet is non-zero. The streamwise distribution of the force produced by the fluid discharge is shown in Fig. 3.9, and this was determined by using the inviscid second-order momentum integral equation as given in Hussein *et al.* [175], modified slightly for the present case as given below

$$I = 2\pi\rho r_i \int_0^\infty (U^2 + \overline{u'^2} - \frac{1}{2}(\overline{v'^2} + \overline{u_\theta'^2}))dr \tag{3.1}$$

where U indicates the mean component of the axial velocity, u' and v' are the axial and radial RMS components of the velocity, respectively, u_θ' is the azimuthal RMS velocity, ρ is the density of air at STP conditions, and r_i is the radius of the embedded electrode. Following the observation in Hussein *et al.* [175], the azimuthal velocity (not obtainable in the 2-D PIV measurements reported in this chapter) was related to the radial RMS velocity as $\overline{u_\theta'^2} \approx 0.5\overline{v'^2}$. In general, for all the four different times within the 1 Hz (period = 1000 ms) pulsing cycle shown, the variation of the imparted momentum peaks very near the actuator at distances less than $0.5d_i$, after which it decreases sharply for distances downstream. No single scaling can be synthesized for the streamwise decay of momentum across all the times shown. Highly unsteady behavior of the jet can be noted, given that the overall maximum impulse increases starting from 12 dynes at 28 ms to 14 dynes at 63 ms, after which the peak value decreases for 153 ms and 300 ms. The far-field (referring to $x > d_i$) decay is sharper for 28 ms and 63 ms, such that the momentum falls to values lower than those for the latter two times shown. This is conjectured to be related to the presence of multiple starting vortices (from previous portions of the actuator cycle) for the 153 ms and 300 ms cases at these far-field streamwise locations (see Fig. 1.11 for flow streamlines).

To assess the amount of energy spent on generating the secondary vortex ring structures that are formed in addition to the synthetic jet, the momentum curves shown in Fig. 3.9 were integrated in the streamwise direction, and the time variation of this fluidic work (or energy imparted by the jet) is shown in Fig. 3.10. The upper bound indicates the integration process performed across the entire cross-stream of the PIV window of observation, while

the lower bound is obtained on integration of momentum across the jet field of view. The average of the work performed by the jet and the associated secondary vortices on the quiescent medium is shown, and the variation of this quantity across different times of observation is highly unsteady, peaking at 63 ms. This is expected in line with observations on the hydrodynamic force discussed earlier. The work done toward generation of secondary vortices is approximately 2 dynes. It is interesting to note that this value is nearly unchanged with time, independent of the variation of momentum imparted by the jet. Figure 3.11 shows the variation of the circulation strength of the secondary vortex (located at the right hand side of flow field) with increasing radial distance across different times of the actuator pulsing cycle. With increasing time, the peak value of circulation increases noticeably between 28 ms to 63 ms, after which it increases only slightly, confirming the relatively steady behavior of work expended for generation of these structures. The time evolution of the maximum axial velocity (Fig. 3.12) shows that the peak value of 65 cm/s occurs at t=63 ms and then plateaus to nearly constant value. This suggests that unsteady operation of the annular PSJA would be optimal in obtaining maximum jet momentum for flow control purposes. Further details of this actuator performance can be found in Santhanakrishnan *et al.* [176].

It must be noted that the annular PSJA, akin to a circular synthetic jet, would introduce three-dimensional structures in the flow. In order to make this actuator easier to analyze in two-dimensional flow situations (such as laminar flow over a flat plate), the linear actuator can be modified to have two exposed electrodes and one embedded electrode (see Fig. 3.13(a)). Such an arrangement can be visualized as that obtained by placement of two linear plasma actuators oriented parallel along their long dimension, so that the entrained flow from each actuator opposes that of the other, and also such that both actuators have a common embedded electrode. Two regions of plasma are thus created along the edges of each exposed electrode, as shown in Fig. 3.13(b). This design induces a vertical jet in the same way as the PSJA described above, but resembles a synthetic jet emanating from a rectangular orifice, which can be considered to be nominally two-dimensional (such as in Smith & Glezer [149]). This particular design, the linear plasma synthetic jet actuator (also referred to as linear PSJA or L-PSJA in the rest of the dissertation), is in effect the limiting case of an elliptical actuator when the major axis goes to infinity. Note that throughout the rest of the dissertation, a reference to a 2-D jet (such as the one induced by the L-PSJA, for example) is used to denote a plane rectangular synthetic jet, and strictly not an axisymmetric jet.

3.1 Summary

This chapter presented some of the characteristics of plasma synthetic jet actuators operated in initially quiescent air, presented for the purpose of introduction to the reader. A toroidal region of plasma is formed on operation of the proposed annular design, which is observed to drive the residual air in the form of a vertical synthetic jet. The jet qualitatively resembles conventional continuous and synthetic jets in terms of its self similarity behavior, when normalized using local maximum axial velocity and actuator embedded electrode dimension. However, the structure of the plasma synthetic jet shows considerable complexity in terms of multiple counter rotating vortices that are created upon actuation, compared to conventional synthetic jets. The starting vortex is advected upstream ahead of the jet similar to conventional synthetic jets, and is conjectured at this stage to affect the streamwise behavior of the plasma synthetic jet. The momentum imparted by the jet is observed to be unsteady across different times of observation along the actuator pulsing cycle, and a nearly steady value of the input energy is expended toward generation of secondary vortical structures present in the flow field. The peak axial velocity of the jet was found to reach a maximum very close to the start of the actuator pulsing cycle, after which it settles to a roughly constant value, once again suggesting the existence of unsteady times within the pulsing cycle for optimal actuator operation.

3.2 Tables and Figures

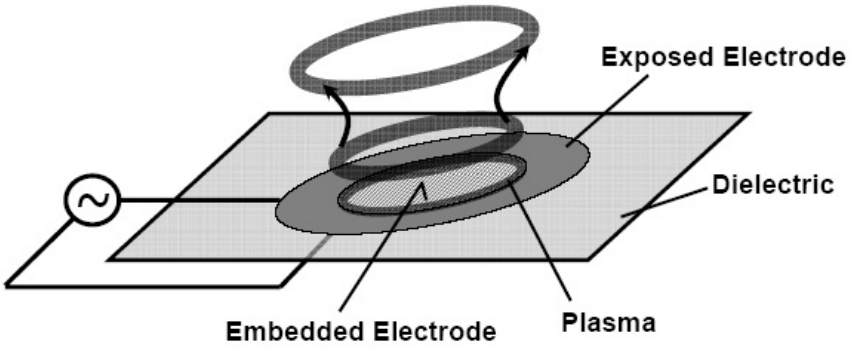

(a)

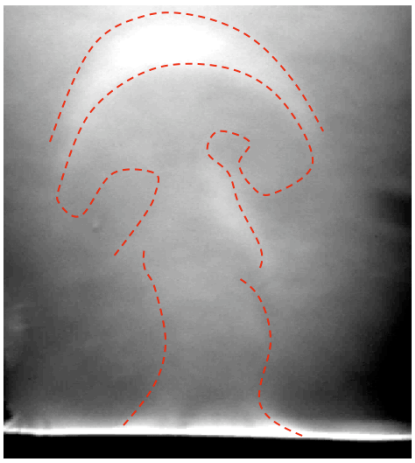

(b)

Figure 3.1: (a): Annular PSJA construction (direction of induced flow is shown), and (b): actuator operation in quiescent flow, instantaneous Schlieren image of starting vortex ring. Lines have been manually added at discernible edges to denote structure.

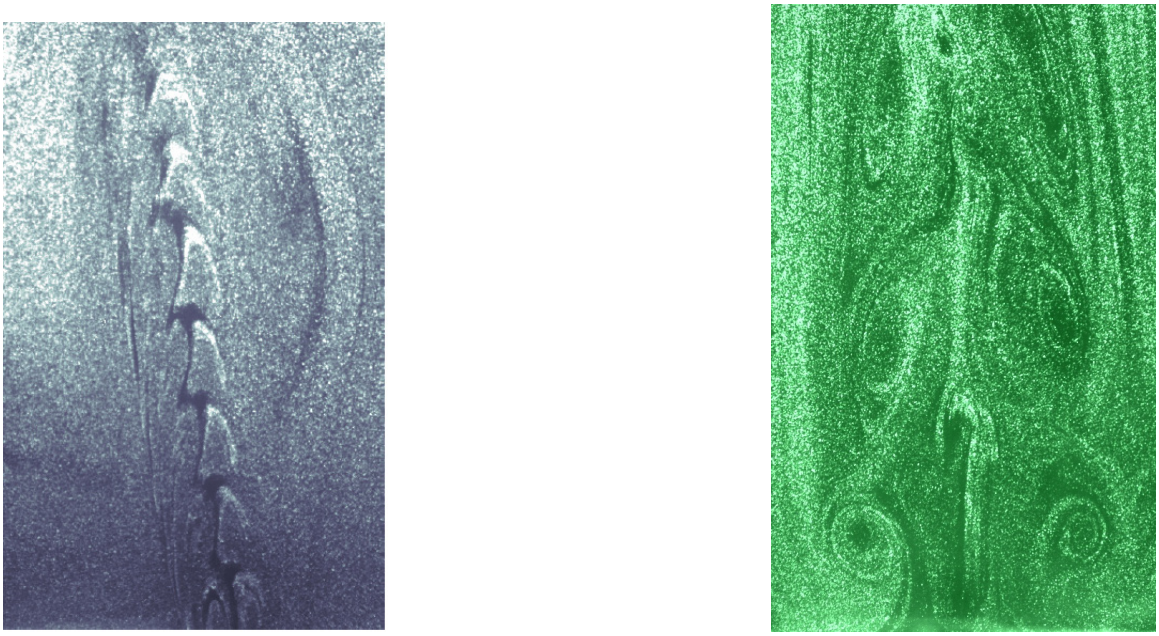

(a) $d_i = 1.27$ cm.

(b) $d_i = 2.54$ cm.

Figure 3.2: Sample flow field images obtained from PIV measurements on 10 Hz pulsed operation of an annular actuator showing trains of starting vortex structures synthesized from the residual air.

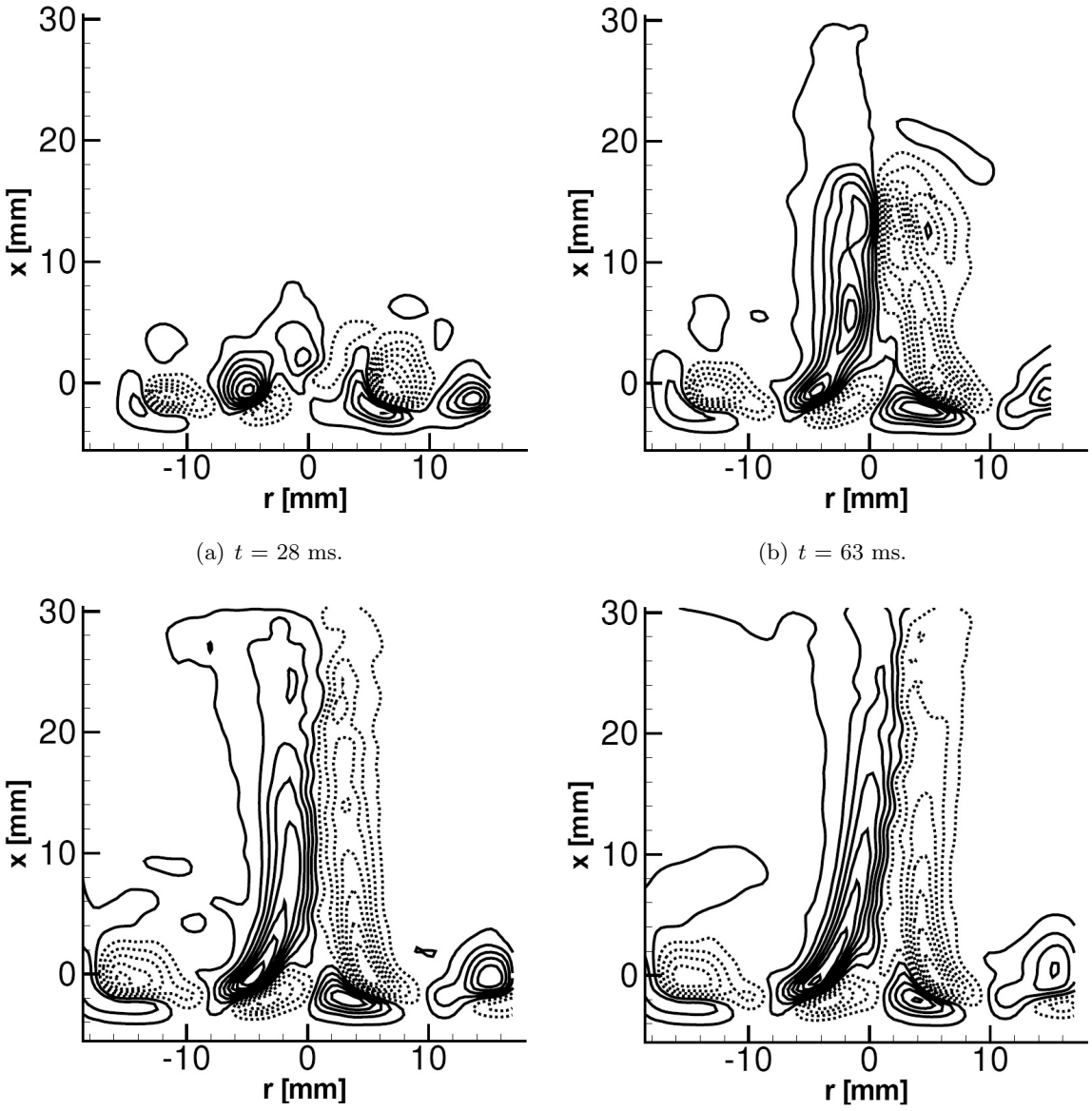

(a) $t = 28$ ms.

(b) $t = 63$ ms.

(c) $t = 153$ ms.

(d) $t = 300$ ms.

Figure 3.3: Averaged PIV results showing vorticity contours of PSJA in quiescent flow. Measurements phase-locked to actuator pulsing frequency f_p=1 Hz; dashed lines indicate negative vorticity.

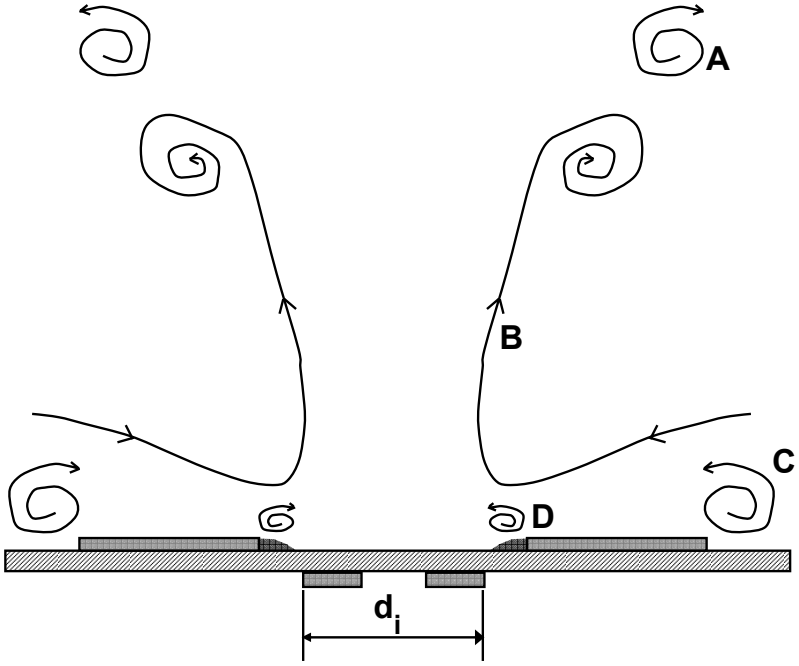

Figure 3.4: Cartoon showing different flow structures observed on pulsed operation of the PSJA. (A) primary/starting vortex ring, (B) plasma induced jet, (C) secondary vortex ring, and (D) tertiary vortex ring.

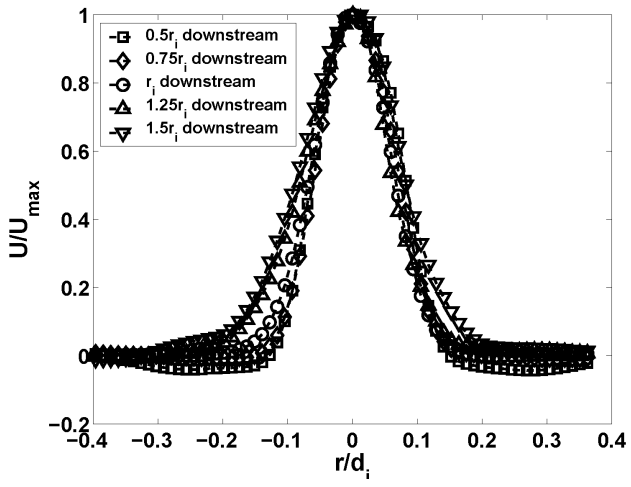

Figure 3.5: Cross-stream distribution of mean axial velocity, t=153 ms, 1 Hz pulsing.

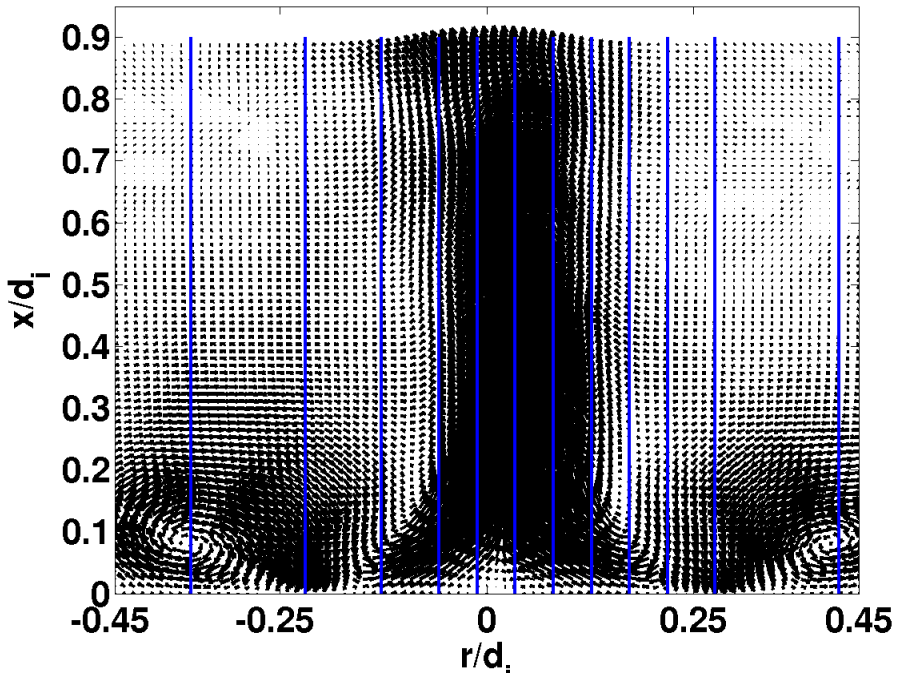

Figure 3.6: Radial locations of velocity profiles on PIV vector plot, 1 Hz pulsing.

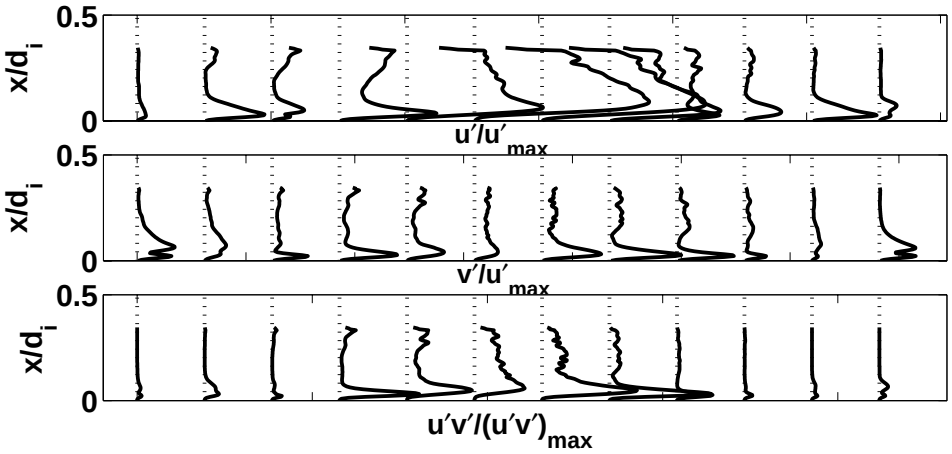

Figure 3.7: Streamwise velocity profiles, 1 Hz pulsing.

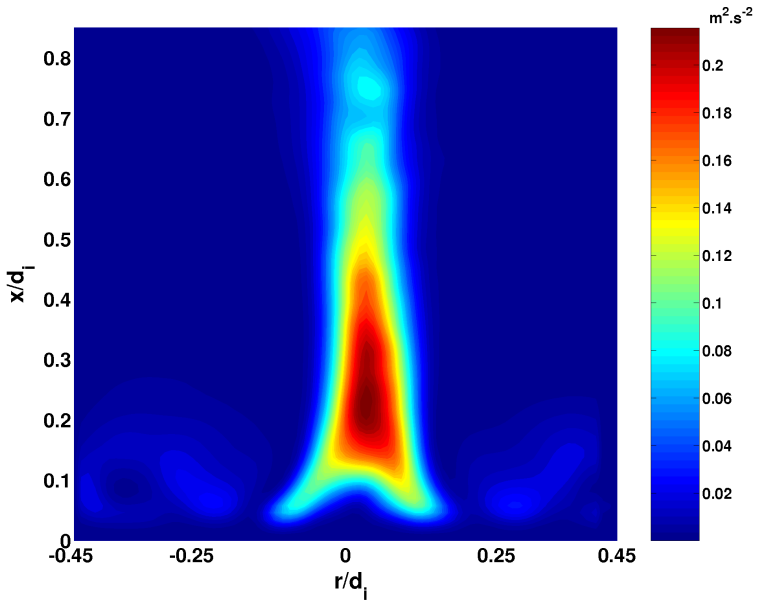

(a)

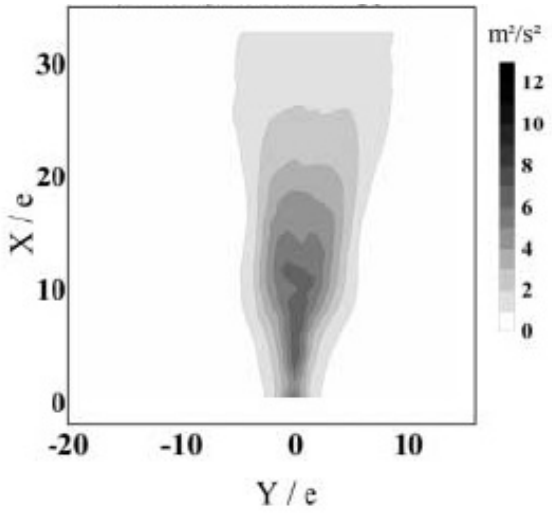

(b)

Figure 3.8: Turbulence kinetic energy distribution for: (a) an annular plasma synthetic jet, actuator pulsed at 1 Hz, and (b) a conventional 2-D synthetic jet, obtained from Béra *et al.* [152]. The dimensionality, length scale, and velocity scale of the jets are not comparable.

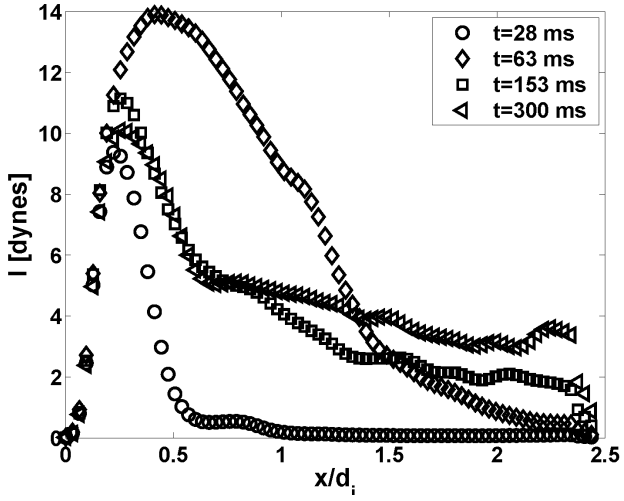

Figure 3.9: Streamwise distribution of fluid impulse, 1 Hz pulsing.

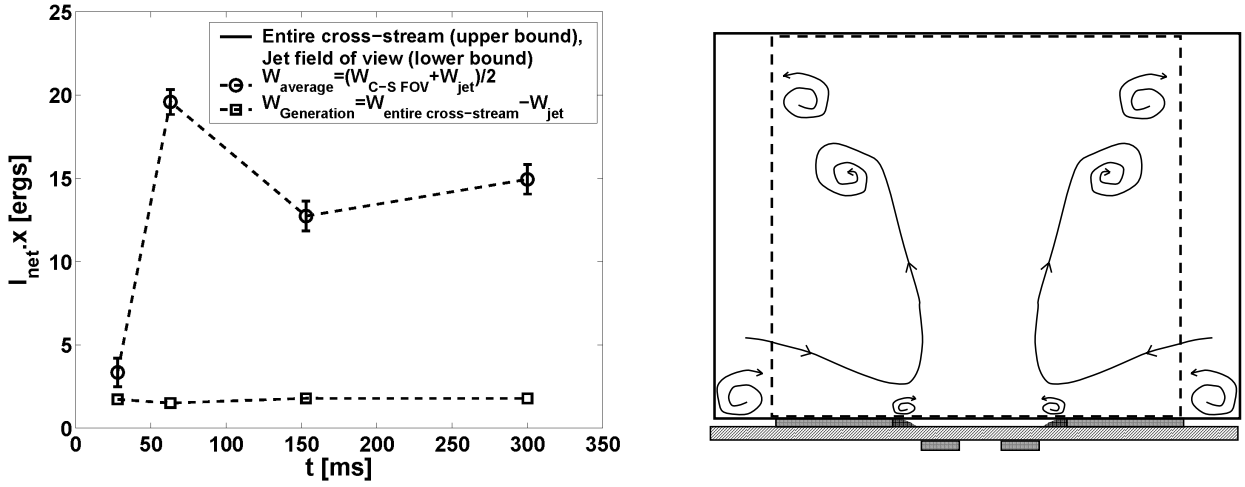

Figure 3.10: Time evolution of fluidic work performed by the jet, 1 Hz pulsing (left). Right hand side shows cartoon of plasma synthetic jet demarcating regions used for integration; dashed lines indicate the jet field of view, and solid lines are used to represent entire area of the PIV window.

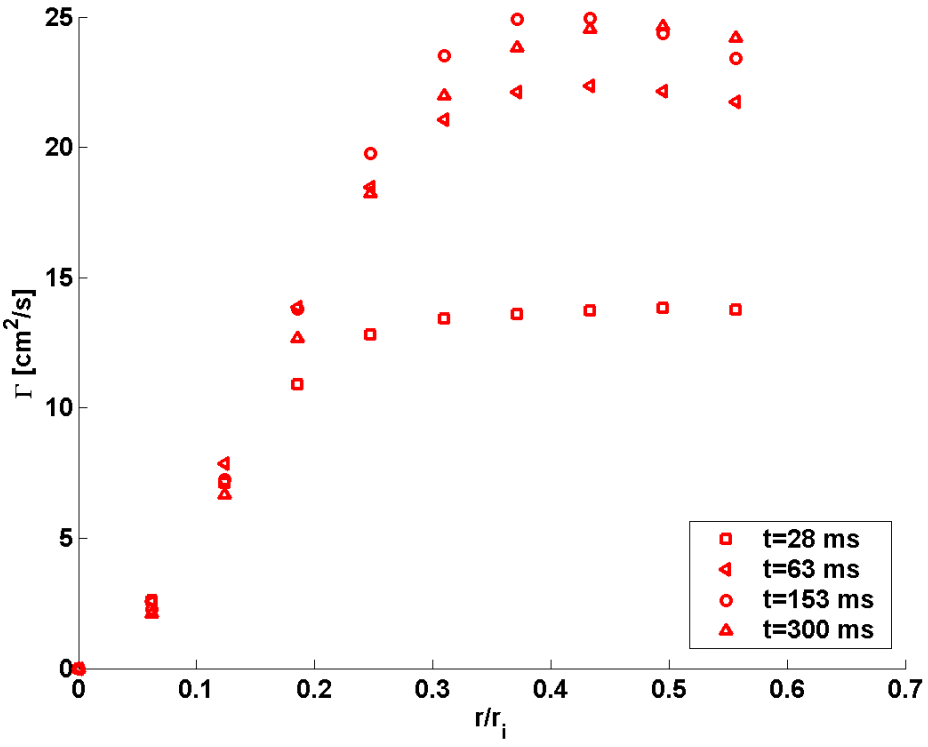

Figure 3.11: Cross-stream variation of circulation strength of the right hand side secondary vortex structure. (Determined using $\Gamma = \oint udl$.)

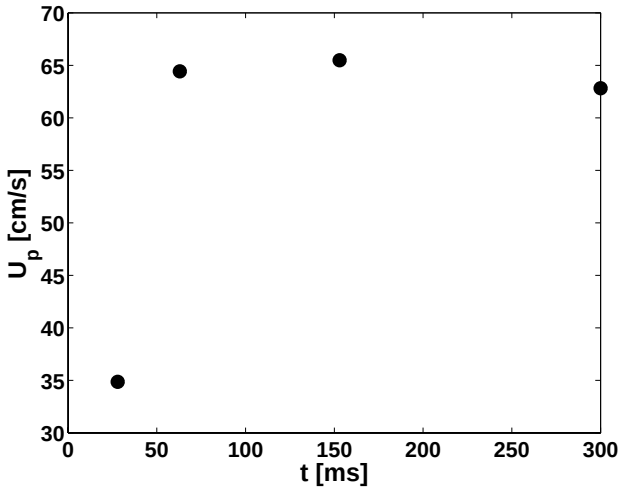

Figure 3.12: Time evolution of peak axial velocity of jet, 1 Hz pulsing.

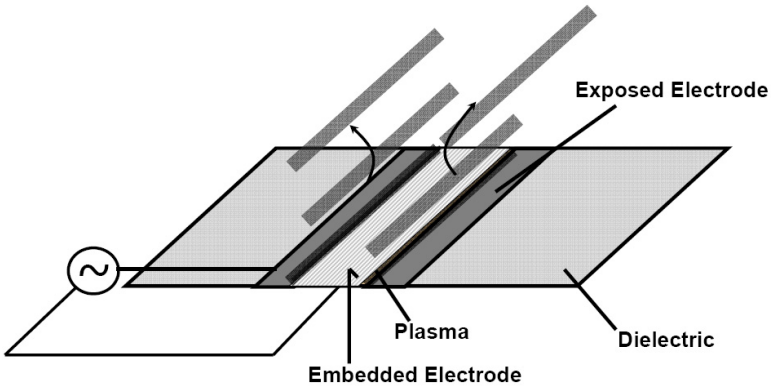

(a)

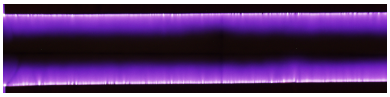

(b)

Figure 3.13: (a) Schematic of Linear PSJA (direction of induced flow is shown), and (b) Plasma structure created on actuation.

Chapter 4

EXPERIMENTAL ARRANGEMENTS

4.1 Overview

A large number of experiments were conducted on annular and linear plasma synthetic jet actuators, and less extensively on the conventional linear plasma actuator. The first phase of experimentation was geared exclusively toward fluid dynamic characterization of plasma induced synthetic jets. The PSJA configurations were implemented in three different flow situations, which included a quiescent medium, actuator mounted on a flat plate parallel to an incoming cross flow, and separation control of the flow over a circular cylinder. These experiments were designed with an intent to provide controlled observations on the effects of imposing an external cross flow, pressure gradient and curvature on the plasma induced jet. Several input parameters, including pulsing frequency, input power, and actuator dimension and orientation were varied to examine their effects on the isolated plasma synthetic jet characteristics. For describing the actuator interaction with a cross flow, the baseline flow velocity and input power were varied. The second phase of experimentation involved simultaneous measurements of the isolated jet flow field, plasma structure, and input power. These experiments were designed so as to correlate the flow field to the plasma morphology, as well as to synthesize scaling relations of plasma synthetic jet actuators. For the entire set of measurements considered, quantitative flow field measurements were obtained using time-averaged and phase-locked particle image velocimetry, time exposed CCD images of the plasma were used to deduce information on its structure, and the actuator power was monitored during each experimental run. The diagnostic hardware and software used were the same throughout. Minor changes were implemented in the actuator power supply, arrangement of equipment, and the procedure employed for the collection of data was similar for most of the measurements. The following sections describe the wind tunnel facility used for cross flow studies, actuator construction and power supply, and the description and arrangement of diagnostics.

4.2 Facility and Apparatus Description

4.2.1 Wind Tunnel

The measurements for characterization of plasma synthetic jet actuators implemented in flat plate boundary layer and circular cylinder flows were conducted in the low speed wind tunnel at the University of Kentucky. The test section of this blow-down, low turbulence, open-circuit tunnel is constructed with acrylic and measures approximately 1.5 m long and 0.4 m across with a depth of 0.2 m. A 7.5 hp DC motor is used to drive a radial fan at the inlet, and this is connected to a nozzle followed by the test section. The flow at the inlet of the nozzle is conditioned upstream by passing through a vibration damper, flow straightener, and turbulence dampening screens. The contraction ratio (ratio of the cross-sectional area of the inlet to that at the throat) of the nozzle was 6.7:1. The cross-sectional areas of the inlet and the outlet were 0.080 m^2 and 0.064 m^2, respectively, producing inlet to outlet area ratio of 1.25:1. With an open exhaust, the maximum exit velocity achievable in the test section was 35 m/s. The nominal value of the free stream turbulence intensity (FSTI) within the test section, given by the ratio of root mean squared of fluctuating velocity normalized with the mean velocity, was measured with a hot-wire anemometer to be approximately 0.6%.

To remove the effects of both curvature and pressure gradient, a flat plate at zero inclination to the free stream was used to study the actuator characteristics. The flat plate was constructed of plexiglass measuring 0.3 m long and 0.4 m wide, with a thickness of 0.005 m. The actuator was mounted inside a square recess 0.114 m in length and $6{\cdot}10^{-4}$ m deep cut at its center. A 1.27 mm (0.05 inch) diameter wire was used to trip the incoming boundary layer, and was located at the leading edge of the flat plate. This plate was mounted such that its bottom surface was located at a distance of 0.025 m from the bottom wall of the test section, such that the leading edge was located 1.2 m downstream from the nozzle exit (or entrance of the section). Another flat plate with the same dimensions, but without any recess, was placed such that its uppermost surface was located 0.025 m from the top wall of the test section. The schematic side and top views of the test section with the flat plate and annular PSJA arrangement is shown in Fig. 4.1. The arrangement was identical for linear PSJA measurements, the only difference being the actuator construction. The entire test section was optically accessible, thus PIV measurements could be conducted along different downstream distances if required (for the cylinder flow control experiments).

4.2.2 Actuator Design and Construction

Annular and linear plasma synthetic jet actuators with varying electrode dimensions were examined. Copper foil tape of thickness $8.89{\cdot}10^{-5}$ m (0.0035 inches) was used as the electrode material for all the actuators constructed and tested. The tape consisted of 0.0021 inch thick foil and 0.0014 inch thick non-conductive acrylic adhesive. The latter factor prevents undesirable electric discharge, and solder can hence be passed over the surface of the tape without adhering to it, making it ideal for plasma actuator construction. The temperature range of the copper tape was -20 °F to +310 °F. This material was easy to be shaped into any desired geometry. For the annular PSJA, the electrode shape required was manually punched and cut out from a sheet of this tape. For the linear actuator and linear PSJA, the rectangular strip shaped electrodes were manually cut from this tape. While constructing the annular plasma actuator, extreme care had to be taken to visually ensure that the curvature was uniform throughout the circumference and align the centers of the exposed and embedded electrodes. Figure 4.2 shows general schematic views of the PSJA construction for both annular and linear variants. The plasma region is formed at the region of highest electric field. The actuator was operated in air at ambient conditions of pressure, temperature, and humidity, and none of these parameters were modulated artificially throughout this research. Reiterating relevant comments stated in chapter 2, it can be noted that for length scales greater than the Debye length, thermal effects at the edges become important. There is a slightly increased electric field distribution at these regions that initiates a charge species imbalance within the plasma, after which plasma expansion occurs. Considering the upper surface of the actuator, it can be seen that the inner (closer to center) edge of the exposed electrode is the region with highest electric field based on the above reasoning. The plasma spreading stops when there is no more available external potential. This occurs when the edge of the embedded electrode has been reached, after which no conductive surface is available for distribution of applied voltage on the actuator. Thus, the most important determinant of the extent of plasma region is the embedded electrode dimension, d_i. The area available for the plasma to expand over the upper surface of the dielectric is given by $\pi\left(d_i + 2w\right)^2/4$. If the lower electrode is not grounded, but instead driven with a potential difference compared to the upper electrode, similar arguments can be used to suggest that plasma formation begins at the outer (farther from center) edge of the embedded electrode and depending on the applied field strength, may spread to the outer edge of the exposed electrode. Typically, the gap width w, defined as the distance between the inner (closer to center) edge of the exposed electrode placement

of the exposed and outer edge of the embedded electrodes on either sides of the dielectric material, was zero in most experiments, and in some cases there was an overlap in electrode placement of approximately 1–2 mm. In order to match the dimensions of the annular PSJA with an equivalent linear PSJA, the embedded electrode dimension has to be maintained the same in both designs, and it is easy to note that

$$w_e = (d_o - d_i - 2w)/2$$

where the quantities have been defined in Fig. 4.2. It is important to note that the above figure refers to the arrangement of PSJA (2-D or 3-D) required to engender a jet in the blowing configuration. Although not presented herein, an inverse configuration effecting suction of the residual air may be constructed by merely reversing the electrode arrangements. The flexibility in tailoring a baseline flow field through the use of combinations of alternating blowing/suction PSJA arrays based arrangements can be realized with these devices, and this powerful aspect obviously has important implications in flow control. This dissertation work is focused to characterization of the blowing configuration exclusively, and the design of suction configuration will not be illustrated herein for sake of clarity. For the interested reader, a brief presentation of the PSJA based suction device may be found in Santhanakrishnan & Jacob [177].

Non-porous alumina ceramic slabs were used as the dielectric material for all quiescent and flat plate boundary layer experiments presented hereon in the rest of this dissertation, unless specified otherwise. The slab was 0.635 mm thick, and 114.3 mm in length and width. This dielectric was capable of handling temperatures up to 2900 °F. This material has a dielectric constant (ϵ_r) of 9.4, mass density of 3700 kg/m^3, and dielectric strength of 15 kV/mm (indicative of the maximum electric field strength prior to breakdown) [108]. The slab was not easily machinable on account of its hardness, as a result of which it was not flexible enough to be adapted to fit on non-flat, curved surfaces. On account of this limitation, 50 micron thick Kapton polyamide film was used as the dielectric material for constructing plasma actuators for the circular cylinder flow separation control study. Kapton is highly flexible, with a dielectric strength of 291 kV/mm, dielectric constant of 2.7, mass density of 1420 kg/m^3, and is capable of handling temperatures up to 464 °F. The thickness of the Kapton layer, albeit not varied during the course of this research, can be increased to enable the actuator to handle increased potentials applied across it, due to the obvious increase in dielectric strength.

For all the experiments with the plasma synthetic jet induced under quiescent conditions, the actuator was placed over a layer of non-conductive material such as acrylic or

plexiglass, and held in a fixed position using electrical tape. This was then covered with a transparent enclosure to provide a quiescent environment. The enclosure had a square cross section measuring 29.6 cm x 29.6 cm and a height of 15.1 cm. Typical windows of observation used for PIV were less than 4.5 cm in wall-normal direction, which roughly amounts to 30% of the entire domain (maximum jet blockage ratio). This is important in identifying any false recirculation introduced in the PIV window on account of the plasma synthetic jet rebounding from the upper wall of the enclosure. Unless mentioned otherwise, the dimensions of the embedded electrode diameter (d_i) of the annular PSJAs used in this work was 1.27 cm and exposed electrode diameter (d_o) was 2.54 cm.

4.2.3 Power Supply

The preferred conditions for the formation of a DBD plasma is pressures in the range of 10 kPa to 500 kPa, and alternating frequencies in the range of 1 kHz to 10 MHz (see Kogelschatz [178]). Several kilovolts of potential are required in order to ionize the air at the interface of the electrodes. The value of breakdown voltage that is necessary for discharge creation depends on other factors in addition to the above, such as electrode dimension, curvature, and most importantly, the dielectric material used. Typical requirements of current can range from 10 mA to several 1000 mA. Based on the equation describing the plasma actuator-flow field effect presented earlier in chapter 2 (see equation 2.16), it can be observed that the input current does not directly affect the gross DBD characteristics as compared to the voltage difference between the electrodes [84]. However, the current input indirectly affects the momentum coupling of the actuator due to its contribution to the net electrical power input to the actuator.

The schematic of the power supply used for driving the plasma actuator is shown in Fig. 4.3, with the annular PSJA included as a general example. For the linear PSJA, the schematic remains the same, except that the exposed electrodes are powered by two separate lines connected in parallel, so that the applied potential is distributed equally. The input alternating waveform required for the actuator is provided via the output of a Hewlett Packard 33120A function generator/arbitrary waveform generator. The voltage output of this device, measured peak-to-peak, was in the range 50 mV to 10 V. Typically, the amplitudes employed for operating the actuators herein were in the range of 1 V to 10 V. This function generator was capable of providing sine, square (range: 10 μHz to 15 MHz), triangle and ramp (range: 100 μHz to 100 kHz). For all the plasma actuator experiments reported hereon, a square waveform was used in general, and typical input frequencies were 1 kHz to 5 kHz. This waveform was provided to the actuator driving circuit at 50% duty cycle

for all experiments, which essentially means that the voltage input is supplied only during half the period of the plasma input AC cycle. Thus, the power input to the actuator would only be half of its actual measured value. The output of the function generator is supplied to a bipolar operational Kepco BPM–01 0–200 V power supply. In some experiments, a 0–100 V Kepco power supply was used, which was capable of providing higher levels of current as compared to the 0–200 V unit. The output of the power supply drives a step-up transformer which provides the necessary amplification of the electrical potential required for operation of the DBD plasma actuator. Two transformers were used in this research across the experiments conducted, and impedance matching of the outputs to minimize losses was not carried out in both these devices. The results presented in chapters 3, 5 and 6 (with the exception of increased power results in the latter two) were obtained using an inductively matched step-up transformer manufactured by Industrial Test Equipment Company, Inc. This unit required an input of 1–250 V RMS at 1–7 kHz, and was capable of 6 kV peak output. The positive output terminal of the transformer is connected to the exposed electrode, while the ground terminal is connected to the embedded electrode. For the measurements presented in chapters 7 and 8, increased power results in chapters 5 and 6, and cylinder flow control experiments, a step-up transformer manufactured by Corona Magnetics, Inc., was used to drive the actuator. This was capable of providing a 5.5 kV output with an input of 40 V RMS at 6 kHz, with a secondary to primary step-up ratio of 137.5:1. A previous study by Jacob [179] in linear plasma actuator based flow control showed that beneficial flow field effects could be obtained by driving the exposed and embedded electrodes out of phase, instead of merely rendering the embedded electrode as a ground connection. This finding supports the observations made by Enloe *et al.* [54] in accordance to the elevated importance of the gradient in the applied voltage between the electrodes of the actuator, as compared to its peak value, in affecting the plasma-neutral air momentum coupling characteristics. Following these suggestions, two Corona Magnetics transformers with the specifications mentioned above were employed (wherever this unit was used), so as to drive the embedded electrode 180° out of phase with repsect to the exposed electrode. Hence, the embedded electrode in Fig. 4.3 corresponding to Corona Magnetics transformer based studies was no longer a ground connection.

4.3 Diagnostics

4.3.1 Particle Image Velocimetry (PIV)

Particle Image Velocimetry is a non-intrusive, two or three dimensional technique that can be used to obtain instantaneous information on a flow field by recording and processing the single or multiple exposed images of tracer particles suspended in the fluid. Before the advent of computerized image capturing software and digital cameras, images of particle motion in a fluid were recorded in photographic plates and the flow field was evaluated by particle tracking using analog optical methods. This was limited to very low speed flows, as the particle motions were individually tracked. The earliest development that is often suggested to be the origin of PIV was in the use of double exposed photographs that result in laser sheet based speckles, also known as laser speckle velocimetry (LSV, see Dudderar & Simpkins [180]). By decreasing the number of particles in the LSV system to a sufficiently homogeneous level, particle images required in PIV can be obtained, which are then processed using correlation based techniques. In the present day, the use of digital image recording and processing methods has rendered Digital Particle Image Velocimetry (DPIV) an extremely powerful technique suitable for velocity measurement across a wide variety of flow scales ranging from a few nanometers (Li *et al.* [181]) to several meters (Fujita *et al.* [182]). DPIV is commonly referred to in the current times as PIV. Adrian [183] presents a recent review that documents the technical advancements in PIV from a historical perspective, and can be referred to for further information. Other detailed reviews of PIV can be found in articles by Adrian [184], Willert & Gharib [185], and Raffel *et al.* [186].

Principle

Figure 4.4 shows a general arrangement employed for PIV measurements of flow through an enclosed area, such as within the test section of a wind tunnel. The requirements for conducting measurements using this technique include a monochromatic coherent light source that is pulsed (either by using two beams, or electronic/mechanical pulsing of a single beam) to illuminate the flow, a camera with a charge coupled device (CCD) sensor, and a homogeneous distribution of small seeding particles. Typically, a laser beam is used as the source of light, and this is passed through a set of optics to convert it to a two dimensional thin sheet that is cast on the plane region in the flow where the measurement is to be conducted. The interval between the two pulses of laser firing Δt is predetermined and controllable. The light scattered by the seeding particles is recorded by the camera as sequential images either in the form of single exposed pairs or as multiple exposures (see

below), and information is stored in the pixels available in the CCD. The displacement $(\Delta x, \Delta y)$ of a single particle (or groups of particles) is deduced from correlation based post processing of these images discussed below. A map of the velocity of motion of the tracers in the flow field can thus be obtained using $(\Delta x/\Delta t, \Delta y/\Delta t)$. Other derived statistics such as vorticity, shear stress, etc., are obtained as spatial derivatives of the velocity field. This, in essence, is the working principle of PIV.

Modes of Implementation

Depending on the type of image capture employed for data collection, several modes of PIV can be realized. Two such common implementations are illustrated in Fig. 4.5, and several other examples can be found discussed elsewhere (as in chapter 4 of Raffel *et al.* [186]) The difference between these modes is in the number of exposures of the photographic medium and the number of frames used. In the first mode, the flow field is illuminated twice and the CCD (or film) is exposed once each time the laser is fired. The resulting double exposed image is stored on to a single image file, resulting in the second image of the seeding particles in the flow field being superimposed over the first (doubly exposed, single frame image). More than two exposures of the flow field can also be used, provided the illumination is available, and the timing between successive exposures is known. The advantage of multiple exposed PIV is that it is not restricted by the image capture rate of the camera. It is possible to capture successive images with very small time interval between them ($\mathcal{O}(\mu s)$), by using two lasers that are activated independent of each other. The disadvantage of single frame, multiple exposed PIV arises from the clustering of images on one frame, as a result of which there is no clear sense of the direction traversed by a group of particles between one image to the next. Although this is not a problem in uniform flows where the direction is known *a priori*, this renders the analysis of flows with substantial rotation (such as separated flows) a problematic task. Many schemes have been proposed to tackle the directional ambiguity problem in multiply exposed PIV. Cho [187] suggested that double exposed images may be obtained by adding single exposed digitized video images. A common scheme known as image shifting is used which involves introducing a fixed displacement on the particle images of the second exposure, such that its value is always greater than the maximum reverse flow component of the flow. As a result, both exposures will in effect not have any directional change. A recent method to rectify this 180° directional ambiguity uses a two color CCD, and this eliminates the need for complicated post processing algorithms of the former approach (see Gogineni *et al.* [188]).

The more common mode of PIV employed in the present day relies on recording a

single exposed image of the particle laden flow field corresponding to each illumination pulse of the laser (Fig. 4.5(b)). This image is stored on a single frame, before the next single exposed image (for the second laser pulse) is captured and stored on a separate frame. Thus, the initial positions of the particles are stored on a different image than the final positions. The temporal order of the images is inherently preserved in this approach, thereby eliminating any directional ambiguity. As no elaborate image shifting algorithms are needed for post processing, more robust velocity results can be obtained using single exposed PIV (Jacob [189]). This mode of image capture has only been possible in the recent years, due to the non-availability of cameras capable of capturing images with very short time periods. It is also the earlier factor that is a limitation of the single exposed PIV method, in that the temporal resolution (minimum time step between successive images) is limited by the camera frame rate unlike the multiple exposed mode. Notwithstanding capture rates $\mathcal{O}$(1000 Hz) in many modern day CCD cameras that are used to conduct time resolved PIV measurements, this limit will have to be continually pushed further to enable this technique to successfully measure small-scale turbulence.

Post Processing

Figure 4.6 shows a cartoon of the general schematic used for processing raw PIV data. The image captured by the CCD consisting of tracer particles is shown, with the flow over a flat plate used as an example for the purpose of illustration. Each image captured as a part of a time sequence either in single or multiply exposed formats are divided into many interrogation windows or subregions. The size of these windows is usually a fraction of the entire FOV (e.g: 32 x 32 pixel window used for FOV of 1008 x 1018 pixels). The window used for two successive images are indicated in Fig. 4.6 using different colors, and magnified views of the particle groups within each window is also shown. The window at a particular spatial location (x,y) in the second image of an image pair is moved over the window of its first image located at (x,y), so as to examine the correlation between the particle distribution in these successive images. The implicit requirement for non-zero correlation herein is that the particle displacement has to be extremely small compared to the dimension of the subregion, meaning that the particle (group) identity within a window between successive images must not be lost. Assuming the simplest case where the particles are only linearly translated (as shown in the figure), it is easy to see that the spatial correlation gives an idea of the displacement of the particle cluster in between the two images separated by Δt, from which the velocity of the subregion can be obtained. Many such small interrogation regions are employed throughout the PIV FOV, and a velocity vector field can be obtained using

the same approach described above. In most cases, for performing the spatial correlation, each subregion is transformed into Fourier space via a Fast Fourier Transformation (FFT). The type of correlation (auto or cross-correlation) depends on the mode used for image capture. Multiply exposed PIV images are analyzed using auto correlation, while single exposed images are analyzed using cross-correlation. If the intensities of successive single exposed images are given by I and I', then the cross-correlation function in physical space is given by the sum of their products as (after [186])

$$R(x,y) = \sum_{i=-K}^{K} \sum_{i=-L}^{L} I(i,j)\, I'(i+x, j+y).$$

Thus, when the particle distributions between identical windows in an image pair are identical, R will reach its peak value, and the shift of the second window (with respect to the first) corresponds to the displacement of particles. Considering that several thousand displacement vectors can be obtained for each image pair, the correlation analysis is commonly carried out in Fourier space to lower the number of computations required. The convolution theorem, which states that the cross-correlation of two functions is equal to the complex conjugate product of their Fourier Transforms, is used as given below (see [186])

$$R = \hat{I}\, \hat{I'}^{*}$$

where $\hat{I}$ and $\hat{I'}$ are the Fourier transforms corresponding to intensities I and I', respectively. After determining the cross-correlation, an inverse Fourier transform is used to convert the intensities back into physical space. This FFT implementation of cross-correlation is common to many DPIV routines, and the subregion hence is specified in terms of base 2 dimensions (16 x 16 pixels, 32 x 32 pixels, etc.).

PSJA Setup

The entire set of PIV measurements conducted for the purpose of this dissertation work employed the single exposed, double frame recording technique. A 10-bit dual channel Kodak MegaPlus ES1.0 monochrome CCD camera was used for all the PIV measurements. The high resolution camera was equipped with an electronic shutter, allowing exposure times as short as 127 μs in single exposure mode. The CCD consisted of a 1008x1018 pixel array resulting in a spatial resolution of roughly 1 million pixels. The active area of the CCD measured 9.072 mm horizontal x 9.162 mm vertical, while that of a pixel was 9 μm x 9 μm. The CCD was capable of full-frame interline transfer, with a readout time of about 1 μs in progressive scan mode (see [186] for definition). The readout time of the CCD corresponds to the portion of the camera frame rate (in Fig. 4.5(b)) following the exposure

of an image, and it directly affects how fast the camera can record images. The pixel depth used herein for images captured for PIV was 8 bits, and the frame rate of the camera was 30 Hz (15 image pairs per second). Depending on the level of flow field magnification required, either a 50 mm focal length lens with 0.22X magnification and adjustable focus, or a close focus manual zoom video lens with 18–108 mm focal length was used.

A dual-head 50 mJ Nd:YAG laser from New Wave Research (Solo PIV III) was used as the light source to construct a two dimensional thin sheet of 532 nm wavelength required to illuminate the flow field. The laser had a maximum repetition rate of 15 Hz per laser head, a pulse period around 5 ns, and the beam intensity variation was approximately Gaussian. The light sheet is constructed using an arrangement of 3 lenses, as shown in Fig. 4.7. The laser beam is first focused using a converging lens. A second lens placed at near the focal length of the first lens is then used to diverge the beam and helps to create a thinner, concentrated beam. This is passed through a cylindrical lens which expands the beam into a plane 2-D sheet of approximately 2 mm thickness and variable width across. The thickness of the beam can be controlled by adjusting the separation between these two lenses, or by using a cylindrical lens of different focal length. Ideally, a thinner laser sheet is recommended over a thicker one so that two-dimensionality of measurement can be better ensured, and more intensity is available per unit area of visualization. All quiescent and cross flow measurements were carried out by aligning the laser sheet along the central plane of the actuator, unless otherwise mentioned. For flow over a circular cylinder, several windows of observation along different downstream distances in the wake with roughly 5% overlap were used. The camera was positioned parallel to the plane of the laser sheet. The arrangement used in Fig. 4.7 was used to construct the laser sheet for both quiescent and cross flow measurements. For wind tunnel experiments, the laser and optics were located parallel to the exit of the test section, such the sheet spreading increased in the upstream direction of flow. For circular cylinder flow control experiments, the cylindrical lens located at the end of the sheet forming optics sequence had a larger radius than that used for quiescent and flat plate boundary layer flows. The cylinder was located closer to the entrance of the test section, as opposed to the flat plate which was located at near the test section exit. In order to preserve the laser intensity and diverge it through a longer distance, the larger radius cylindrical lens was used. The timing between two pulses of the laser Δt (as in Fig. 4.5(b)) was controlled by a unit from Taitech Inc., and this allows separation intervals from 1 μs to 250 ms. In order to minimize the delay between laser pulses, the first laser firing occurs toward the end of the frame grabbing of the first exposure, while the second laser firing is placed near the beginning of the successive exposure, also illustrated in Fig. 4.5(b). The

timing must also be adjusted such that each pulse of the laser corresponds to a separate exposed frame of the camera, so that the second frame constituting an image pair will not have captured any residual light from the first laser pulse. If this condition is not satisfied, the second image will appear distorted in the form of streaks of particles.

In general, the choice of Δt is governed by a combination of the magnification, speed of the flow, and interrogation window size. For a given amount of time, particles in higher speed flows will travel a greater distance as compared to a lower speed flow. Also, when the magnification of imaging in PIV is increased, more pixels of information are available for every cm of the flow. Thus, the particle displacements for a given flow are greater in an image with greater magnification as opposed to a lesser magnified image. In both cases, there is more possibility of the particle displacement being larger than the interrogation window dimension, thereby leading to tracking of windows with completely different identity of particles. In addition, while conducting 2-D PIV studies on flows with regions of three dimensionality (e.g. transition/rotation locations), it is possible for particles illuminated by the light sheet to travel out of the plane, which once again results in the PIV algorithm tracking non-similar groups of particles, resulting in spurious velocity vectors. To lessen these errors, a thumb rule that is commonly followed is to ensure that the displacement of particles within a subregion to be equal or lesser than one-third of the dimension of the subregion. This amounts to displacements of roughly 5 pixels in a window of size 16 x 16 pixels, 10 pixels in a window of size 32 x 32 pixels, and so on. Lowering the timing between pulses in the above flow situations is one way of avoiding aliasing in sampling displacements, where the condition is that the particle displacement must be greater than half the interrogation window size. Another solution lies in increasing the window size, which inevitably filters out the data, and is often not desirable due to loss of valuable information. Out of plane motions of particles can also be tackled by increasing the thickness of the laser sheet, but not without a compromise in the available intensity for illumination. For the PIV measurements conducted herein, separation intervals between laser pulses were varied in the range 40 μs–300 μs. A photodiode manufactured by Thorlabs Inc. (model DET 200) was placed along the path of the laser pulsed beam at low intensity (to avoid burn out of the detector), and the timing between the pulses was read out through an oscilloscope. Since the velocity field is inversely proportional to Δt, it is easily seen that the accuracy of PIV technique in measuring velocity can be increased by increasing Δt within certain limits. However, it must also be noted that such an increase would warrant an increase in the measurement noise, as discussed above.

A SAFEX 2010 Fog Generator manufactured by Dantec Dynamics Inc., was used for

generating the smoke particles required for seeding the flow. The material used for seeding was oil droplets with a nominal 1 micron diameter, available under commercial name "Fog Fluid Blitz" from Dantec Dynamics Inc. Typical longevity of the fog material in confined regions was roughly 5–10 minutes. In the quiescent flow experiments, the seeding is inserted in the enclosure manually, while for cross flow experiments the fog generator is placed near the inlet of the radial fan that drives the wind tunnel flow, so that the seeding is uniformly mixed with the air that enters the test section. The seeding density is visually optimized to achieve a compromise between particle scattering and particle homogeneity. The requirement for homogeneous distribution of particles is necessary to obtain an unbiased estimate of the displacement field, and this distinguishes PIV from conventional qualitative flow visualization techniques such as the smoke-wire and other dye based methods (see Freymuth [190], Gharib *et al.* [191], and Van Dyke [192] for example). The particle density must be adjusted in relation to the other factors that control image brightness, the laser intensity and aperture of the lens field of view. A higher density of smoke particles will naturally scatter more amount of light. Essentially, if this scattered light exceeds a certain limit, it will register on a greater range of surrounding pixels. This may result in a distortion of the actual sizes of the particles to such an extent that tracing individual particle movements becomes extremely difficult. Thus, it is important to tune the level of seeding with respect to how dark or bright the flow field is, based on the lens aperture and laser intensity. It is important to adjust all of these three factors until a satisfactory image of homogeneous, well demarcated particle distribution is obtained in the flow field. An inherent error involved with the PIV process is the assumption that the tracer particles closely follow the motion of fluid particles, without altering the properties of both the fluid or the flow. Theoretical treatment of the error involved in particle motion based fluid velocity measurement can be found in the works of Agui & Jiménez [193], and Jacob [194]. Also, the particles are required to have a density as close to that of the fluid, so that the effect of gravitational forces on both these species are not different. A discussion of this problem along with experimental observations can be found in [186]. In general, larger sized seeding particles require lesser intensity than smaller sized particles, but follow turbulent fluctuations at a substantially lower rate.

Image Capture and Storage

The images were acquired using frame grabbing software XCAP and hardware provided by EPIX Inc., and saved in a 8-bit binary format (256 gray scale image) on a local hard disk drive. The raw images for each PIV run required roughly 300 megabytes of memory,

while the processed data (in the form of tensors, see below) required 16 megabytes of space per run. An RS-232 cable was used to transfer images from the CCD to the local hard drive of the computer with the frame grabber. The raw images, after visual inspection, were stored on an external hard drive that was connected to the main computer with the XCAP software via a USB 2.0 cable or an IEEE 1394 interface (firewire) cable. For each PIV run, 122 images were recorded for processing resulting in a minimum of 61 vector and vorticity fields from which to generate mean flow field and statistics. The maximum number of images captured (122 herein) was limited by the available memory of the data acquisition computer. Typically, the spatial resolution of the visualized flow field was 200–300 pixels/cm. The flow field statistics were obtained from calculations based on the post processed flow field, ensemble averaged over 61 image pairs for a particular PIV run. No optical correction techniques such as distortion correction, data smoothing, or noise filtering were applied to the acquired raw images or the processed results. For this dissertation, measurements were obtained using both time-averaged and phase-locked PIV. The former method essentially describes data acquisition along unknown points along the duty cycle of the AC input to the plasma actuator (and also along the larger period of the actuator pulsing duty cycle for unsteady operation) and produces a bulk picture of the flow field, averaging out the temporal events that may play an important role in the observed flow physics. In the latter method, images are acquired at a particular rate coincident with some characteristic time scale of the system along predetermined temporal locations, and is discussed later in slightly more detail in this section.

Data Reduction and Analysis

The raw images acquired by the CCD are analyzed by a DPIV algorithm. In general, the essence of a single exposed PIV based post processing technique is in dividing the image into several interrogation windows and performing cross-correlation analysis between successive image pairs, so as to effectively calculate a displacement vector corresponding to every subregion and hence produce an overall velocity vector map of the visualized flow field. For this study, the Wall Adaptive Lagrangian Parcel Tracking (WaLPT) algorithm developed by Sholl & Savaş [195] was employed for post processing of image pair realizations. In this algorithm, individual subregions are treated as Lagrangian parcels, and these are tracked to determine both their translations and deformations. Traditional PIV algorithms suffer from a serious limitation of being able to track only the translations of particle clusters. In flow fields with substantial rotation, deformation, or shear, the displacement gradients are often poorly predicted resulting in spurious velocity vectors. To somewhat resolve this

problem, most DPIV algorithms use adjustable windows as part of their processing routine in order to increase the resolution of measurement, where a new interrogation window is introduced at a certain distance (defined as the overlap ratio) between two adjacent windows. Thus, a new displacement vector is calculated in between two windows. Typical overlap ratios used are 50%, which implies that the third window lies roughly centered at the interface of the two adjacent windows. In the flow field of a vortex, adjustable windows can be used to determine the gradients. However, values on the edge of a window are calculated from only overlapping half of the data of both adjacent windows, and hence the correlation of this window is lesser than the peak value of the adjacent windows. This leads to the under prediction of velocity gradients (and any related information such as vorticity, shear stress, etc.) and is referred to as *bias error*. The WaLPT algorithm tackles this biasing problem by first passing the raw data through a standard DPIV routine [185] to obtain a rough estimate of the velocity field. The Lagrangian parcels (interrogation windows) are then advected backwards in the flow using this crude velocity field. The fluid particles registered by individual pixels are advected with individually estimated velocities and the resultant windows are cross-correlated. Using the initial velocity gradient tensor as a reference, spurious velocity vectors are identified and corrected. A rigorous peak-detection scheme is employed for determining velocity vectors. The WaLPT routine works well in flow fields characterized by sharp gradients and high deformation rates, such as vortex dominated flows.

In order to improve the number of valid velocity vectors, the WaLPT routine employs an iterative predictor-corrector scheme (following Fabris [196]). Once matching interrogation windows are determined by cross-correlation, the regions surrounding the tip and tail of the predicted displacement vector are subdivided into smaller windows (Fig. 4.8). This smaller window is then shifted inside the subregion and cross-correlated to result in a more accurate velocity vector. A unique feature of the WaLPT algorithm is in the integration of the Image Parity Exchange (IPX) routine for accurate determination of velocities and velocity gradients near a surface (see Tseui & Savaş [197] for details). Essentially, the velocity profile near a wall is artificially extended and mirrored about the flow interface and reversed in direction. Traditional PIV algorithms suffer from near wall resolution as illustrated in Fig. 4.9(a), where the subregion closest to the wall results in a displacement vector (taken to be near its center and indicated by dashed lines) that is located far away from it. When IPX routine is included in the PIV algorithm, interrogation windows can be extended across the surface so that velocities very close to the wall can be calculated, as shown in Fig. 4.9(b). The WaLPT algorithm with IPX was used for the post processing of

cross flow measurements on the PSJA.

The velocity fields are calculated by the WaLPT algorithm and scaled in terms of pixels. Vorticity is calculated spectrally and therefore does not suffer from typical numerical differentiation problems [195]. The interrogation window size used in the analysis of all experimental data presented in this dissertation was 32 x 32 pixels, with 50% overlap. The resultant flow field consisted of an array 83 vectors (vertical) x 82 vectors (horizontal direction), where each vector was separated by a step of 12 x 12 pixels. The algorithm was in the form of a FORTRAN executable file, and the above parameters were user specified in a separate input file that was read in by the progrm. Conventional PIV algorithms output the two dimensional velocity vector fields alone. The WaLPT algorithm, however, includes gradients as well, in the form of a 3 x 2 tensor of rank 2 given by

$$C_{ij} = \begin{bmatrix} u & v \\ \partial u/\partial x & \partial u/\partial y \\ \partial v/\partial x & \partial v/\partial y \end{bmatrix}$$

The calculation of vorticity fields as well as a check for continuity can readily be accomplished from the above information. The deviation of the latter from zero is indicative of the error in measurement on account of the resolution. The information provided from the above tensor after processing using the WaLPT routine is scaled into physical units by using the image resolution (in pixels/cm) as the length scale and the interval between firing of the laser pulses as the time scale. The tensor information was used to examine various flow field characteristics, including jet profiles, vortex trajectories, momentum distribution, and self similarity, and the post processing was performed using MATLAB.

Error estimates were determined by constructing fake image pairs with similar particle characteristics including shape, distribution and number density. The particles were advected between the pairs with a known velocity distribution similar to those measured herein, including jets with high shear and vortex pairs. The processed velocity and vorticity fields were then compared with the actual fields. Typical errors are on the order of less than 1%, though errors in the cores of tightly wound vortices (as compared to the interrogation region size) may be as high as 5%, particularly in the vortex center where vorticity tends to be underestimated on account of biasing discussed earlier.

Phase-Locked PIV

To observe the evolution of the jet induced by the plasma actuator in unsteady pulsed operation, measurements were conducted by acquiring PIV data phase-locked to the pulsing frequency. Figure 4.10(a) shows the schematic of the duty cycle of the plasma actuator AC

input with frequencies $\mathcal{O}(10^3$ Hz) superimposed on a pulsing square wave that is roughly two reduced orders of magnitude in frequency. The pulsing mode can be merely thought of as switching the actuator on and off at a period $1/f_p$. It is important to note that the phase locking herein is performed with respect to the duty cycle of the pulsing frequency waveform, and not the plasma AC input waveform. As the fluid flow time scales are in the order of the actuator pulsing frequency, the effects of the high frequency AC input to the actuator can be assumed to be decoupled to the flow field features. This observation has been noted previously in the context of experimental investigations on conventional synthetic jet actuators pulsed at frequencies $\mathcal{O}(100$ Hz), and is discussed in Glezer *et al.* [174]. The pulsing frequency f_p is hence more important in influencing the flow field characteristics. Hence, phase-locked measurements were conducted by capturing images at a rate of $1/f_p$ at along different times t in the pulsing wave form duty cycle (as shown in Fig. 4.10(b)).

Figure 4.11 shows the flow of information across the different components of the phase-locked PIV system employed herein. A function generator provides the pulsing waveform with frequency f_p in the form of a TTL signal ($\pm$5 V) to a timing control box and simultaneously to the actuator power supply circuit. As a result, the power input to the actuator is synchronized to the pulsing waveform, such that an effective duty cycle resemblant of that shown in Fig. 4.10(a) is effected. The timing control unit 1 serves to provide the delay t shown in Fig. 4.10(b), between the start of the pulsing duty cycle (frequency f_p) and the image captured by the CCD. In this manner, several PIV runs taken along different times in the $1/f_p$ pulsing can be acquired. When the CCD begins its first exposure, it sends a signal to the laser to fire its first pulse. The first single exposed image in an image pair is thereby obtained. Another timing control unit (independent of the TTL input) is used to set the delay Δt for firing the second pulse, only after the first pulse has been completed. This way, the second exposure of the CCD is recorded onto another frame to form the image pair that is analyzed using the WaLPT algorithm. The CCD is triggered to capture images by user command relayed via the frame grabber.

Averaging Comments

The flow field observations presented in this dissertation were obtained from both phase-locked and time-averaged PIV. Regardless of the mode of image capture, 61 image pairs were used (essentially translating to 61 data points) throughout. In the time-averaged PIV image capture mode, the frame grabber software (XCAP) was set to acquire image pairs (where the images within a pair are spaced by Δt between successive laser pulses) at a rate of 10 Hz. Note that the software skipped images regularly, and hence the 10 Hz

image capture rate is only a rough estimate. The total time taken to acquire 61 image pairs for a time-averaged PIV run was thus 6.1 seconds. For the time-averaged measurements on steady PSJA operation (where the actuator was switched on the entire time of data acquisition), the images were captured along random points along the plasma AC input frequency waveform (with frequency f_{AC}), and the ensemble average of 61 image pairs were used to obtain the results presented in this dissertation. For the time-averaged PIV measurements acquired on pulsed PSJA operation (where the actuator was switched on and off at frequency f_p values of 1 Hz, 10 Hz, and 100 Hz), the ensemble average of the tensor information extracted from 61 image pairs was used. Thus, any such time-averaged results of pulsed PSJA operation are representative of averaging data acquired across roughly 6 cycles along a 1 Hz pulsing frequency f_p waveform, roughly 61 cycles along a f_p=10 Hz pulsing waveform, and roughly 610 cycles along a f_p=100 Hz pulsing waveform. Note, however, that the time-averaged PIV image capture rate of 10 Hz translates to 10 points per cycle of a f_p=1 Hz waveform, 1 point per cycle of a f_p=1 Hz waveform, and 0.1 points per cycle of a f_p=100 Hz waveform. The above observation must be used as a caveat to carefully interpret the time-averaged PIV results on pulsed PSJA operation in the following chapters.

For all phase-locked PIV measurements acquired on pulsed PSJA operation, the camera was set to acquire images at the rate of the actuator pulsing frequency f_p. This means that the camera acquired image pairs at a rate of 1 Hz for actuator pulsed at 1 Hz and 10 Hz for actuator pulsed at 10 Hz (phase-locked PIV on the 100 Hz pulsed actuator was not conducted, owing to the obvious limitation of the 15 Hz camera frame rate). A single phase point along the pulsing waveform of frequency f_p was chosen for measurement, and the camera acquired 61 image pairs at a rate of f_p along the *same phase point* of the pulsing waveform (with frequency f_p). The location of the phase point along the pulsing waveform chosen for observation is indicated through the symbol t (in $\mathcal{O}$(ms)) wherever phase-locked PIV results are presented in this dissertation. Thus, phase-locked results of an actuator pulsed at frequency f_p (which is treated to be safely decoupled to the plasma AC input frequency f_{AC} in $\mathcal{O}$(kHz)) were obtained by ensemble averaging 61 image pairs acquired at a rate of f_p at a single phase point t (in milliseconds) chosen along the pulsing waveform.

Finally, due to the decoupling between the plasma AC input frequency f_{AC} ($\mathcal{O}$(kHz)) with the PIV image capture frequency of 10 Hz as well as actuator pulsing frequency ($f_{p_{max}}$=100 Hz), no information of the phase point location along the plasma AC input waveform (with frequency f_{AC}) corresponding to a PIV image pair capture could be deduced, irrespective of whether time-averaged PIV or phase-locked PIV was used.

4.3.2 Power Measurements

In order to determine the efficiency of the plasma actuator in coupling momentum with the neutral air, the input electrical power was calculated as the product of input voltage and current.The voltage measurements were conducted by using a high voltage probe designed for high frequency applications manufactured by NorthStar High Voltage Inc.(model PVM-11). The probe was capable of measuring maximum AC voltages of around 12 kV with frequencies in the order of 50 MHz. No calibration of this device was necessary. The probe was either located in the terminal electrical connection powering the exposed electrode. Depending on the transformer used, it was placed either on an interim connection in between the transformer output and the actuator (Industrial Test Equipment transformer driven cases), or in the output of the step-up transformer unit (Corona Magnetics Inc.) connected to the actuator. The output of the probe was read out using a TDS 3012 oscilloscope manufactured by Tektronics Inc., and the reading from the probe had to be re-scaled using a 1000:1 factor. Typical voltage inputs to the plasma actuators were in the range of 1–16 kW per 100% duty cycle. To calculate the electrical power, simultaneous measurement of current input was also performed in addition to the voltage. For this purpose, a fixed core AC current transducer manufactured by NK Technologies Inc. (model number AT2–010–000–FT) was used. The electrical connection that powered the exposed electrode of the actuator was passed through the aperture of the transducer that monitored the variation in its current input. The output of this unit was in terms of voltage and was read using the above TDS 3012 oscilloscope, and was re-scaled by a factor of 10 A/V. The placement of the high voltage probe and the AC current transducer is indicated as a part of the actuator power supply schematic shown in Fig. 4.3.

Figure 4.12 shows a sample voltage and current reading for a representative PSJA input of 2.8 kHz, square wave form AC. The power is calculated by averaging the product of instantaneous voltage and current inputs shown in the figure, measured by the voltage probe and current transducer. Note that this measurement corresponds for a full cycle of the AC input. The AC input is, however, maintained at 50% duty cycle for all experiments presented in this dissertation and as a result, only 50% of the above average power value is supplied to the actuator. The voltage supplied to the actuator, as measured with the arrangement herein, must be distinguished from the electric field potential of the plasma. The latter is not quantified in any manner in these measurements, and is rather independent of the quantity that is actually measured herein, namely the applied *external* potential to the actuator. This was experimentally evidenced during some of these measurements, where

the plasma region was observed to distort the oscilloscope reading (and in some cases even turning off the driving unit!), ostensibly due to some sort of feedback of its own electric field to the driving circuit. This effectively resulted in a misrepresentation of the input signal, and the measurements had to be repeated. The waveform of the discharge is clearly affected by electrical response from the different components of the power supply (Fig. 4.3), as observed from the non-square waveform like behavior of the voltage output. In addition, it is seen that the positive and negative going portions of the AC cycle are not symmetric. The current reading shows an irregular, "spiky" appearance with sudden peaking that is not coincident with the peak in the voltage. Asymmetry of the current behavior during both positive and negative portions of the AC cycle is observed. Each of the peaks in the current signal correspond to the occurence of numerous discharge events [84], and it is seen that the discharges are shorter during the times close to the start of the negative going cycle. The irregularity in the current pulses occurs at a much smaller time scale than that of the voltage input. These measurements were acquired at a nominal sampling rate of 1 million samples per second. To examine the current pulses in more detail, the sampling rate of the TDS 3012 oscilloscope was unequally adjusted to 1 gigasamples per second for current and 2.5 million samples per second for voltage (maximum possible rate was 5 Gs/s). With an increased sampling rate of the oscilliscope, the number of points displayed along the length of the cycle was also increased, resulting in a highly irregular voltage signal, as shown in Fig. 4.13(a). The individual identity of the cycles is not very clear at this point. The averaging process used for calculation of the input power, however, now included more cycles of the input waveform (as opposed to $\tilde{3}$ cycles shown in Fig. 4.12). The current signal at the microsecond time scale, shown in Fig. 4.13(b), clearly shows distinctive spikes indicative of the microdischarge events as before, except that these are not as closely clustered as with the larger time scale discussed before. Uniformity in the surges can also be observed across different portions of the cycle. Due to the highly irregular nature of the voltage waveform at slightly increased time scales compared to the current, a measurement of the voltage input at time scales same as the current was not attempted. As a result, no observations on any correlation of the current peaks (discharge events) with the nature of the waveform cannot be deduced. These measurements are supported by the experimental results of Enloe *et al.* [84], where for a sinusoidal input, the authors observed that the discharge events are not uniform across the positive and negative going portions of the cycle.

4.3.3 Photographic Arrangement

The second phase of experimentation involved simultaneous measurements of plasma morphology and flow field of plasma synthetic jet actuators in a quiescent medium. Figure 4.14 shows a schematic of the arrangement of cameras used for obtaining these measurements. The PIV camera (CCD1) was placed so as to acquire 2-D images of the PSJA flow field. The optics arrangement used for light sheet construction remained the same as discussed earlier with reference to Fig. 4.7. Another CCD was placed such that it was 90° to CCD1, and also so that it examined the entire region of plasma morphology, located in a plane perpendicular to the laser sheet and parallel to the actuator surface outside of the seeding enclosure. Time exposed images of the plasma structure were taken by using an Olympus Camedia E-20 camera with a 2560x1920 pixel array, with fixed field of view and exposure settings. The non-dimensional intensities (indicative of the brightness value of the pixels) of these images were used to make a relative comparison between the different test cases. The underlying assumption herein was that the brightness of the plasma must be related directly to its intensity, which in turn would have to affect the flow field characteristics. The goal of these measurements was to examine the relation between plasma intensity to the jet characteristics such as peak velocity and momentum, across various operating conditions. The spatial resolution of these measurements was in the range of 325–340 pixels/cm, and an exposure time of 8 seconds was used. The procedure of acquiring these measurements was to switch off all external light sources available in the laboratory (including the PIV laser), so as to eliminate as much background noise as possible. The CCD then captured a high resolution image (of 2–5 megabytes size) of the plasma, prior to the start of the PIV run. This image served as a metric of the relative plasma intensity (presented in chapter 7) for that particular PIV run. The reference brightness levels (arbitrary units, relative to each image) was in the order of 2–3. Due to trapping of residual air within the enclosure, gradual deposition of seeding material on the surface of the actuator and the flat plate was observed to occur. The plasma region, as a consequence of this, was noticed to weaken over successive PIV runs. To include the effects of seeding contamination, images were acquired before and after every PIV run. This is discussed in more detail in chapter 7.

4.4 Tables and Figures

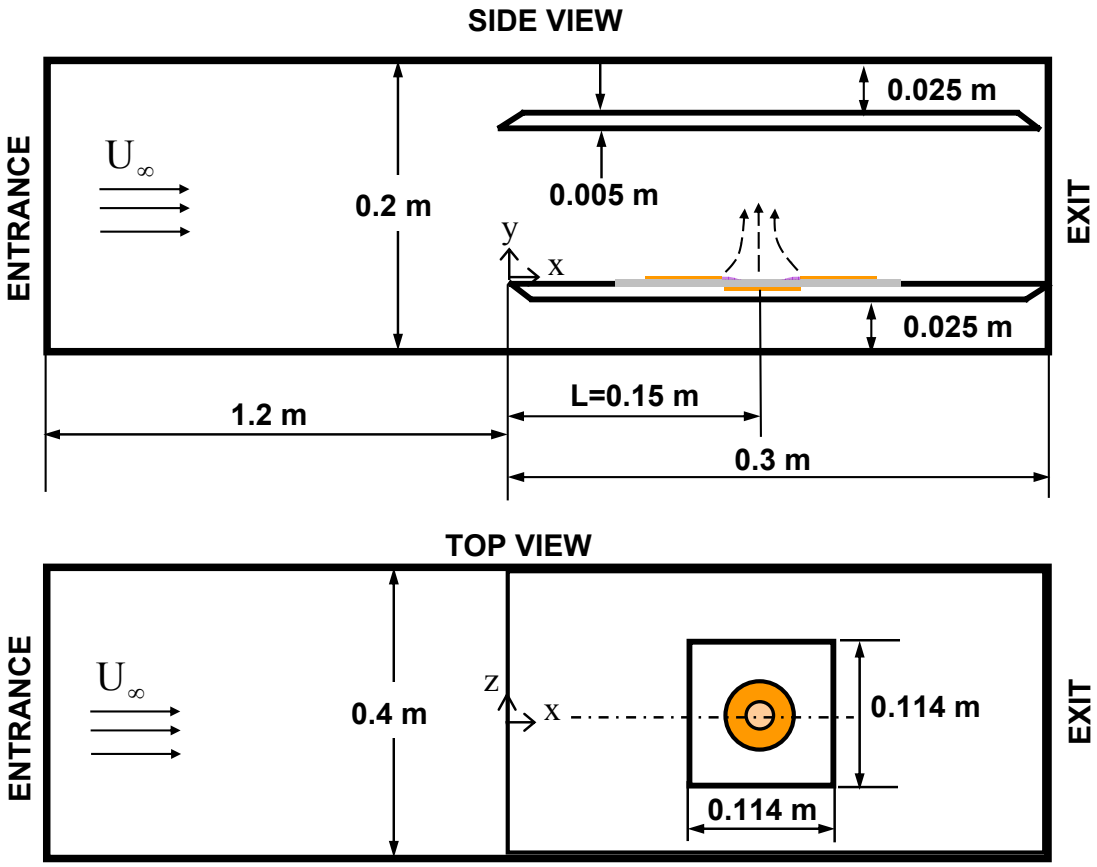

Figure 4.1: Side and top view schematic of wind tunnel test section with flat plate and actuator arrangement. Flow direction is from left to right. The definition of coordinate system is also shown. Note that the trip wire (not shown) is located at the leading edge of flat plate, x=0.

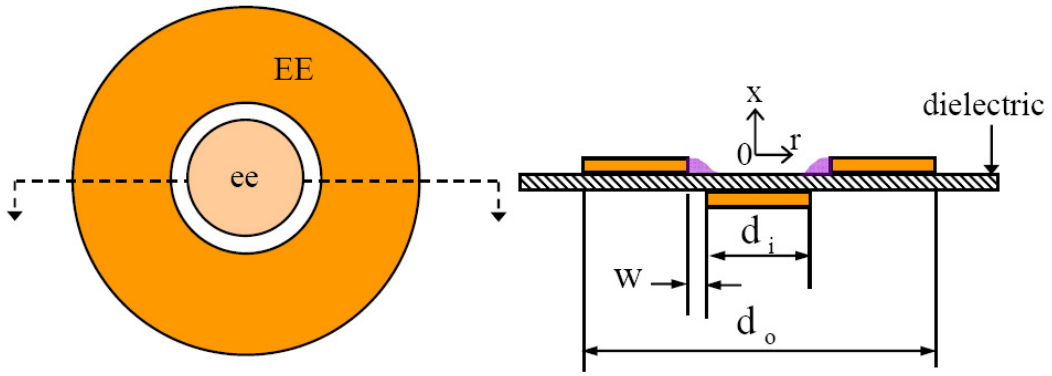

(a) Annular PSJA.

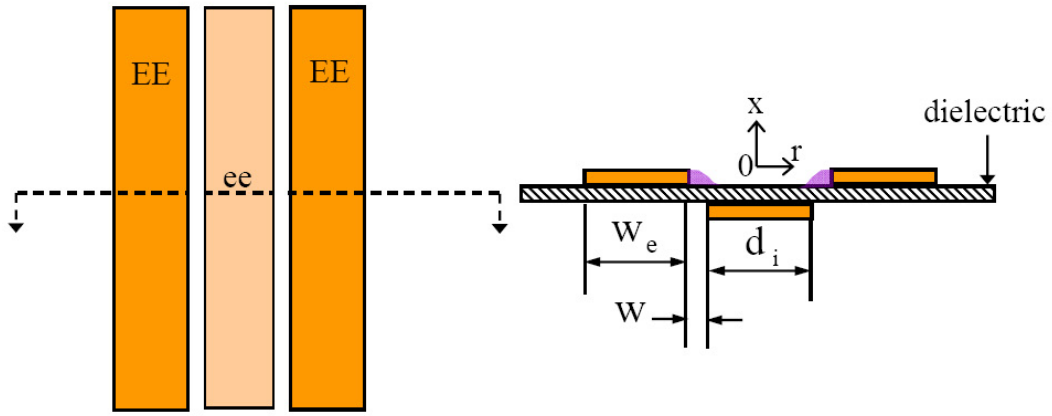

(b) Linear PSJA.

Figure 4.2: Top and side view schematic of PSJA: (a) annular (3-D), and (b) linear (2-D) configurations. `EE` refers to exposed electrode and `ee` refers to embedded electrode; d_o and d_i are diameters of exposed and embedded electrodes, respectively, and w is the gap between the asymmetric placement of electrodes; w_e refers to width of exposed electrode of the linear PSJA. Both the region of plasma and coordinate axes definition are shown.

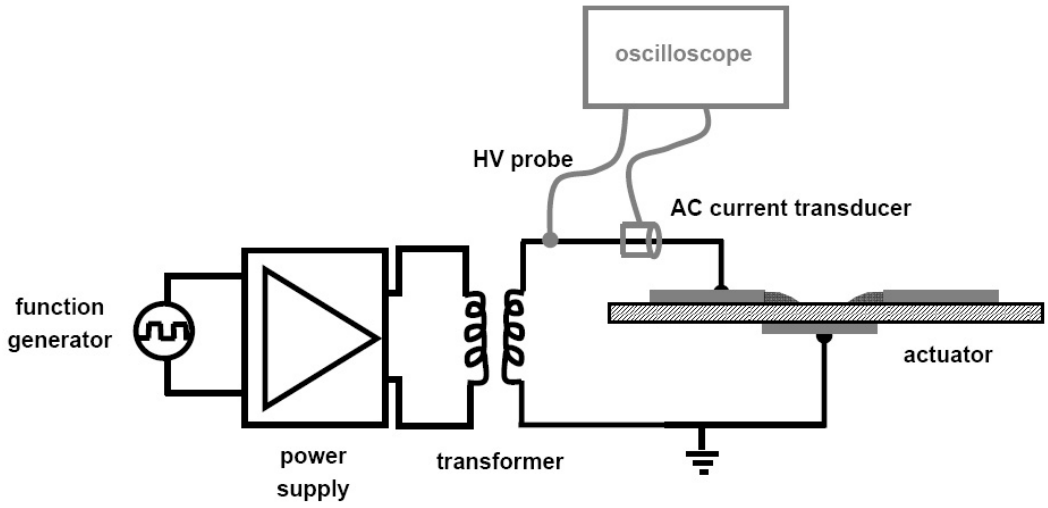

Figure 4.3: Actuator power supply schematic. Also shown in gray lines are the locations of placement of high voltage (HV) probe and current transducer used for measurement of input power.

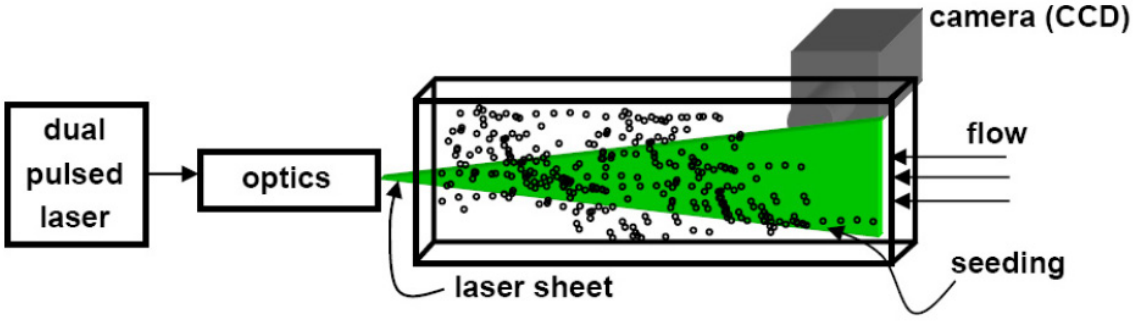

Figure 4.4: Experimental arrangement used for conducting particle image velocimetry in a wind tunnel.

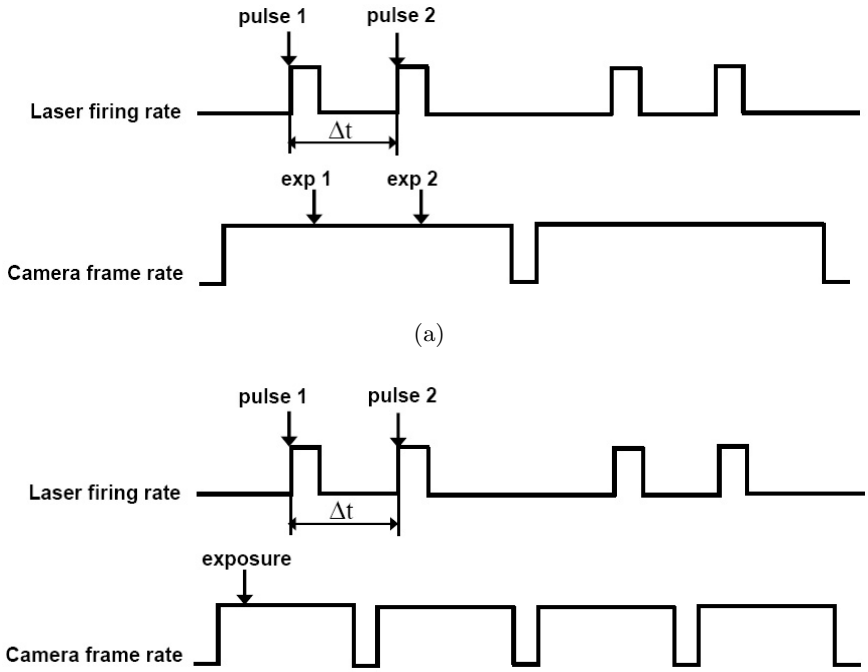

Figure 4.5: Laser and camera timing diagram for two commonly employed PIV image recording techniques. (a) Single frame, multiply exposed mode, and (b) double frame, single exposed mode. Δt refers to the timing between two individual laser pulses.

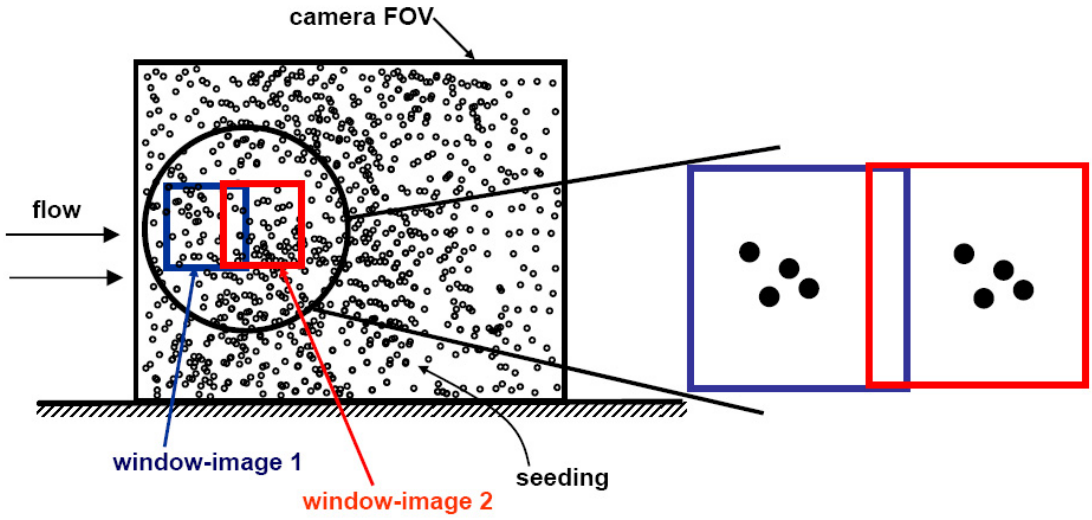

Figure 4.6: PIV post processing via spatial correlation of successively captured flow field images with predetermined time interval. FOV refers to field of view of the raw image.

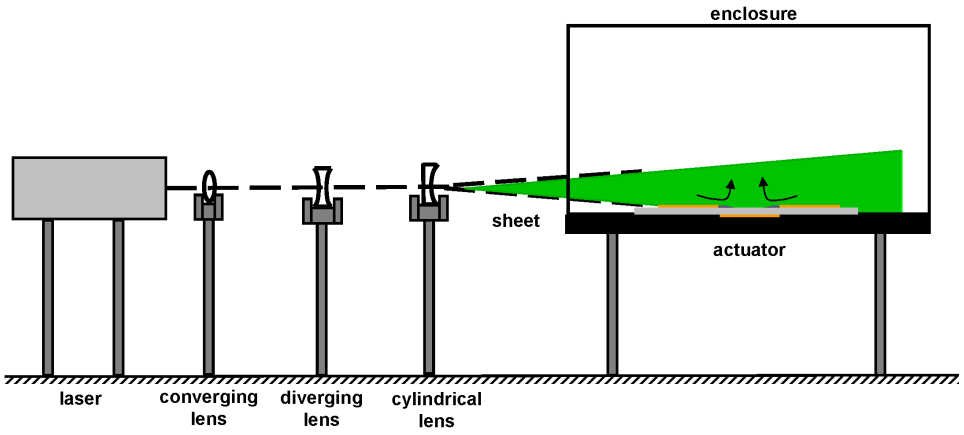

Figure 4.7: Optical arrangement employed for construction of light sheet used for PIV measurements of PSJA flow field characteristics. For flat plate boundary layer experiments, the same arrangement was used, and the equipment was located at the exit of the test section such that the spreading of the sheet increased in the direction opposite to the free stream.

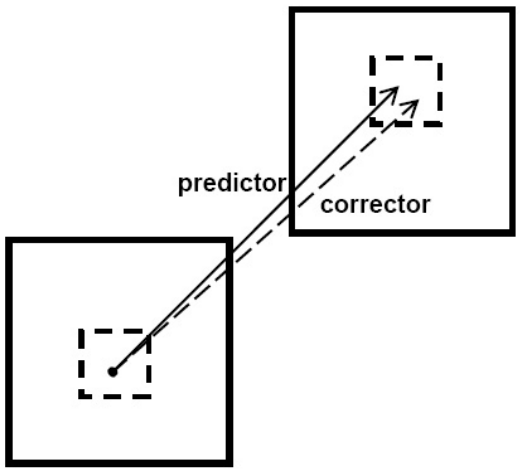

Figure 4.8: Predictor-corrector algorithm.

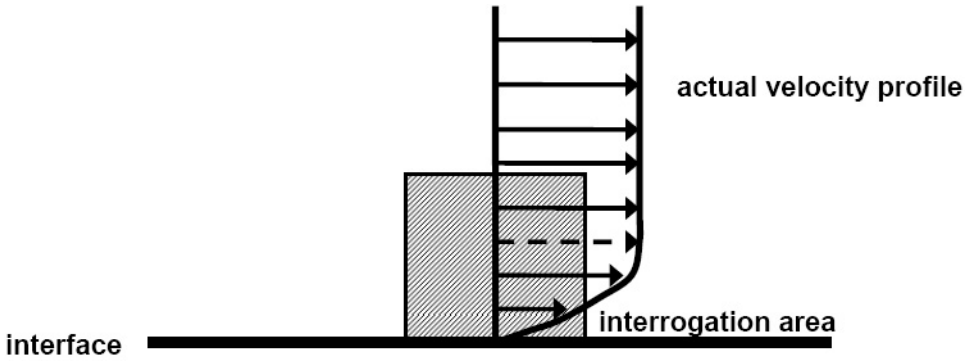

(a) IPX off.

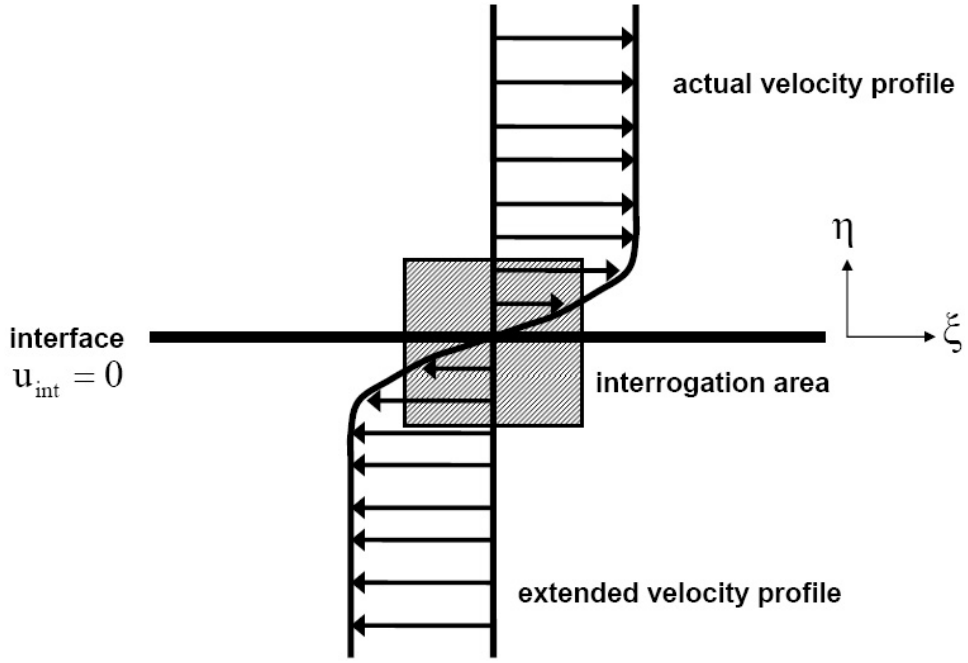

(b) IPX on.

Figure 4.9: Boundary layer velocity profiles of flow over an arbitrary surface showing the use of Image Parity Exchange (IPX) routine as included in the WaLPT PIV algorithm. Shaded region indicates the interrogation window closest to the surface. The dashed vector in the profile (a) represents the resultant velocity vector of the interrogation window, obtained via spatial correlation analysis.

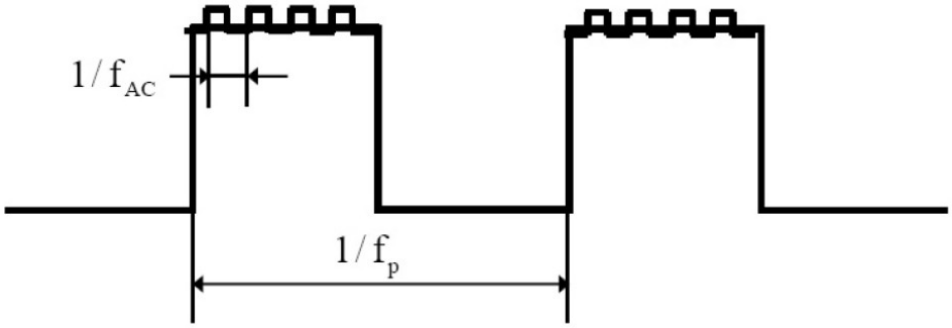

(a)

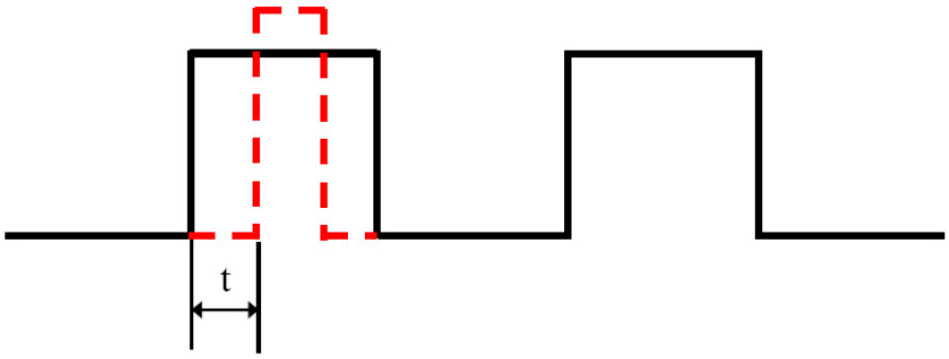

(b)

Figure 4.10: Phase-locked PIV measurements of pulsed operation of the PSJA. (a) Plasma input AC frequency f_{AC} is imposed on a low frequency on/off pulsing waveform with frequency f_p, and (b) pulsing duty cycle (with period $1/f_p$) is shown by the solid square wave, and the dashed square wave indicates PIV image capture with time delay t. Note that the plasma actuator duty cycle shown in (a) is merely illustrative, actual input AC frequencies to the actuator are $\mathcal{O}(1000)$ Hz, and correspondingly contain more than 4 complete periods.

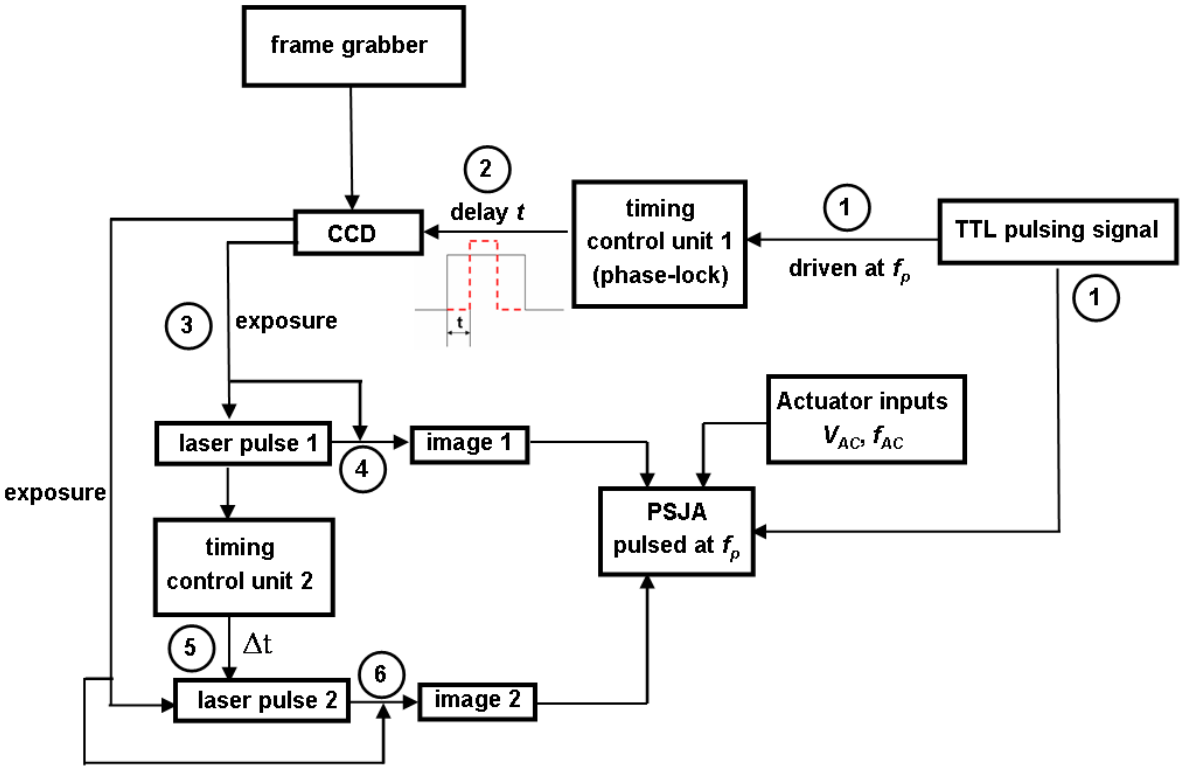

Figure 4.11: Flow of information for acquiring CCD images phase-locked to actuator pulsing frequency.

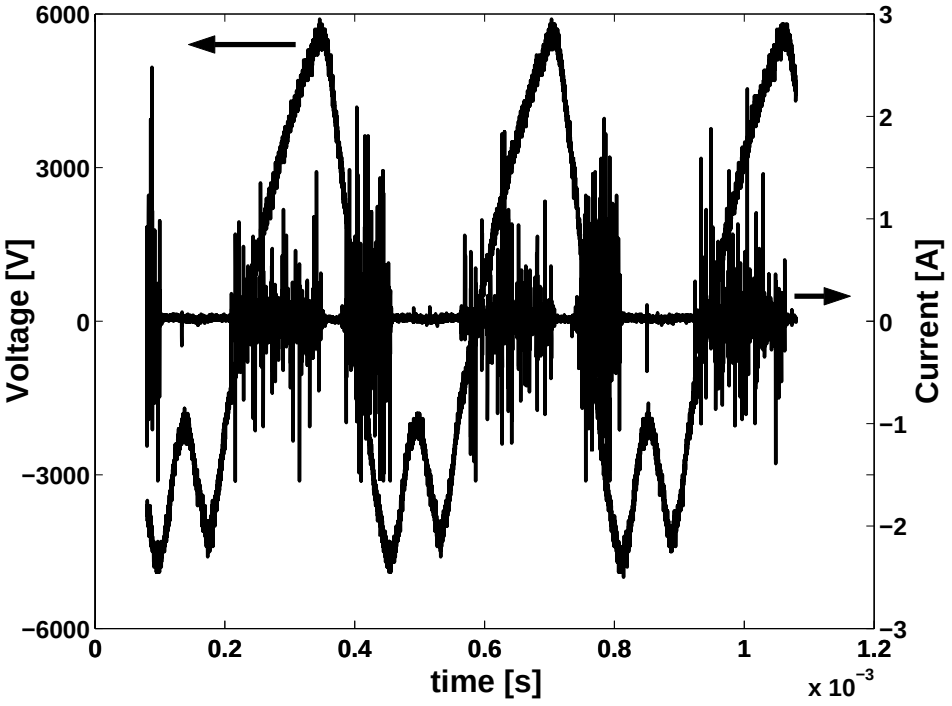

Figure 4.12: Input voltage and current characteristics of a plasma synthetic jet actuator. $f_{AC} = 2.8$ kHz, square wave form AC, 50% duty cycle, $\overline{P} = 3.52$ W/m for 100% duty cycle.

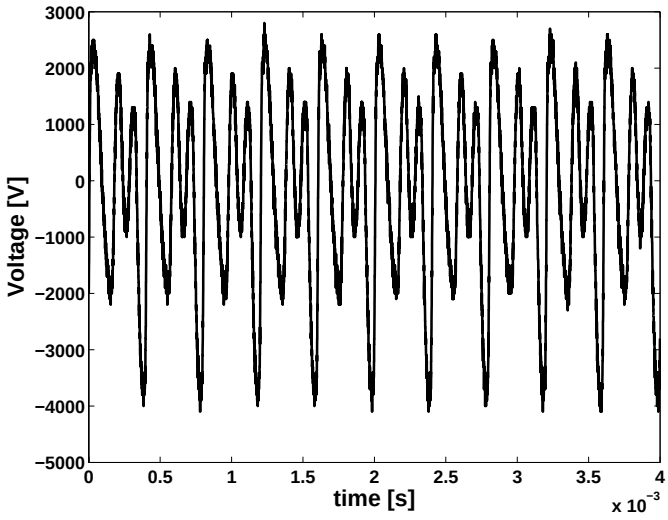

(a) Voltage.

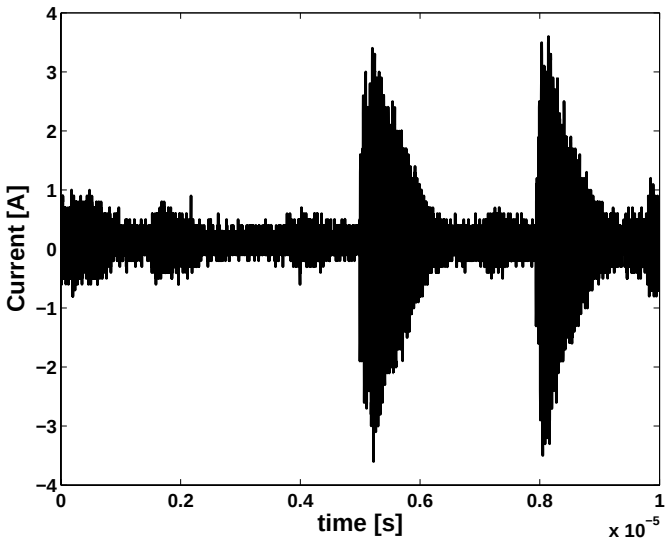

(b) Current.

Figure 4.13: Input characteristics of a plasma synthetic jet actuator with higher sampling rate. $f_{AC} = 2.5$ kHz, square wave form AC, 50% duty cycle, $\overline{P} = 17$ W/m for 100% duty cycle. The plasma morphology for this particular observation was stronger than that of Fig. 4.12.

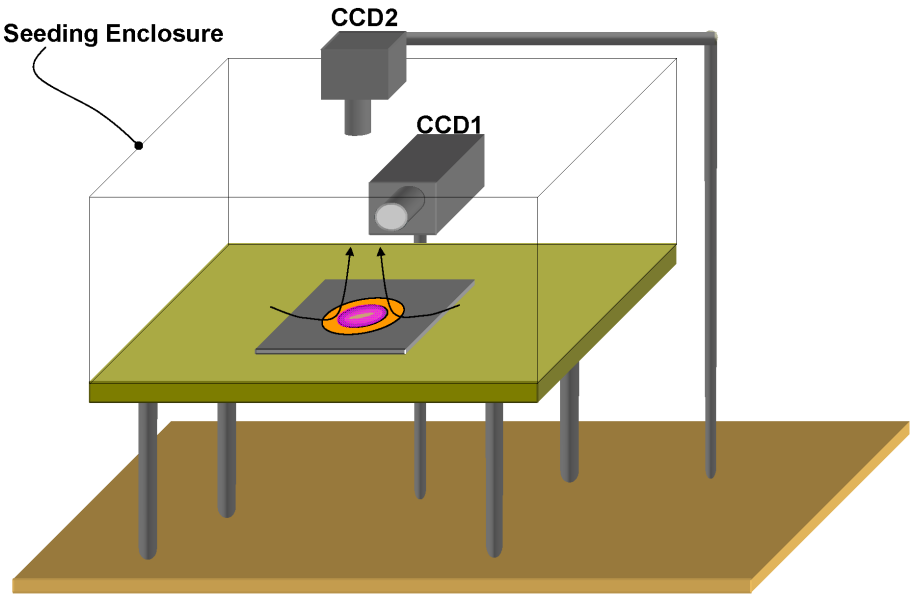

Figure 4.14: 3-D view of experimental setup used for simultaneous flow field (PIV, CCD1) and plasma morphology (CCD2) measurements of isolated plasma synthetic jets.

Chapter 5

OBSERVATIONS IN AN INITIALLY QUIESCENT MEDIUM

5.1 Introduction

This chapter examines the behavior of the plasma synthetic jet in the absence of an external cross flow. The results presented here were obtained from phase-locked and time-averaged PIV measurements conducted as described in the previous chapter. A total of 84 runs were recorded on the isolated plasma synthetic jet across varying input parameters that included pulsing frequency, input power, and actuator orientation. The actuator size was held constant throughout the course of these measurements, with the diameters of the exposed (d_o) and embedded (d_i) electrodes being 25.4 mm and 12.7 mm respectively, with either no air gap or 1–2 mm overlap. All the results reported herein were obtained using 0.635 mm thick alumina ceramic as the dielectric material. The effect of varying the actuator dimension was investigated from comparison of the above results to a set of 9 PIV runs conducted on an actuator with d_i=19.05 mm and d_o=25.4 mm. Three pulsing frequencies were examined, each differing by an $\mathcal{O}(1)$ magnitude: 1 Hz, 10 Hz and 100 Hz, in addition to a baseline case with steady actuator operation. These frequencies were chosen to determine an optimum operating range of the actuator to maximize the jet momentum and peak velocity. For 100 Hz pulsing, the induced flow resembled closely to that seen on steady operation of the actuator. The effects of varying the pulsing frequency on the plasma induced flow field will be examined in the first part of this chapter, which will be followed by a discussion of the jet characteristics for all the different cases studied. It is important to note that the power input (per cycle) for pulsed operation of the actuator was nearly a constant, irrespective of pulsing frequency, and was 50% less than that for steady actuator operation. In addition to pulsing frequency, the effects of varying input power, actuator dimension and orientation on the formation and resultant flow field characteristics of plasma synthetic jets will be presented in the final portion of this chapter.

5.2 Basic Flow Field

Figures 5.1 and 5.2 show vorticity contours obtained from phase-locked PIV measurements for pulsed operation at 1 Hz and 10 Hz respectively, and several times of evolution of the jet are shown. The data is ensemble averaged from 122 realizations. The power

input for steady operation at 50% duty cycle was 11.5 W. For pulsed operation at 1 Hz, the starting vortex is seen within the FOV for all times except at t=183 ms (Fig. 5.1(l)), where a steady jet is observed. The location of the starting vortex is fairly steady at 1 Hz, centered around x=6 mm for times from 20 ms to 28 ms (Figs. 5.1(a)–(c)), after which it advects downstream to around x=12 mm for times from 48 ms to 63 ms (Figs. 5.1(d)–(f)). The location of the starting vortex starts to become unsteady beyond 63 ms (Figs. 5.1(g)–(k)), and a general tendency for its downstream motion with increase in jet evolution time is observed. The width of the jet near the plasma region (from the actuator base to 10 mm downstream of the jet) remains constant for times from 20 ms to 28 ms, after which it increases marginally and remains constant for the rest of the cycle. The starting vortex also moves outward from the centerline, as seen on comparing the 94 ms (Fig. 5.1(h)) and 153 ms (Fig. 5.1(k)) cases, the latter being the time with maximum jet width. The size of the vortex ring is observed to be largest for the 100 ms and 130 ms times. At t=183 ms (toward the end of the actuation cycle, Fig. 5.1(l)), the jet becomes fully-developed (reaches steady state condition). The starting vortex has advected downstream of the window of observation in this case, although it still influences the flow field as evidenced by the regular entrainment of fluid at distances greater than $2.5d_i$ downstream.

For a pulsing frequency of 10 Hz (Fig. 5.2), the starting vortex is seen at all times and, in general, appears to be more unsteady compared to the 1 Hz case. With an increase in time, there is a definite downstream motion of the starting vortex. The jet reaches steady state condition at t=48 ms (not shown). The last two times (57 ms and 83 ms) examine the portion of the actuation cycle when the plasma is turned off. It is interesting to observe the advection of the starting vortex, even in the absence of actuation. This can be explained as follows: the flow has less time to respond to the 10 Hz pulsing as compared to 1 Hz pulsing. As a result, the starting vortex ring that forms at a particular time encounters another starting vortex that was created in an earlier portion of the actuation cycle (which was not dissipated due to the short time available). This interactive entrainment effect is seen in the case of t=24 ms, as the streamlines far downstream (see Fig. 5.3(a), x=30 mm and beyond) are pulled in by the advection of the starting vortex that was created at an earlier time. This compression of streamlines in the far-field is in sharp contrast to those seen at the same downstream locations for the 1 Hz case, where there was only a single starting vortex ring within the entire flow field (see for example, Fig. 10(b)). In order to maximize the peak velocity (and hence the fluidic impulse) of the jet for minimum input power, it is desirable to have the vortex ring interacting through advection with the previous vortex ring incarnation, which will be made clearer later in this section.

The basic action of the plasma, as seen from these figures, is to draw in fluid adjacent to the surface. Due to the current actuator design (which constrains the electric field lines in a particular manner), the residual fluid is ejected normal to the wall as a jet. During the course of these experiments, it was observed that the strength and uniformity of the plasma were important determinants of the peak velocity that can be obtained on actuation. The longevity of the jet, however, seems to be more strongly dependent on presence of the starting vortex ring. In general, the streamwise extent of the jet was found to be controlled by a combination of two factors: (a) the advection and interactions of the starting vortex rings across different times of evolution, and (b) strength and uniformity of the plasma.

Although some images show presence of some vortical activity near the actuator surface (such as in Fig. 5.1(f) and Fig. 5.2(f)), in all these experiments, the secondary vortex rings were not visible within the FOV. This is largely due to limited near-wall spatial resolution, mostly due to reflection from the plasma itself. Some tests with more zoomed-in observation windows confirmed the presence of secondary and tertiary vortex rings in the flow structure (Fig. 5.4), albeit in much reduced scales as compared to the starting vortex ring. On comparison with the measurements made with a larger size actuator presented in Chapter 3, it is suspected that there is some scaling relation between the actuator dimension and the secondary vortex strength, and this will be discussed in future chapters.

The starting vortex center trajectories for pulsed operation of the actuator is shown in Fig. 5.5(a), while Fig 5.5(b) shows the time variation of the streamwise trajectories. The maximum vorticity location was identified from the PIV data to define the center of the starting vortex. It must be noted that the times at which the centers were determined (in Fig. 5.5(a))—are not identical for the 1 Hz and 10 Hz cases. It is seen that for 10 Hz pulsing, the trajectory is largely uniform, with the starting vortex moving downstream with increasing time and lesser cross-stream motion—as compared to the highly wandering motion observed for 1 Hz. The jet is more symmetric at 10 Hz, as the location of the left and right side vortex centers lie nearly at the same streamwise coordinate for most times. The strength of the plasma was observed to be an important factor affecting vortex center motion. Figure 5.6 shows the cross-stream distribution of mean axial velocity along the starting vortex ring centerline (line connecting the centers of the left and right side vortex) at different times for pulsed operation. In contrast to 1 Hz pulsing (Fig.5.6(a)), the profiles are symmetric about the centerline for 10 Hz (Fig.5.6(b))—with a peak velocity of 103 cm/s at t=24 ms. The suction effect of the plasma region is seen up to t=48 ms for both 1 Hz and 10 Hz cases. For both frequencies, the jet wandering increases with time, and this may be a possible reason for the highly symmetric behavior of 10 Hz case (shorter times) than

1 Hz.

5.3 Jet Characteristics

Figure 5.7 presents the cross-stream distribution of mean axial velocity non dimensionalized by the local maximum axial velocity and streamwise distribution of local maximum mean axial velocity for steady operation and several times of pulsed operation of the PSJA with frequencies 1 Hz, 10 Hz and 100 Hz. The cross-stream and streamwise distances are non-dimensionalized with embedded electrode diameter d_i. The profiles collapse reasonably well for all cases, despite the fact that the farthest axial station chosen was as close as $5r_i$ downstream. For steady operation of the actuator (Fig. 5.7(a)), entrainment of residual fluid by the plasma is seen at a distance $0.5r_i$ downstream (where r_i is the radius of the embedded electrode). The same effect is seen for distances lesser than r_i downstream in the case of 1 Hz pulsing at t=20 ms (Fig. 5.7(c)), 10 Hz pulsing at t=24 ms (Fig. 5.7(e)), and 100 Hz pulsing. This is in contrast to the similarity profiles seen in conventional (non-ZNMF) pulsed jets. Except for actuator operation in Figs. 5.7(a) and 5.7(c), all the other profiles show asymmetry in their collapse (see, for instance Fig. 5.7(f), where the left hand side of the profiles do not collapse in the same manner as the right hand side). This is because of jet wandering in the direction of asymmetry, which may be either due to convection driven currents in the glass enclosure where the tests were conducted, or the variation in the plasma induced flow itself, and the exact reason is not clear at this stage. For the actuator pulsed at 100 Hz (Fig. 5.7(b)), the velocity profiles collapse well, resembling steady actuator operation (Fig. 5.7(a)), unlike the 1 Hz and 10 Hz pulsed cases.

The peak velocity obtained on steady operation of the actuator (Fig. 5.8(a)) is 64 cm/s, after which the velocity remains nearly constant up to $1.8d_i$ downstream, similar in behavior to continuous jets. Pulsing the actuator at 1 Hz increases the peak velocity to 90 cm/s at 20 ms time (Fig. 5.8(b)), after which it drops slightly for t=94 ms, and to about 53 cm/s for t=183 ms, where the actuator reaches steady state condition. For the 1 Hz, t =20 ms case, the peak occurs at $0.5d_i$ downstream (which is the center of the starting vortex ring in Fig. 5.1(a), after which it drops to zero value at about $1.5d_i$. The spreading of the jet increases with time (and advection of the starting vortex), as seen in the 94 ms, 1 Hz case, where the peak value starts to linearly decrease with downstream distance. Also, the peak value of the velocity (t=94 ms, 1 Hz operation) occurs at $0.5d_i$ as in the t=20 ms case, even though the starting vortex has now advected to a farther downstream distance (Fig. 5.1(h)). The spreading of the jet for t=183 ms at 1 Hz closely resembles

steady actuation (Fig. 5.8(a)), and the peak value occurs at around $0.75d_i$ downstream.

An increase in the pulsing frequency by an order of magnitude increases the peak velocity (from 90 cm/s in the 1 Hz case) to 103 cm/s, as seen in the t=24 ms, 10 Hz operation of the actuator (Fig. 5.8(c)). At this frequency, the value of the peak velocity is about 98 cm/s for t=12 ms, while it drops for t=57 ms to about 58 cm/s, suggesting the optimum time of operation is less than 24 ms. The peak occurs at around $0.5d_i$ downstream for all these times, with the jet spreading increasing with time. An interesting observation is the non-return to zero velocity for all the 10 Hz times throughout the entire streamwise extent of observation, which is clearly not the case for the t =20 ms in the 1 Hz case (Fig. 5.8(b)), yet again suggesting an optimum operational frequency closer to 10 Hz. The decrease from the peak axial velocity for 10 Hz, t=57 ms is almost linear up to $2.5d_i$ downstream, while it is rather steep for t=12 ms and t=24 ms. The slight increase in axial velocity far downstream for the 10 Hz case is thought to be triggered by the vortex ring interaction effect discussed earlier. A further increase in pulsing frequency to 100 Hz renders the jet nearly steady, as the plasma does not have enough time for response. The peak value of axial velocity obtained for 100 Hz pulsing is 76 cm/s (Fig. 5.8(d)), which is considerably higher than the peak value obtained on steady operation (Fig. 5.8(a)). The decrease from the peak value is linear for the 100 Hz case, which is in contrast to the nearly flat slope seen in steady operation. This suggests that pulsed operation of the PSJA at high frequencies where the jet is nearly steady is still more efficient (in terms of obtaining higher jet momentum for lower input power) than steady operation.

Figures 5.9 and 5.10 show the streamwise distribution of fluid impulse of the actuator pulsed at 1 Hz and 10 Hz, respectively, at four different times of evolution. These were determined by using the inviscid second-order momentum integral equation as given in Hussein *et al.* [175] shown below that takes into account the mean and RMS axial components of velocity, along with RMS components in the radial ($\overline{v'^2}$) and θ ($\overline{u_\theta'^2}$) directions.

$$I = 2\pi\rho \int_0^\infty (U^2 + \overline{u'^2} - \frac{1}{2}(\overline{v'^2} + \overline{u_\theta'^2}))rdr \tag{5.1}$$

The peak value of impulse for 1 Hz case is about 10 dynes and occurs at 94 ms (Fig. 5.9), and later decreases in nearly linear manner to zero value at $3.5d_i$ downstream. For the other three times (20, 48, 183 ms), the peak value decreases to zero value by $2.5d_i$ downstream, and thus it can be seen that the 94 ms case spreads the most. The peak value of impulse for the 10 Hz case (Fig. 5.10) is about 9 dynes (occurs at 12 ms), which is slightly less than the value obtained from 1 Hz pulsing. However, the peak velocity of the jet is highest (103 cm/s) when operated with 10 Hz pulsing. The most interesting behavior of the 10

Hz case is the non-return to zero impulse, which is in sharp contrast to the 1 Hz case. Specifically, for t=12 ms (Fig. 5.10), the impulse peaks to about 6 dynes at $3.5d_i$, and the additional entrainment effected by an earlier starting vortex in the flow field is thought to be the reason, supporting the earlier observations made in Figs. 5.2(c) and 5.8(c). Thus, to have a longer downstream extent of the jet, pulsing the actuator at 10 Hz would be a more "optimum" choice as compared to 1 Hz. Figure 5.11 shows a comparison between the steady operation and nearly steady 100 Hz pulsed operation in terms of the streamwise distribution of fluid impulse. The pulsed actuation cases clearly produce a higher fluidic impulse as compared to the cases in Fig. 5.11. It is seen that the peak value of impulse is higher for the 100 Hz case as compared to steady actuation, in accordance with the observations made in Fig. 5.8(d) earlier.

Figure 5.12 shows the variation of the peak axial velocity as a logarithmic function of the pulsing frequency f_p. The different points for a particular frequency indicate various jet evolution times the data was recorded. The peak value obtained for any particular frequency is higher than the maximum velocity obtained for steady operation (64 cm/s). At 1 Hz, the peak velocity obtained increases with decreasing size of the actuator, as seen on comparing the values obtained from larger (d_o=58 mm, d_i=38 mm) and smaller (d_o=25.4 mm, d_i=12.7 mm) actuators. The 10 Hz pulsing case shows the highest peak value of 103 cm/s (at 24 ms) and values greater than 95 cm/s for three different jet evolution times (12, 18, 36 ms). This is followed by 1 Hz case with a highest peak value of 90 cm/s, and 100 Hz with 76 cm/s. It is important to note that the power input for all the pulsed cases was constant, and was 50% less than that for steady actuator operation. Thus, for the limited range of frequencies investigated here, it can be concluded that to obtain maximum jet velocity and streamwise spreading of jet momentum, it is optimal to operate this actuator at 10 Hz pulsing.

5.4 Other Factors Affecting the Formation of Plasma Synthetic Jets

The following subsections examine the characteristics of the plasma synthetic jet as affected by the input power, embedded electrode diameter and plasma temperature.

5.4.1 Input Power Effects

The effects of varying input power on the quiescent flow field characteristics of the PSJA (d_i=12.7 mm, d_o=25.4 mm) is shown in Fig. 5.13. Both steady and 10 Hz (t=24 ms) pulsed operation are compared for two values of input power. It is seen that the values of

both peak velocity and impulse for pulsed operation are higher than their respective steady counterparts regardless of input power, once again confirming that unsteady actuation is optimal for increased performance. The values of peak velocities obtained for both steady and pulsed operation in the high power mode are almost twice the corresponding values obtained in the low power mode (Fig. 5.13(a)). The peak axial velocity obtained for steady operation in the high power mode coincides with that obtained for pulsed operation ($\approx$ 100 cm/s) in the low power mode. Increasing the power input affects the fluid impulse substantially, increasing it by nearly three times as compared to the low power input case (Fig. 5.13(b)). The most remarkable effect is observed for pulsed operation, where the peak values of fluid impulse and mean axial velocity are almost identical. Besides increasing the velocity, the width of the plasma synthetic jet is observed to be larger for higher input power, as a result of which the momentum of the jet is increased. The spreading and streamwise extent of the jet are also increased for the higher power input case. Whether there is a plateau on the jet performance with increasing input power is still not clear.

5.4.2 Embedded Electrode Diameter Effects

Enloe *et al.* [54] observed that the width of the exposed electrode does not affect the discharge and thinner electrodes produce a greater body force. Since the electric field driving the plasma is limited to the region between the electrodes, the plasma will not spread downstream of the outer edge of the embedded electrode. Thus, the width (or diameter in the PSJA) of the embedded electrode directly affects the extent or expansion of plasma on the actuator as also observed previously by Enloe *et al.* [54]. As the thickness of the electrodes (copper tape) used in these experiments is very small, the most important PSJA length scale is thus the embedded electrode diameter d_i.

Fig. 5.14 shows the vorticity contours obtained from PIV measurements phase-locked to the PSJA pulsing frequency of 10 Hz at 24 ms in the actuator duty cycle. The results from two actuators with different embedded electrode diameters (1.27 cm and 1.9 cm) are shown. It is clearly seen that increasing the diameter of the embedded electrode results in increased width and streamwise extent of the jet. Also, the vorticity contours for the d_i=1.9 cm actuator show more lobes (especially near the wall) than the smaller actuator, indicating increased strength of the starting vortex. The jet structure in itself appears to be similar for both actuators, indicating that the jet scales with d_i. Fig. 5.15 shows a comparison of the streamwise distribution of local maximum mean axial velocity and fluid impulse for the above two actuators. Increasing d_i increases both the peak velocity and fluid impulse to at least two times the corresponding smaller actuator values. The streamwise distance

at which the peak velocity (or impulse) occurs (around $0.5d_i$) appears to scale well with embedded electrode diameter. For pulsed actuation, the well demarcated "dual-lobes" seen at around x=$1.4d_i$ for the d_i=1.9 cm actuator are thought to be indicative of slightly slower travel times of the starting vortices, as compared to lobes seen at around x=$1.5d_i$ for the d_i=1.27 cm actuator. At the limit of the window of observation, the jet decelerates faster for pulsed operation. Fig. 5.16 shows the time variation of the peak axial velocity of the PSJA pulsed at 10 Hz, where both the above actuators are compared. While the velocity plateaus after 30 ms for d_i=1.27 cm actuator, the larger actuator shows a lobed variation due to the slower advection of vortex rings mentioned above. Although increasing d_i herein produces better jet performance, it is expected that there would have to be an optimum value of d_i after which increasing the diameter no longer increases the peak velocity, on account of increased jet width.

5.4.3 Buoyancy Effects

The effect of heating by the plasma on the bulk fluid has been addressed by few researchers. Leonov *et al.* [85] speculated that bulk heating was the main factor responsible for thrust generation by the actuator on account of the reduced viscosity of the air. However, Enloe *et al.* [84] found experimentally that the thrust was dependent on the nature of the waveform, even though the bulk plasma structure was the same, thereby suggesting that bulk heating was not the mechanism for thrust generation. Recently, Enloe *et al.* [112] conducted detailed temporal measurements of density perturbations in the plasma region and observed that heating actually affected the spatial structure of air near the actuator. In this regard, it was desired to understand the contribution of plasma heating to the formation of the synthetic jet produced on operation of the PSJA. Thermocouple based measurements show that at a distance of $0.25d_i$ downstream of the actuator, the temperature of the plasma synthetic jet was: T_s=112±5°F. To characterize buoyancy effects, the calculation of the non-dimensional Grashof number for the flow induced by the annular PSJA is given below

$$Gr = \frac{g\,\beta\,(T_s - T_\infty)\,{d_i}^3}{\nu^2} \tag{5.2}$$

where g is the acceleration due to gravity, β is the volumetric thermal expansion coefficient and ν is the kinematic viscosity of air. The ambient temperature during these experiments was measured to be: T_∞=70°F, which is roughly equal to 20°C. Properties of air at this temperature are: $\beta = 3.43 \times 10^{-3}$ K^{-1} and $\nu = 15.11 \times 10^{-6}$ m^2/s. Hence the Grashoff

number can be calculated as follows

$$Gr = \frac{9.81 \times 3.43 \times 10^{-3} \times (112 - 70) \times (1.27)^3 \times 10^{-6}}{(15.11)^2 \times 10^{-12}} = 12679.28$$

As this value of Gr is greater than 1000, the contribution of natural convective (buoyant) motion cannot be disregarded (see Bejan [198]), and hence it becomes essential to assess the effect of heating on the formation of plasma synthetic jet. It was suspected that the formation of the plasma synthetic jet could be triggered by the buoyant motion of air in the upward direction on account of the high temperature of the plasma. To investigate the effects of buoyancy, three actuator orientations (d_i=12.7 mm, d_o=25.4 mm) were tested in quiescent conditions as shown in Fig. 5.17, such that the actuator was directed upwards (position A), downwards (position B), and sidewards (position C). Any buoyancy driven drift of fluid would appear as differences in the velocity profiles of the three actuator positions, and therefore they would not be comparable. The streamwise extent of the jet in position B would be less than that in position A, while the cross-stream velocity profiles in position C would exhibit visible left-right asymmetry.

Figure 5.18 shows contours of spanwise vorticity obtained from time-averaged PIV measurements for steady operation of the actuator in each different orientation. The contour plots have been presented so that the jet matches the particular orientation of the actuator. It is seen that the streamwise extent of the jet in all orientations is nearly the same. It is interesting to note the symmetry of the flow field about the actuator centerline for all the cases. As buoyancy driven drift or change in the jet spreading are not observed, these results indicate that changing the orientation of the actuator does not affect the basic quiescent flow field. At a streamwise distance of $2d_i$ downstream, the cross-stream mean axial velocity profiles for all orientations collapse well (Fig. 5.19(a)), showing that in the actuator near field, both the local jet velocity and spreading are not affected by the actuator orientation. Fig. 5.19(b) shows a comparison of the streamwise distribution of local maximum mean axial velocity between the different positions, where each profile was non dimensionalized by the peak velocity value for the respective position. The streamwise variation for all positions collapse reasonably well with minor scatter. These results suggest that within the actuator near field, buoyancy effects are not significant to the formation of the plasma synthetic jet.

5.5 Summary

This chapter presented detailed observations on the flow field characteristics of plasma synthetic jet actuators in quiescent air. The plasma region effects fluid entrainment near

the actuator surface, which is tailored in the form of a vertical synthetic jet for the PSJA design. The primary or starting vortex ring advects downstream ahead of the jet, and was found to be important in determining both the maximum velocity of the jet and its streamwise extent. To obtain a higher peak jet velocity, pulsed operation of the PSJA at specific jet evolution times in the actuation cycle (where advection and interaction of the plasma induced vortical structures occurred) was found to be optimal over steady operation, thereby resembling conventional synthetic jet behavior. Of the three pulsing frequencies examined here (1 Hz, 10 Hz and 100 Hz) plus steady actuation, an optimum based on peak jet velocity for constant input parameters was found to lie in the 10 Hz range, and the maximum velocity obtained in quiescent flow for 10 Hz pulsing at 24 ms time of jet evolution was over 100 cm/s. The input power and embedded electrode dimension were found to have a direct effect on the jet characteristics. Increasing the former results in an increased jet velocity and momentum, as expected. Increasing the latter parameter was also observed to positively enhance the jet characteristics, as more surface area was available for the plasma to expand. The effect of plasma related heating was found to not affect the near actuator behavior, as the measurements between different actuator orientations yielded a fairly good collapse in streamwise and cross-stream profiles.

5.6 Tables and Figures

This page is intentionally blank.

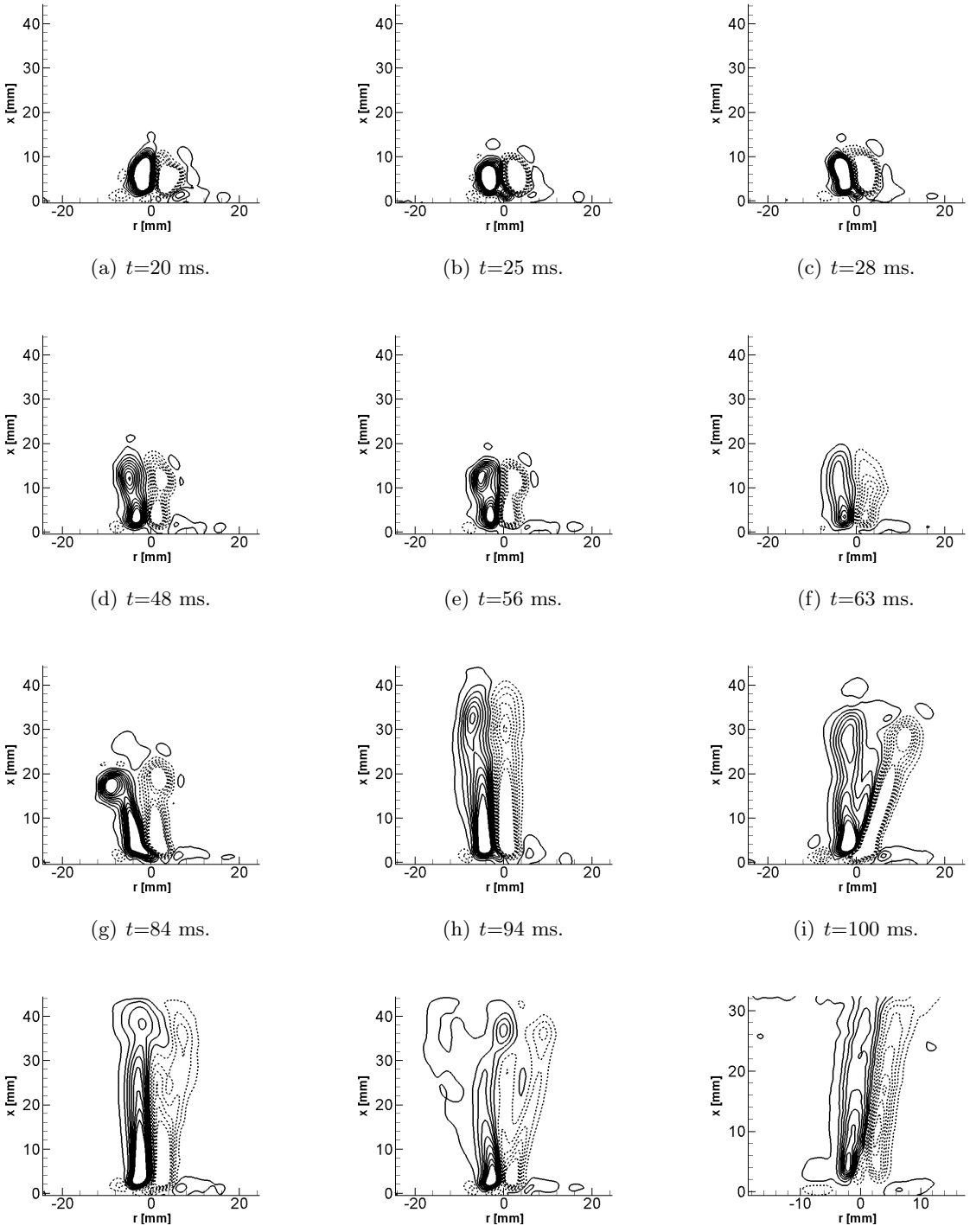

(a) t=20 ms. (b) t=25 ms. (c) t=28 ms.

(d) t=48 ms. (e) t=56 ms. (f) t=63 ms.

(g) t=84 ms. (h) t=94 ms. (i) t=100 ms.

(j) t=130 ms. (k) t=153 ms. (l) t=183 ms.

Figure 5.1: Averaged PIV results showing vorticity contours for actuator in quiescent flow with measurements phase-locked to actuator pulsing frequency f_p=1 Hz. Dashed line indicates contours of negative vorticity.

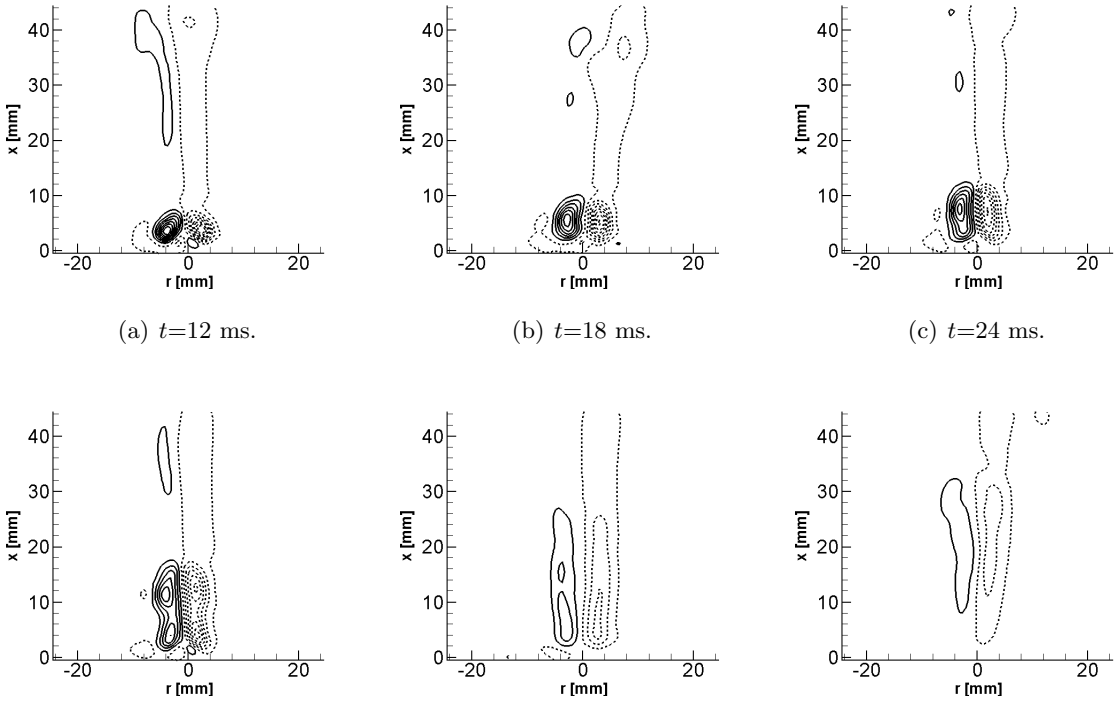

(a) t=12 ms. (b) t=18 ms. (c) t=24 ms.

(d) t=36 ms. (e) t=57 ms. (f) t=83 ms.

Figure 5.2: Averaged PIV results showing vorticity contours for actuator in quiescent flow with measurements phase-locked to actuator pulsing frequency f_p=10 Hz. Dashed line indicates contours of negative vorticity.

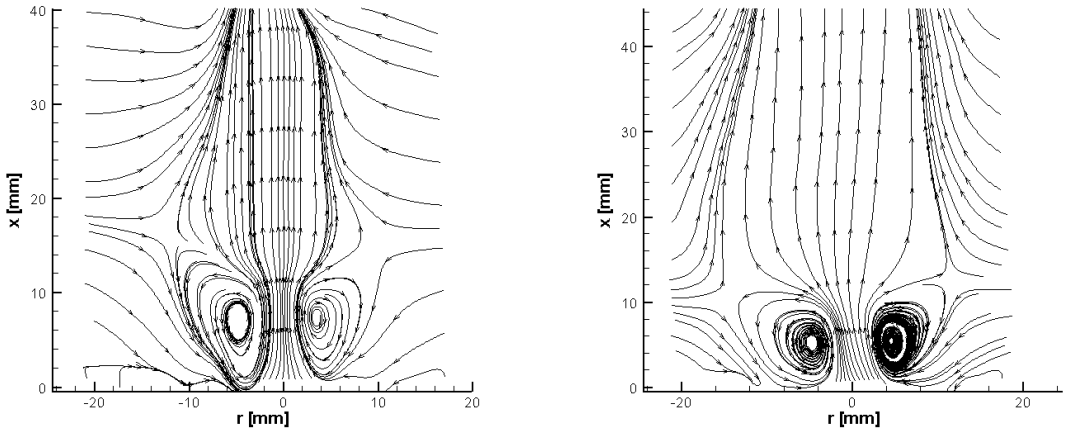

(a) t=24 ms, 10 Hz pulsing. (b) t=25 ms, 1 Hz pulsing.

Figure 5.3: Flow field streamlines for pulsed operation of actuator.

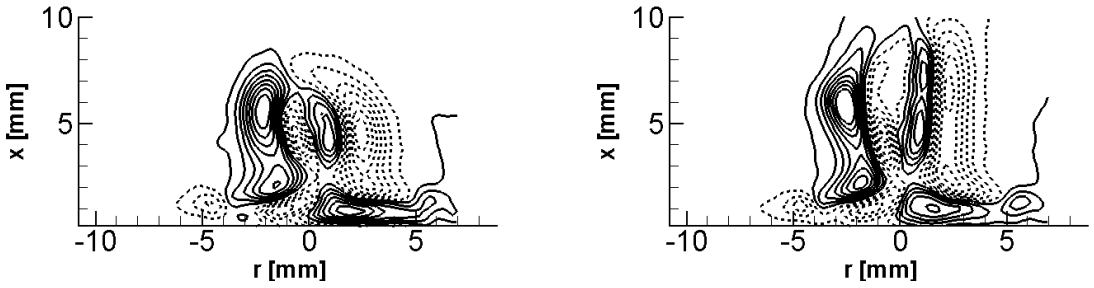

(a) t=26 ms, 1 Hz pulsing.

(b) t=26 ms, 10 Hz pulsing.

Figure 5.4: Phase-locked vorticity contours for pulsed operation of the actuator, showing presence of secondary and tertiary vortical structures in the flow field.

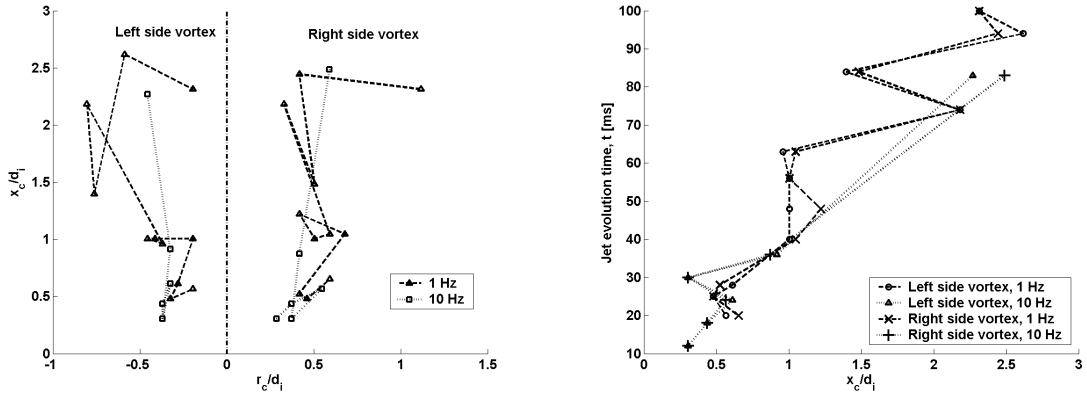

(a) Vortex center trajectories.

(b) Vortex center (streamwise coordinate): time variation.

Figure 5.5: Starting vortex characteristics for pulsed actuator operation.

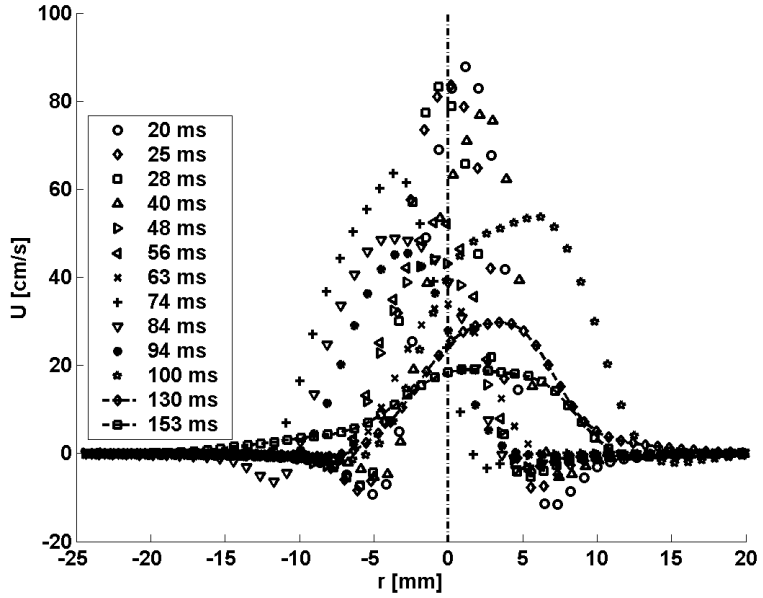

(a) 1 Hz.

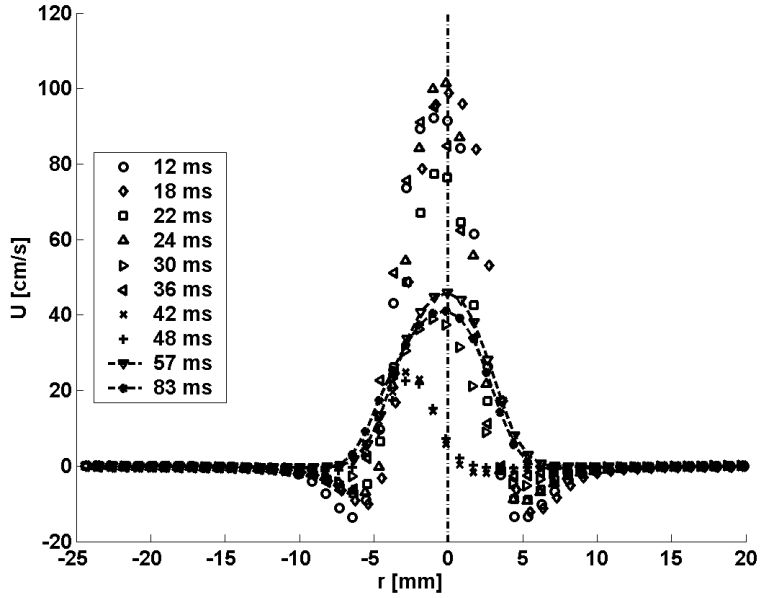

(b) 10 Hz.

Figure 5.6: Cross-stream distribution of mean axial velocity along starting vortex centerline for pulsed actuator operation.

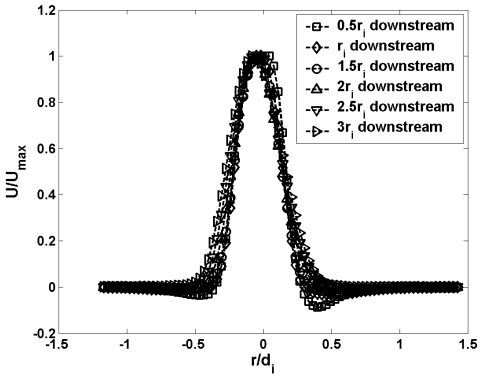

(a) Steady actuator operation.

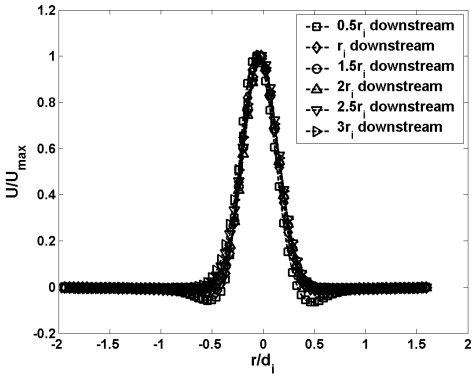

(b) 100 Hz pulsing.

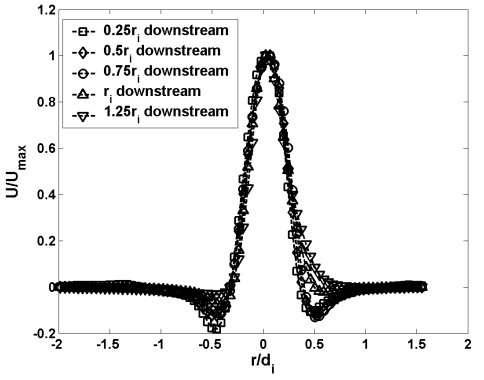

(c) 1 Hz pulsing, t=20 ms.

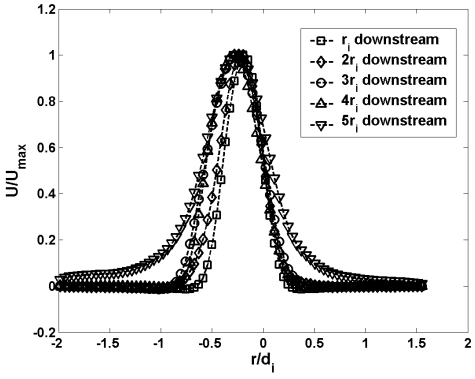

(d) 1 Hz pulsing, t=94 ms.

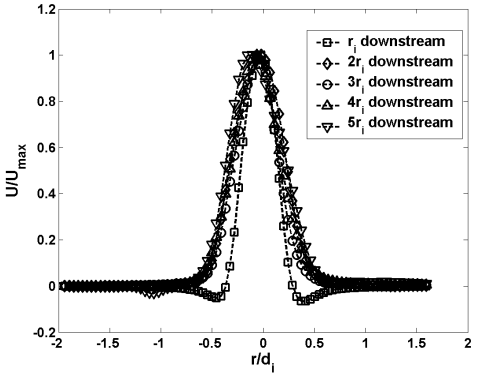

(e) 10 Hz pulsing, t=24 ms.

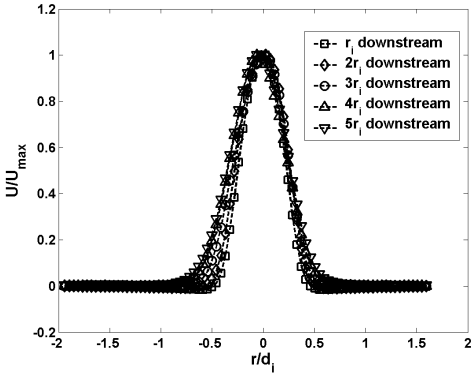

(f) 10 Hz pulsing, t=57 ms.

Figure 5.7: Cross-stream distribution of mean axial velocity.

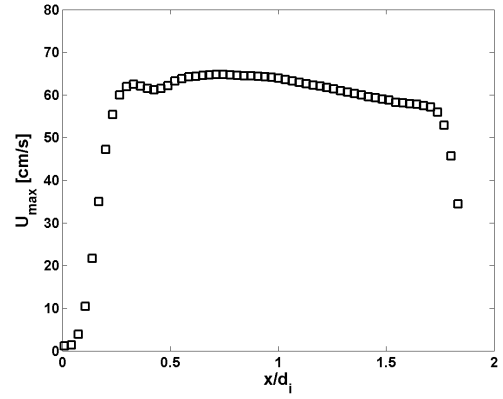

(a) Steady actuator operation.

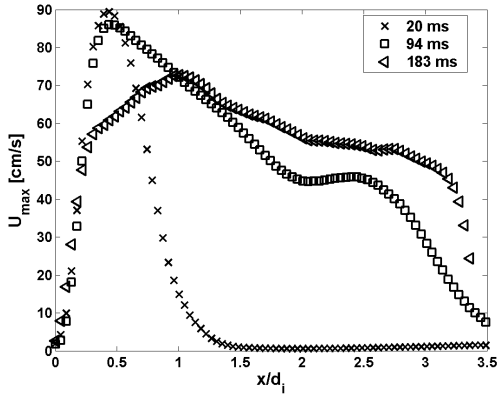

(b) 1 Hz pulsing.

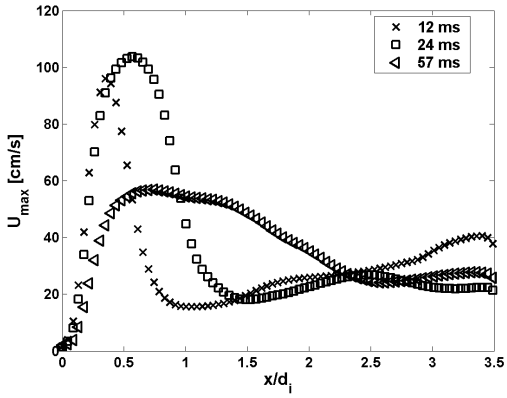

(c) 10 Hz pulsing.

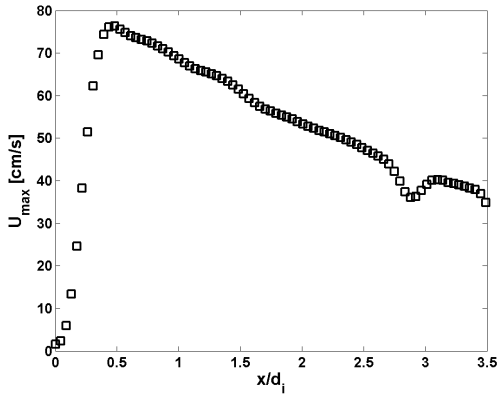

(d) 100 Hz pulsing.

Figure 5.8: Streamwise distribution of local maximum mean axial velocity.

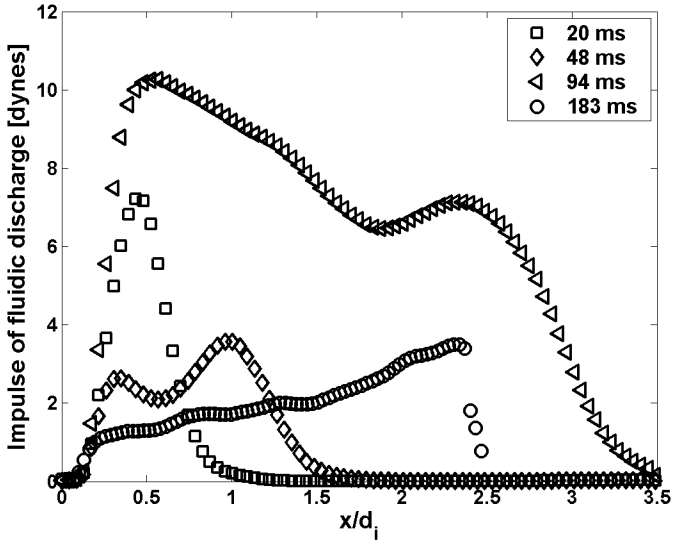

Figure 5.9: Streamwise distribution of fluid impulse at 1 Hz.

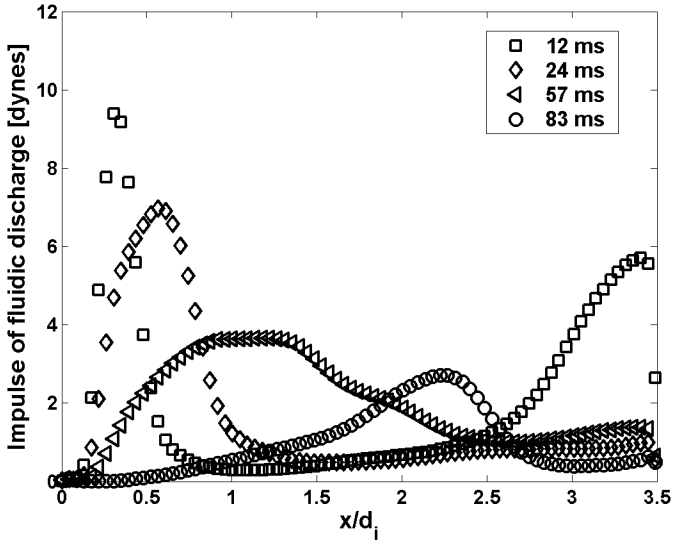

Figure 5.10: Streamwise distribution of fluid impulse at 10 Hz.

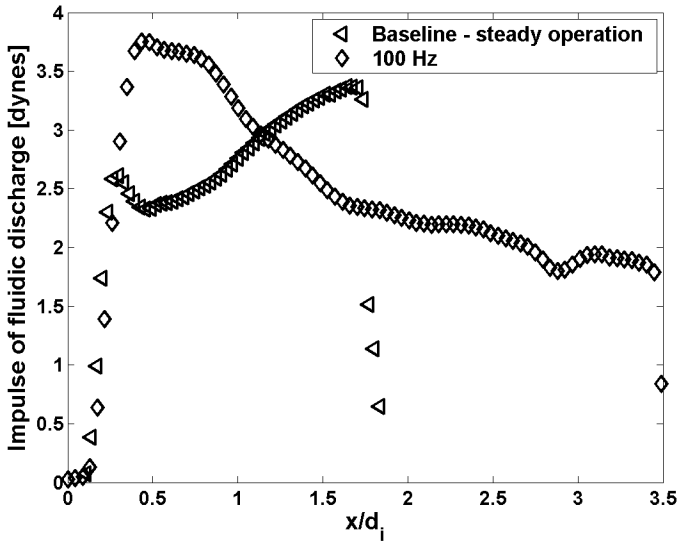

Figure 5.11: Streamwise distribution of fluid impulse: steady operation and 100 Hz comparison.

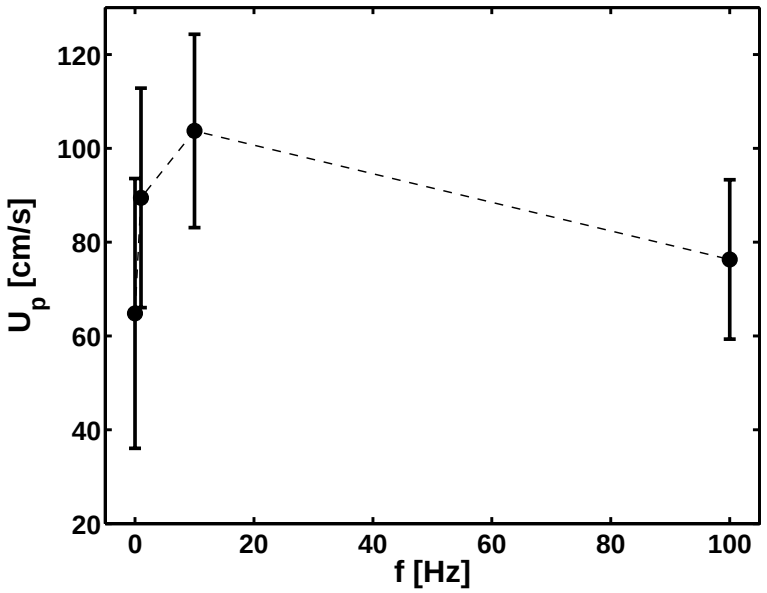

Figure 5.12: Peak axial velocity variation with pulsing frequency.

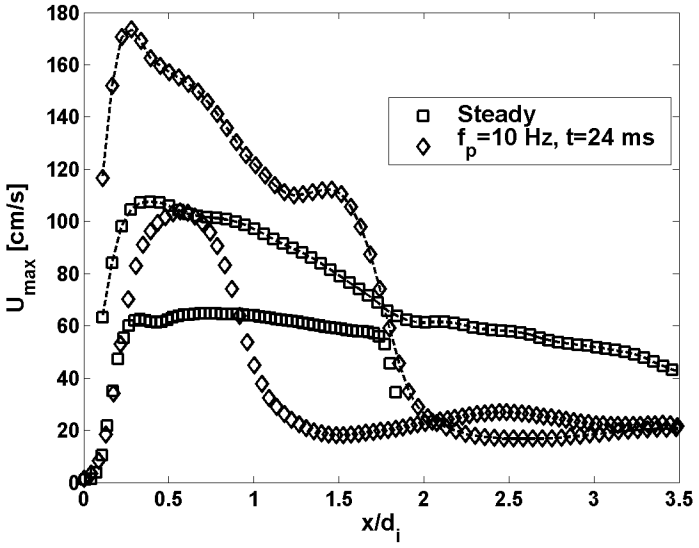

(a) Local maximum mean axial velocity.

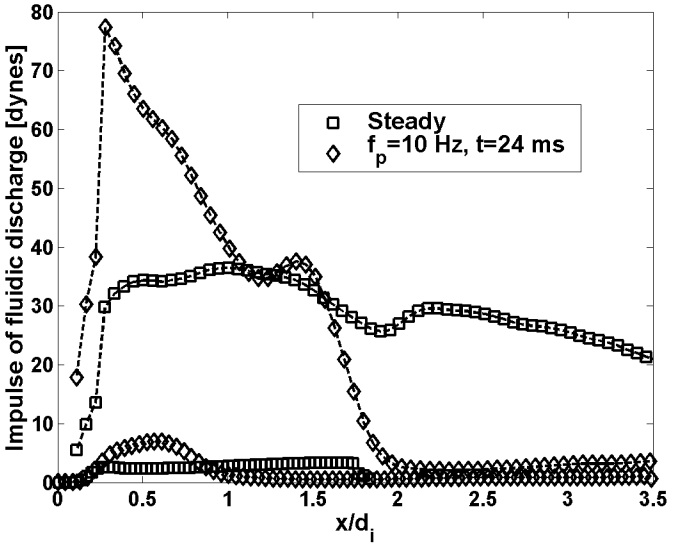

(b) Fluid impulse.

Figure 5.13: Effects of varying input power on streamwise distribution of flow field characteristics. d_i=1.27 cm; dashed line curves indicate high power input, plain symbols (without connecting lines) indicate low power input.

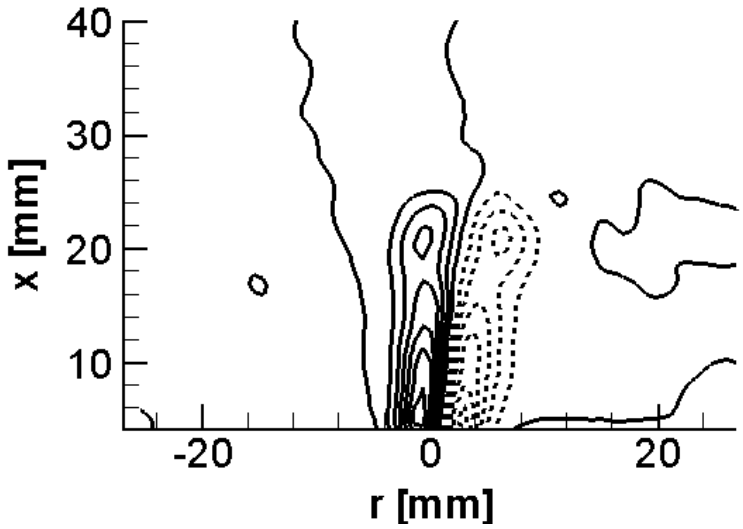

(a) d_i=1.27 cm.

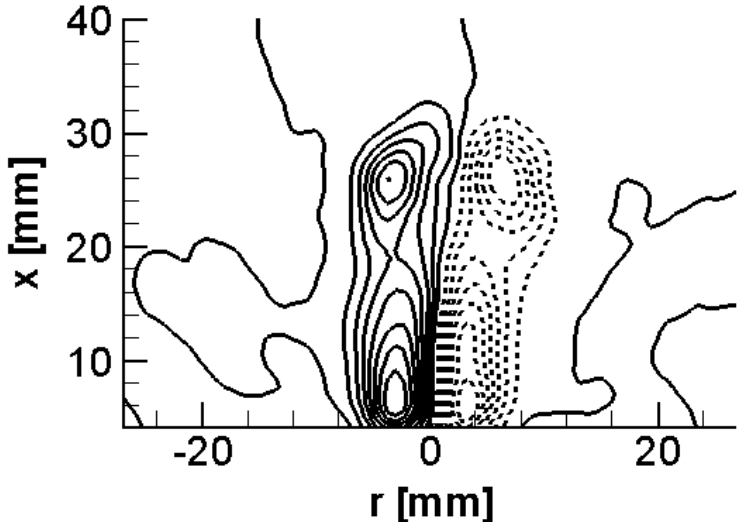

(b) d_i=1.9 cm.

Figure 5.14: Phase-locked vorticity contours showing the effect of varying embedded electrode diameter on the flow field. 10 Hz pulsed operation of the PSJA at t=24 ms in the actuator duty cycle.

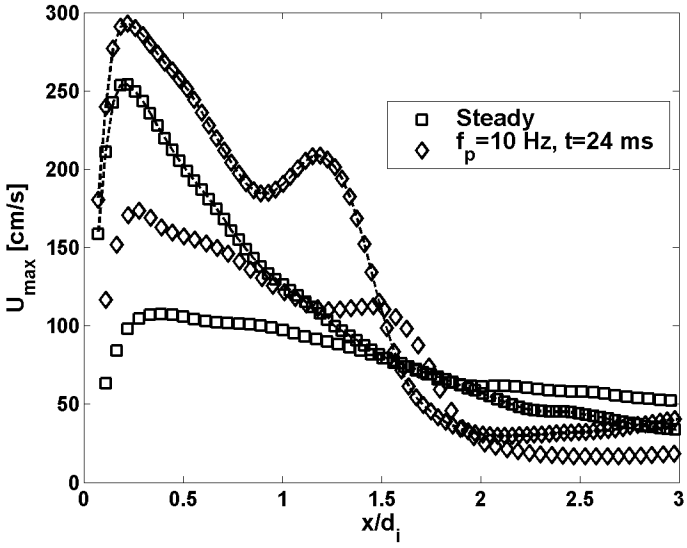

(a) Local maximum mean axial velocity.

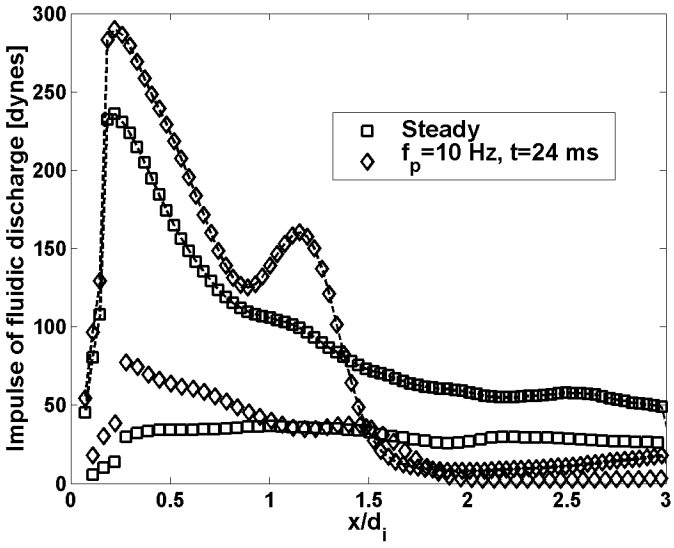

(b) Fluid impulse.

Figure 5.15: Effects of varying PSJA embedded electrode diameter on streamwise distribution of flow field characteristics. Dashed line curves correspond to d_i=1.9 cm, plain symbols (without connecting lines) correspond to d_i=1.27 mm.

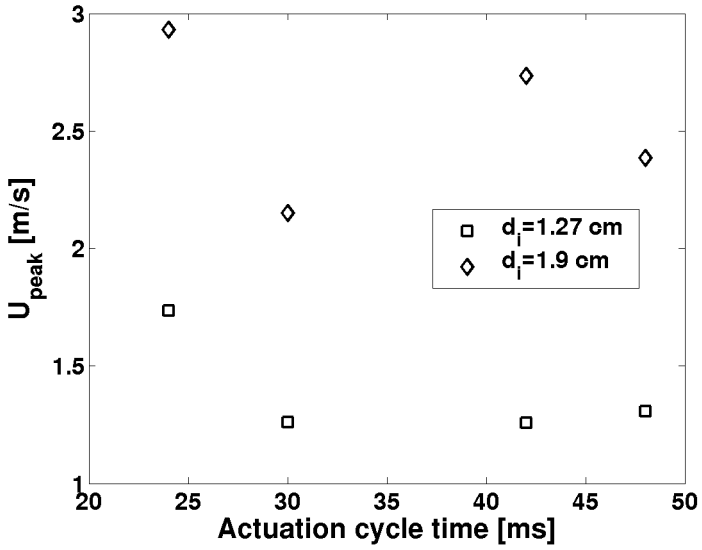

Figure 5.16: Peak axial velocity versus actuation cycle time. PSJA pulsed at 10 Hz.

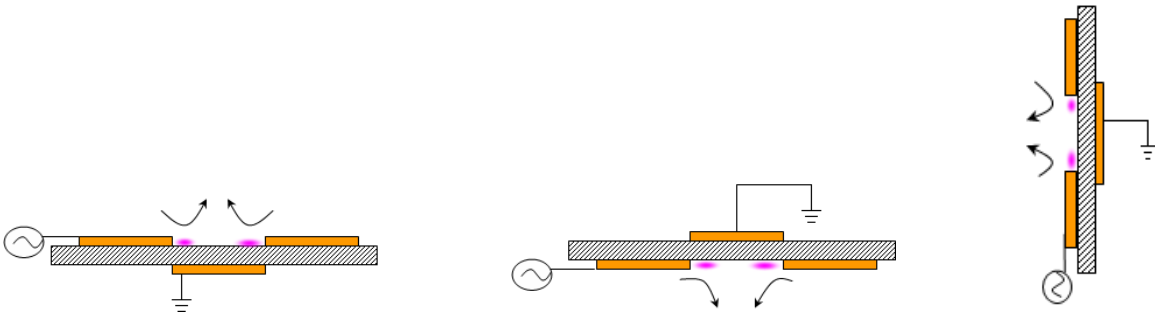

(a) Position A. (b) Position B. (c) Position C.

Figure 5.17: Buoyancy effects: cartoons illustrating the various positions tested.

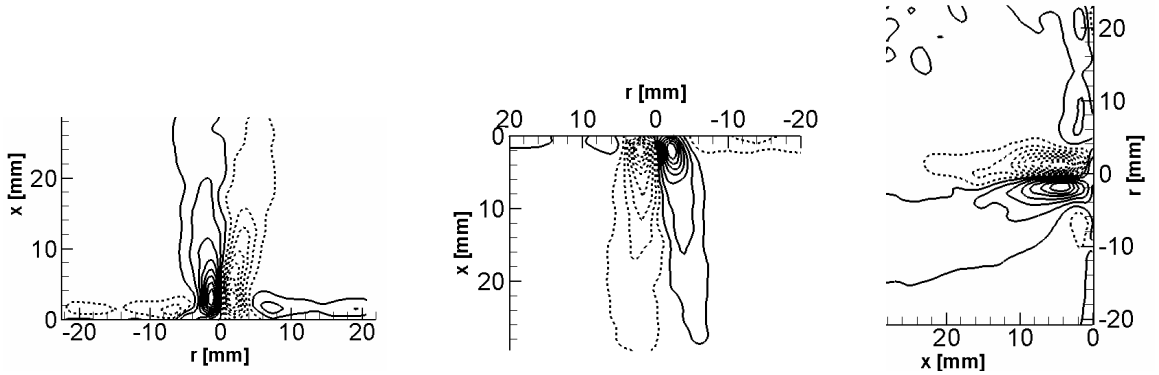

(a) Position A. (b) Position B. (c) Position C.

Figure 5.18: Averaged PIV results showing vorticity contours for various actuator orientations. PSJA in steady operation.

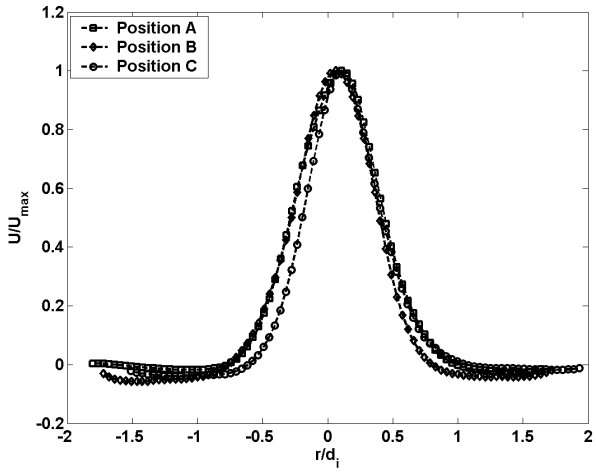

(a) Cross-stream distribution of mean axial velocity, x=2d_i downstream.

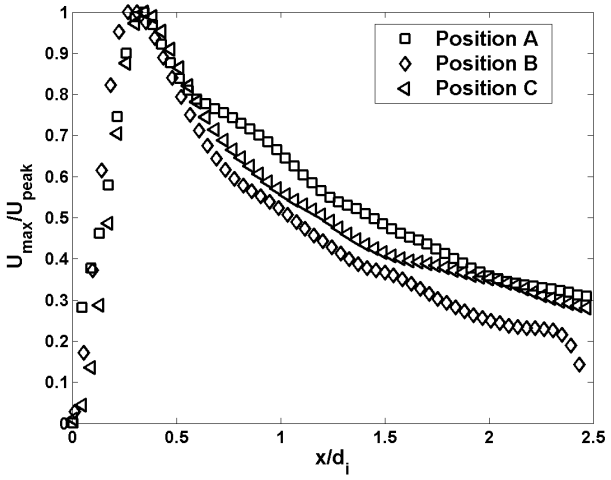

(b) Streamwise distribution of non-dimensional local maximum mean axial velocity.

Figure 5.19: Effects of changing the actuator orientation in quiescent flow, PSJA in steady operation. Note that the quantity U_{peak} in (b) corresponds to the peak axial velocity of the jet for the respective actuator orientation. The dimensional values of U_{peak} are: 147.86 cm/s (position A), 200.42 cm/s (position B), and 125.68 cm/s (position C). Standard deviations of local maximum mean axial velocities are: 38.2417 cm/s (position A), 59.4656 cm/s (position B), and 32.5387 cm/s (position C).

Chapter 6

JET INTERACTION WITH A CROSS FLOW

6.1 Introduction

The previous chapter discussed the characteristics of the plasma synthetic jet in a quiescent environment. This chapter examines the interaction of the plasma synthetic jet with non-zero cross flows. Based on the quiescent flow measurements, the actuator was operated at a pulsing frequency f_p=10 Hz (where the maximum PSJA jet velocity U_{jp}=104 cm/s) in addition to a baseline steady operation case (U_{js}=62 cm/s). The measurements were conducted for three different cross-stream velocities: 0.85 m/s (case A), 1.25 m/s (case B) and 1.75 m/s (case C), as denoted in Table 6.1. These values were chosen to investigate the interaction of the jet with cross flows that were lower, nearly the same and higher in strength as the peak jet velocity at 10 Hz pulsing. The actuator center was located at a distance of 14.8 cm from the leading edge of the flat plate, the test Reynolds numbers based on this length Re_L were approximately $9 \cdot 10^3$, $13 \cdot 10^3$ and $18 \cdot 10^3$. Two sets of values of jet blowing ratios were calculated based on the free stream velocity and the peak PSJA velocity obtained for each mode of operation, and these are shown in Table 6.1. A total of 104 PIV runs were recorded for the annular PSJA, while 25 runs were recorded for the linear PSJA, both across varying times in the actuator pulsing cycle as well as input power. The diameters of exposed (d_o) and embedded (d_i) electrodes of the annular PSJA tested herein were 25.4 mm (1 inch) and 12.7 mm (0.5 inch) respectively, with either no air gap (w=0) or a 1–2 mm overlap. The dimensions of the linear PSJA (also referred to as L-PSJA) used were chosen so as to match the PSJA, and the width of the exposed electrodes and embedded electrode of the L-PSJA were 6.35 mm (0.25 inch) and 12.7 mm (0.5 inch) respectively, with no air gap (w=0) and a spanwise length of 90 mm. A 0.025 inch thick alumina ceramic slab was used as the dielectric material. Figure 6.1 shows the flat plate and actuator arrangement used for this study, and the locations where velocity profiles were extracted (and presented later in this chapter) are also shown. The basic flow field will be examined first, followed by a discussion of derived flow characteristics for both the annular and linear plasma synthetic jet actuators. This will be followed by a discussion of the cross-stream flow field of the annular actuator.

6.2 Annular PSJA

6.2.1 Basic Flow Field

Figure 6.2 shows vorticity contours obtained from time-averaged PIV measurements for steady operation of the PSJA in cross flow. It can be seen that the behavior of the plasma synthetic (ZNMF) jet in a cross flow is similar to a conventional (non-ZNMF) jet. The suction of fluid by the plasma region immediately upstream of the actuator center is not predominant as it is opposed by the incoming flow. A clear separation streamline (not shown) was observed to start from near the actuator center for all the three velocities, which divides the flow field into a global region with the mean flow, and an inner region where the effects of the plasma synthetic jet are observed. The amount of penetration, viz., the cross-stream distance to which the inner region prevails is affected by the incoming flow. On comparing figures 6.2(a)–(c), it can be seen that the penetration of the jet decreases with increasing cross flow velocity, as expected. While a clear two-region flow is observed for case A (figure 6.2(b)) and case B (figure 6.2(b)), the inner region is almost non-existent for case C (figure 6.2(c)). The starting vortex ring has advected out of the FOV for steady operation of the actuator for all the three cases.

Figures 6.3–6.5 show vorticity contours obtained from phase-locked PIV measurements for 10 Hz pulsed operation of the PSJA in cross flow, and several times of evolution of the jet are shown. For case A (figure 6.3), the starting vortex is clearly seen within the FOV for all times except t=83 ms. It should be noted that the last two times (57 ms and 83 ms) examine the portion of the actuation cycle when the plasma is turned off. The separation streamline (not shown) originates at 14.6 cm from the leading edge of the flat plate for times from 18 ms to 24 ms, after which the location shifts downstream to 14.7 cm for times from 36 ms to 57 ms. The penetration of the jet is around 0.5 cm for t=18 ms, then increases and stays constant at 0.6 cm up to t=36 ms, after which it peaks to around 0.8 cm for t=48 ms toward the end of the actuation cycle. At t=57 ms, where the plasma is turned off, the penetration of the jet reduces to 0.5 cm, and the flow returns to baseline free stream flow at t=83 ms. The starting vortex advects with the flow 18 ms to 36 ms, after which it loses structure due to dissipation in the global flow region. A new starting vortex incarnation starts to form near the actuator base at 24 ms, and the resulting interactive entrainment with the earlier vortex can be attributed to the increase in penetration depth from 24 ms to 57 ms. It is interesting to note that at t=18 ms, the left hand side of the starting vortex ring (that is nearest facing to the incoming flow) is almost completely weakened by the free stream, while the right hand side of the ring causes the fluid rotation in the inner fluid

region. In this regard, a visual comparison of the inner region flow for times 18 ms and 48 ms shows that while the inner region streamlines are parallel to the free stream for 18 ms (due to negative vorticity added by the right hand side of the ring), the inner region streamlines for 48 ms are inclined to the free stream. This suggests that the strength of the right hand side of the vortex ring decreases with increasing time. Furthermore, the area of the inner region (with separated flow) increases with time from 18 ms to 48 ms. Since the side of the vortex ring with rotational sense opposing the free stream causes the fluid to separate, the strength of the left hand side vortex would have to increase with increasing time. This asymmetry in the vortex ring strength is believed to be important to effecting jet penetration with the mean flow.

For case B (figure 6.4), the starting vortex ring is seen at all times when the actuator is on (18 ms to 48 ms). At t=18 ms, the jet penetration is around 0.4 cm, after which it increases to a maximum value of around 0.5 cm at t=24 ms, and then decreases and stays nearly constant at 0.4 cm up to t=48 ms. The separation streamline at 1 m/s starts just downstream of the actuator center location (x=15 cm), compared to x=14.8 cm for case A. In general, the reverse flow region is lesser in extent for the 1 m/s case. For case C (figure 6.5), the jet penetration is around 0.2 cm, and it stays constant for all times when the actuator is on. Also, the separation streamline (not shown) has moved downstream to 15 cm from the 1 m/s location, as expected. The reverse flow region is non-existent at this particular velocity. The effectiveness of the actuator in affecting a cross flow is limited by the value of the penetration depth of the jet, and it was found to be less than 1 cm for all the cases tested herein. It is suspected that increasing the input power could increase this value to some extent, and this will be discussed in the sections below.

6.2.2 Streamwise Flow Characteristics

Figures 6.6 and 6.7 show the velocity profiles of the mean component of streamwise velocity obtained for baseline (actuator off) flow and steady operation of the PSJA respectively, where the individual profile curves are separated by a distance of Δ=3.3 mm. For PSJA case A, the flow separates at the actuator center due to the jet interaction, and starts to recover at 2Δ downstream (figure 6.7(a)). The influence of the jet on the cross flow for case A extends to a distance of y=0.5 cm, and the increase in mean velocity is very near the wall (at y=0.1 cm for x=4Δ downstream, figure 6.7(a)). With increase in free stream velocity to case B (PSJA), the flow separates immediately downstream of the actuator center, and the reverse flow region is smaller compared to case A (figure 6.7(b)). The flow does not recover to the baseline profile, however, even at 4Δ downstream. The

effect of the jet is weakened for case C of the PSJA (figure 6.7(c)), and there is no reverse flow. It is interesting to note that for all these cases, the profiles with steady actuation are shifted upward in the cross-stream direction, at distances downstream of the actuator center indicating the jet penetration. However, the peak in velocity stays at nearly constant cross-stream location even as we move downstream, in contrast to what was observed in the linear actuator in [199]. Also, at distances upstream of the actuator center, the profiles only deviate slightly, which is also observed in the case of the linear actuator [199]. Figure 6.8 shows the displacement (δ^*) and momentum (θ) thicknesses calculated using their standard integral definitions [14]. Both steady operation and 10 Hz pulsing of the PSJA are presented. Note that the values of δ^* and θ have been normalized to the initial values determined from the first profile station (subscript 1). For steady operation of the PSJA in case A, the displacement thickness (figure 6.8(a)) for all three velocities increases from the start of the plasma region (around x=-1Δ, due to the adverse pressure gradient introduced by the plasma synthetic jet) and peaks at the center of the actuator. The displacement thickness values decrease after the center and reach a constant level. The increase in displacement thickness is about 40% (case A), 30% (case B) and 20% (case C) higher than their respective initial values. The PSJA adds additional energy to the flow field, and hence the momentum thickness values are lowered in the vicinity of the plasma for all three speeds. At the center of the actuator, an impressive 40% reduction in momentum thickness is observed for case A (figure 6.8(a)), while it is lowered to about 10% for case B. The actuator seems to have negligible effect on the momentum thickness for case C. Downstream of the actuator center, the momentum thickness values increase, similar to what is observed in a linear actuator [199]. For cases B and C, the momentum thickness returns to its initial value at downstream station x=3Δ. For case A, a 10% reduction in momentum thickness is still seen at the farthest downstream station. Pulsing the PSJA at 10 Hz (figure 6.8(b)) results in about 60% momentum thickness reduction for case A, 20% higher than steady operation of the PSJA for the same freestream velocity (figure 6.8(a)). The action of the PSJA is thus similar to an active boundary layer trip, and when compared to a linear actuator [199], the PSJA produces a larger reduction of the momentum thickness, albeit with a larger increase in displacement thickness.

6.2.3 Cross-Stream Flow Field

To visualize the flow field of the annular PSJA in the the spanwise direction, PIV measurements were conducted at two cross-stream (y-z) planes, one located at the center of the actuator and the other at $2d_i$ downstream of the actuator center as shown in Fig. 6.9.

Fig. 6.10 shows the vorticity contours obtained from these measurements. At the center plane of the actuator, the structures resemble those seen in two-dimensional quiescent flow measurements (presented in Chapter 4), revealing the three-dimensionality of the actuated flow field. The vortical structures diminish with increasing free stream velocity, as expected. For the lowest mean velocity, at distance $2d_i$ downstream of the actuator center, the effect of stretching and twisting the vortex ring by the free stream is seen in Fig. 6.10(d), and the flow field now shows single signed vorticity. At free stream values greater than 85 cm/s, there are no discernible vortical structures at distances downstream of the actuator center.

6.3 Linear PSJA

6.3.1 Basic Flow Field

Figure 6.11 shows vorticity contours overlaid with streamlines obtained from time-averaged PIV measurements for steady operation of a L-PSJA in cross flow, and the three different free stream cases are compared. A stationary cross-stream vortex centered at around x=15.7 cm is seen at all three velocities. The penetration of the plasma synthetic jet is effected through this standing vortex, and it is about 0.3 cm for case A, and about 0.2 cm for cases B and C. Note that any such cross-stream vortical structures were absent in the case of steady operation of the PSJA (Fig. 6.2). The suction effect of the upstream facing plasma region in the L-PSJA is seen to start at around x=14.5 cm for all three velocities. The center of the vortex is located at the outer edge of exposed electrode (edge farthest to the free stream and away from the plasma region), and it is created as a result of near-wall fluid entrainment by the plasma region.

Figures 6.12–6.14 show vorticity contours obtained from phase-locked PIV measurements for 10 Hz pulsed operation of the L-PSJA, and three times of jet evolution corresponding approximately to starting, middle and "plasma-off" phases of the actuation cycle (respectively, in the order of increasing time) are shown. For case A, at t=18 ms (Fig. 6.12(a)), fluid is sucked in upstream of the actuator center at x=14.6 cm, and a cross-stream vortex centered at x=15.7 cm is seen. With increase in time to 36 ms, the size of the vortex is increased, indicating additional entrainment by the plasma. The location of the vortex remains nearly stationary, however. At t=57 ms (in the portion of cycle where the plasma is turned off, Fig. 6.12(c)), the size of the vortex increases to effect a jet penetration of around y=0.8 cm, and the vortex location has shifted downstream and upward. This is higher than the equivalent case of the PSJA (Fig. 6.3(e)), suggesting the mechanism of the L-PSJA in affecting a flow field, on account of its two-dimensionality, is not similar to

the PSJA. For L-PSJA, case B (Fig. 6.13), the sequence of events are the same as in case A, albeit with a reduction in the cross-stream vortex size (and therefore, reduced jet penetration), as expected. It is interesting to note that for all velocities, the L-PSJA induced cross-stream vortex is "trapped" for both jet evolution times (18 ms and 36 ms, when the plasma is on) observed herein. A similar near-wall "trapped" vortex ring was observed in the case of pulsed operation of the PSJA [177]. This was a secondary vortical structure, however, as opposed to only the primary vortex seen in the L-PSJA. For L-PSJA, case C (Fig. 6.14), the effect of the plasma is diminished, but the standing vortex is still seen during both times when the plasma is on. In general, at the end of the actuation cycle, the standing vortex is released into the free stream, and advects downstream of the actuator and in the positive cross-stream direction. A similar cross-stream vortex structure has been observed on the pulsed operation of a linear actuator [200]. It is clear that the near-wall fluid entrainment by the plasma is singularly responsible for both creating and sustaining the standing vortex. In the case of a linear actuator, there is a single plasma region spanwise that creates this downstream facing cross-stream vortex. The L-PSJA produces two such spanwise plasma regions on actuation. Based on symmetry arguments, it was expected that the plasma region of the L-PSJA that is located closest to the incoming flow would have to create another cross-stream vortex, opposite in sign to the observed "trapped" vortex. Such a structure was not observed in the experiments, however, and it appears that the incoming flow completely eradicates any such upstream facing rotation. Hence, it is conjectured that the effect of the upstream facing plasma region would be in adding a finite circulation to the vortex. A comparison of the circulation strengths of the cross-stream vortex created by the linear and L-PSJA actuators would have to be examined to see if the upstream facing plasma region has any effect on the flow field at all. Similar behavior has been studied for linear plasma actuators [69].

6.3.2 Flow Characteristics

The cross-stream variation of normalized Reynolds stress for baseline and steady actuator operation is shown in Figure 6.15, where three locations corresponding to upstream, downstream and center of actuator are considered for each free stream velocity. For the PSJA (Figs. 6.15(a), (c) and (e)), the peak in the Reynolds stress values appear to be shifted more into the flow (i.e. at a higher value of y) on operation of the actuator, as compared to the baseline case for all the three velocities, especially at center of the actuator and downstream. This indicates that the plasma synthetic jet actually introduces significant turbulent diffusion in the mean flow field, and thus can be used for control of laminar and

turbulent shear flows. For the L-PSJA (Figs. 6.15(b), (d) and (f)), the peak normalized Reynolds stress values are increased from their respective baseline values. In contrast to the PSJA, however, for all three velocities, the locations of the peak Reynolds stress values are nearly at the same cross-stream distances as in the respective baseline flows. This indicates that the L-PSJA promotes turbulent diffusion mainly in the streamwise direction, unlike the PSJA, which affects the turbulence characteristics in the cross-stream direction.

6.4 Effects of Increasing Input Power

Figure 6.16 shows vorticity contours obtained from time-averaged PIV results for steady operation of an annular PSJA in a flat plate boundary layer, with increased power input as compared to Fig. 6.2. In addition to the increased depth of penetration of the plasma induced jet into the free stream, it can be seen clearly that an increase in actuator power input results in a considerably different flow field in terms of the formation of a new cross-stream vortex upstream of the actuator center. The strength of the vortex (proportional to its size) is found to decrease with increasing free stream velocity, as expected. However, even with increasing cross flow magnitude, the location of this structure is relatively unchanged. This stationary vortex is also observed for unsteady 10 Hz pulsed operation of the actuator, as seen from the vorticity contours presented in Figs. 6.17–6.19. Note that similar to results presented in earlier sections in this chapter, the times 57 ms and 83 ms correspond to that portion of the pulsing cycle (f_p = 10 Hz, period = 100 ms) where the plasma is off. For a particular cross flow, within all the times in the pulsing cycle where the plasma is on ($t \leq$ 48 ms), the location and size of the cross-stream vortex appear to be nearly unaffected. The plasma region extends from 14.17 cm to 15.44 cm (14.8 cm $\pm$ $0.5r_i$) in the measurement window. A careful examination of the flow field reveals that the cross-stream vortex is centered within the region of plasma at $\sim$14.4 cm, which is upstream of the vorticity concentration observed in the lower power case (see Fig. 6.2(a)).With increase in input power to the actuator (roughly translating into increased plasma strength), the plasma synthetic jet is not completely eradicated by the incoming cross flow. Also, the flow structures are created in the upstream direction. With increase in cross flow velocity to 125 cm/s (case B, Fig. 6.18), the penetration of the jet is lowered as expected. Interestingly, the cross-stream vortex upstream of the actuator center, as well as other flow structures in the plasma synthetic jet are stretched in the direction of the free stream. This stretching is evident on comparing the signs of the flow field vorticity in Figs. 6.17 to that in Fig. 6.18, where dashed lines indicate contours of negative (clockwise oriented) vorticity. The regions

of vorticity corresponding to the plasma induced jet in the higher free stream velocity case (Fig. 6.18) resembles quiescent plasma synthetic jet contours presented in chapters 3 and 5, with counterclockwise sense in the left hand side (opposing the cross flow direction) and clockwise sense on the right hand side. In contrast, the concentrations of vorticity corresponding to the jet in case A have the opposite sign (Fig. 6.17), where the upstream region follows the direction of the incoming flow. Changing the input power thus alters the flow field quite differently for a particular free stream value. The upstream standing cross-stream vortex seen in case A is also observed in case B, centered roughly around 14.2 cm in the latter. With further increase in cross flow magnitude to 175 cm/s (case C, Fig. 6.19), the flow field shows less penetration compared to case B, with further stretching of the stationary cross-stream vortex. The signs of vorticity are similar to those observed in case B. In both case A and B, a right hand side cross-stream vortex centered around 15.9 cm is observed, ostensibly on account of advection of structures in case A flow field by the now faster free stream. For any cross flow magnitude, the depth of penetration of the plasma synthetic jet and the size of the stationary cross-stream vortices are found to not change substantially across the different times in pulsing duty cycle.

Increasing the input power to the linear PSJA also increases the penetration of the plasma induced jet further into the free stream, as seen in the time-averaged (steady operation) and phase-locked (f_p=10 Hz) vorticity contours for the actuator in cross flow case A shown in Fig. 6.20. Compared to the equivalent low power case in Figs. 6.11(a) and 6.12, the synthetic jet does not bend along the free stream direction with increased input power. This is exactly similar to what was observed in the annular PSJA, where increasing input power increased the resistance of the jet to being eradicated by the free stream. The downstream standing vortex centered roughly around 15.5 cm is increased in size (and hence circulation strength) for the increased input power case. Also, similar to the annular actuator, the flow structures appear to be fairly steady for this cross flow velocity.

6.5 Flow Over a Circular Cylinder

To study the applicability of the plasma and plasma synthetic jet actuators for separation control, the laminar flow over a circular cylinder was chosen as a test problem. The effects of both pressure gradient and curvature are included in this case, and it is well known from theory that laminar separation occurs at around 82° to the free stream for diameter based Reynolds numbers less than $30 \cdot 10^3$ [14]. The diameter (D) and length (L) of the cylinder used for experiments was 38.1 mm (1.5 inches) and 203 mm (8 inches) respectively,

and it was transparent for clean optical access. Two different free stream velocities were investigated, and the diameter based Reynolds numbers (Re_D) were $5 \cdot 10^3$ (U_∞=2 m/s) and $10 \cdot 10^3$ (U_∞=4 m/s). The experiments were conducted in the low-turbulence open-circuit blow-down wind tunnel described in chapter 4. The results presented hereon were obtained from time-averaged PIV measurements, and four windows of observation were used to obtain the flow field information from the center of the cylinder x=0 to x=11D downstream in the wake. The linear actuator and L-PSJA configurations were tested, with Kapton used as the dielectric material. As the flow was treated to be nominally two-dimensional, the PSJA configuration was not tested. The cylinder was covered with a layer of Kapton, on which the actuators were constructed. Two actuators were mounted downstream of the laminar separation point, at 90° and 270° to the freestream for symmetric forcing of the cylinder wake. A schematic of the cylinder, actuator arrangement and power supply is shown in Fig. 6.21. The Corona Magnetics Inc. transformer was used to power the actuators for this series of experiments, and the input voltage supplied to the exposed and embedded electrodes of the actuators were driven with 180° phase difference. The exposed and embedded electrodes for both L-PSJA and linear actuator were 5 mm in width (spanwise length of 510 mm).A nominal 2 kV amplitude, 1.1 kHz frequency square wave AC input operated with a 50% duty cycle was used. In addition to steady actuator operation, pulsing the actuator at non-dimensional pulsing frequency f^+ equal to Strouhal number St (non-dimensional wake shedding frequency) value of 0.2 was considered, where f^+ is given by

$$f^+ = f_p D/U_\infty \tag{6.1}$$

where f_p is the pulsing frequency of the actuator. Figures 6.22–6.23 show vorticity contours overlaid with streamlines from time-averaged PIV measurements for both the linear actuator and L-PSJA. In each of these figures, the baseline flow with actuator off is shown for comparison. For Re_D=$5 \cdot 10^3$, the reverse flow region in the wake extends to around $2D$ downstream (Fig. 6.22(a)), and a set of counter-rotating vortices are seen. The reverse flow region is reduced to about $1D$ downstream on steady operation of the linear actuator at this Re_D (Fig. 6.22(b)). The wall jet induced by the plasma region of the two linear actuators force the separation streamlines to move closer to the surface, resulting in tightening of the wake. Note that the counter-rotating wake vortices actually reverse their sense of rotation on actuation compared to the baseline case. The reverse flow region is reduced on steady operation of the L-PSJA (Fig. 6.23(b)), but the actuation does not have as much impact as the linear actuator. The wake width is not changed on steady operation of L-PSJA at Re_D=$5 \cdot 10^3$, and the wake vortices do not change their rotational sense. At this Re, pulsing

at f^+=St does not seem to promote any major improvement from steady actuation in the flow for both the actuators (Figs. 6.22(c) and 6.23(c)), other than changing the rotational sense of the wake vortices in the case of the linear actuator.

For Re_D of 10,000 (Figs. 6.24–6.25), the wake region in the baseline flow was lower than the equivalent case at Re_D=5,000, as expected. Note that the smaller additional wake vortex seen on the negative half of cross-stream coordinate in Fig. 6.24(a) is an artifact of patching multiple PIV windows. The reverse flow region for the baseline case at Re_D=$10{\cdot}10^3$ extends to about 10 cm downstream (Figs. 6.24(a),6.25(a)). Steady operation of the linear actuator at this Re results in marginal reduction of the reverse flow region and changing the rotation sense of the wake vortices, and pulsing at f^+=0.2 does not produce any major changes (compared to steady operation) in the flow field (Figs. 6.24(b) and (c)). At this higher speed, both steady and pulsed operation of the L-PSJA reduces the reverse flow region, if only slightly (Figs. 6.25(b) and (c)).

Figures 6.26 and 6.27 show the cross-stream variation of velocity deficits in the cylinder wake for Re_D $5 \cdot 10^3$ and $10 \cdot 10^3$ respectively, and the baseline defect is compared to that of steady (f^+=0) and pulsed (f^+=0.2) actuator operation. For each Re_D, the deficits of the linear actuator and L-PSJA are compared for two streamwise stations at 1 diameter and 10 diameters downstream. For Re_D of $5 \cdot 10^3$, operation of the linear actuator (in both steady and pulsed modes) actually tightens the near wake, as seen from the narrow velocity defects (reduced cross-stream width) in Fig. 6.26(a), although the actual defect value is itself increased slightly from baseline value. Operation of the L-PSJA (both steady and pulsed modes) does not alter the velocity defect from the baseline curve (Fig. 6.26(b)). At downstream distance of x=$10D$, the pulsed operation of the linear actuator reduces the velocity defect marginally from the baseline case (Fig. 6.26(c)), while steady operation of the L-PSJA reduces the velocity defect from the baseline case (Fig. 6.26(d)). For Re_D of $10{\cdot}10^3$, the linear actuator still promotes tightening of the near wake at x=$1D$ (Fig. 6.27(a)), while the L-PSJA does not produce any major changes in the near wake (Fig. 6.27(b)). At this Re, both steady and pulsed operation of the linear actuator reduce the deficit at 10 diameters downstream (Fig. 6.27(c)), with pulsed operation producing the lowest velocity deficit. The effectiveness of the L-PSJA at Re_D=$10 \cdot 10^3$ is lowered so that the actuator operation does not produce any significant changes in the velocity deficits at x=$10D$ downstream (Fig. 6.27(d)).

In general, the effectiveness of both these actuators for separation control decrease with increase in Re. Overall, the linear actuator seems to be more promising in cylinder flow separation control than the L-PSJA. The difference in the observed flow is because of the

fundamental difference in the induced flow field of the linear actuator and L-PSJA. While a linear actuator in this arrangement actually accelerates the flow by adding momentum in the downstream direction in the near wall region, the L-PSJA adds momentum by penetrating the mean flow.

6.6 Summary

The characteristics of a plasma synthetic jet actuator in flat plate boundary layer flows were presented in this chapter. In the presence of a free stream, the plasma synthetic jet acts in a manner similar to conventional (mass flux) jets, as seen from the flow field streamwise vorticity contours. Cross-stream measurements reveal that the structure of the round plasma synthetic jet is three dimensional. Both the streamwise and cross-stream jet vorticity concentrations were found to diminish with increasing free stream velocity. The annular construction thus introduces a round jet into the flow field. For applications in plane fluid flows, the linear plasma synthetic jet actuator can be used. The enhanced jet penetration and addition of longitudinal vorticity obtained on using the PSJA expands the range of applicability of linear plasma actuators for flow control. Within the annular and linear plasma synthetic actuator designs, each actuator was observed to affect the flow field in a different manner. The interaction of the linear plasma synthetic jet actuator with a cross flow resulted in the formation of a cross-stream vortex downstream of the plasma region similar to the linear actuator. The annular PSJA was observed to affect the mean flow field, as opposed to the linear PSJA and linear actuators that affect the near-wall flow. The effectiveness of the plasma synthetic jet in penetrating the mean flow was found to decrease with increase in Re. Variations in momentum thicknesses obtained upon actuation suggests that the actuator actively modifies the bulk fluid momentum. In the case of flow over a circular cylinder, the linear actuator geometry was more effective in reducing the wake deficits than the L-PSJA.

The overall physical mechanism of the interaction of a plasma synthetic jet actuator with an external flow is shown by the cartoon in Fig. 6.28. The plasma region presents a strong favorable (suction) pressure gradient to the incoming boundary layer, just upstream of the actuator. This results in fluid being entrained close to the actuator surface, and depending on the level of entrainment, standing cross-stream vortices with rotational sense not opposing the free stream direction can be created. The entrainment level was found to be increased with input power, and therefore, the amount of plasma available. It appears that the side of the starting vortex in the isolated plasma synthetic jet that is nearest

to the free stream is diminished by the incoming flow, as expected. This leads to the generation of positive signed vortices (viz., rotation in the same direction as the incoming flow) downstream of the actuator. Increasing the input power produces major changes in the flow field, such that the quiescent jet structure can actually be preserved even in the presence of a cross flow. The velocity profiles downstream of the actuator show considerable modification from the incoming profiles, such that they peak near the actuator on account of separated "inner region" flow and do not recover back to the incoming values within the extent of the flow field penetrated by the plasma synthetic jet.

6.7 Tables and Figures

Table 6.1: Flat plate experiments; peak velocity of steady jet U_{js}=65 cm/s, peak velocity of 10 Hz pulsed jet U_{jp}=104 cm/s.

Case	U_∞ [cm/s]	Re_L	U_{js}/U_∞	U_{jp}/U_∞
A	85	$9 \cdot 10^3$	0.76	1.22
B	125	$13 \cdot 10^3$	0.52	0.83
C	175	$18 \cdot 10^3$	0.37	0.59

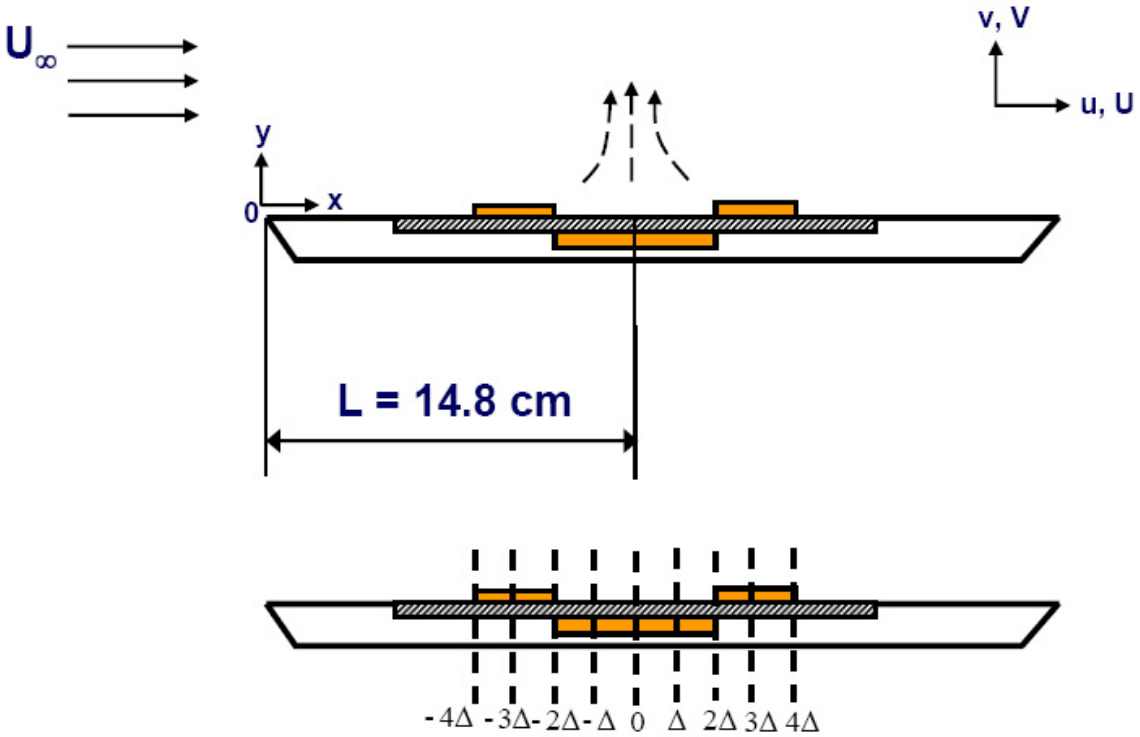

Figure 6.1: Schematic of the flat plate and actuator arrangement. Note that the lines in the lower figure (equally spaced by 0.33 cm, not to scale) indicate the locations of velocity profiles presented in later figures, and Δ=0 corresponds to the actuator center.

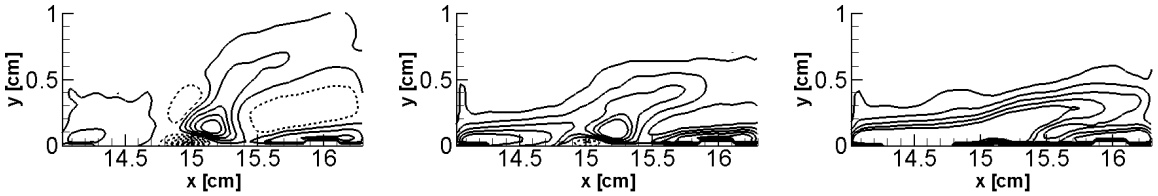

(a) Case A. (b) Case B. (c) Case C.

Figure 6.2: Averaged PIV results showing vorticity contours for steady operation of PSJA in cross flow. Flow direction is from left to right.

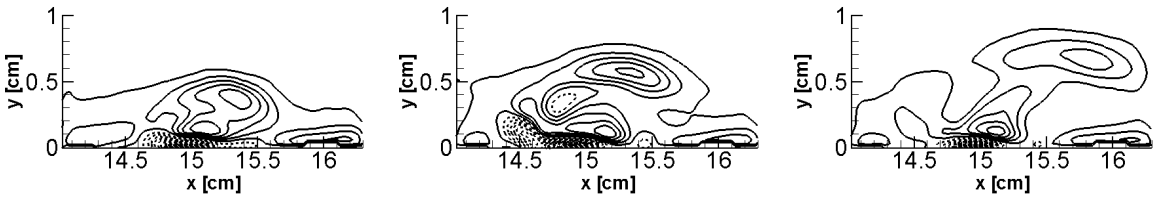

(a) t=18 ms. (b) t=24 ms. (c) t=36 ms.

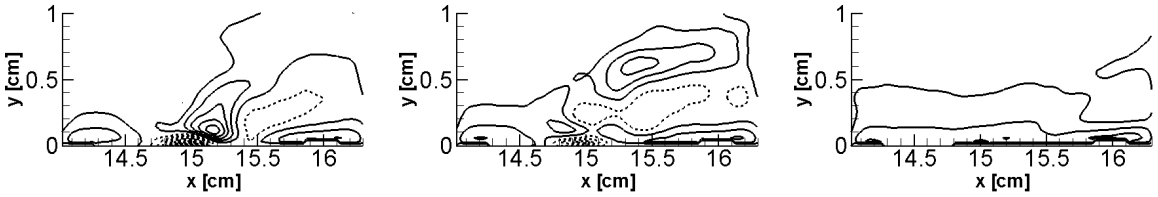

(d) t=48 ms. (e) t=57 ms. (f) t=83 ms.

Figure 6.3: Averaged PIV results showing vorticity contours for PSJA in cross flow case A. Measurements phase-locked to actuator pulsing frequency f_p=10 Hz. Flow direction is from left to right.

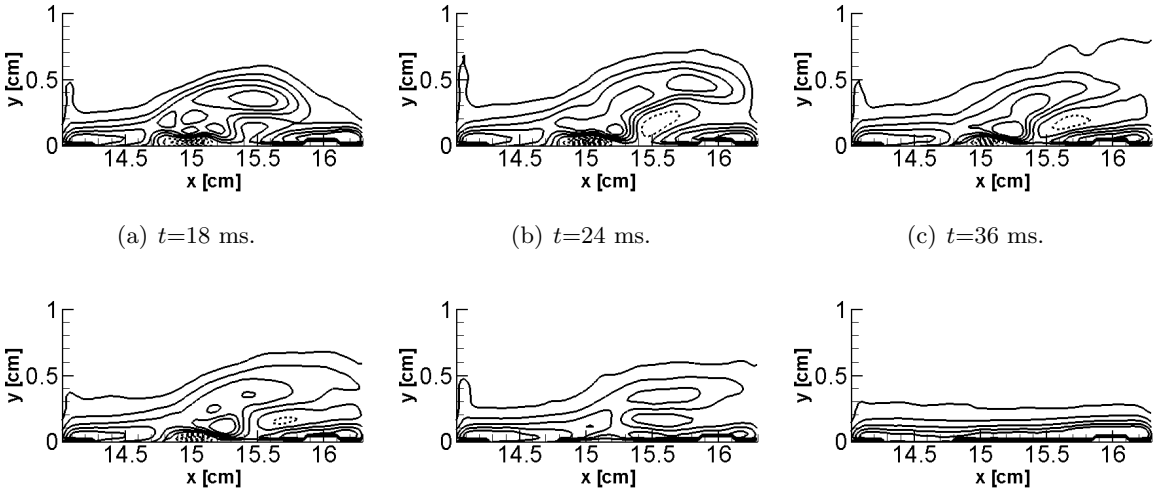

(a) t=18 ms. (b) t=24 ms. (c) t=36 ms.

(d) t=48 ms. (e) t=57 ms. (f) t=83 ms.

Figure 6.4: Averaged PIV results showing vorticity contours for PSJA in cross flow case B. Measurements phase-locked to actuator pulsing frequency f_p=10 Hz. Flow direction is from left to right.

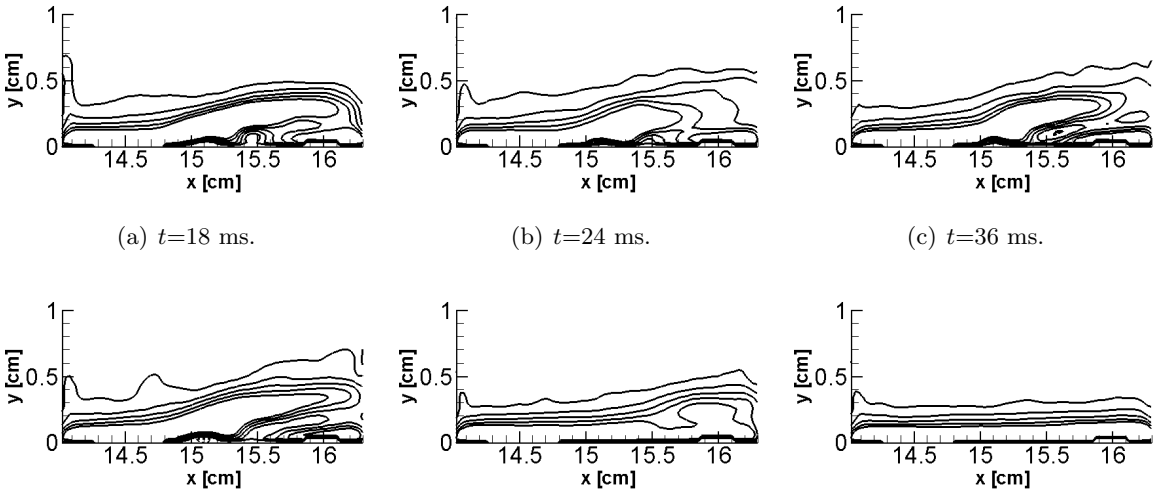

(a) t=18 ms. (b) t=24 ms. (c) t=36 ms.

(d) t=48 ms. (e) t=57 ms. (f) t=83 ms.

Figure 6.5: Averaged PIV results showing vorticity contours for PSJA in cross flow case C. Measurements phase-locked to actuator pulsing frequency f_p=10 Hz. Flow direction is from left to right.

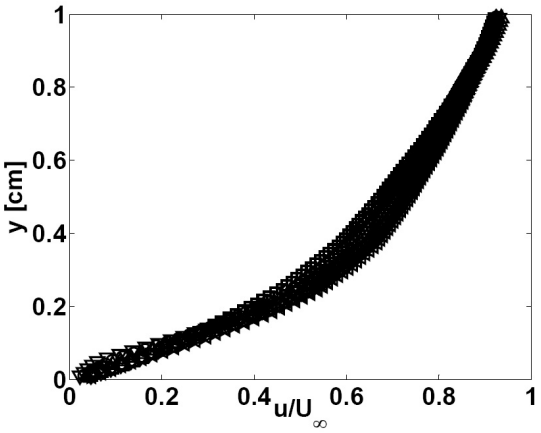

(a) Case A, u/U_∞.

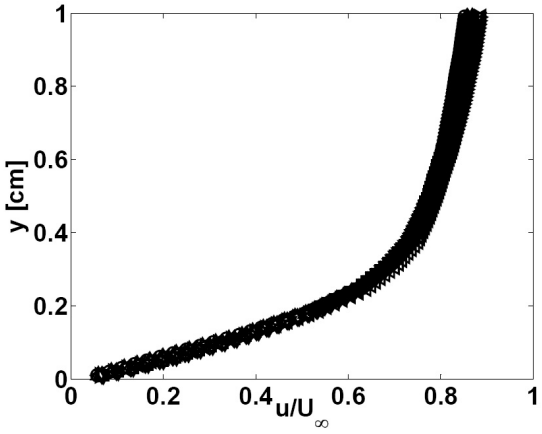

(b) Case B, u/U_∞.

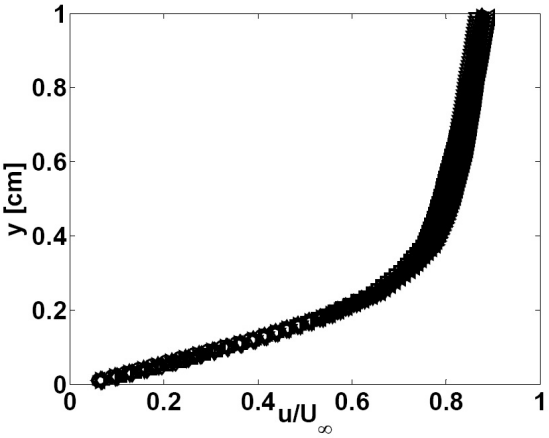

(c) Case C, u/U_∞.

Figure 6.6: Baseline flow (actuator off), mean velocity profiles at different streamwise locations. $\square$, $r = 2\Delta$ upstream; $\diamond$, $r = 1\Delta$ upstream; $\circ$, $r = 0$; $\triangle$, $r = 1\Delta$ downstream; $\triangledown$, $r = 2\Delta$ downstream; $\triangleright$, $r = 3\Delta$ downstream; $\triangleleft$, $r = 4\Delta$ downstream; Δ=3.3 mm; r=0 corresponds to actuator center location x=14.8 cm.

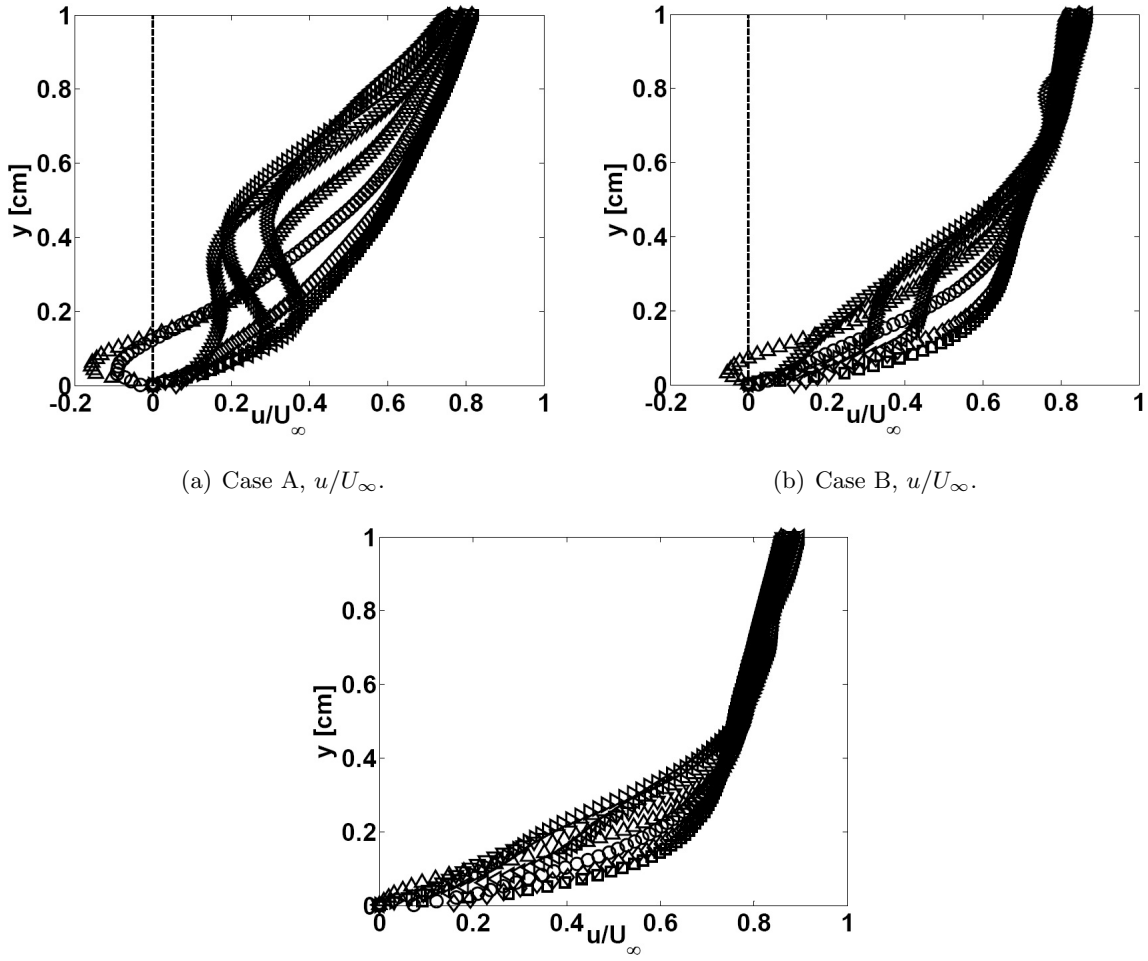

(a) Case A, u/U_∞.

(b) Case B, u/U_∞.

(c) Case C, u/U_∞.

Figure 6.7: Mean velocity profiles for steady operation of the PSJA at different streamwise locations. $\square$, $r = 2\Delta$ upstream; $\diamond$, $r = 1\Delta$ upstream; $\circ$, $r = 0$; $\triangle$, $r = 1\Delta$ downstream; $\triangledown$, $r = 2\Delta$ downstream; $\triangleright$, $r = 3\Delta$ downstream; $\triangleleft$, $r = 4\Delta$ downstream; Δ=3.3 mm; r=0 corresponds to actuator center location x=14.8 cm.

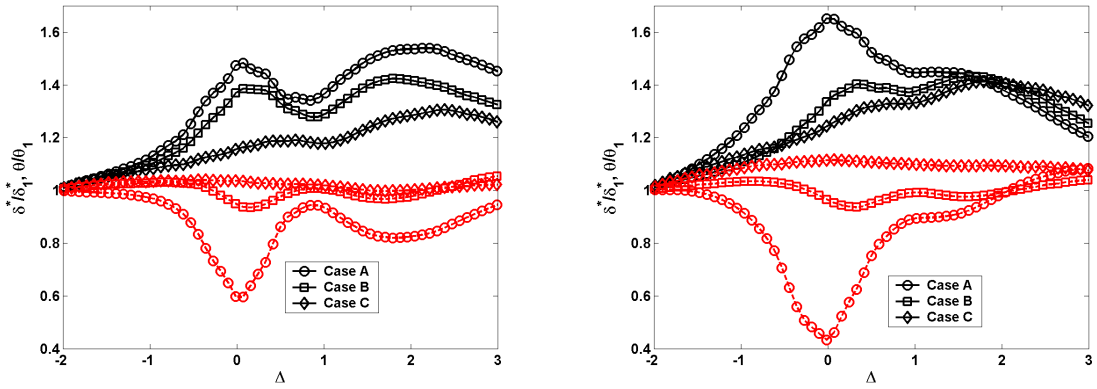

(a) Steady operation.

(b) 10 Hz pulsing.

Figure 6.8: Displacement, δ^* (solid black lines) and momentum, θ (dashed red lines) thicknesses for cases A, B, and C. Δ=3.3 mm, Δ=0 corresponds to PSJA center location at x=14.8 cm. ${\delta_1}^*$ and θ_1 indicates displacement and momentum thickness values respectively, for the first upstream station at -2Δ. Steady operation ${\delta_1}^*$ values are: 0.3226 cm (case A), 0.2190 cm (case B), and 0.1856 cm (case C). Steady operation θ_1 values are: 0.1601 cm (case A), 0.1457 cm (case B), and 0.1326 cm (case C). 10 Hz pulsing ${\delta_1}^*$ values are: 0.2911 cm (case A), 0.2138 cm (case B), and 0.1404 cm (case C). 10 Hz pulsing θ_1 values are: 0.1544 cm (case A), 0.1431 cm (case B), and 0.1079 cm (case C).

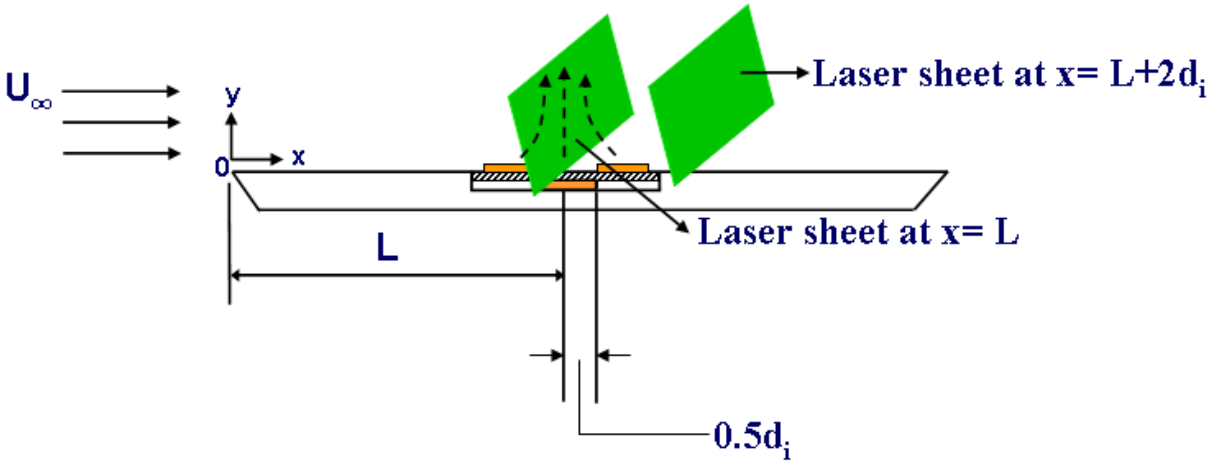

Figure 6.9: Laser sheet locations (in green) showing y-z planes used for conducting cross-stream PIV measurements on the annular PSJA in cross flow.

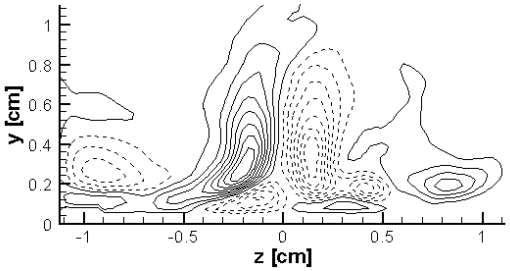

(a) $U_\infty = 85$ cm/s, $x = L$.

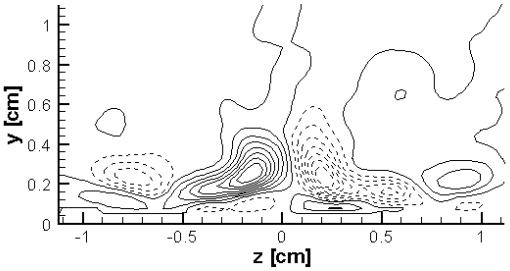

(b) $U_\infty = 125$ cm/s, $x = L$.

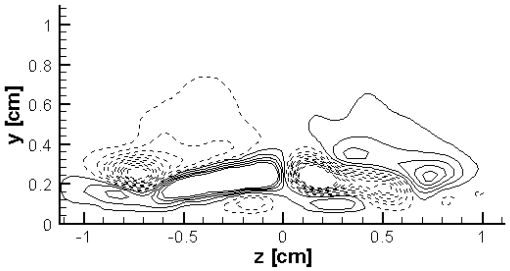

(c) $U_\infty = 175$ cm/s, $x = L$.

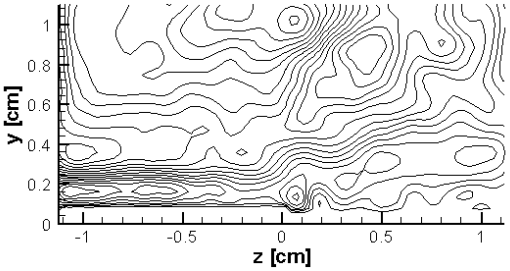

(d) $U_\infty = 85$ cm/s, $x = L + 2d_i$.

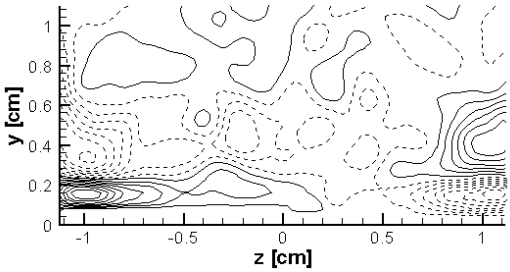

(e) $U_\infty = 125$ cm/s, $x = L + 2d_i$.

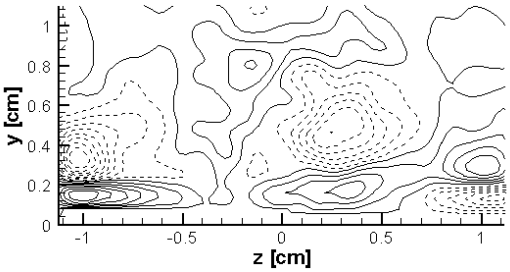

(f) $U_\infty = 175$ cm/s, $x = L + 2d_i$.

Figure 6.10: Averaged PIV results showing vorticity contours for steady operation of the PSJA in cross flow. Cross-stream measurements with actuator mounted on a flat plate; L=14.8 cm, indicates distance of the actuator center from leading edge of the flat plate.

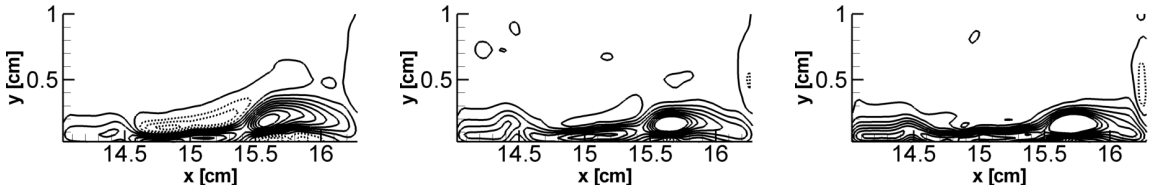

(a) Case A. (b) Case B. (c) Case C.

Figure 6.11: Averaged PIV results showing vorticity contours for steady operation of the linear PSJA in cross flow. Flow direction is from left to right.

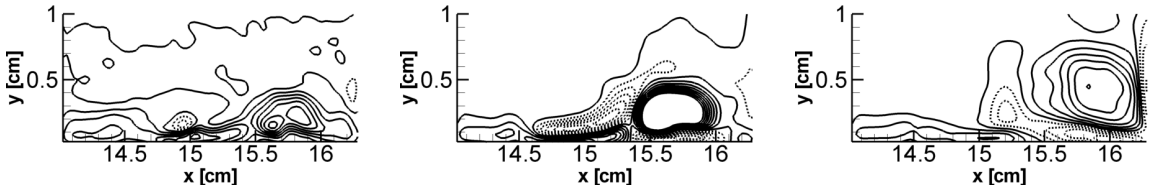

(a) t=18 ms. (b) t=36 ms. (c) t=57 ms.

Figure 6.12: Averaged PIV results showing vorticity contours for linear PSJA in cross flow case A. Measurements phase-locked to actuator pulsing frequency f_p=10 Hz.

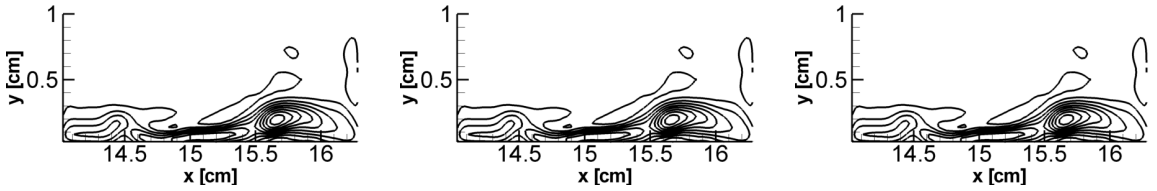

(a) t=18 ms. (b) t=36 ms. (c) t=57 ms.

Figure 6.13: Averaged PIV results showing vorticity contours for linear PSJA in cross flow case B. Measurements phase-locked to actuator pulsing frequency f_p=10 Hz.

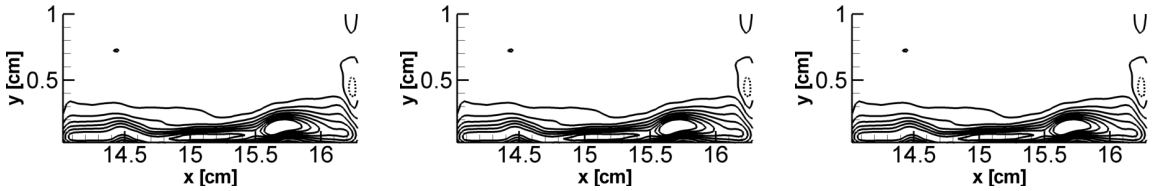

(a) t=18 ms. (b) t=36 ms. (c) t=57 ms.

Figure 6.14: Averaged PIV results showing vorticity contours for linear PSJA in cross flow case C. Measurements phase-locked to actuator pulsing frequency f_p=10 Hz.

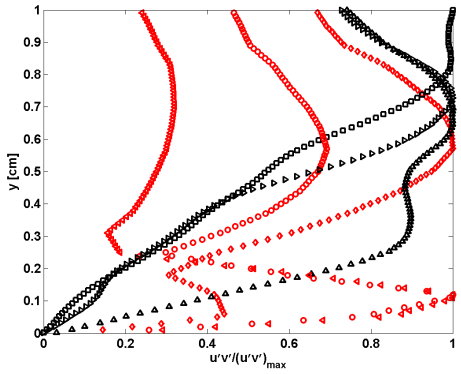

(a) Case A, Annular PSJA.

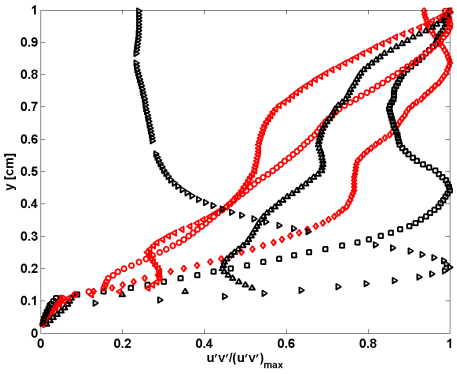

(b) Case A, Linear PSJA.

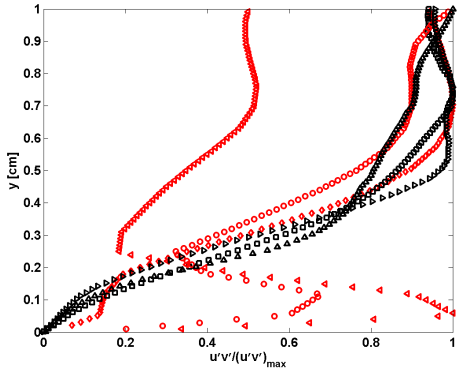

(c) Case B, Annular PSJA.

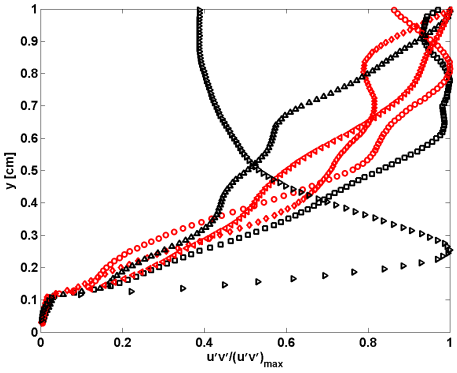

(d) Case B, Linear PSJA.

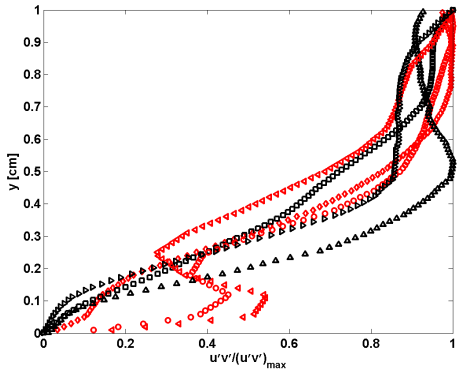

(e) Case C, Annular PSJA.

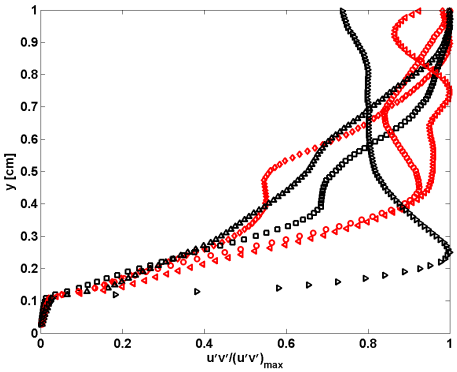

(f) Case C, Linear PSJA.

Figure 6.15: Normalized Reynolds stress cross-stream distribution for baseline case (actuator off) and steady operation. $\diamond$, actuator off (x=14.2 cm); $\square$, steady operation (x=14.2 cm); $\circ$, actuator off (x=14.8 cm, r=0); $\triangle$, steady operation (x=14.8 cm, r=0); $\triangleleft$, actuator off (x=15.4 cm); $\triangleright$, steady operation (x=15.4 cm); color of the data indicates actuation state.

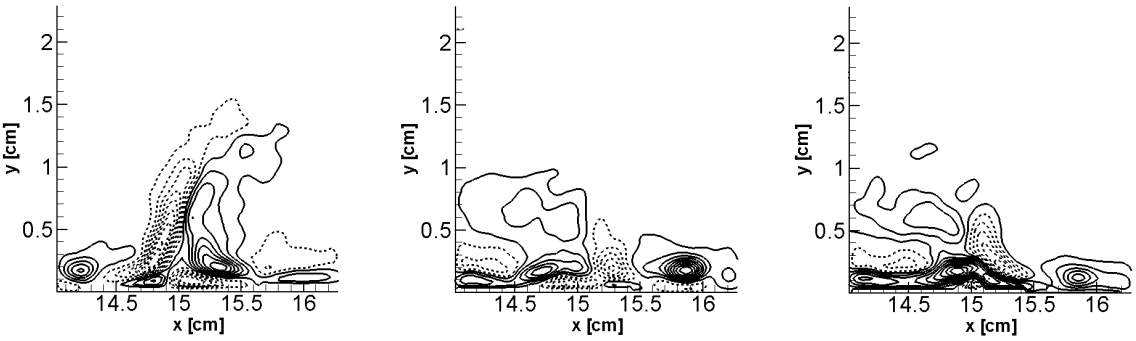

(a) Case A. (b) Case B. (c) Case C.

Figure 6.16: Averaged PIV results showing vorticity contours for steady operation of PSJA in cross flow with increased input power. Flow direction is from left to right.

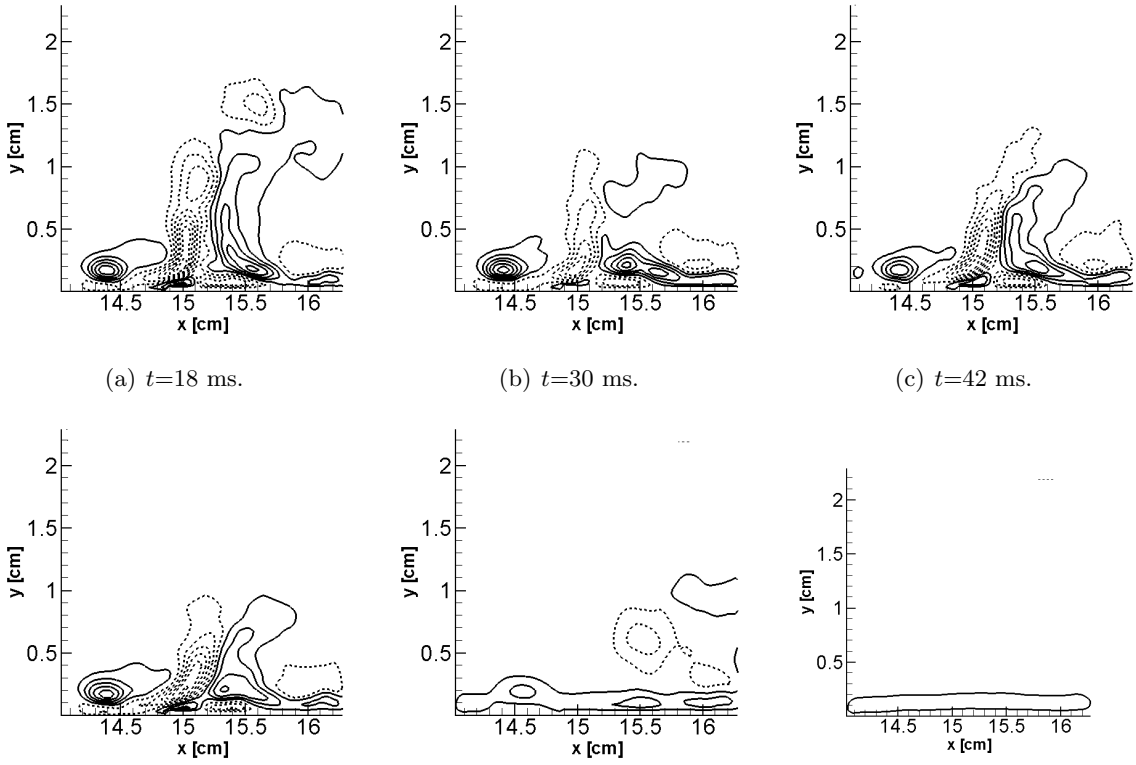

(a) t=18 ms. (b) t=30 ms. (c) t=42 ms.

(d) t=48 ms. (e) t=57 ms. (f) t=83 ms.

Figure 6.17: Averaged PIV results showing vorticity contours for PSJA in cross flow case A with increased input power. Measurements are phase-locked to actuator pulsing frequency f_p=10 Hz.

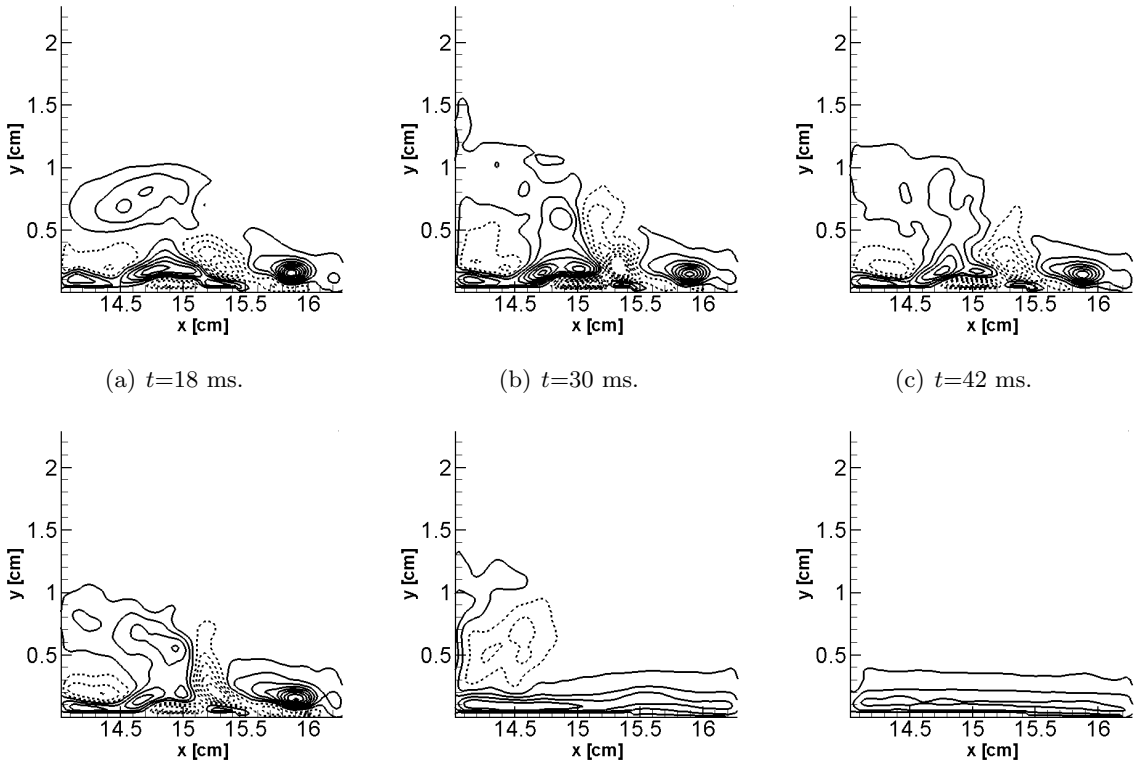

(a) t=18 ms. (b) t=30 ms. (c) t=42 ms.

(d) t=48 ms. (e) t=57 ms. (f) t=83 ms.

Figure 6.18: Averaged PIV results showing vorticity contours for PSJA in cross flow case B with increased input power. Measurements are phase-locked to actuator pulsing frequency f_p=10 Hz.

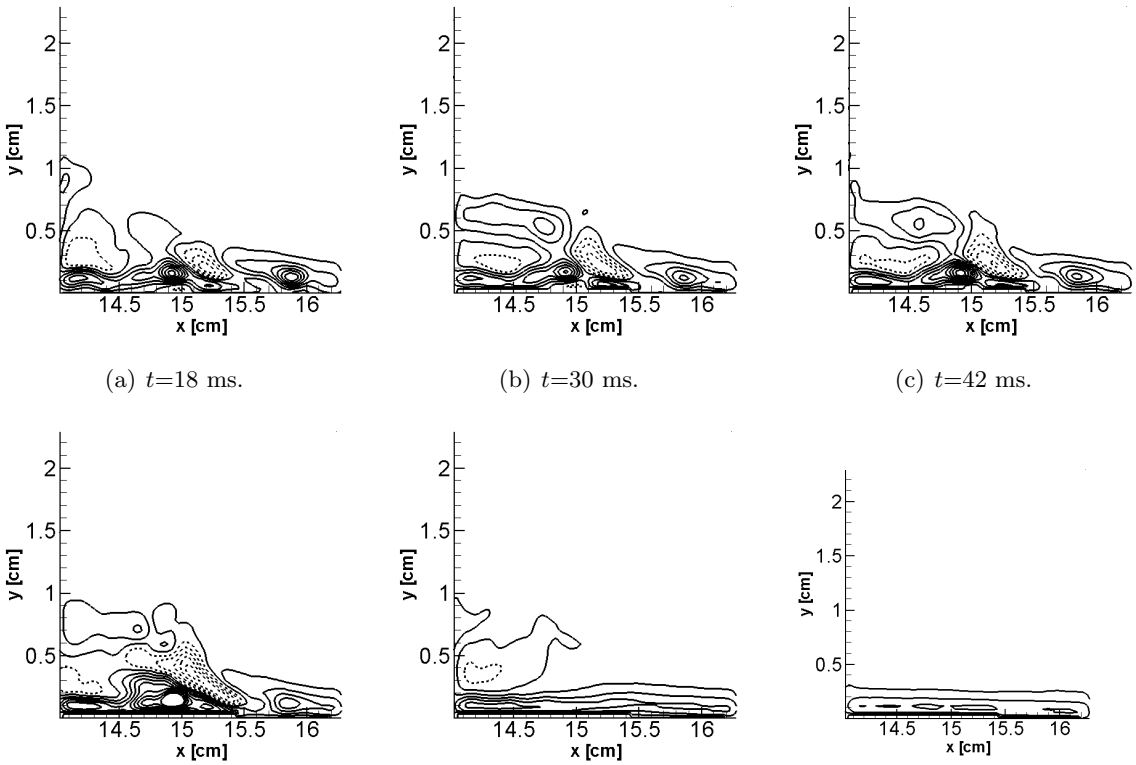

(a) t=18 ms. (b) t=30 ms. (c) t=42 ms.

(d) t=48 ms. (e) t=57 ms. (f) t=83 ms.

Figure 6.19: Averaged PIV results showing vorticity contours for PSJA in cross flow case C with increased input power. Measurements are phase-locked to actuator pulsing frequency f_p=10 Hz.

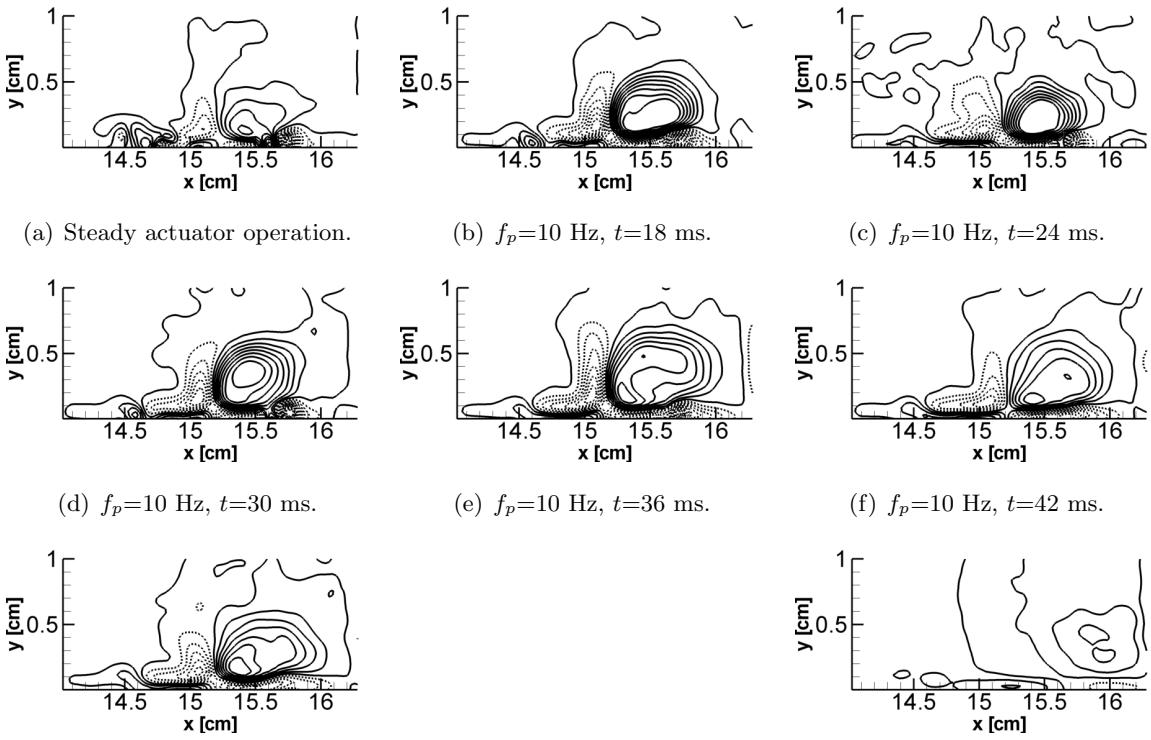

(a) Steady actuator operation.

(b) f_p=10 Hz, t=18 ms.

(c) f_p=10 Hz, t=24 ms.

(d) f_p=10 Hz, t=30 ms.

(e) f_p=10 Hz, t=36 ms.

(f) f_p=10 Hz, t=42 ms.

(g) f_p=10 Hz, t=48 ms.

(h) f_p=10 Hz, t=57 ms.

Figure 6.20: Averaged PIV results showing vorticity contours for the linear PSJA in cross flow case A with increased input power. Flow direction is from left to right.

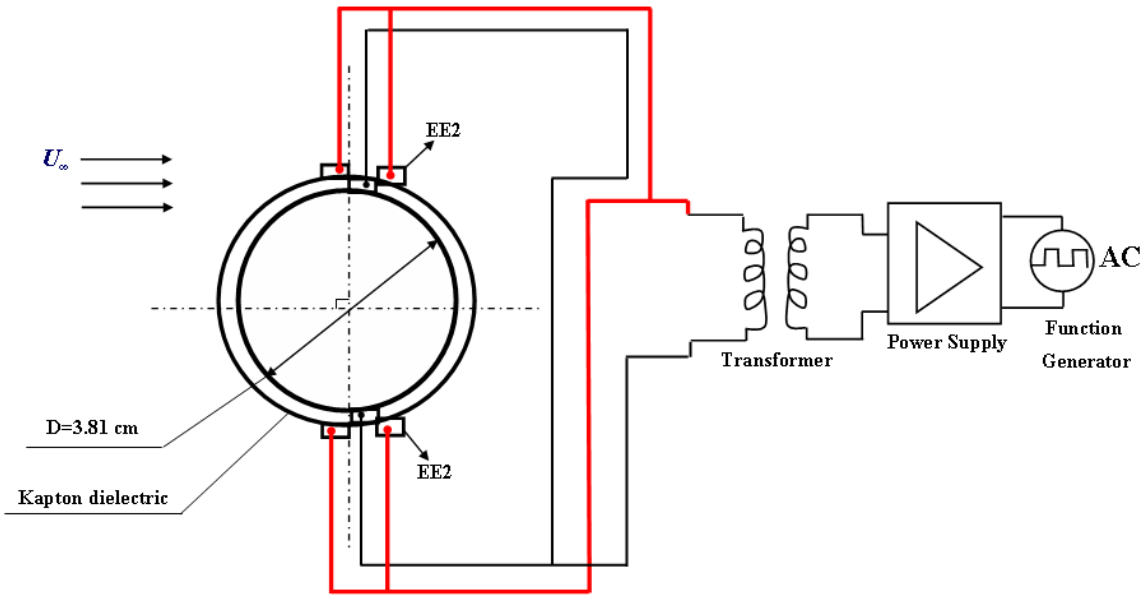

Figure 6.21: Schematic of two L-PSJAs mounted on the circular cylinder at 90° and 270° to the incoming free stream (the arrangement is the same for two linear actuators, with the absence of exposed electrodes EE2). Thicker red lines indicate connections from the exposed electrode, thinner black lines indicate connections from the embedded electrode.

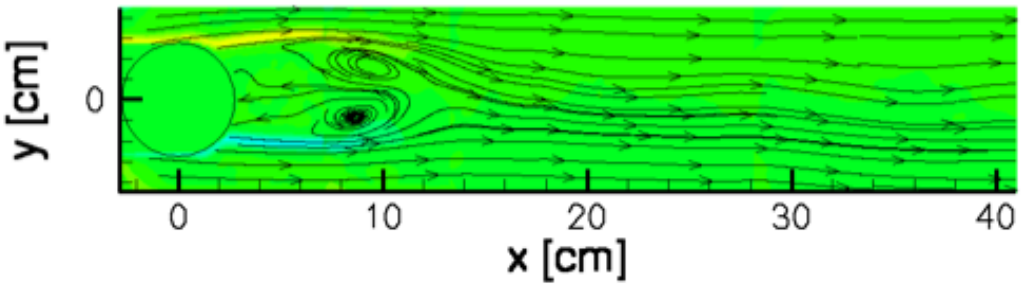

(a) Baseline, actuator off.

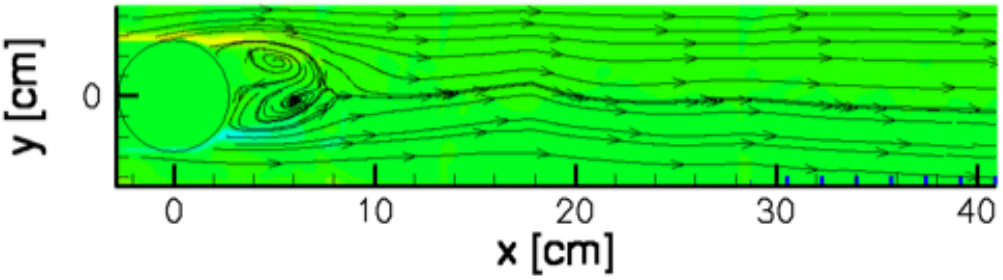

(b) Steady operation.

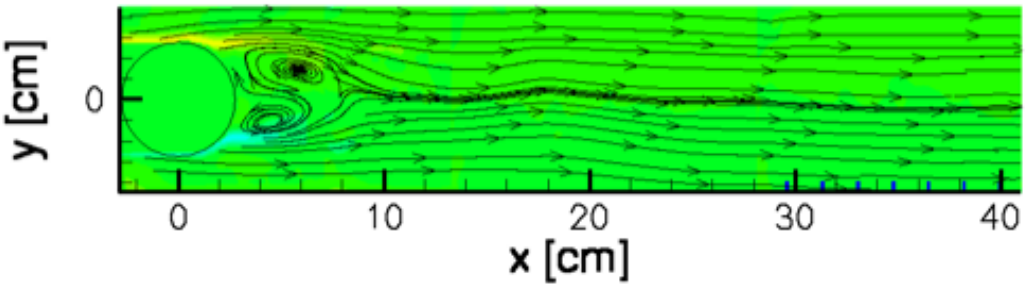

(c) 10 Hz pulsing (f^+=0.2).

Figure 6.22: Averaged PIV results showing vorticity contours overlaid with streamlines for linear actuator mounted on circular cylinder for Re_D=$5 \cdot 10^3$.

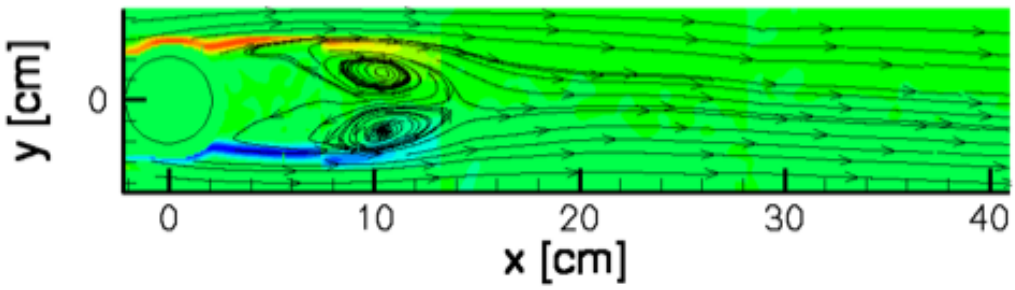

(a) Baseline, actuator off.

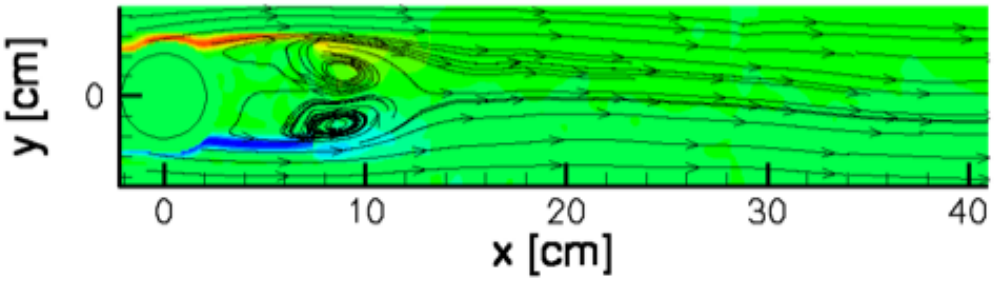

(b) Steady operation.

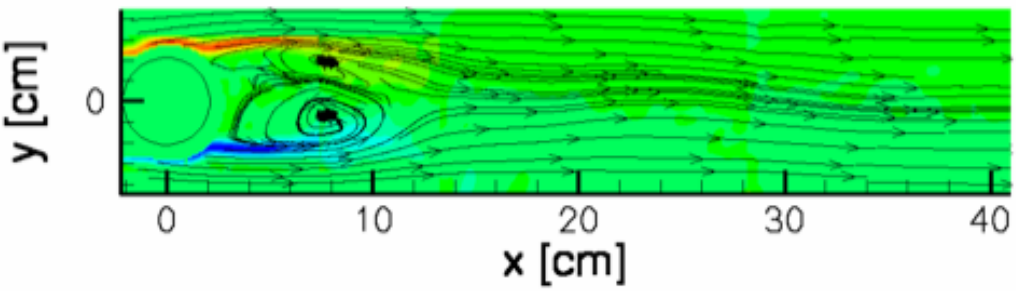

(c) 10 Hz pulsing (f^+=0.2).

Figure 6.23: Averaged PIV results showing vorticity contours overlaid with streamlines for L-PSJA mounted on circular cylinder for Re_D=$5 \cdot 10^3$.

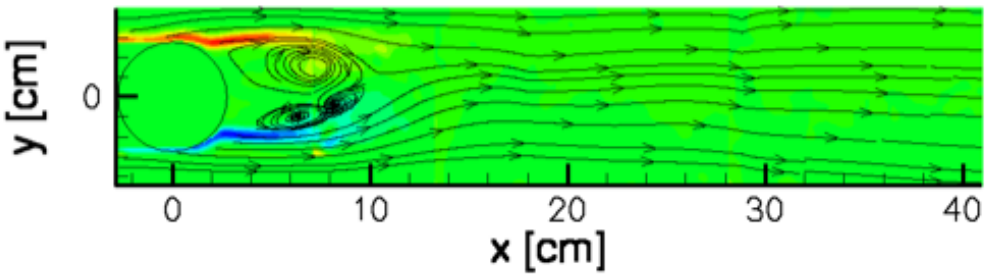

(a) Baseline, actuator off.

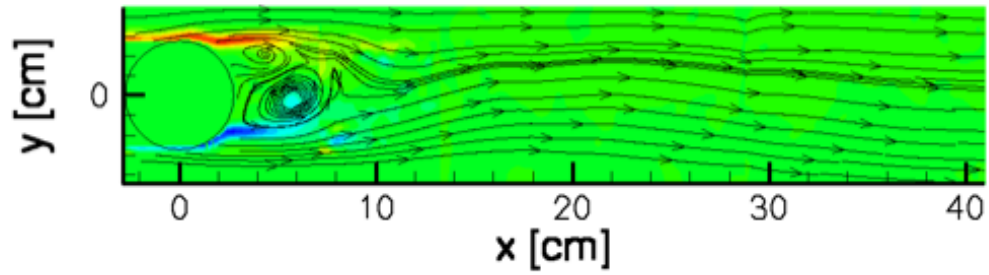

(b) Steady operation.

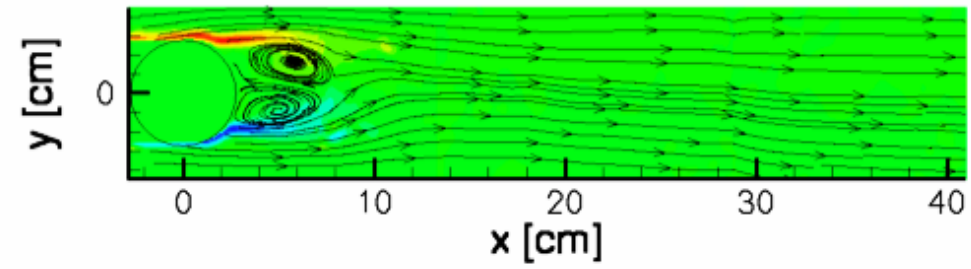

(c) 20 Hz pulsing (f^+=0.2).

Figure 6.24: Averaged PIV results showing vorticity contours overlaid with streamlines for linear actuator mounted on circular cylinder for Re_D=$10 \cdot 10^3$.

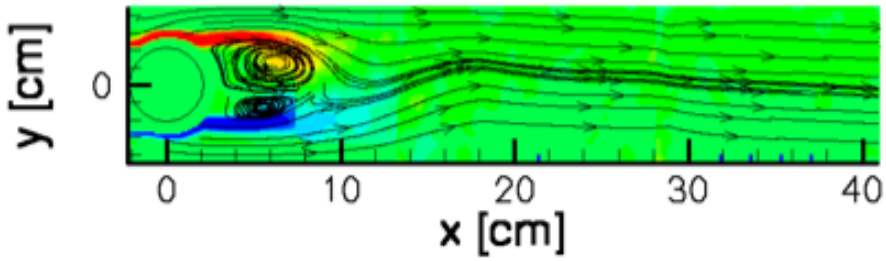

(a) Baseline, actuator off.

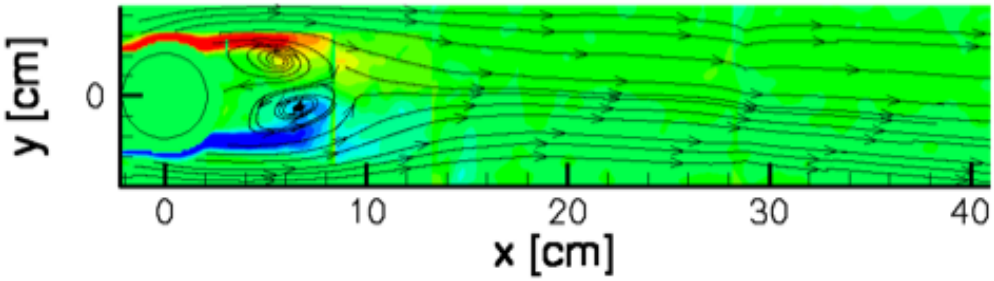

(b) Steady operation.

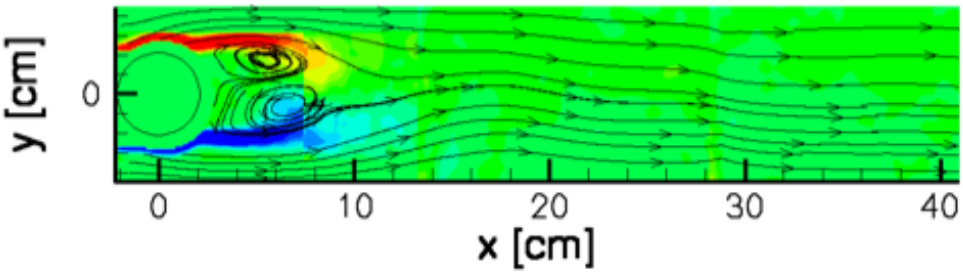

(c) 20 Hz pulsing (f^+=0.2).

Figure 6.25: Averaged PIV results showing vorticity contours overlaid with streamlines for L-PSJA mounted on circular cylinder for Re_D=$10 \cdot 10^3$.

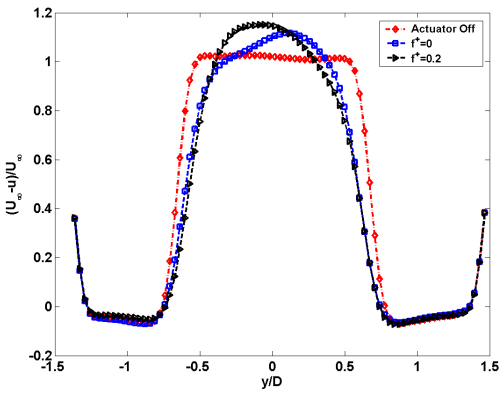

(a) Linear actuator, x=1D downstream.

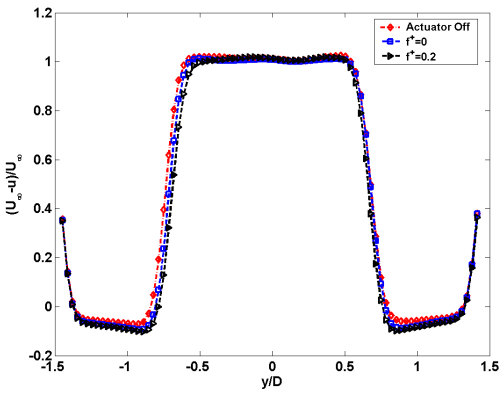

(b) L-PSJA, x=1D downstream.

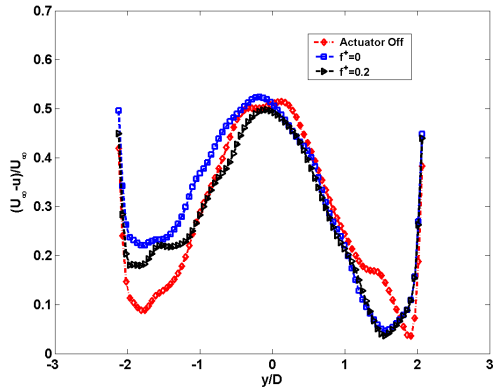

(c) Linear actuator, x=10D downstream.

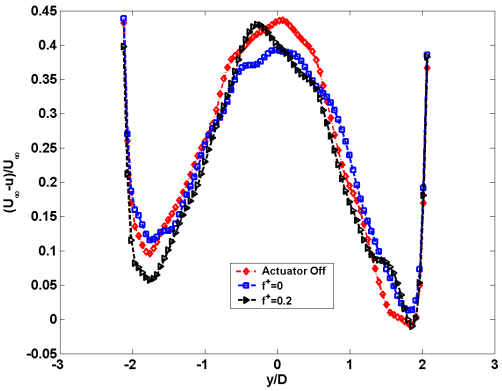

(d) L-PSJA, x=10D downstream.

Figure 6.26: Cross-stream variation of velocity deficits for Re_D=5 · 10^3.

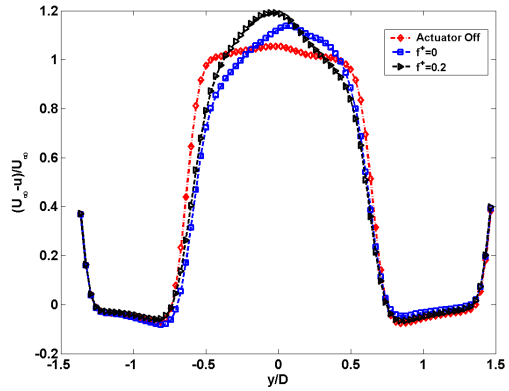

(a) Linear actuator, x=1D downstream.

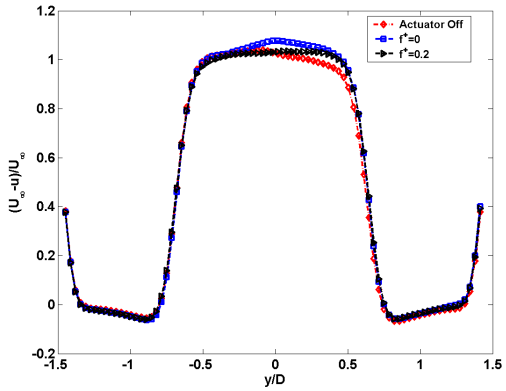

(b) L-PSJA, x=1D downstream.

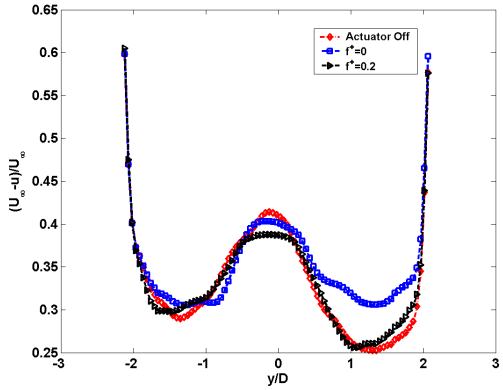

(c) Linear actuator, x=10D downstream.

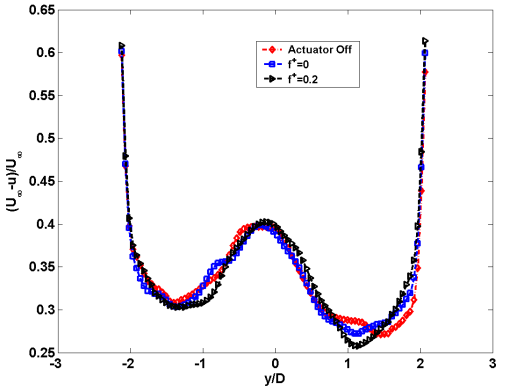

(d) L-PSJA, x=10D downstream.

Figure 6.27: Cross-stream variation of velocity deficits for Re_D=10 · 10^3.

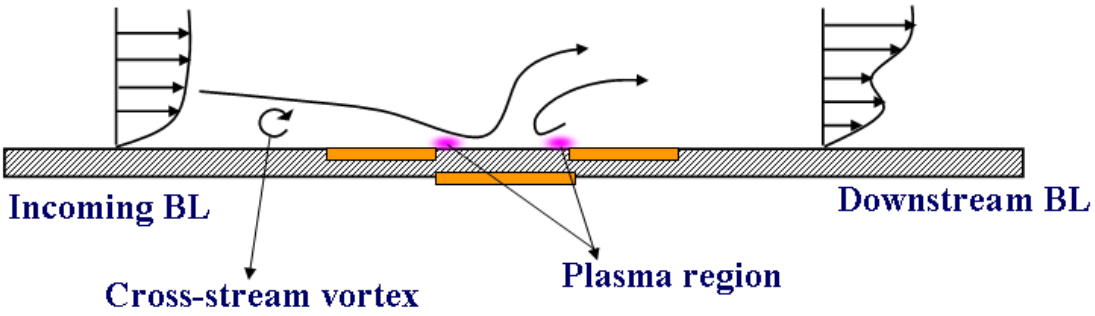

Figure 6.28: Cartoon showing mechanism of PSJA in cross flow.

Chapter 7

EFFECTS OF PLASMA MORPHOLOGY

7.1 Introduction

The question of how the plasma structure affects the resultant flow field characteristics has rarely been addressed in the literature. Enloe *et al.* [84] first observed that the structure of the DBD affects the efficiency of momentum coupling by the actuator, and conducted detailed measurements on the plasma structure [91, 84] and its effects on neutral air density [112], but these efforts do not relate the plasma structure and the bulk flow characteristics in conjunction. In this context, the maximum velocity and streamwise extent of the isolated plasma synthetic jet was observed to be strongly related to the plasma strength [177]. Since the jet is exclusively produced by the plasma, it is desirable to have a stronger plasma for obtaining better performance. To understand how the actuator design is optimized, it would be necessary to simultaneously measure the flow field characteristics as well as the plasma structure. Measurements on the plasma structure can be accomplished using a variety of optical techniques, including photodiodes and CCD sensors. Photodiodes, with their high temporal response, provide a direct link between the power input and plasma. CCD sensors, which were used herein, allow a field measurement of the plasma structure, particularly important for PSJA studies where the actuator geometry may directly affect the plasma structure. Time exposures for a PSJA are shown in Fig. 7.1. Note that as power input is increased, the plasma structure varies significantly. The annular region of plasma starts in the form of a ring with non-uniform streamers at low power inputs. With increasing power, the ring transitions into a thicker disk-like region with more uniform structure. If the power is increased further, the plasma region occupies the entire available surface area of the embedded electrode. The above morphological states were identified to form in an abrupt manner, viz., the plasma structure did not change continuously with input power. Furthermore, the relation between the input power per cycle and plasma morphology appears to be linear, as seen from Fig. 7.2. It must be noted that since the PSJA was operated at 50% duty cycle, only half of the input values in Fig. 7.2 were actually used for actuation. Of particular interest is the limiting case where the plasma ring closes to form a disk of self sustaining plasma. This arrangement can be created by either decreasing the size of the actuator or increasing the power input such that the field lines

converge. It is interesting to note that the extent of the plasma region does not directly translate into increased actuator performance. Preliminary measurements indicate that an optimum PSJA exists somewhere between the initial formation stages and the limiting disk case (Fig. 7.3). Further, the relationship between the different variables in the problem: input power, actuator dimension, pulsing frequency and plasma morphology appears to be highly interdependent. Thus, increased power input alone does not appear to translate into increased momentum addition. Obviously, this has important implications in developing efficient actuators.

The objective of this chapter is to examine the effect of plasma intensity (for fixed actuator dimensions) on: the peak axial velocity and momentum of the jet and the actuator efficiency. For this purpose, PIV based flow field measurements on the isolated jet were coupled with measurements of both power input and plasma structure (obtained in a relative sense from the CCD sensors). The sections below describe the experimental arrangements used for this study, followed by a discussion of the results. The experiments were conducted in quiescent flow for both steady and pulsed operation of the PSJA. The plasma actuator tested consisted of conductive copper annular arrays separated by a 0.025 inch thick alumina ceramic dielectric. The diameters of the exposed (d_o) and embedded (d_i) electrodes were 25.4 mm (1 inch) and 12.7 mm (0.5 inch) respectively, with either no air gap (w=0) or a 1–2 mm overlap. Three pulsing frequencies were examined, differing by $\mathcal{O}(1)$ magnitude: 1 Hz, 10 Hz, and 100 Hz. In quiescent flow conditions, it was observed that the plasma weakened due to seeding material (oil droplets) deposition on the electrodes and the dielectric plate. To include the effects of seeding contamination, two images of the plasma structure were taken before and after every PIV run (Fig. 7.4). Note that buildup of the seeing oil on the actuator results in substantial plasma degradation and hence loss in actuator effectiveness. Filamentary structures are impacted first, which serve as a indicator of contamination. The bulk plasma structure remains relatively constant except in cases of extreme contamination from long or multiple PIV runs. The results presented herein were obtained from the images taken at the end of each PIV run. The following section will describe the plasma intensity curves for three different morphological states (ring, quasi disk, and full disk, Fig. 7.1), and their associated effects on the basic flow field and jet characteristics for the above modes of actuator operation.

7.2 Plasma Structure

To examine the plasma structure and intensity in the PSJA, time exposed images captured by the CCD camera described in the previous section were used. Fig. 7.5 shows one such sample image of the full disk morphology, along with the circular coordinate system and region used for analysis. From any raw CCD image, it is possible to extract a non-dimensional brightness value of each pixel in the entire array. To obtain an idea of the plasma structure, we then employ the observation that this pixel brightness value is directly indicative of the plasma intensity in that particular spatial location in the actuator. Albeit not a dimensional measure, this brightness value can still be used to examine the distribution of plasma intensity in the region of interest in the actuator. If the field of view and exposure settings used to obtain different morphological images are held constant, it is then possible to use this measure to quantitatively compare their non-dimensional plasma intensities *relative* to each other. To remove any external light contribution, the images analyzed herein were captured in a dark environment, where the plasma was the exclusive light emitting source.

Fig. 7.6 shows the radial and circumferential variation of the plasma intensity for the three morphological states obtained for steady operation of the PSJA. The radial coordinate was marched from the actuator center to just outside the plasma region ($r_{max} \approx$ 7 mm). The circumferential (azimuthal) coordinate was swept from 0° to 360° starting from the first quadrant (Fig. 7.5). The radial variation of plasma intensity is similar for all morphologies, with the actuator center registering the lowest value of intensity. After, it increases nonlinearly with radius, reaching a maximum at the actuator circumference (r=6.35 mm), after which it drops back to reference values for distances beyond. As expected, the ring and quasi disk states show very low intensities (due to absence of plasma) near the actuator center. The plasma region starts around r=3 mm for the ring state (Fig. 7.6(a)) and around r=2 mm for the quasi disk (Fig. 7.6(b)), while it starts at the actuator center for the full disk. At any radial location, the circumferential variation of plasma intensity is highly non-uniform for the ring and quasi disk morphologies, while it is nearly uniform for the full disk. The irregularities in the circumferential variation of intensity are highest at the actuator circumference for the ring and quasi disk.

Fig. 7.7 shows the radial variation of median relative plasma intensity, with the error bars indicating circumferential deviation. The intensities for different morphologies are compared for each mode of actuator operation. The trend of radial intensity variation is similar for all morphologies, with the full disk having the highest intensity, followed by the

quasi disk and the ring states. Also, the peak values occur very near the actuator circumference, and this location is the same for all states and modes of actuator operation. The full disk peak intensities are nearly the same across steady and pulsed operation of the actuator. The quasi disk state shows the highest intensity for 100 Hz pulsed operation, followed by 1 Hz and 10 Hz pulsing, and is lowest for steady operation. It is interesting to note that, compared to steady operation, unsteady actuation (especially at f_p=100 Hz) shows increased area of the quasi disk plasma region. The ring state shows increased intensity for both steady and 100 Hz pulsed operation. It is expected that the jet characteristics would be directly related to the plasma intensity. By using the maximum variation over the circumference, it is seen that the maximum value of intensity occurs near the actuator circumference for all three cases. For unsteady operation, near the actuator circumference, the maximum intensities of the quasi disk coincide with the full disk values. The peak intensities of the ring state for 100 Hz pulsing are very close to the full disk. The median values of intensity show the same trend as the average and maximum values presented in earlier figures. The cases with unsteady actuator operation show greater circumferential deviation than the steady actuation case. This is possibly due to the variability in plasma formation and quenching for pulsed operation of the actuator.

On the issue of seeding material weakening the plasma structure, Fig. 7.8 shows the radial variation of median relative plasma intensity before and after a representative PIV run, with the error bars indicating circumferential deviation. The maximum intensity value is decreased as a result of seeding deposition on the actuator. However, the trend of radial variation is unaffected, such that the profiles before and after a PIV run are merely offset from each other. It is important to note that this weakening occurs only after long term actuator use within the confines of the enclosure seeded with oil droplets, and no observable degradation in the plasma structure was observed if the actuator surface was cleaned between consecutive PIV runs.

7.3 Basic Flow Field

Figs. 7.9–7.10 show contours of spanwise vorticity obtained from time-averaged PIV results for both steady and pulsed operation of the PSJA. The vorticity values were normalized with the respective maximum values such that: $\omega_z{}^*=\omega/\omega_{max}$. Dashed lines indicate contours of negative vorticity. Within each figure, the effect of variation in plasma morphology is compared. For steady operation of the actuator (Fig. 7.9), the starting vortex has clearly advected out of the window of observation, and a steady jet is observed for all mor-

phologies. The full disk shows higher vorticity levels within the near field of the actuator, indicating stronger entrainment of the near wall fluid by the plasma. The starting width of the jet (at $x \leq 10$ mm) is highest for the ring state compared to the other morphologies. It is interesting to note the increase in spreading of the jet at distances greater x=20 mm as we progress from the ring to full disk states. Both secondary and tertiary vortical structures are seen for all three states, and are relatively unchanged in their spatial location. Pulsing the actuator at a frequency of 10 Hz results in increasing the jet width (Fig. 7.10) as compared to steady operation. The width of the jet near the actuator decreases as we progress from ring to full disk states, similar to that seen for steady operation. Farther downstream, the jet width is increased for the the quasi and full disk morphologies. Also, the remnants of the vortex rings generated in the previous cycle are seen in the flow field for these two morphologies. For the ring morphology, pulsing results in increased vorticity levels far downstream of the actuator (at x=40 mm, Fig. 7.10(a)) than the equivalent case in the steady jet (Fig. 7.9(a)).

As the vorticity contours presented in Fig. 7.10 were time-averaged over the actuation cycle, specific details on the starting vortex are not clear. In order to understand the effect of morphology on starting vortex formation and evolution, PIV measurements were conducted phase-locked to the actuator pulsing frequency, and the contours of normalized spanwise vorticity are shown in Figs. 7.11–7.14. The results for two pulsing frequencies (1 Hz and 10 Hz) and two morphological states (quasi and full disk) are presented. In each figure, the evolution of the jet along three times in the actuator duty cycle (24 ms, 36 ms and 48 ms) are shown. Note that for 10 Hz pulsing, t=48 ms corresponds to the end of the actuation cycle. For both pulsing frequencies, the starting vortex ring is highly unsteady for the quasi disk morphology, and in general show downstream motion with increasing time. At t=24 ms, the 10 Hz pulsing case shows more downstream motion and larger size of starting vortices (Fig. 7.12(a)) as compared to that seen for 1 Hz pulsing (Fig. 7.11(a)). With increase in time from 24 ms to 36 ms for 1 Hz pulsed PSJA operation, the starting vortex from the previous cycle is seen along with the new incarnation emanating from the plasma region, as evidenced from the dual lobed vorticity contours (Fig. 7.11(b)). The position of the starting vortex for the 10 Hz, quasi disk operation of the actuator at 36 ms (Fig. 7.12(b)) is upstream of the vortex location in the equivalent 1 Hz case, and the previous cycle vortex incarnation is also not seen in the field of view, on account of shorter times of advection at 10 Hz. For quasi disk operation at t=48 ms, the flow field for 1 Hz and 10 Hz pulsed operation appear very similar.

For both pulsing frequencies, a change in the plasma morphology from the quasi disk

to full disk structure affects the flow field considerably, and results in an increase in the streamwise extent of the jet, even for times very near the start of the actuation cycle (Figs. 7.13(a) and 7.14(a)). Also, for both frequencies, two well demarcated lobes in the contours are seen, indicating that the rate of vortex generation by the plasma has changed from that seen in the quasi disk operation. This suggests that the plasma morphology affects the time scale of PSJA vortex ring formation. The 1 Hz and 10 Hz flow fields appear similar in the full disk state. For 1 Hz pulsing, the starting vortex pinch off from the jet body is clearly seen with increasing time (Fig. 7.13). The pinch off process is faster for pulsed operation at a higher frequency of 10 Hz, as expected (Fig. 7.14). The extent of streamwise vorticity increases with increase in time for 1 Hz case (Fig. 7.13), while it stays nearly a constant for the 10 Hz pulsing (Fig. 7.14).

Overall, the plasma ring morphology is seen to produce lower vorticity concentrations compared to the quasi and full disk states. For the ring morphology, the starting width of the synthetic jet is larger because fluid entrainment occurs only around the circumference of the embedded electrode circle. In case of the quasi and full disk plasma morphologies, however, fluid is entrained over a larger surface area, and consequently the initial jet width is smaller. The downstream jet width would have to increase for the quasi and full disk states in order to compensate for the larger mass of fluid pulled in by the plasma, as compared to the ring morphology. These suggest that for a constant embedded electrode diameter (which is the maximum available region for plasma expansion [201]), the fluid entrainment by the actuator is primarily affected by the amount of plasma that is present during its operation. Increasing the amount of plasma by increasing the input power not only results in increasing the streamwise extent of the jet, but also affects the generation and interaction of vortex rings, which in turn has been shown to influence the resultant jet characteristics substantially [177]. Therefore, it is expected that the full disk configuration would result in increased jet performance characteristics.

7.4 Jet Characteristics

Fig. 7.15 shows the cross-stream distribution of mean axial velocity normalized with local maximum mean axial velocity for steady operation of the PSJA. The jet reaches self similarity very close to the actuator ($x \geq 1r_i$, where r_i is the radius of the embedded electrode) for the ring morphology, as seen in Fig. 7.15(a). The entrainment of fluid by the plasma occurs at distances lesser than $0.5r_i$ from the actuator. As this morphology has the weakest plasma strength, it is expected that the quasi and full disk plasma synthetic jet

will also reach self similarity, albeit at different downstream distances. An examination of the velocity profiles very near the actuator surface (at x=0.25d_i, Fig. 7.15(b)) shows that changing plasma morphology affects the fluid entrainment and jet width. The full disk plasma, while with the most entrainment, has the lowest jet width compared to the quasi disk and ring morphologies, supporting the observations made on the vorticity contours presented in the previous section.

Fig. 7.16 shows the effect of plasma morphology on the cross-stream distribution of dimensional mean axial velocity at a distance of 0.5d_i downstream of the actuator, for both steady and pulsed operation at frequencies 1 Hz, 10 Hz and 100 Hz. It must be noted that these velocity profiles and the results presented hereon were derived entirely from time-averaged PIV measurements. In all the different cases of actuator operation, the full disk morphology produces the highest jet velocity, followed by the quasi disk and the ring morphologies. The maximum jet velocity is therefore directly related to the extent of plasma in the actuator. Steady operation of the PSJA with the full disk plasma results in a peak jet axial velocity of around 225 cm/s (Fig. 7.16(a)), which is a substantial increase from the respective peak values of quasi disk and ring morphologies. The peak axial velocity obtained for pulsed actuator operation at any frequency is lesser than that obtained for steady operation. As the results are averaged over the actuator cycle, the peak values seen in Fig. 7.16 actually correspond to maximum time-averaged velocity $\overline{u}_{max}$, and not the time-average of maximum velocity $\overline{u_{max}}$. The latter values are higher for pulsed actuator operation over steady operation, and have reported in other articles [177, 202]. For the full disk morphology, steady actuator operation results in a wider jet as compared to unsteady pulsing. The jet width for the quasi disk and ring morphologies are nearly the same across all modes of actuator operation. For 100 Hz pulsing, it is interesting to note that the ring morphology reaches a peak value nearly the same as quasi disk (Fig. 7.16(d)), greater than the peaks obtained for this morphology for any other case. Despite the weak plasma strength of the ring morphology itself, it is thought that this increase in performance is tied to the faster forcing of the synthetic jet at 100 Hz, which introduces the most unsteadiness into the fluid. Also, an examination of the relative plasma intensity curves for the ring morphology (Fig. 7.7) show that for this set of experiments, the 100 Hz pulsed operation had the highest plasma intensity as compared to the other modes of actuator operation. These differences are only marginal, suggesting that the jet characteristics are highly sensitive to the plasma strength maintained during the actuator operation. Comparing the profiles for steady operation at different distances downstream (Fig. 7.15(b) and 7.16(a)), it is seen that fluid entrainment decreases with increasing distance from the actuator, as expected. The

axial component of the suction velocity of fluid entrained by the plasma at $0.5d_i$ downstream (Fig. 7.16) is in the 15 cm/s range for all modes of actuator operation. The profiles for the quasi disk show some asymmetry about the jet centerline, and since this is observed for both both steady and pulsed operation, it is suspected that this plasma morphology contributes to jet wandering.

Figs. 7.17–7.19 show the streamwise distribution of local maximum mean axial velocity and fluid impulse for the different plasma morphological states. The fluid impulseis essentially the rate of change of momentum of the jet, viz., the hydrodynamic force imparted by the plasma synthetic jet on the quiescent fluid. The different modes of actuator operation (steady and pulsed) are compared within each figure. In general, it is seen that the output velocity and impulse are the highest for full disk plasma, followed by the quasi disk and ring morphologies. The maximum axial velocity obtained occurs at $0.5d_i$ downstream of the actuator, regardless of the plasma morphology and the operational mode. The streamwise location of the maximum impulse is, however, affected by both the pulsing frequency and plasma morphology. For the ring plasma state, pulsing the actuator at 100 Hz increases the jet outputs by several times of those obtained from other modes of operation (Fig. 7.17), for reasons of increased plasma intensity for this case (discussed above in the observations made on Fig. 7.16(d)). On account of jet spreading, the jet impulse and axial velocity for 100 Hz pulsing show opposite behavior with increasing downstream distance, with the former increasing and the latter decreasing respectively, both in an almost linear manner. The multiple small scale peaks in the impulse curves indicate the locations of the primary vortices shed in the flow field. The peak impulse value for the ring morphology (at 100 Hz pulsing) is almost comparable to the corresponding value for the quasi disk case (Fig. 7.18(b)). Comparing the different plasma states, it is interesting to observe that there exists no unique choice of actuator pulsing frequency to maximize jet outputs. However, for a particular plasma morphology, there is a unique operational mode (such as f_p=100 Hz for the plasma ring) that produces maximum jet outputs. This suggests that in order to optimize the actuator design for maximum resultant jet velocity and momentum, the plasma intensity is the more critical factor. It is important to note that this observation does not in itself consider variation in actuator dimensions, and this has been discussed elsewhere [201].

An examination of the streamwise profiles of the jet impulse for the quasi and full disk morphologies (Figs. 7.18(b) and 7.19(b)) show that these plasma structures induce more unsteadiness in the pulsed jet compared to the ring morphology (Fig. 7.17(b)). This is indicated by the bumpy nature of the impulse curves for these cases, and it is suspected that

the plasma structure for these states also affects the rate of vortex ring generation, in addition to the pulsing frequency. With the exception of 100 Hz pulsing, the ring morphology impulse curves show very low values of impulse at x=3.5d_i, implying reduced streamwise extent of the jet for this case, as compared to the quasi and full plasma disk states. Note that for the morphology with the weakest plasma strength, the 100 Hz pulsing had the highest plasma intensity (see Fig. 7.7) compared to the other modes of operation. Thus it is not the actuator operation mode, but actually the plasma strength, that directly affects the streamwise extent of the jet. For steady operation of the actuator, the peak jet velocity and momentum, as well as its streamwise extent, seem to be directly proportional to the intensity and extent of the plasma region. For unsteady operation, the relation between pulsing frequency and plasma morphology is not clear.

7.5 Actuator Performance

While it is clearly seen from the above discussion that the full disk plasma adds the most momentum to the fluid, it is desirable to see whether it is the most efficient morphology in terms of actuator output. The efficiency η of the actuator in injecting momentum into the quiescent fluid through the plasma synthetic jet can be calculated as the ratio of mechanical energy output of the jet to the electrical energy input to the actuator:

$$\eta = \frac{E_{out}}{E_{in}}.$$

The input electrical energy to the actuator can be calculated as the product of electrical power input (see Fig. 7.2) and the period of the actuator cycle T_{act}:

$$E_{in} = P_{in} \times T_{act},$$

where T_{act} can be calculated as the inverse of the input AC frequency f_{AC}. The output energy imparted by the jet to the residual fluid can be given by the product of the average hydrodynamic force F and the characteristic length scale of the actuator (that affects the actuator output). Since the plasma is solely responsible for creating the jet, the embedded electrode diameter d_i (which limits the maximum extent of plasma) is the appropriate length scale for the PSJA. Therefore, we have the following expression for actuator efficiency,

$$\eta = \frac{F \cdot d_i \cdot f_{AC}}{P_{in}} \tag{7.1}$$

Fig. 7.20 shows the effect of variation of plasma morphology (shown in terms of input electrical power, values the same as Fig. 7.2) on normalized actuator performance characteristics. Both steady and pulsed actuator operation are presented in each figure, and the

maximum values of the characteristics for any particular operating mode was used to normalize the respective curves. While the values of hydrodynamic force F used in Fig. 7.20(a) were calculated by averaging the corresponding impulse values in the streamwise curves presented in Figs. 7.17–7.19, the efficiency was calculated using equation 7.1. The error bars indicate deviation of the streamwise impulse used in calculation of F and η. The maximum value of hydrodynamic force imparted by the synthetic jet is obtained for the full disk morphology, irrespective of the mode of actuator operation. This is followed by the quasi disk, while the ring morphology shows little variation of force (except 100 Hz pulsing, for reasons of increased plasma intensity discussed above) for steady or pulsed operation. Also, pulsed operation of the actuator at any frequency produces greater force than steady operation. For the quasi disk morphology, an increase in the pulsing frequency from 1 Hz to 10 Hz nearly doubles the force value, after which the force for 100 Hz pulsing drops lower than the 1 Hz case.

The highest actuator efficiency is obtained for full disk plasma (Fig. 7.20(b)), with the exception of 100 Hz pulsed operation, where the ring morphology produces the highest efficiency. The increase in performance at 100 Hz pulsing is related to the increased plasma intensity for this case compared to other modes of operation. Similar to the hydrodynamic force, pulsed operation of the actuator at any frequency renders better actuator performance than steady operation. For steady operation, there is almost an order of magnitude performance improvement when we progress from the quasi disk to full disk plasma states. The difference in efficiencies between the quasi and full disk states drops with increase in pulsing frequency. It is interesting to note that the efficiency curves show an increase in performance starting from steady actuator operation to 1 Hz pulsing and thereafter to 10 Hz pulsing, and this change appears to be oscillatory about the full disk maximum value. Thus, it is seen that for the particular actuator design investigated herein, the performance efficiency is affected by both the plasma morphology and pulsing frequency. The full disk plasma morphology with the largest intensity and extent of plasma produces the highest performance efficiencies for steady and pulsed operation at frequencies 1 Hz and 10 Hz.

7.6 Summary

This chapter presented an investigation on the effects of plasma morphology on the quiescent characteristics of the vertical jet created by an annular plasma synthetic jet actuator (PSJA) for both steady and pulsed modes of operation. Time-averaged PIV measurements on the actuator flow field were related in conjunction with details on the plasma structure

and intensity obtained from CCD sensors. Increasing the region of plasma, in addition to increasing the near wall fluid entrainment, also appeared to affect the rate of vortex ring generation by the actuator. The output velocity, momentum and streamwise extent of the jet were found to increase with plasma intensity and extent. For any plasma morphology, the actuator efficiency was observed to be higher for pulsed operation as compared to steady operation. The actuator efficiency was found to be affected by a combination of the plasma morphology and pulsing frequency, with the former being the more critical factor.

7.7 Tables and Figures

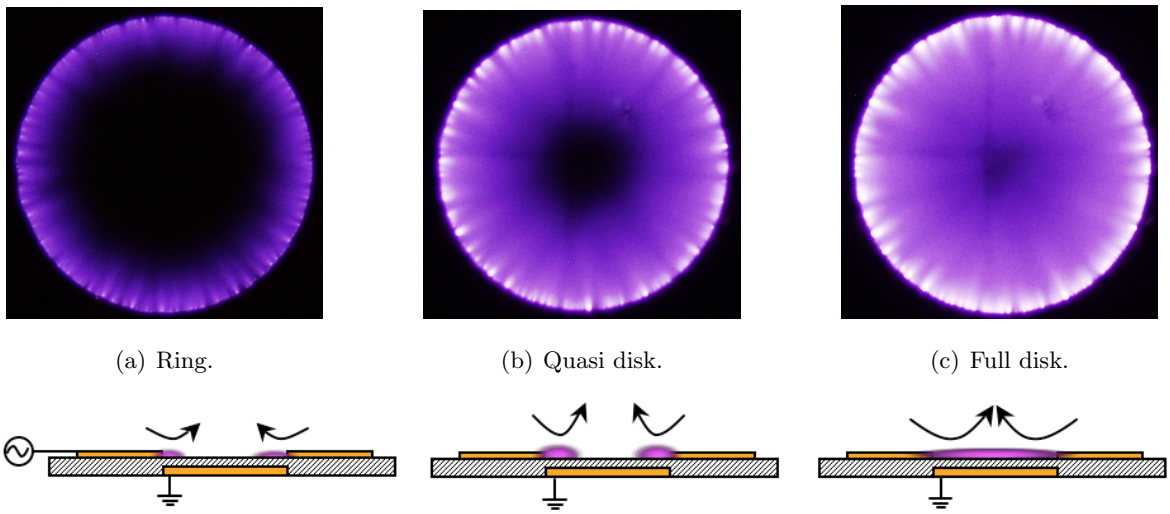

(a) Ring. (b) Quasi disk. (c) Full disk.

Figure 7.1: Photographs showing the formation of the annular plasma region. Plasma streamers (left) at initial stages progresses to a mature annular ring (center), which later progresses to a full disk if the power input is great enough (right). Corresponding cartoons are shown below indicating the body force on the fluid.

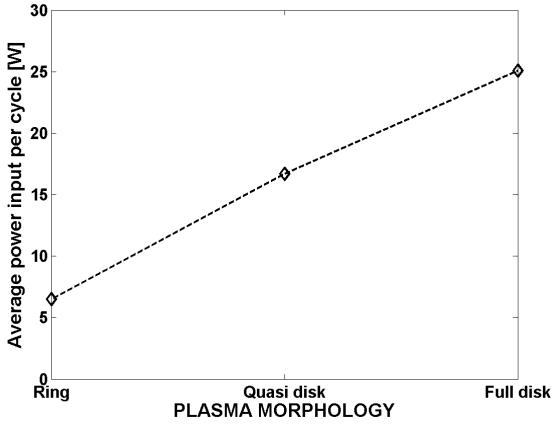

Figure 7.2: Input electrical power P_{in} for the different morphological states of the PSJA.

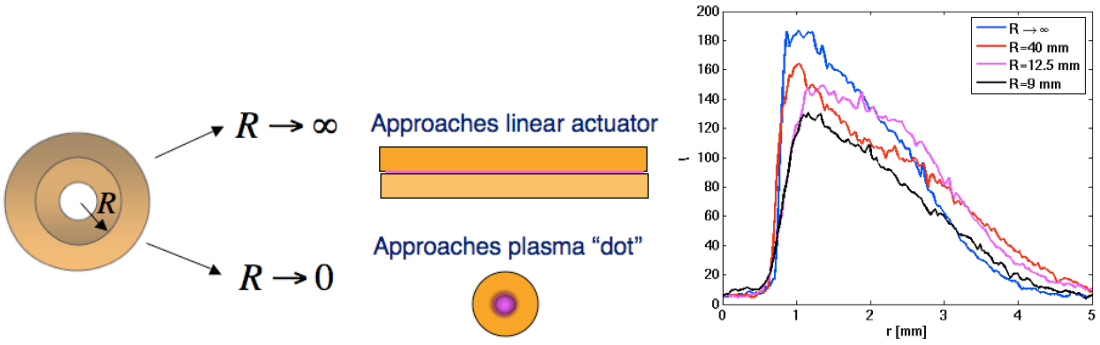

Figure 7.3: Strength of plasma region as actuator is varied from a linear to annular array with increasingly smaller radii.

(a) (b)

Figure 7.4: Photographs showing the effect of seeding contamination on the plasma before (a) and after (b) a quiescent flow PIV run.

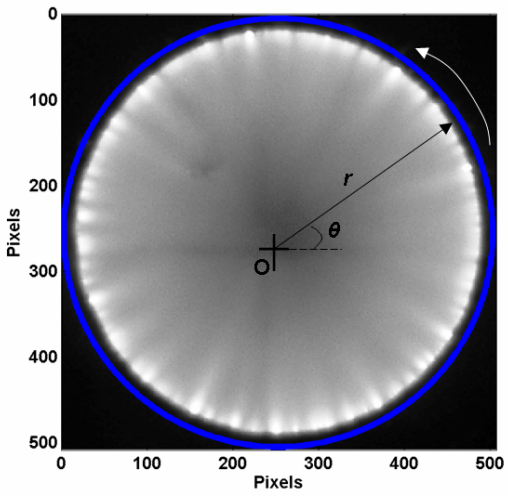

Figure 7.5: Sample CCD image showing the circular region (bounded by the band in blue) with coordinate system used for analysis of plasma structure. Arrow is used to indicate the direction of circumferential θ sweep from 0° to 360° (counter clockwise from origin, starting from the first quadrant).

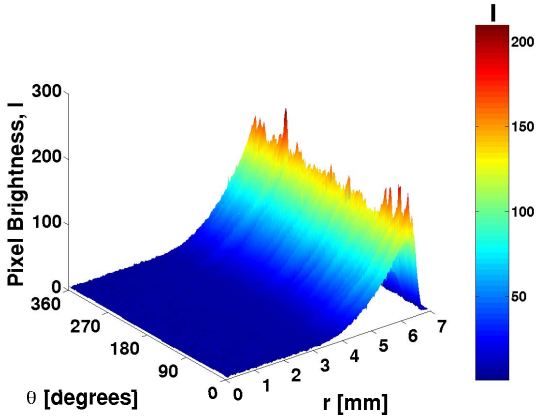

(a) Ring.

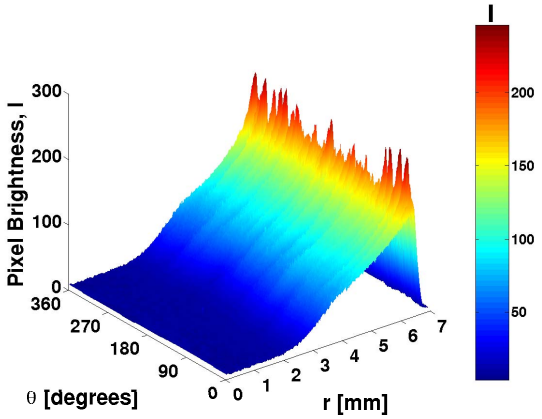

(b) Quasi disk.

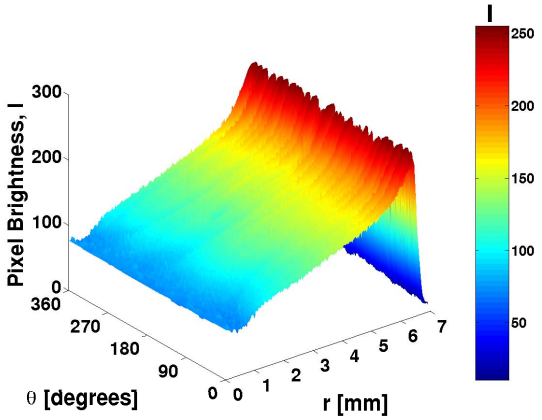

(c) Full disk.

Figure 7.6: Radial (r) and circumferential (θ) variation of plasma intensity in the annular region above the embedded electrode. PSJA in steady operation; note that the intensities are measures of the pixel brightness values and are relative to one another.

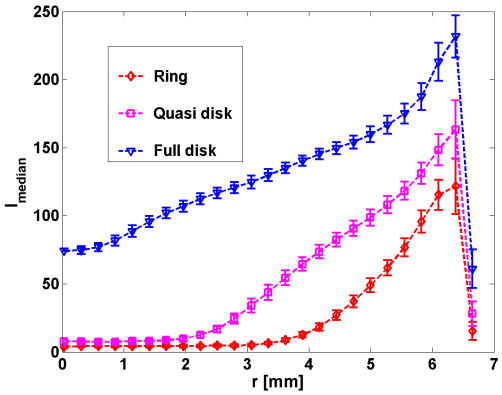

(a) Steady operation.

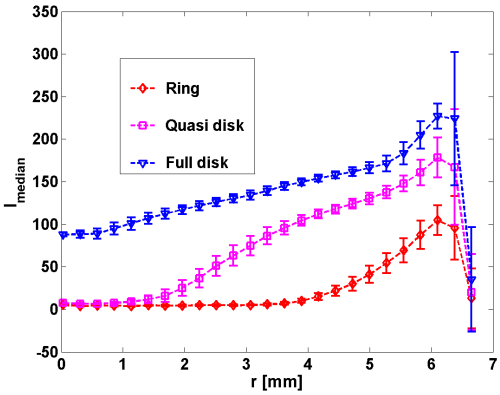

(b) f_p=1 Hz.

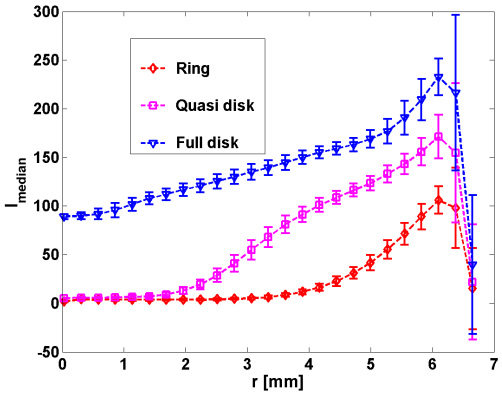

(c) f_p=10 Hz.

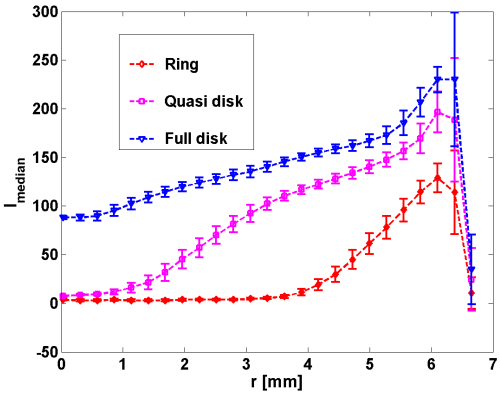

(d) f_p=100 Hz.

Figure 7.7: Radial variation of median relative plasma intensity. Error bars indicate circumferential deviation.

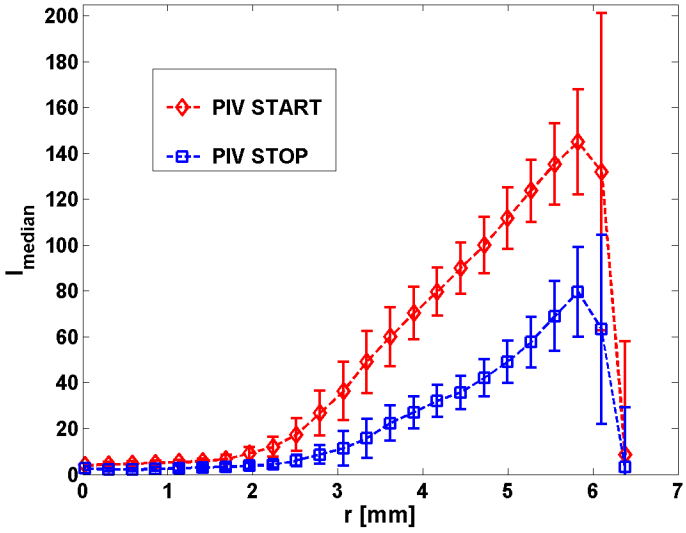

Figure 7.8: Profiles of relative radial median plasma intensity variation before and after a PIV run.

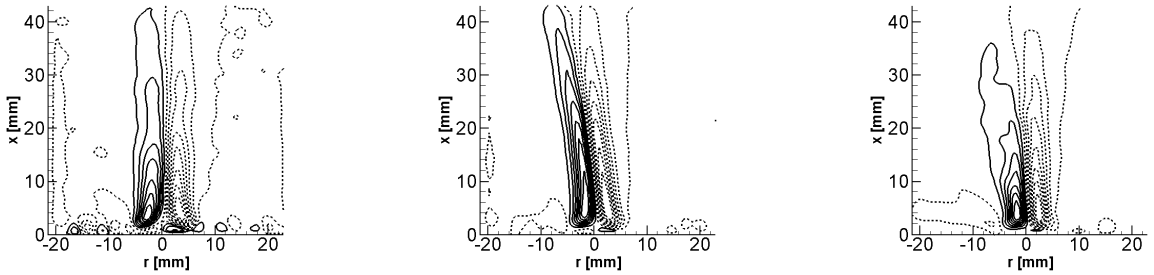

(a) Ring. (b) Quasi disk. (c) Full disk.

Figure 7.9: Time-averaged contours of normalized spanwise vorticity $\omega_z{}^*$. Contour levels begin at $\omega_z{}^*$=-0.893 and end at $\omega_z{}^*$=0.874, with increments of ± 0.126; steady operation of the PSJA.

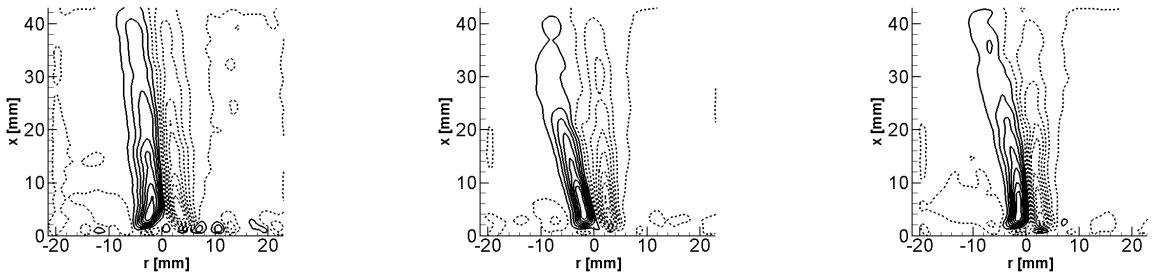

(a) Ring. (b) Quasi disk. (c) Full disk.

Figure 7.10: Time-averaged contours of normalized spanwise vorticity $\omega_z{}^*$. Contour increments are same as Figure 7.9; 10 Hz pulsed operation of the PSJA.

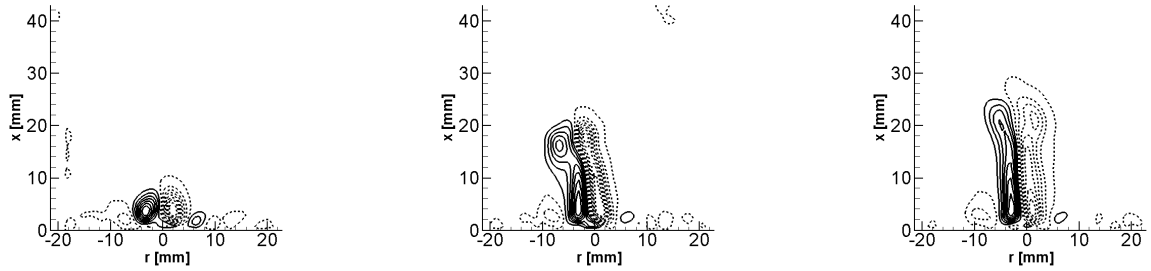

(a) t=24 ms. (b) t=36 ms. (c) t=48 ms.

Figure 7.11: Phase-locked contours of normalized spanwise vorticity $\omega_z{}^*$. Contour increments are same as Figure 7.9; 1 Hz pulsed operation of the PSJA in quasi disk morphology.

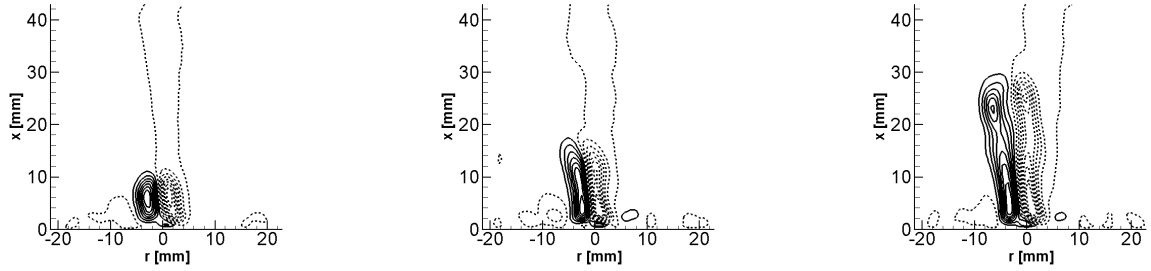

(a) t=24 ms. (b) t=36 ms. (c) t=48 ms.

Figure 7.12: Phase-locked contours of normalized spanwise vorticity $\omega_z{}^*$. Contour increments are same as Figure 7.9; 10 Hz pulsed operation of the PSJA in quasi disk morphology.

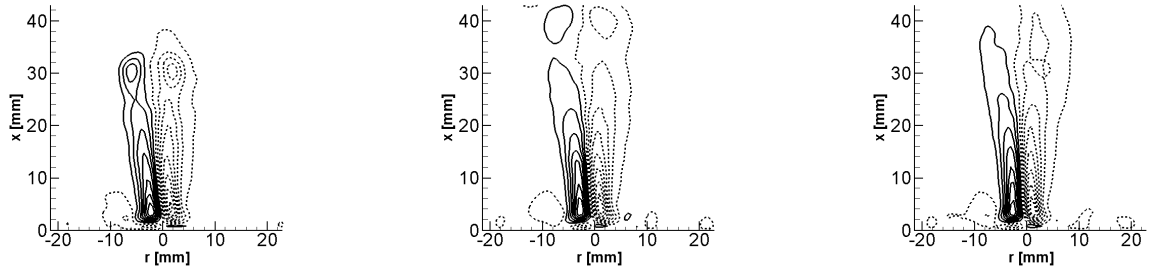

(a) t=24 ms. (b) t=36 ms. (c) t=48 ms.

Figure 7.13: Phase-locked contours of normalized spanwise vorticity $\omega_z{}^*$. Contour increments are same as Figure 7.9; 1 Hz pulsed operation of the PSJA in full disk morphology.

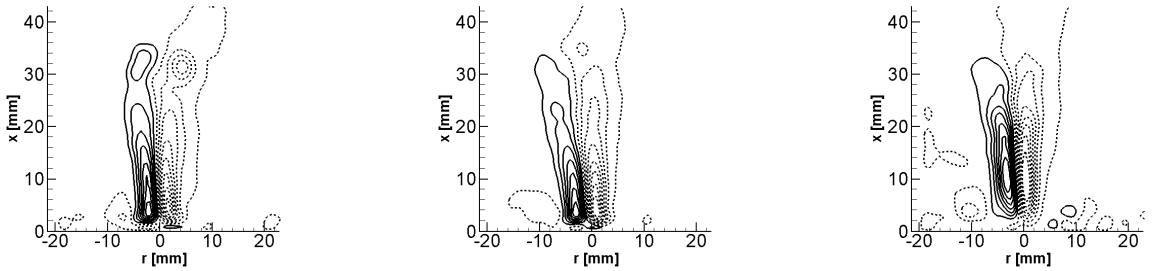

(a) t=24 ms. (b) t=36 ms. (c) t=48 ms.

Figure 7.14: Phase-locked contours of normalized spanwise vorticity $\omega_z{}^*$. Contour increments are same as Figure 7.9; 10 Hz pulsed operation of the PSJA in full disk morphology.

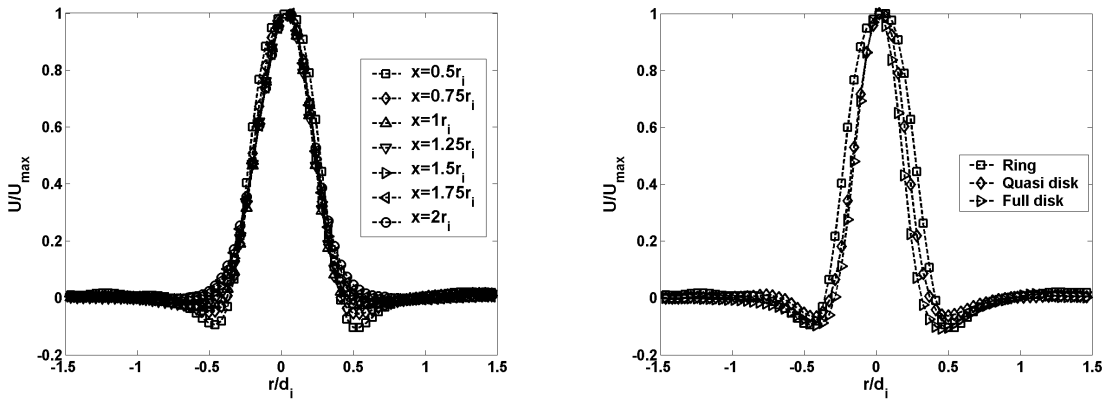

(a) Ring morphology only at various downstream locations. (b) All morphologies at x=0.25d_i downstream.

Figure 7.15: Cross-stream distribution of normalized mean axial velocity; steady operation of the PSJA.

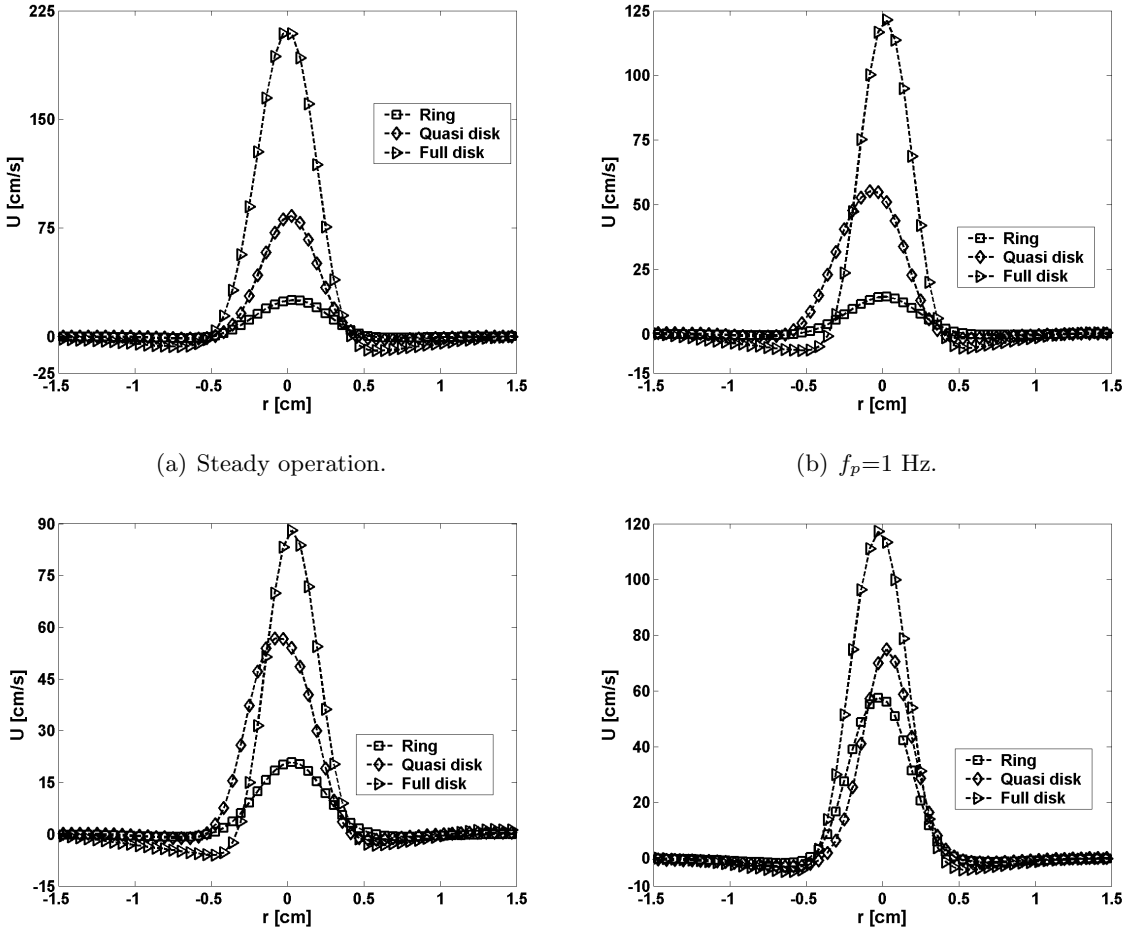

(a) Steady operation.

(b) f_p=1 Hz.

(c) f_p=10 Hz.

(d) f_p=100 Hz.

Figure 7.16: Cross-stream distribution of mean axial velocity at x=0.5d_i downstream of the PSJA.

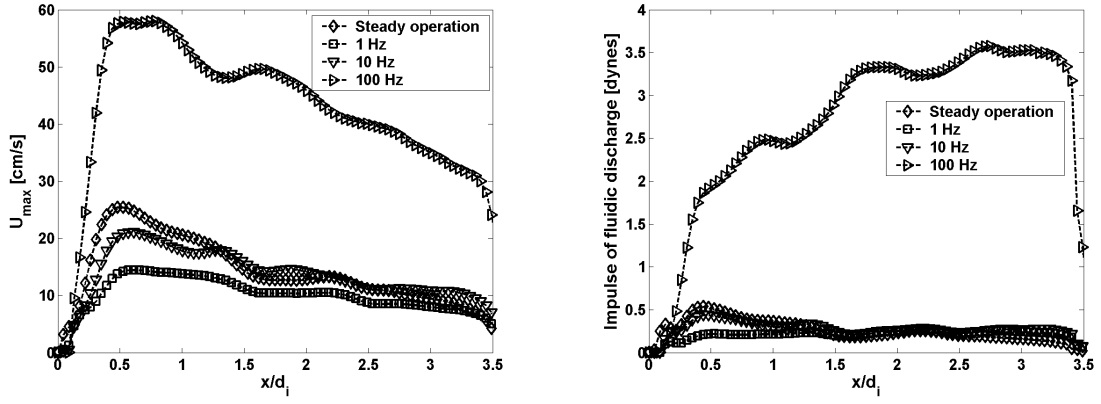

(a) Local maximum mean axial velocity.

(b) Impulse.

Figure 7.17: Ring morphology: streamwise distribution of jet characteristics.

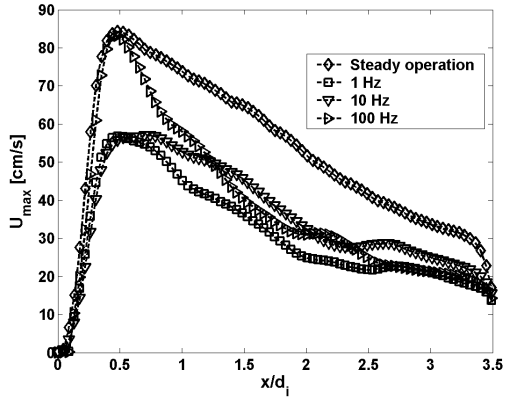

(a) Local maximum mean axial velocity.

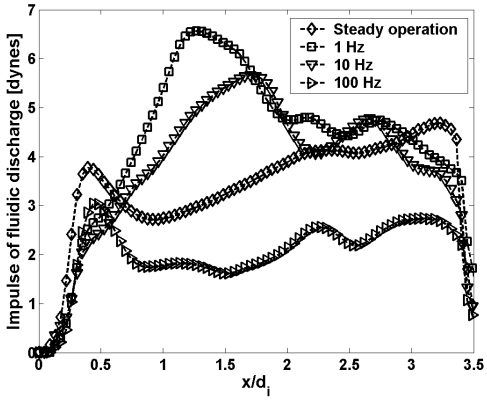

(b) Impulse.

Figure 7.18: Quasi disk morphology: streamwise distribution of jet characteristics.

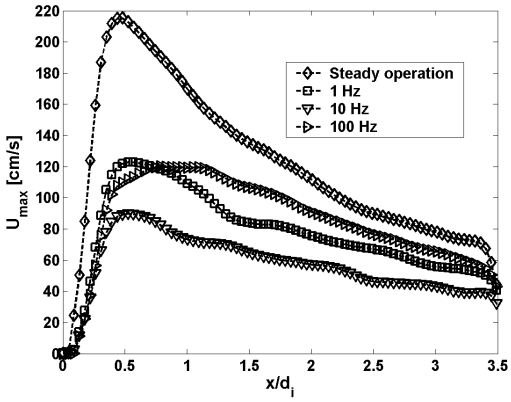

(a) Local maximum mean axial velocity.

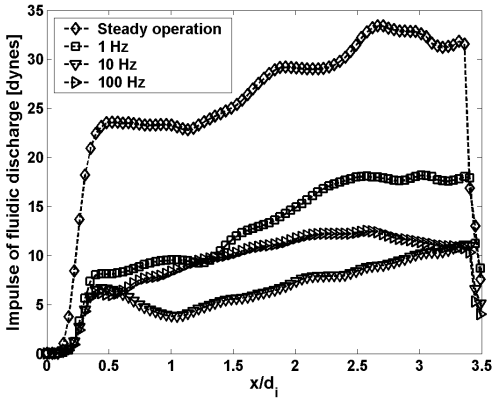

(b) Impulse.

Figure 7.19: Full disk morphology: streamwise distribution of jet characteristics.

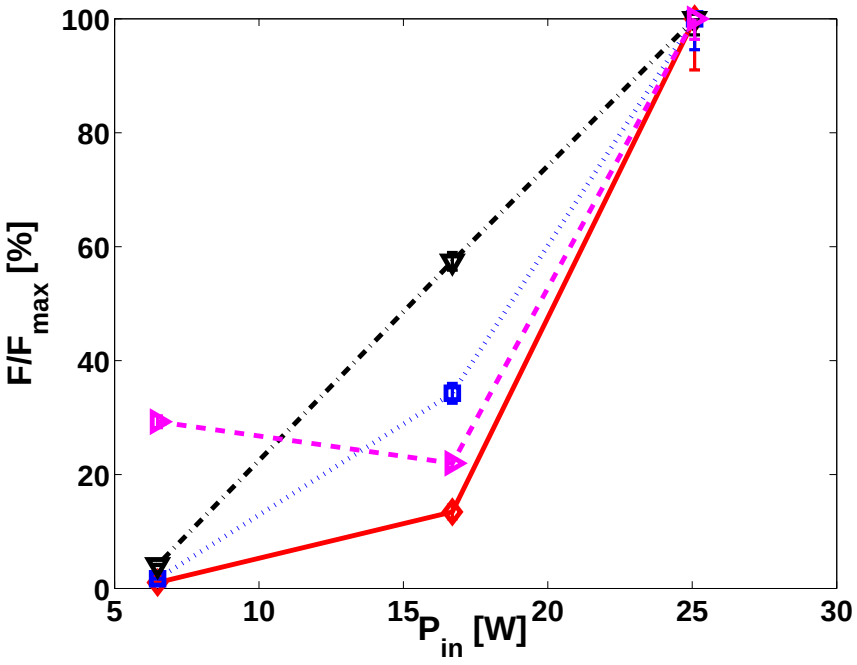

(a) Hydrodynamic force.

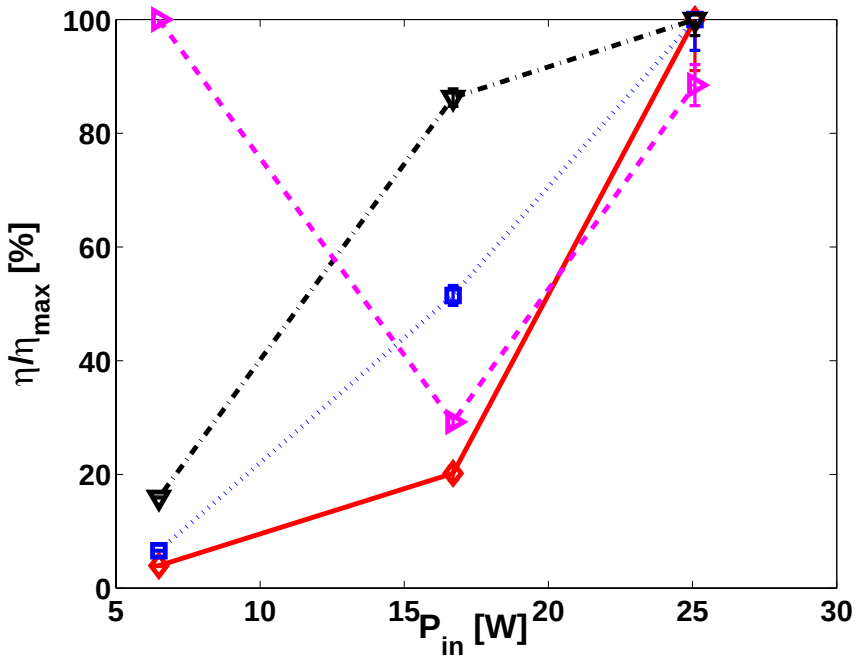

(b) Efficiency.

Figure 7.20: Normalized actuator performance characteristics. ⋄, steady operation; □, 1 Hz; ∇, 10 Hz; ▷, 100 Hz; error bars indicate deviation of streamwise impulse; color of the data indicates mode of actuator operation.

Chapter 8

SCALING RELATIONS

The observations on the factors affecting the formation of quiescent plasma synthetic jets were discussed in Chapter 4, and these merely illustrated the effects of varying different parameters affecting the PSJA performance. However, the exact relationships between the actuator dimension, input power, plasma morphology, pulsing frequency on the output peak jet velocity and momentum need to be investigated. This would aid in optimizing the design of the actuator so as to maximize jet velocity and momentum, and a detailed quantitative understanding of the above relations would be necessary to tailor the actuator construction for a particular application. The objectives of this chapter are to relate, under quiescent conditions, the effects of varying actuator dimension, input power, plasma morphology and pulsing frequency on the resultant jet velocity, momentum and actuator efficiency. The sections presented below describe efforts to model the scaling relationships of the plasma synthetic jet actuator.

8.1 Analytical Model

Since the power input P_i of a plasma actuator is directly proportional to the actuator length, for an annular geometry such as in the PSJA, scaling suggests that

$$P_i \propto d \propto c$$

where c is the actuator circumference. Note that the above observation neglects any effect of actuator curvature. The electrical power input per unit length of the actuator is thus a constant. In case of the PSJA, we have:

$$\frac{P_i}{d} = \frac{iV}{d} = C$$

where C is a constant. Likewise, P_i is also a function of the duty cycle, τ/T (where τ is the pulse width and T is the period), such that maximum power is required for a 100% duty cycle and no power is used for a 0% (actuator always off) duty cycle.

$$P_i \propto \tau/T$$

Also, the electrohydrodynamic (EHD) body force induced by the plasma on the bulk fluid is a function of several parameters such as the AC potential between the electrodes ϕ (which

is in turn dependent on the voltage drop ΔV), electric field density E, electrode thickness t, embedded electrode size l, electrode gap width w, dielectric material thickness t_d, and is given by Enloe *et al.* [54] as

$$F = \rho E = -\frac{\epsilon_0}{{\lambda_D}^2}(\phi E)$$

where

$$F = f(\Delta V, t, l, w, t_d, ...)$$

From the above relations, it can be seen that for a fixed actuator and power input, the actuator output given by the EHD body force (hence the induced velocity) will be invariant. The jet velocity scaling can be constructed by maintaining the power input per unit length constant and varying the characteristic actuator dimension, which in this case is the embedded electrode diameter d_i (see discussion in previous section). To derive the jet velocity scaling, a simple mass conservation analysis of the plasma synthetic jet is performed, assuming that the plasma characteristics are sufficiently modeled using a round wall jet (neglecting the EHD force). Fig. 8.1 shows the control volume used for analysis of the PSJA, where u_i is the plasma induced jet velocity, u_j is the velocity of the plasma synthetic jet and h is the incoming jet width. The plasma induced velocity u_i has been shown [54] to be nonlinearly related to the voltage drop across the electrodes ΔV

$$u_i \propto \Delta V^{7/2}$$

While the above power law relation was not observed in these experiments, the proportionality (without the 7/2 exponent) will be employed in formulating scaling relations. The incoming jet velocity magnitude and extant are therefore functions of the actuator configuration and input power. We would like to know how the output synthetic jet velocity u_j scales. Applying steady, incompressible flow mass conservation to the control volume yields

$$\rho \int_0^h u_i \; c \; dx = \rho \int_0^{2\pi} \int_0^{r_i} u_j \; r_i \; dr \; d\theta$$

where the LHS of the above relation is the incoming mass flux and the RHS is the outgoing (synthetic jet) mass flux. Treating u_i and u_j as uniform properties along the cross-section of the actuator, we can consider average values of these velocities and simplify the above integrals to

$$\overline{u}_i d_i h = \overline{u}_j \frac{{d_i}^2}{4}$$

where $\overline{u}_i$ is the average plasma induced velocity crossing the actuator interface, and $\overline{u}_j$ is the average PSJA velocity. Thus, we have

$$\overline{u}_j = \frac{4\overline{u}_i h}{d_i} \tag{8.1}$$

Assuming that the incoming jet velocity magnitude and extent are only functions of the actuator configuration and input power, this becomes

$$\overline{u}_j \propto \frac{1}{d}$$

such that the PSJA velocity increases with decreasing actuator size.

To derive a scaling for the hydrodynamic force imparted into quiescent fluid by the jet, start with conservation of linear momentum applied to the steady flow within the control volume considered herein,

$$\oint_{A_{CV}} \rho u_x \left(\vec{u} \cdot \hat{n}\right) dA = \Sigma \vec{F}$$

where F contains contributions from the jet, plasma induced electrostatic force and gravitational force. Neglecting the latter two, and assuming incompressible uniform flow,

$$F_j = \rho \overline{u_j{}^2} \pi {r_i}^2.$$

The average of the mean axial velocity squared is to be determined from PIV measurements. However, considering the limited spatial resolution available (number of data points near the plasma region ≈ 10), squaring the velocity and averaging it would, in result square the error in measurement. Hence, the square of the average jet axial velocity $\overline{u_j}$ is used, and the error can be accounted for through the introduction of a correction term,

$$\overline{u_j{}^2} = \alpha \overline{u_j}^2$$

where the value of α is governed by the velocity distribution. Calculations show that for a parabolic velocity distribution resemblant of a pipe flow, the value of α is approximately 2 for laminar flows, and 1–1.1 for turbulent flows. Thus, the hydrodynamic force imparted by the jet is given by

$$F_j = \pi \alpha \rho \overline{u_j}^2 {r_i}^2$$

To find F_j in terms of u_i, substitute equation 8.1 above,

$$F_j = 4\pi \alpha \rho \overline{u_i}^2 h^2 \tag{8.2}$$

The actuator efficiency η is determined as the ratio of output to input power. The output power can be written as the product of the hydrodynamic force of the synthetic jet times the PSJA velocity:

$$P_o = F_j \ \overline{u}_j = \frac{16\pi \rho \alpha h^3 \overline{u_i}^3}{d_i}$$

Assuming the input power is constant for a given actuator, it can be related to the circumference of the actuator as

$$P_i \propto \pi d_i \quad \Rightarrow P_i = C_1 \pi d_i$$

where C_1 is a constant of proportionality with units of g cm^{-3}. Thus, the efficiency can be determined as follows:

$$\eta = \frac{P_o}{P_i} = \frac{16\alpha\pi\rho h^3 \overline{u}_i{}^3}{C_1 \pi {d_i}^2}$$

$$\eta = \frac{C_2 \rho h^3 \overline{u}_i{}^3}{{d_i}^2} \tag{8.3}$$

where C_2 is 16 times the inverse of C_1, and the contribution of α (albeit non-trivial) has been neglected. Treating all terms except the diameter as constant, we see that

$$\eta \propto \frac{1}{{d_i}^2}$$

The above scaling relation suggests that more efficient actuators can be built by decreasing their size, and the dependence is the inverse square of the actuator diameter. This is in agreement with conventional jet theory, where higher jet velocities (and hence more fluidic forcing) can be obtained by decreasing the exit orifice. However, the mechanism of formation of the plasma synthetic jet is not the same as those in continuous or conventional (cavity driven) synthetic jets. There is no fluid entering an orifice in the PSJA, but rather, the jet is produced due to strong suction and boundary layer level fluid entrainment by the plasma (hence the secondary vortices seen in PIV visualizations). Due to this fundamental difference in the reason behind jet formation, the plasma synthetic jet is expected to deviate from the hydrodynamically driven round jet scaling behavior derived above. It is important to observe that while a smaller embedded electrode (which serves as the virtual "orifice" for the PSJA) would mean greater resultant jet velocities in accordance with mass conservation, it would also mean that there would be less plasma formed. Since the plasma is responsible for generating the body force, the latter line of reasoning for jet velocity scaling appears to be more physically intuitive. Hence, it is expected that below a critical size, a smaller actuator would actually result in *lower* jet velocities as a result of its limitation in surface area for the plasma to form and expand.

To include the effects of plasma input on the above model, we use the observation [54] that the maximum plasma induced jet velocity is a function of the embedded electrode dimension

$$\overline{u}_i = f(d_i) \propto {d_i}^n$$

where $n \approx 0.95$. If we assume a linear relation between u_i and d_i, for an embedded electrode dimension of 1 cm and for a maximum induced velocity on the order of 1 m/s, the value of the proportionality constant C would be on the order of 100 s^{-1}. For the PSJA, we then have:

$$\overline{u}_i = C_3 \; d_i \tag{8.4}$$

where C_3 is a constant, and represents a function of the plasma input. Rewriting the mass balance with the above relation for $\overline{u}_i$ gives the output jet velocity in terms of the plasma input and incoming jet width as

$$\overline{u}_j = C_3\ h \tag{8.5}$$

The incoming jet width h is reflective of the extent of the plasma induced EHD force on the fluid, and hence is directly proportional to the output velocity of the plasma synthetic jet. The constant C_3 can thus be treated as a correction factor to account for discrepancies between the values of $\overline{u}_j$ calculated using: (a) experimental data (that includes effect of plasma input), and (b) equation 8.1 above (that excludes plasma effects), and thereby refine the above scaling model to suit the non-traditional plasma driven synthetic jet.

8.2 Experimental Results

The following experiments were conducted in quiescent flow on three different annular plasma synthetic jet actuators with dimensions shown in Table 8.1. For each actuator, two morphological states (ring and quasi disk), power inputs (3 W and 4 W), and pulsing frequencies (1 Hz and 10 Hz) in addition to steady operation were investigated. This section describes the basic flow field and jet characteristics for the above actuators. A comparison of the average jet velocities ($\overline{u}_j$) obtained from PIV measurements and the analytical model equations will be presented.

Fig. 8.2 shows sample contours of spanwise vorticity obtained from PIV measurements phase-locked to the PSJA pulsing frequency of 10 Hz at t=24 ms in the actuator duty cycle. The vorticity values were normalized with the respective maximum values such that $\omega_z{}^*=\omega/\omega_{max}$. Dashed lines indicate contours of negative vorticity. The effect of variation in actuator embedded electrode diameter d_i is compared. The streamwise extent of the jet is seen to increase with increase in d_i. This was expected on account of increasing region of plasma with d_i, as discussed in the previous section. The secondary vortices (located outside the region of plasma) can be seen for all actuators, and their sizes are comparable. Note that this structure is created purely due to the favorable pressure gradient type flow experienced by the near wall fluid entrained by the plasma. The similarity of vortex size observed herein suggests that with increasing d_i (for the ranges examined herein), the strength of the secondary vortex (directly proportional to the radius) remains nearly constant. This would mean that with increasing extent of plasma (viz., increasing d_i), more input energy is available to turn the entrained fluid into the synthetic jet, in excess of the amount of energy expended in sustaining the secondary vortex generation process. For the d_i=25.4 mm

actuator, primary, secondary and tertiary vortical structures are observed. The primary vortex is seen within the window of observation for all cases, and both its strength and streamwise location is seen to increase with increasing d_i. Note that these observations are specific to the quasi disk morphology, and a more detailed discussion of morphology effects on the flow field is presented elsewhere. [203] As expected, the width of the jet is seen to scale closely with d_i.

Fig. 8.3–8.5 show the variation of peak axial velocity of the jet with actuator diameter for steady and pulsed cases of PSJA operation. For each mode of actuator operation, the effects of change in morphology and input power are compared. The error bars indicate the standard deviation of the measured velocity from PIV. The peak velocity shows a nearly linear relation with actuator diameter for the quasi disk morphology at all modes of actuator operation. For the steady and 1 Hz pulsed operation of the PSJA in ring morphology state, the actuator with d_i=1.27 cm is seen to be the optimum value for obtaining the highest value of jet velocity. For this actuator size at this morphology (with low plasma strength), there is a greater available area of plasma compared to the d_i=0.635 cm actuator. Also, the 1.27 cm diameter actuator would not increase the jet width as much as the 2.54 cm diameter actuator. Increasing the region and intensity of plasma to the quasi disk morphology increases the velocity of the jet substantially. For this morphology (with increased plasma strength), it is the extent of plasma that appears to control the output jet velocity. Consequently, the peak jet velocity of the PSJA operated in quasi disk morphology increases with increasing d_i.

The variation of peak jet velocity with input power for the different actuators shows non-uniform trends for steady and pulsed operation of the PSJA. For steady operation (Fig. 8.3(b)), the d_i=0.635 cm and d_i=1.27 cm actuators exhibit marginal variation in the peak velocity values with increasing input power. The peak velocity of the d_i=2.54 cm actuator, however, increases by three times with the increase in input power. For steady operation with P_{in}=3 W, the d_i=1.27 cm actuator appears to be the optimum actuator size. Increasing the input power by 1 W changes the above variation such that the peak velocity is directly proportional to actuator diameter. For 1 Hz pulsed operation of the PSJA (Fig. 8.4(b)), it is interesting to observe that the jet is not sensitive to a 1 W change in input power, as the peak velocities are unchanged for both input conditions. With increase in pulsing frequency to 10 Hz (Fig. 8.5), the d_i=0.635 cm actuator performs the best for 3 W input power, while there is not any substantial variation of peak velocity between the actuators at P_{in}=4 W. For any morphology or input power, pulsed operation of the actuator results in lower velocities than those for steady operation. The results in

Figs. 8.3–8.5 were obtained from time-averaged PIV results, and hence the values used in these figures are indicative of the maximum time-averaged velocity ($\overline{u}_{max}$), and not the average of the maximum velocity ($\overline{u_{max}}$). The latter values are greater for pulsed operation as compared to steady operation, and have been reported elsewhere. [177]

Figs. 8.6–8.8 show the variation of the hydrodynamic force of the jet with actuator diameter for steady and pulsed cases of PSJA operation. For each mode of actuator operation, the effects of change in morphology and input power are compared. The hydrodynamic force was calculated by averaging the fluid impulse (obtained from the inviscid second-order momentum integral equation given in Hussein *et al.* [175]) along the streamwise direction, and the values of force (for any particular input condition) were normalized with the maximum value of force for the particular case. Except in the case of 1 Hz pulsing, for all remaining modes of operation, the d_i=2.54 cm actuator produces the highest force compared to the other actuators at any morphology or power input. This was expected since larger the surface area of the actuator (based on d_i), the larger the jet width is (compare Fig. 8.2(a)–(c)) and hence the jet momentum. For pulsed operation of the PSJA at 1 Hz in ring morphology (Fig. 8.7(a)), the d_i=1.27 cm actuator produces the highest force. Between the two morphological states examined, it is interesting to note that the ring morphology produces a greater force for steady and 10 Hz pulsed operation (Fig. 8.6(a) and Fig. 8.8(a)). This was thought to be on account of the increased starting jet width for the ring morphology cases as compared to that for the quasi disk. The hydrodynamic force for the actuators at constant input power conditions (3 W and 4 W) varies with actuator dimension in a relatively uniform trend for all modes of operation. The difference in force between d_i=0.635 cm and d_i=1.27 cm actuators remains well within 20%. The force increases at least by 70% with increase in d_i from 1.27 cm to the 2.54 cm. This follows the same trend as seen for morphology variations (Figs. 8.6(a) and Fig. 8.8(c)), for reasons discussed above. For both steady and pulsed operation, the values of force for 4 W power input were lesser than those obtained with 3 W input, which is opposite to the trend seen for peak jet velocity with power input.

In general, it is seen from the above discussion that optimizing the size of the actuator for maximum jet velocity and momentum is strongly dependent on the input conditions of power, plasma morphology, and pulsing frequency. For steady operation of the actuator, some trends in the variation of the velocity and momentum with actuator dimension can be identified. For the highest value of input power (4 W) examined herein, both the peak jet velocity and momentum were observed to be proportional to the embedded electrode diameter d_i. When operating in the ring morphology, the jet velocity appears to reach an

optimum value with increasing d_i, after which the value drops. For the same morphology, the jet momentum reaches its highest value for the largest size actuator. When operating in the quasi disk morphology, the jet velocity linearly increases with d_i, while the momentum increase with d_i is nonlinear. It is important to note that any optima identified in this discussion were selected from the limited range of parameters and actuator diameters examined herein. Much of the parameter space beyond those investigated in this work would still need to be explored for identifying true global optimum values.

8.3 Model Validation

In general, three metrics of the actuator characteristics, the average jet velocity, hydrodynamic force, and actuator efficiency were considered for comparison of experimental results with the theoretical relation presented above. Figure 8.9 shows the variation of average plasma synthetic jet velocity $\overline{u}_j$ with diameter d_i for steady operation of the PSJA. In each figure, the values of average jet velocity obtained from PIV data are compared with those obtained from the scaling model equation 8.1. It is important to note that the values of $\overline{u}_i$ used in the calculation of average jet velocities by equation 8.1 were actually obtained from PIV data at a streamwise distance h=0.2169 cm from the actuator. The error bars indicate the standard deviation of the PIV measurement velocity at h=0.2169 cm. Fig. 8.9(a) shows average jet velocity variation with d_i for the two morphological states investigated herein. For the ring morphology, the values of the experiment and the model match within 2 cm/s for the 0.635 cm and 2.54 cm actuators, while the difference in values are larger ($\approx$ 5 cm/s) for the 1.27 cm actuator. The difference in values between experiment and model are larger for the quasi disk morphology, especially for the actuator with d_i=1.27 cm. Fig. 8.9(b) shows the model and experiment comparison of $\overline{u}_j$ for the two input power conditions considered herein. For an input of 3 W, the model velocity variation with d_i follows what was expected from conventional round jets, viz., increasing velocity with decreasing actuator size. The deviation of the plasma synthetic jet from classical jet theory is clearly seen for this case (Fig. 8.9(a)), with the velocity increasing with d_i for the 0.635 cm and 1.27 cm actuators, after which it drops for the 2.54 cm actuator. The model and experiment values are well within 10 cm/s difference for a power input of 4 W. Overall, in matching the average PSJA velocity $\overline{u}_j$, the analytical model presented herein compared reasonably well (with average difference $\approx \mathcal{O}$(5 cm/s)) to the experimental results for most of the cases. The differences between the model and experiment values of $\overline{u}_j$ are primarily due to the effects of plasma, actuator curvature and jet entrainment that are not considered

in the simplified model. The values of the constant C_3 that relates the plasma effects via the actuator dimension d_i were determined from equation 8.5 using PIV data based values of $\overline{u}_j$, and are presented in table 8.2 below. No single value of the constant was arrived at, across the entire parameter space of plasma morphology and input power. With the exception of the 4 W power input case, the value of C_3 across different actuators for any given operating condition appears to reach a maximum for the d_i=1.27 cm actuator. The value of h used for calculation of C_3 was the same as above (0.2169 cm).

Figure 8.10 shows the variation of normalized hydrodynamic force of the plasma-induced jet with actuator size for the two different plasma morphology states and power inputs to the actuator. The data obtained from PIV measurements, already presented in Fig. 8.6, is also shown for comparison. The force imparted by the jet onto quiescent air was calculated using equation 8.2, where $\overline{u_i}$ is obtained from the PIV data. In general, the model over-predicts the force value for most of the cases, on account of the lack of inclusion of curvature effects in the derivation. For both the quasi disk morphology and specified power input of 4 W, the trend of force variation predicted by the scaling model is same as that observed in PIV data, where the force increases nonlinearly with increasing d_i. As expected, the force was highest for the 2.54 cm diameter actuator for the above two states, on account of increased jet width as discussed previously. This feature is also captured by the scaling model, and the values of forces predicted by the model relation match within $\pm$15%. At sufficiently low power and plasma strength examined here, the actuator behavior becomes nonuniform, and hence a unique scaling for the force imparted by the jet could not be identified within the bounds of this study. Note that the term α in the force calculations was assumed to be 1 for all cases, essentially because this value was not derivable from measurements. Considering the argument that α equals 1.3 when the velocity varies in a parabolic manner (which is ideal for the entrainment driven plasma jet), it is highly probable that the mismatching of predictions with experiment was in part a result of this simplification.

The calculation of the actuator efficiency based on the derivation presented earlier for equation 8.3 was performed using the induced flow velocities obtained from experiment (with the same control volume as before), and Fig. 8.11 shows a summary of the dependence of this quantity on the actuator size. It is clearly seen that there exists no unique optimum actuator size exists across all the controlled operational parameters considered in these experiments. However, some definite trends in actuator behavior can be observed. For the plasma ring, the 1.27 cm actuator produces the maximum efficiency similar to the force variation discussed earlier. Whether this is a result of non-uniformity of the plasma structure or if this is

indeed an optimum is not clear. Note that the definition of efficiency is based on the input power applied to the actuator, and it is important to distinguish this from the power available across the plasma. Exact measurements of the electric field across the plasma are necessary to develop a more definite understanding of actuator behavior. Interestingly, the actuator efficiency increases with actuator size for the quasi disk, which is in direct opposition to conventional jet theory. This indicates that the plasma strength is certainly an important factor in controlling the momentum coupling of the actuator, to the extent that both wider jet spreading and increased performance efficiency can be simultaneously obtained without any compromise in a larger sized actuator. Identical actuator efficiencies are obtained for all the actuators at both the 3 W and 4 W power input levels as shown in Fig. 8.11(b). Across this change in the power inputs, actuator efficiency is inversely proportional to its characteristic dimension controlling plasma expansion, as expected from the analytical explanation provided earlier. While this variation clearly does not follow an inverse square relation, the trend of increasing efficiency with decreasing actuator size shows that the power input across small incremental values does not substantially affect the efficiency of any particular plasma synthetic jet actuator. At constant power input conditions, these results suggest that while decreasing the size of the actuator produces lower peak jet velocities, it results in increased actuator efficiency.

8.4 Comparison with Conventional Jets

In this section, the flow field characteristics of plasma induced jets are compared to similar jets produced by mechanical devices. Of the latter category are two types of jets, including those with added mass flux input (referred to as conventional jets hereon) and without (referred to as synthetic jets). The jet induced by the PSJA arrangement is synthesized from the fluid volume available within the working system, and hence very broadly resemble a "zero-net-mass-flux" or synthetic jet. However, the mechanisms of both these devices (and conventional jets) are fundamentally different. A synthetic jet actuator consists of a cavity with an orifice through which equal amount of fluid is alternatively sucked into and ejected out of in a time-periodic manner, generating trains of vortices which create a jet upon advection with their self induced velocities. Plasma based synthetic jets are engendered due to the entrainment of fluid effected near a DBD plasma region symmetric about the actuator centerline, thereby creating a vertical (wall-normal) jet which exhibits unsteady flow structures if operated in an unsteady manner. The local maximum mean axial velocity and inner electrode dimension are selected as the normalization factors for

cross-stream distribution profiles of a PSJA, which in turn collapse reasonably well across various streamwise locations as near to the actuator as one length of the actuator dimension and exhibits self similarity. This characteristic for synthetic and conventional jets, on the other hand, are normalized using the centerline velocity and half-width as the appropriate scales. The attainment of self similarity in conventional and synthetic jets occur in the far field of the flow, roughly around 10 lengths downstream. Also, in both plasma driven and conventional synthetic jets, negative (downward) directional flow is seen in the similarity profiles measured very close downstream of the actuator, on account of the entrained flow occurring due to the action of the jet driver and any associated rotational effects. Essentially, the peak value of velocity occurs close to the actuator in a PSJA, at distances less than a length of the characteristic dimension. This is followed by a decay in jet velocity and momentum, and the rates at which these occur will be discussed below. Unsteady pulsing of the actuator at frequencies close to the time scales of the fluid flow reveal that a generation of multiple trains of vortices is initiated and sustained by the plasma region, and these starting vortices introduce additional entrainment in their wake, thereby resembling synthetic jets. Within the field of observation, the effect of these vortices are prevalent in the entire flow field such that they promote two effects: to draw fluid away from the wall during their advection, and to entrain additional fluid on either side of the jet column. This is similar to synthetic and conventional pulsed jets, in that the interactive entrainment between groups of vortices plays an important role in sustaining the jet. Of course, since the source of these vortices is a combination of the plasma and pulsing frequency (former being more important), modeling PSJA effects across widely varying scales and formulating an analytical flow model (as attempted herein) becomes inherently a complicated problem. A fluid dynamic approximation may be considered by ignoring the plasma discharge events and concomitant entrainment, as well as its effect on the compressibility of the fluid medium, with constant factors that can be used to match to experiments. Depending on the actuator dimension, input power, and plasma morphology, multiple counter rotating vortical structures are generated in addition the jet. These flow features are typically not observed in conventional pulsed and synthetic jets, and are associated with the strong "virtual" favorable pressure gradient like effect of the plasma region that entrains a large volume of residual fluid and fluxes this momentum out in the form of a jet. System complications such as cavity design and implementation on a smooth surface are not of any concern in the no-moving parts design of the PSJA as compared to conventional and synthetic jets. Thus, the PSJA obviously has a powerful application potential in the control of shear flows within the low Re range.

To quantify the comparison between the different types of jets discussed above, scaling relations are determined based on experimental results. Specifically, the characteristics that are examined include the local maximum mean axial velocity U_{max}, centerline axial velocity U_c, and half-width b of the jet in each case. These provide an estimate of the extent of the plasma induced jet as compared to other drivers, as well as the relative differences between each flow field. Figure 8.12 shows the streamwise distribution of the above quantities for an annular PSJA with embedded electrode diameter $d_i = 1.27$ cm. The symbols represent the actual experimental data, and each of the lines are indicative of the scaling of jets. Note that the solid line represents the empirical curve fit to the behavior of the PSJA, while the dashed and dotted lines indicate the trends for conventional and synthetic jets, respectively. The relations for the latter two jets were obtained from the from the data obtained using hot wire anemometry by Smith & Glezer [149], PIV measurements of Béra *et al.* [152], and analytical formulations of conventional jets presented in Schlichting & Gersten [14]. No effort was undertaken to extract any relations from the increasing (upward sloped)portion of the velocity plots. In general, for a conventional turbulent rectangular (2-D) jet, the relations follow

$$\frac{U_{max}}{U_p} \sim x^{-0.5}, \ \frac{U_c}{U_{c,p}} \sim x^{-0.5}, \ \frac{b}{d_i} \sim x$$

where each velocity has been normalized with its respective peak value, and the half-width of the jet was normalized using d_i. The half-width of the jet was defined as the cross-stream location of the jet measured from the jet centerline where the mean axial velocity equals half the maximum value at the same streamwise location ($U = 0.5U_{max}$, after Béra *et al.* [152]). In the context of PIV, the calculation of this quantity was problematic due to the limited spatial resolution available (few points across the entire jet). To resolve this, the ensemble averaged axial velocity data obtained after post processing the raw data was interpolated using MATLAB to provide a sampling resolution in the radial (cross-stream) direction that was 4 times that of the original velocity vector flow field. This increased the number of points available and allowed for a new definition of half-width based on the r location ($r = 0$ along jet center) where $U = 0.49U_{max}$ to $0.51U_{max}$, thereby introducing a maximum error of 2% in the values reported herein. For a rectangular synthetic jet, the following relations hold

$$\frac{U_{max}}{U_p} \sim x^{-0.4}, \ \frac{U_c}{U_{c,p}} \sim x^{-0.58}, \ \frac{b}{d_i} \sim x^{0.88}.$$

Note that both the above scaling relation sets have been written in terms of the normalizing factors defined above. For all different characteristics, the PSJA decay rates in the velocities are not identical to any of the other two actuators. Some similarities can be noted in

the trends, however. The PSJA local maximum velocity reaches a peak at a downstream distance close to the actuator, after which it decays as $\sim x^{-0.9}$. Conventional 2-D synthetic jets also exhibit the exact same trend in U_{max} behavior, but the downstream distances where the peak occurs is located much farther away, around $x = 10d$–$12d$. This type of variation is in sharp contrast to conventional (mass flux) jets, where the peak is located at the orifice exit of the air supply system required to form the jet and decreases nonlinearly with streamwise distance. Obviously, the difference in behavior between conventional mass flux jets and plasma/mechanical synthetic jets is due to the entrainment occurring in the near field of the actuator, as a result of which there exists an apparent local minimum at the actuator location. It is interesting to note that although the PSJA shown is in steady operation, the curve fits for the PSJA and synthetic jet actuator (always pulsed) are not widely separated. The variation of the centerline axial velocity (Fig. 8.12(b)) shows the same trend as conventional synthetic jets in that there is a rather rapid increase in its value up to a certain level, after which it decays with streamwise distance. In case of the synthetic jet, this process occurs over much larger streamwise distances. The peak value of U_c is typically realized around $x = 10d$, and this sort of variation in centerline velocity has been attributed in the literature to generation of laminar vortex structures, advection, and formation of a mean turbulent jet observed during the formation of a conventional synthetic jet. In case of the plasma synthetic jet, the peaking in centerline value can also be explained through the formation and advection of starting vortices. The decay in a PSJA occurs much faster, as $\sim x^{-1.23}$, similar to its U_{max} behavior. Also, the location of the peaks in local maximum and centerline velocities are identical, suggesting that is indeed the starting vortex that is responsible for the localized sharp increase in velocity. While it is clear that the plasma synthetic jet decays faster in the streamwise direction as compared to conventional continuous and synthetic jets, the half-width variation (Fig. 8.12(c)) also shows an interesting behavior. The spreading of the plasma synthetic jet varies as $\sim x^{0.5}$ and is less than the other two jets, as compared to the $\sim x^{0.88}$ relation seen for conventional synthetic jets and linear growth of width in conventional jets. This suggests that the plasma induced jet spreads slower in the cross-stream direction than both conventional mass-flux driven jets and synthetic jets. In summation, compared to conventional continuous and synthetic jets, the annular plasma induced synthetic jet has lower lateral expansion, faster decay of velocity profiles in the streamwise direction. Note that all the scaling relations presented here for the conventional jets and synthetic jets are two dimensional, and so this warrants examining the linear PSJA for a more accurate comparison, and also to identify any dimensionality related effects.

Figure 8.13 compares the characteristics of linear (2-D) plasma synthetic jets with conventional rectangular continuous and synthetic jets. The dimensions of the actuator tested herein was equivalent to the annular PSJA results reported above with reference to Fig. 8.12 (see chapter 4 for matching dimensions). The spanwise length of the actuator was 90 mm, with no air gap between the top and bottom electrodes. In general, it is seen that the trend of variation in velocities and half-width is unaffected due to the change in dimensionality of the plasma synthetic jet. Compared to the annular PSJA, the exponents in the empirical curve fits for the linear PSJA change for the local maximum axial velocity and centerline velocity, whereas they remain the same for the half-width. The local maximum axial velocity decays as $\sim x^{-0.82}$ for the linear PSJA, which is slower when compared to the annular PSJA $\sim x^{-0.9}$. The discrepancy between 2-D and 3-D becomes worse for centerline velocity, where the linear PSJA decays as $\sim x^{-0.93}$ compared to $\sim x^{-1.23}$ for the annular PSJA. The streamwise peak locations of both the local maximum and centerline velocities have moved to around $0.6d_i$ for the linear PSJA, which is slightly downstream of the corresponding value for annular PSJA as expected due to the increased surface area. Interestingly, the larger area of plasma available for the linear PSJA (11.43 cm^2) would imply that the resultant jet would have lower velocity as compared to the annular PSJA with a smaller area (1.27 cm^2), from simple incompressible mass conservation. However, the rate of decay of velocity (both U_{max} and U_c) show that the linear PSJA actually has a higher induced flow velocity (normalized) at any particular streamwise location than its equivalent annular configuration. It is suspected that the difference in plasma intensity might have initiated this difference. Although the jet half-width scaling for the annular and linear PSJA are identical, the linear PSJA records generally higher values of b compared to the annular PSJA, indicating increased spreading in accordance with increased surface area available.

To investigate the dependence of the scaling relations on the actuator dimension and input power, the data obtained on the three different annular actuators used in the scaling model validation experiments was used. Figures 8.14–8.16 show the streamwise distribution of local maximum mean axial velocity for 2 conditions of input power and d_i. As expected, the larger sized 2.54 cm actuator induces a wider jet, and the decay of the PSJA curve for this actuator at 4 W power input $\sim x^{-0.5}$ matched exactly that of conventional 2-D jets, while it was marginally different $\sim x^{-0.5}$ at 3 W power input. It must be noted that the FOV of PIV measurements on the 2.54 cm actuator was limited to $x \sim 1.5d_i$, as a result of which there is an erroneous sudden drop in U_{max} at this streamwise location. Also, as a caveat, the data sets shown for the 1.27 cm actuator across Figs. 8.12, 8.14(a)–(b)

were all sampled at a different plasma morphology condition relative to each other, thereby modifying the flow field and consequently modifying the scaling behavior. A variation in the input power would immediately change the electric potential available to the plasma, and hence its morphology. It is virtually impossible to control both power and morphology at the same instance in PSJA spatial scaling experiments. Typically, a controlled input power across different actuator sizes would result in different plasma morphologies and vice versa. This effect is heavily perceived in Fig. 8.14, where the 4 W power input case spreading shows a steep streamwise decrease as $\sim x^{-2.1}$ reaching almost zero values at around $x \approx d_i$. The centerline axial velocity (Fig. 8.15) shows a similar trend as the local maximum velocity discussed previously. The decay of centerline velocity for the 2.54 cm actuator is identical to the theoretical $\sim x^{-0.5}$ rate of conventional mass-flux input jets. An increase in the PSJA diameter by two times affects the flow field characteristics considerably, to the extent that the larger actuator now shows a rate of spreading and decay exactly identical to conventional jets. Yet again, the limited FOV in the 2.54 cm measurements must be cautiously considered against this previous statement, as it is probable that the streamwise decay might be affected differently if data at more streamwise locations were available. In general, however, the variation in scaling relations between the 1.27 cm and 2.54 cm actuators was expected, considering the increased area available for the plasma to expand. It is interesting to note that the streamwise location of peak velocity across the two power inputs is unchanged for a particular actuator. This observation is directly related to the plasma entrainment, the plane of which is located at very small distances away from the wall. This plane acts as a "virtual origin" for the ejected fluid flow, and is where the peak in axial velocity value occurs. The 3 W input to the 1.27 cm actuator shows a slightly increased spreading rate compared to the equivalent variation in Fig. 8.12, while the 4 W input shows a sharp deceleration in streamwise direction.

Figure 8.16 shows the streamwise distribution of the jet half-width for variation in actuator size and diameter. The 1.27 cm actuator with 4 W power input is not shown, as there was a large amount of scatter in the calculated values. For a power input of 3 W, the 1.27 cm actuator showed a slower increase in spreading with streamwise distance compared to the $\sim x^{0.5}$ relation observed in the above discussion. Interestingly, increasing the diameter to 2.54 cm affects the flow field such that the half-width scaling is the same as that for the 1.27 cm actuator discussed earlier (Fig. 8.12(c)). Thus increasing the actuator diameter increases the spreading of the jet and decreases the rate of streamwise decay of centerline and local maximum axial velocities. The plasma induced jet, in general, shows resemblance to synthetic jets in terms of flow features and entrainment driven characteristics. Both jets

show a departure from conventional jet similarity scaling, mostly due to the non-invariance of the time-averaged momentum in the streamwise direction of the flow field. Also, the scaling relations for conventional synthetic jets and plasma synthetic jets do not match for the range of parameters examined herein. The plasma induced synthetic jet reaches self similarity at shorter cross-stream distances from the actuator, peak value within less than a diameter, and decays faster than both conventional continuous and synthetic jets.

As a final comment, since the streamwise decay of centerline velocity of plasma synthetic jets was observed to be faster than mechanically driven jets, it was expected that the rate of increase of the plasma synthetic jet half-width must also be faster on account of mass conservation. However, the above experimental results confirm an abnormal trend of steep centerline velocity decay along with slower spreading of the plasma synthetic jet. It was conjectured that the reverse flow from the impingement of the plasma synthetic jet on the upper wall of the quiescent enclosure (see Fig. 4.14) was playing an important part in establishing this behavior. The plasma synthetic jet spreading and decay characteristics obtained from the results of numerical simulations of an L-PSJA in quiescent flow by Reasor [204], with a computational setup identical to the experiments presented in this dissertation (including the upper bounding wall), do not match with the above experimental behavior of the actuator. This suggests that the upper wall to not be the primary reason for slow jet spreading and steep centerline velocity decay of the plasma synthetic jet. The reason for this trend is not clear at this stage, and it is suspected that 3-D effects of the primary vortex interactions and jet turbulence, as well as horizontal outflux from the jet body could be possible factors contributing to this behavior.

8.5 Summary

The scaling properties of the annular plasma synthetic jet actuator were presented in this chapter. The effects of varying pulsing frequency, plasma morphology and input power on the jet characteristics of three different actuators was investigated experimentally. The actuator size required to obtain maximum jet velocity and momentum was found to be affected by a combination of the above factors, such that no unique optimum values across all parametric variations were identified. A simple analytical model of jet scaling was derived from fundamental fluid dynamics principles, and the results from PIV experiments were used for model validation. Factors in actuator construction such as its curvature and outer electrode dimension, pulsing frequency for unsteady actuator operation, plasma induced electrostatic force, compressibility of the induced flow, gravitational effects, and

the entrainment action of the plasma were not included within this model. A reasonable level of matching was achieved comparing this model with experimental data. In general, the model was observed to follow the trend of variation closely to the experiment, but over predicted the jet output characteristics mostly on account of its simplifications. Streamwise characteristics of the plasma induced jet were used to identify scaling relations governing the decay of centerline and local maximum axial velocities, and these were compared to those for conventional rectangular (mass flux added) jets and synthetic (ZNMF) jets.

8.6 Tables and Figures

Table 8.1: Actuator dimensions tested.

d_i [mm]	d_o [mm]
6.35	25.4
12.7	25.4
25.4	50.8

Table 8.2: Scaling model constant C_3 values (units of s^{-1}.)

Parameter	State	$d_i = 0.635$ cm	$d_i = 1.27$ cm	$d_i = 2.54$ cm
Morphology	Ring	5.5059	9.0506	4.1817
	Quasi disk	15.0784	66.0163	24.0748
Power	3 W	8.2377	12.8437	11.0795
	4 W	0.4409	11.5734	37.6995

Table 8.3: Scaling model constant C_1 values (units of 10^5 g.cm^{-3}.)

Parameter	State	$d_i = 0.635$ cm	$d_i = 1.27$ cm	$d_i = 2.54$ cm
Morphology	Ring	2.5064	4.0102	0.3760
	Quasi disk	5.0128	0.7519	1.0026
Power	3 W	1.5038	0.7519	1.0026
	4 W	2.0051	1.0026	0.5013

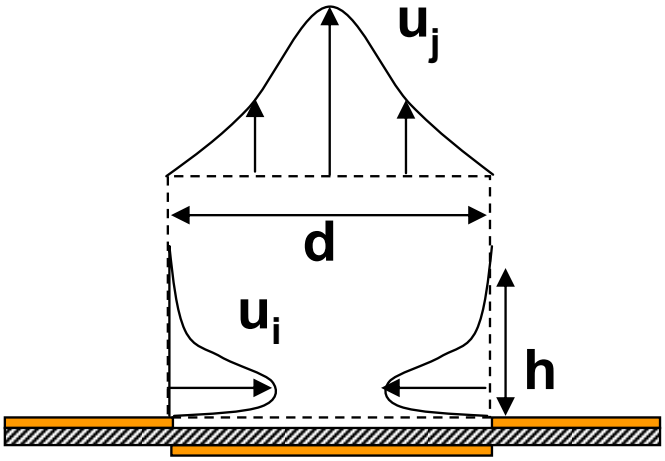

Figure 8.1: PSJA scaling schematic.

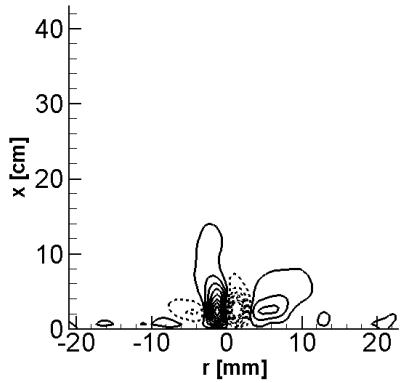

(a) d_i = 6.35 mm.

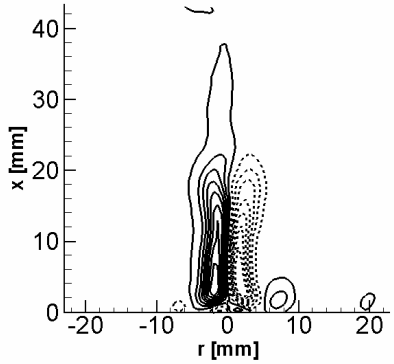

(b) d_i = 12.7 mm.

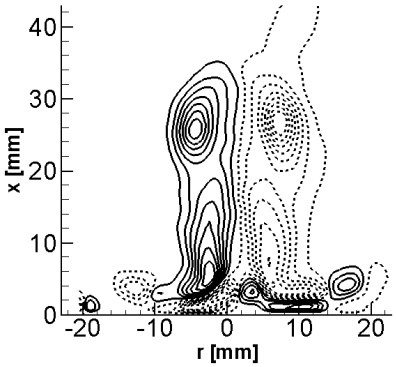

(c) d_i = 25.4 mm.

Figure 8.2: Phase-locked contours of normalized spanwise vorticity $\omega_z{}^*$. Contour levels begin at $\omega_z{}^*$=-0.843 and end at $\omega_z{}^*$=0.877, with increments of ± 0.123; 10 Hz pulsed operation of the PSJA in quasi disk morphology at t=24 ms in the actuator duty cycle.

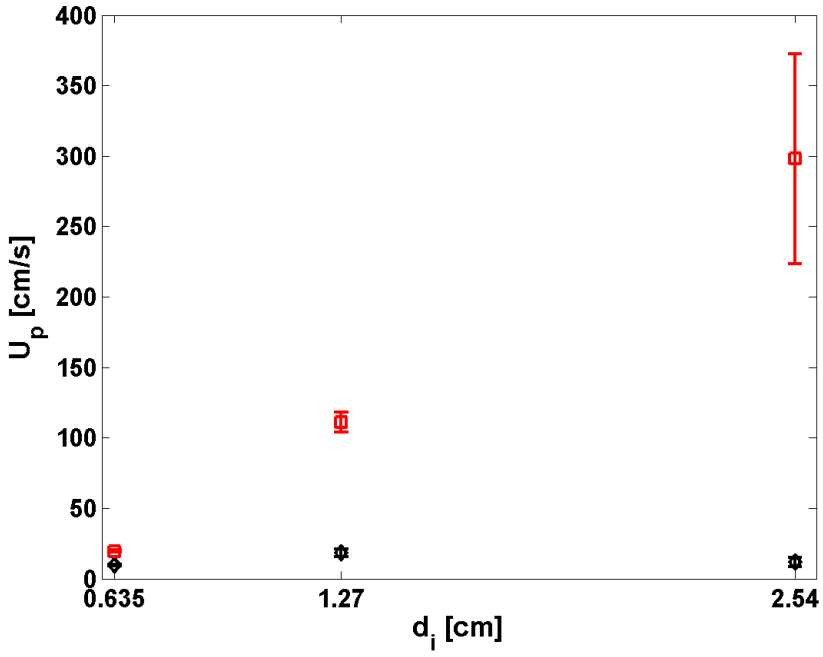

(a) Morphology variation.

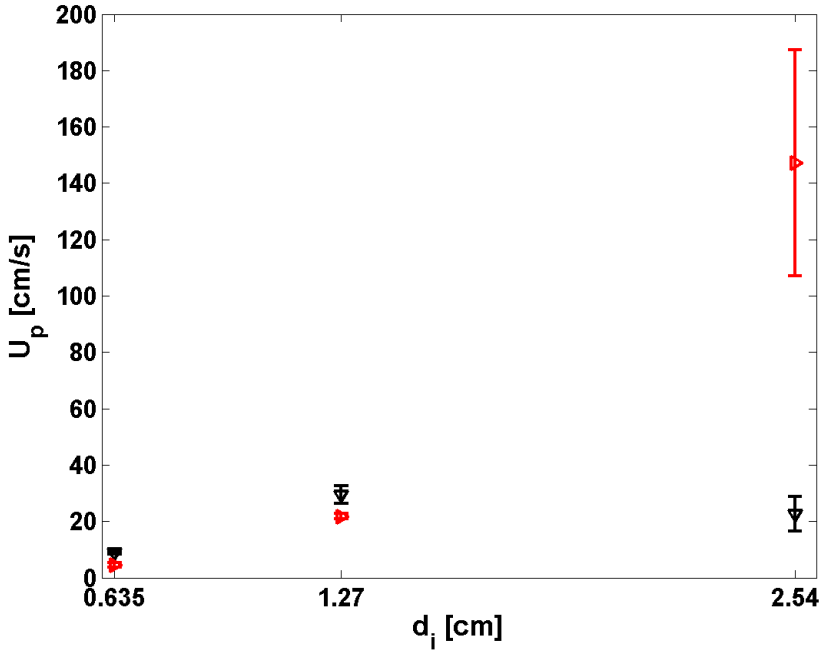

(b) Power variation.

Figure 8.3: PSJA in steady operation, peak axial velocity of the jet. $\diamond$, ring; $\square$, quasi disk; ∇, P_{in}=3 W; $\triangleright$, P_{in}=4 W; error bars indicate variation in the measurement of velocity.

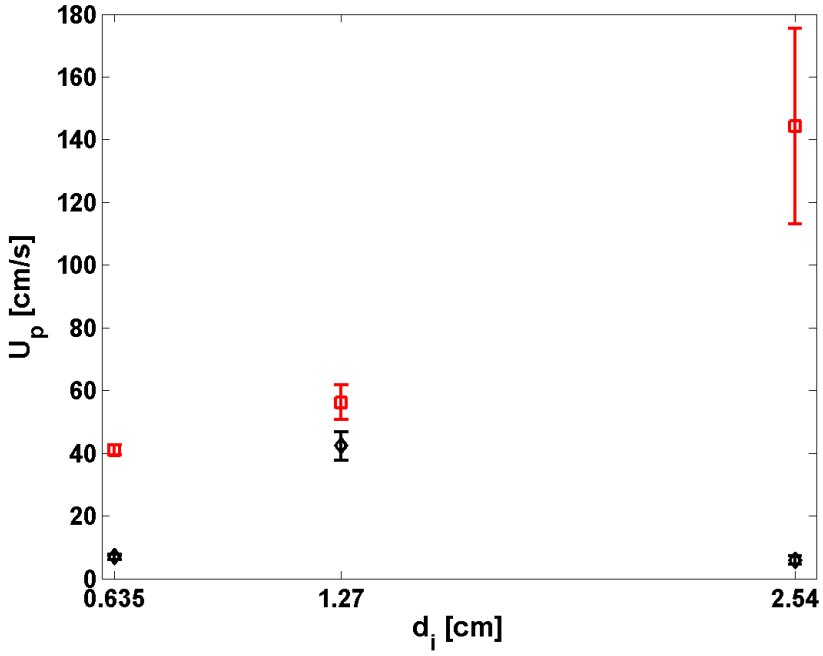

(a) Morphology variation.

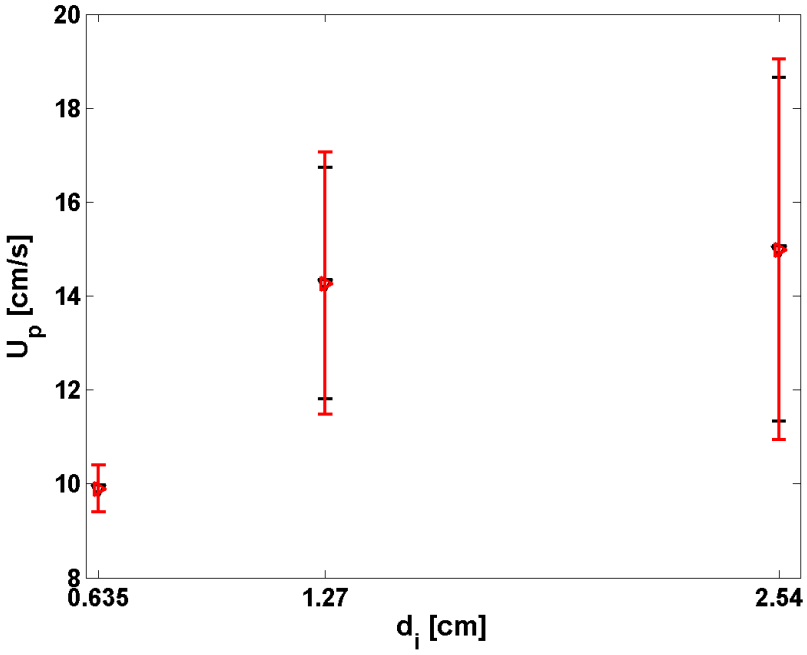

(b) Power variation.

Figure 8.4: 1 Hz pulsed operation of the PSJA, peak axial velocity of the jet. $\diamond$, ring; $\square$, quasi disk; ∇, P_{in}=3 W; $\triangleright$, P_{in}=4 W; error bars indicate variation in the measurement of velocity.

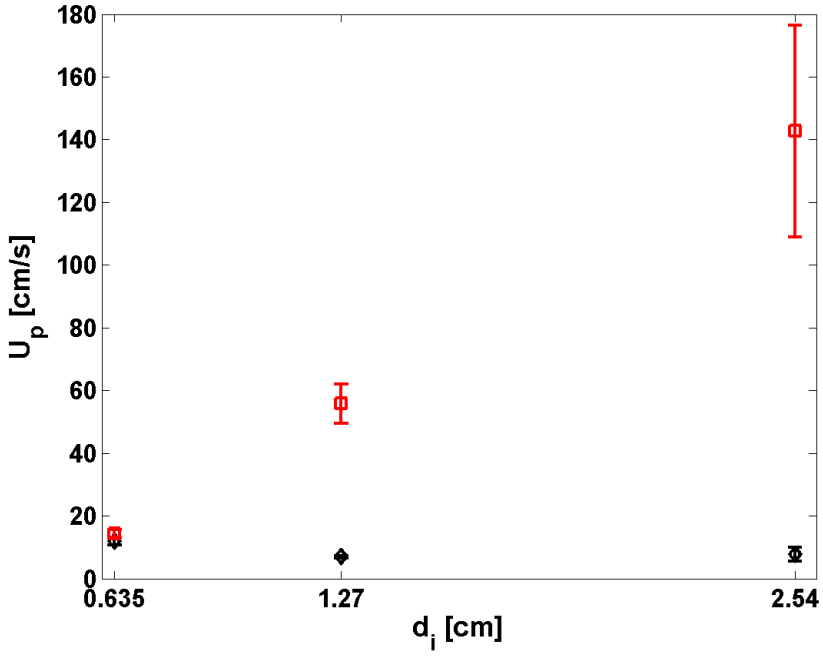

(a) Morphology variation.

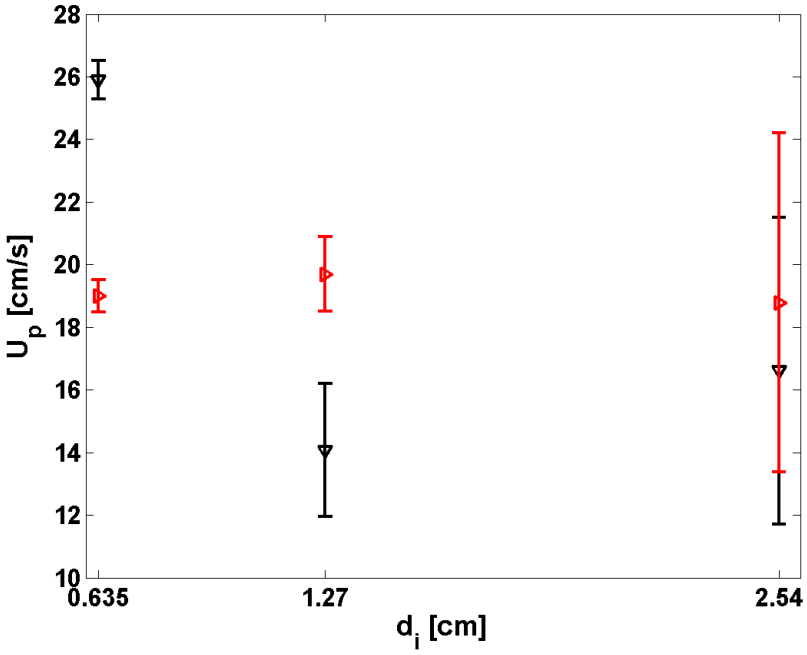

(b) Power variation.

Figure 8.5: 10 Hz pulsed operation of the PSJA, peak axial velocity of the jet. $\diamond$, ring; $\square$, quasi disk; ∇, P_{in}=3 W; $\triangleright$, P_{in}=4 W; error bars indicate variation in measurement of velocity.

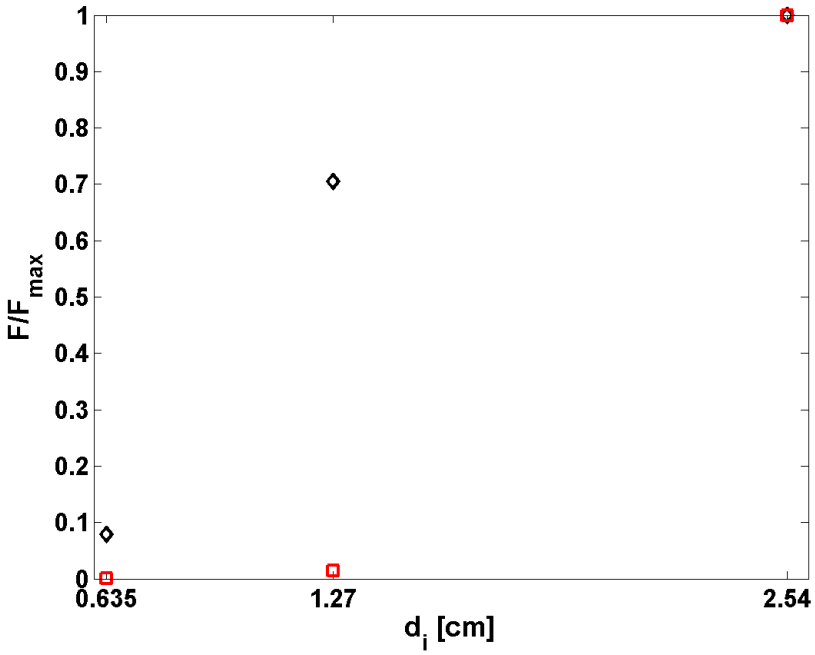

(a) Morphology variation.

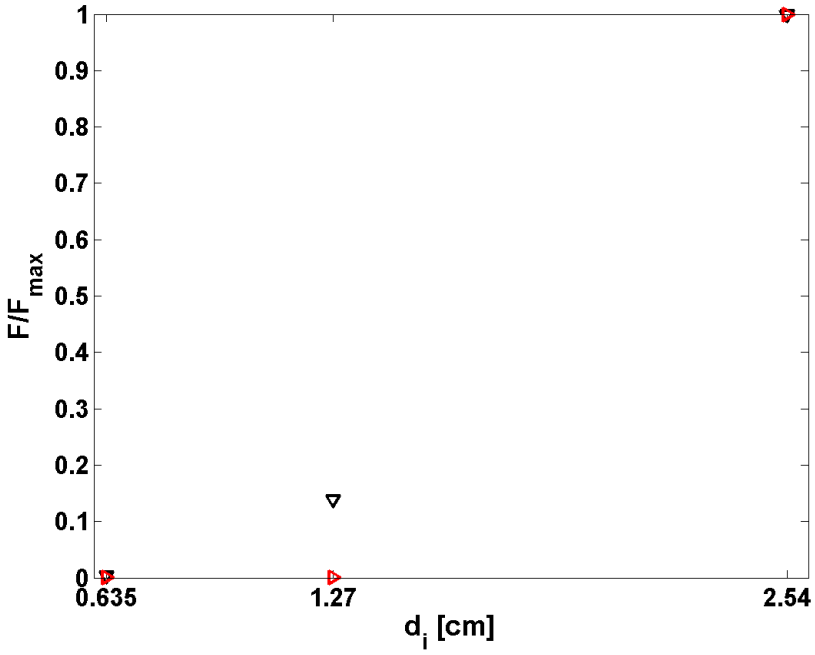

(b) Power variation.

Figure 8.6: PSJA in steady operation, normalized hydrodynamic force. $\diamond$, ring; $\square$, quasi disk; ∇, P_{in}=3 W; $\triangleright$, P_{in}=4 W.

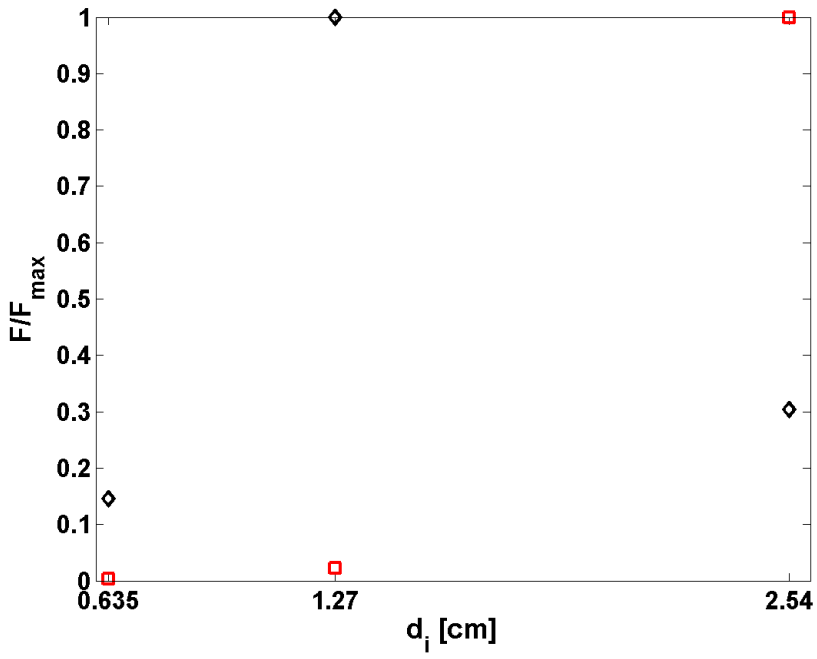

(a) Morphology variation.

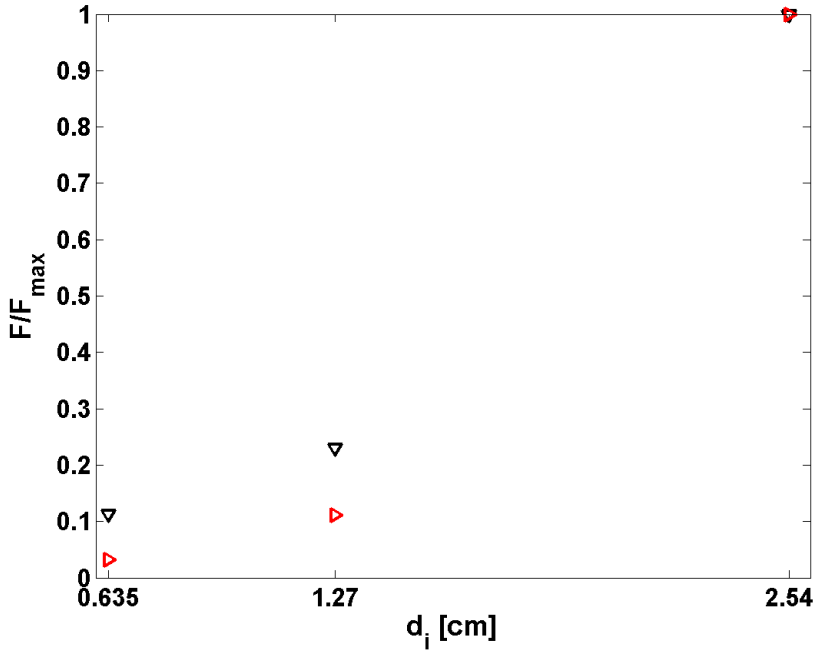

(b) Power variation.

Figure 8.7: 1 Hz pulsed operation of the PSJA, normalized hydrodynamic force. $\diamond$, ring; $\square$, quasi disk; ∇, P_{in}=3 W; $\triangleright$, P_{in}=4 W.

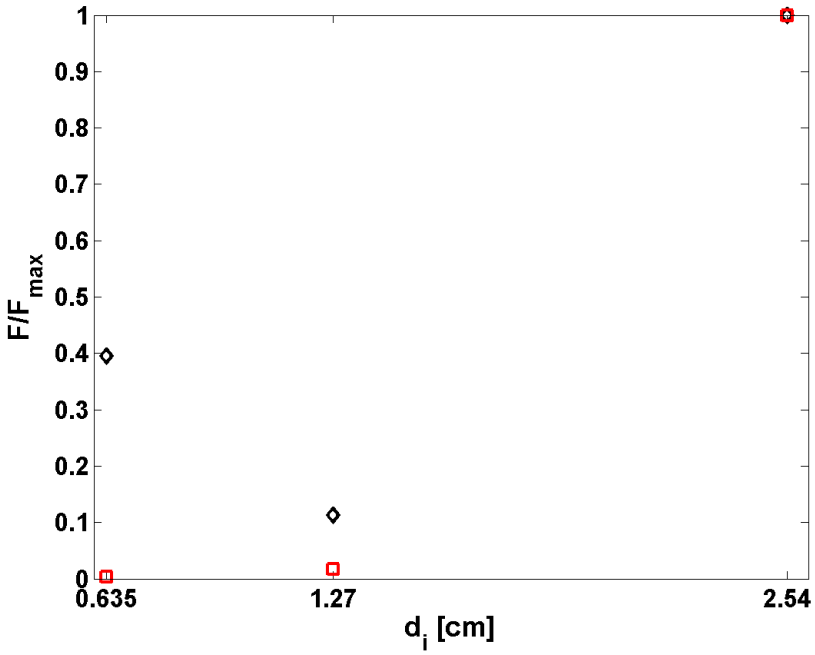

(a) Morphology variation.

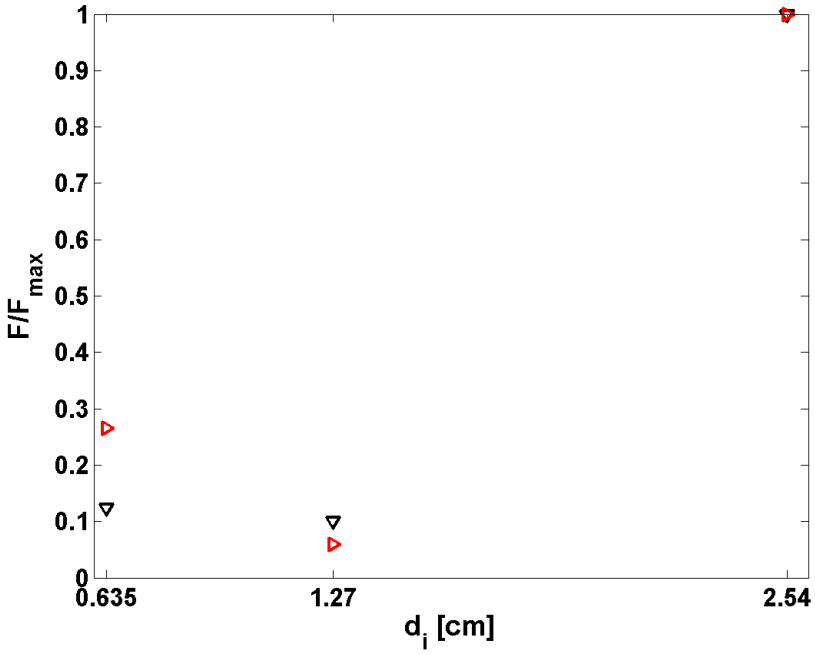

(b) Power variation.

Figure 8.8: 10 Hz pulsed operation of the PSJA, normalized hydrodynamic force. $\diamond$, ring; $\square$, quasi disk; ∇, P_{in}=3 W; $\triangleright$, P_{in}=4 W.

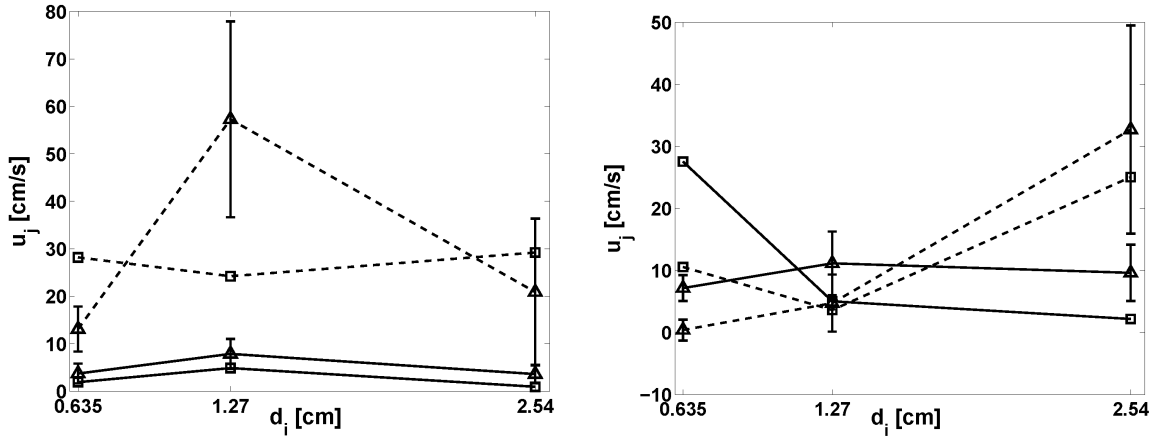

(a) Morphology variation.

(b) Power variation.

Figure 8.9: PSJA in steady operation, comparison of average jet axial velocity ($\overline{u}_j$) values at h=0.2169 cm. Solid lines indicate ring morphology and P_{in} = 3 W; dashed lines indicate quasi disk morphology and P_{in} = 4 W; Δ, PIV; $\square$, scaling model; error bars indicate the variation in measurement of velocity.

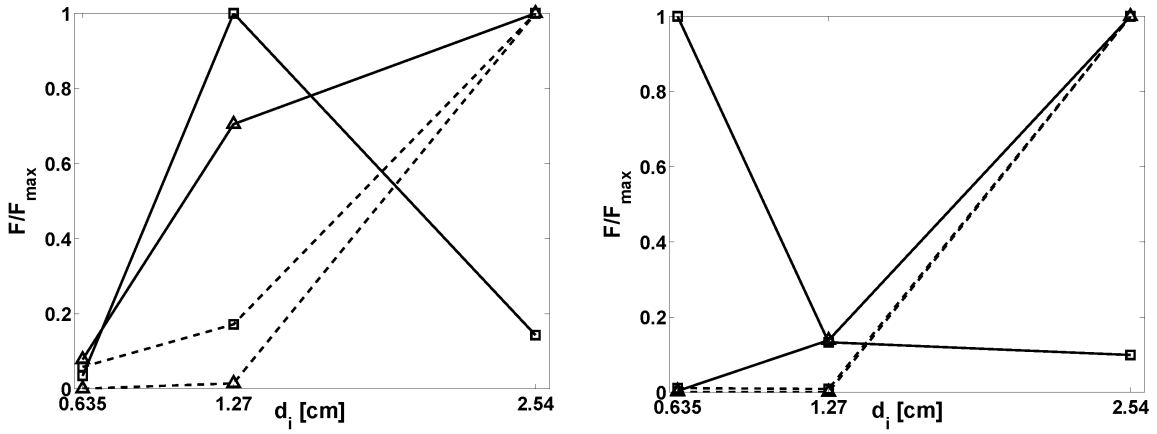

(a) Morphology variation.

(b) Power variation.

Figure 8.10: PSJA in steady operation, comparison of hydrodynamic force of the jet F values at h=0.2169 cm. Solid lines indicate ring morphology and P_{in} = 3 W; dashed lines indicate quasi disk morphology and P_{in} = 4 W; Δ, PIV; $\square$, scaling model.

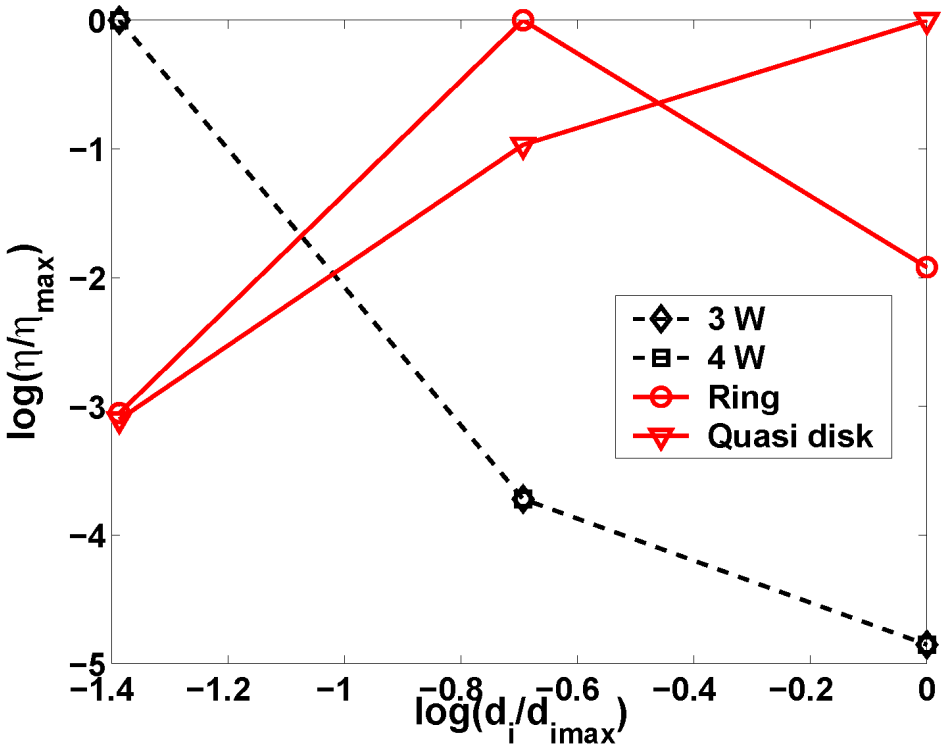

Figure 8.11: PSJA in steady operation, normalized actuator efficiencies calculated from eqution 8.3. The dashed (black) and solid (red) lines indicate variation in input power and plasma morphology, respectively, and the data has been presented in logarithmic scale for clarity.

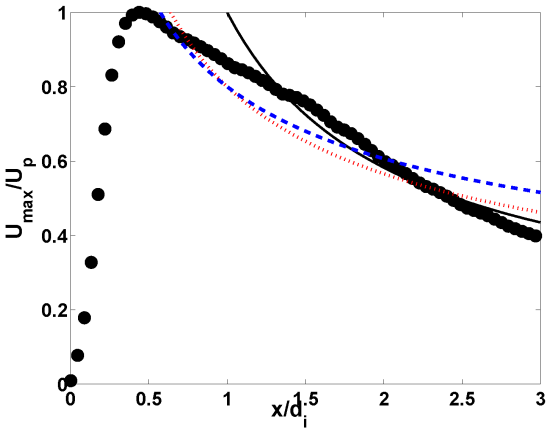

(a) Local maximum mean axial velocity.

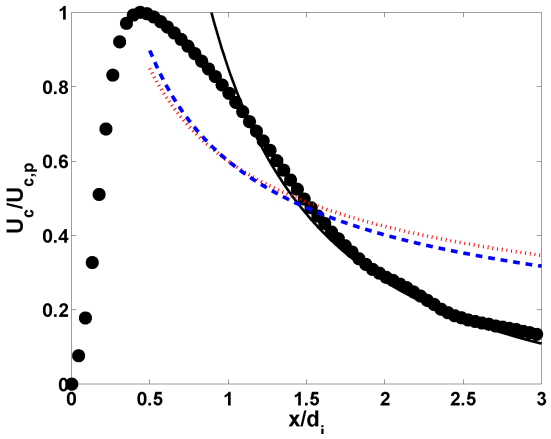

(b) Centerline axial velocity.

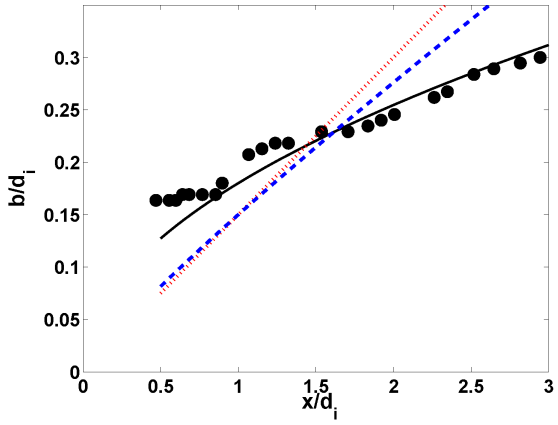

(c) Half-width.

Figure 8.12: Streamwise distribution of jet characteristics for an annular PSJA in steady operation (solid circles). Solid line (in black), dashed line (in blue), and dotted line (in red) represent empirical curve fits of the plasma induced jet, conventional rectangular synthetic (zero-net-mass-flux), and conventional rectangular (with added mass flux input) jets, respectively.

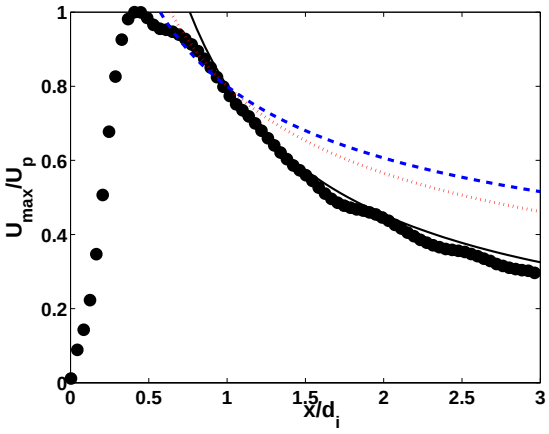

(a) Local maximum mean axial velocity.

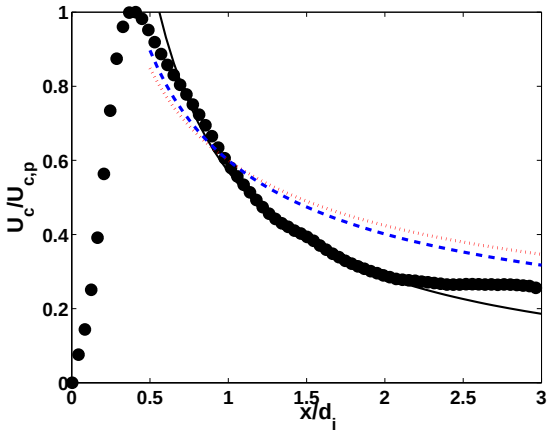

(b) Centerline axial velocity.

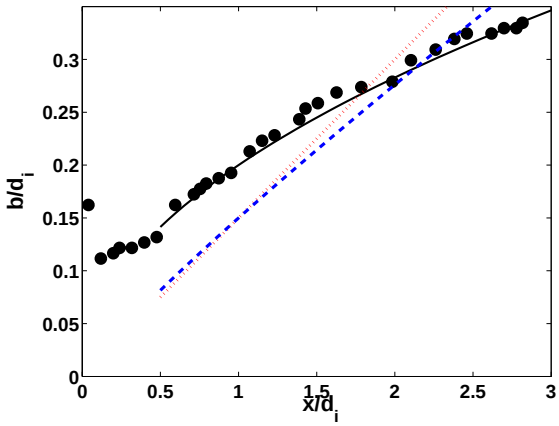

(c) Half-width.

Figure 8.13: Streamwise distribution of jet characteristics for a linear PSJA in steady operation (solid circles). Solid line (in black), dashed line (in blue), and dotted line (in red) represent empirical curve fits of the plasma induced jet, conventional rectangular synthetic (zero-net-mass-flux), and conventional rectangular (with added mass flux input) jets, respectively. The embedded electrode width was equal to the value of d_i of the actuator in Fig. 8.12.

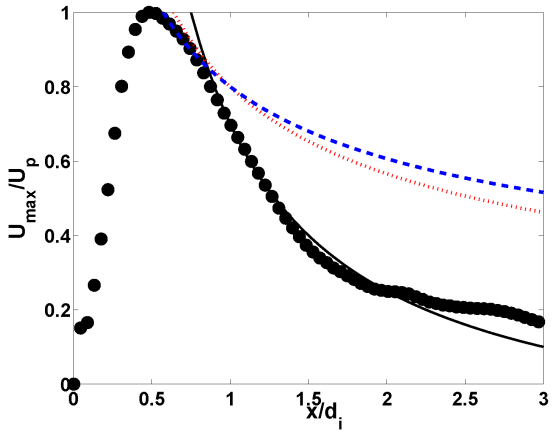

(a) $d_i = 1.27$ cm, $P_{in} = 3$ W.

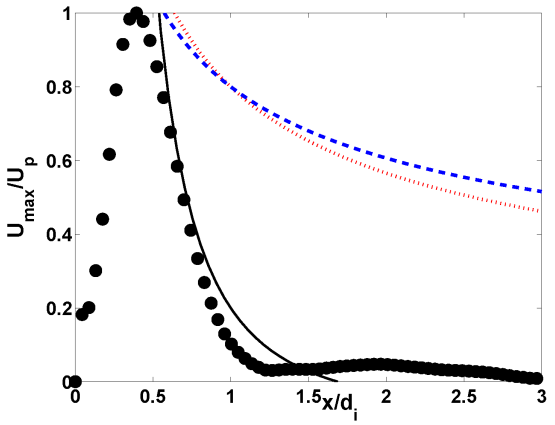

(b) $d_i = 1.27$ cm, $P_{in} = 4$ W.

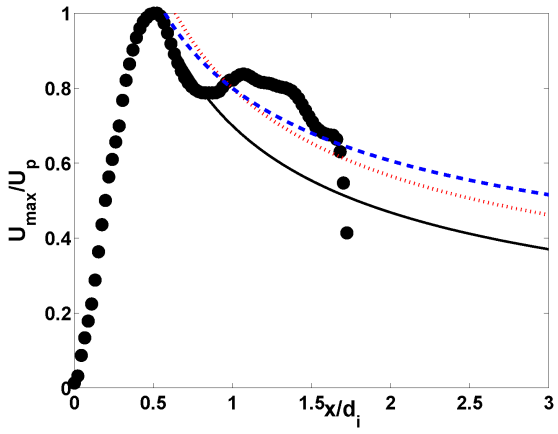

(c) $d_i = 2.54$ cm, $P_{in} = 3$ W.

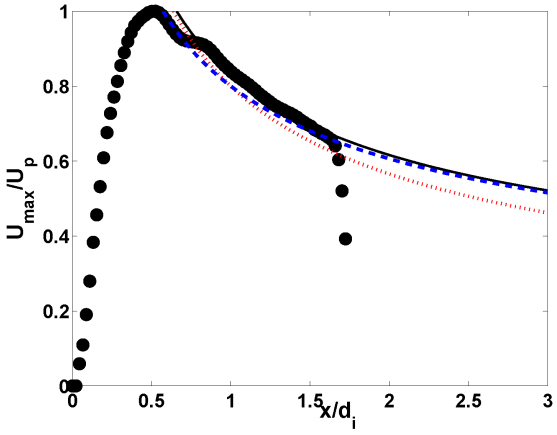

(d) $d_i = 2.54$ cm, $P_{in} = 4$ W.

Figure 8.14: Streamwise distribution of local maximum mean axial velocity for steady operation of annular PSJA (solid circles): effect of input power and d_i variation. Solid line (in black), dashed line (in blue), and dotted line (in red) represent empirical curve fits of the plasma induced jet, conventional rectangular synthetic (zero-net-mass-flux), and conventional rectangular (with added mass flux input) jets, respectively.

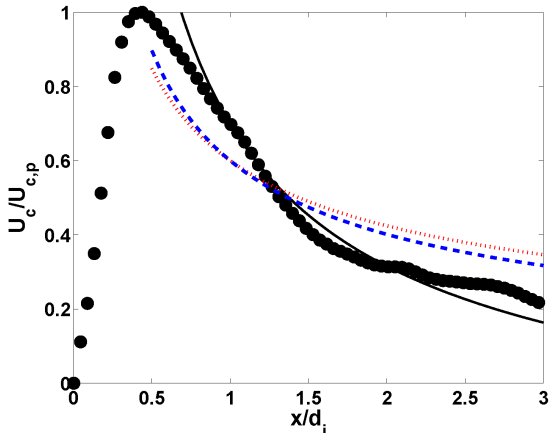

(a) $d_i = 1.27$ cm, $P_{in} = 3$ W.

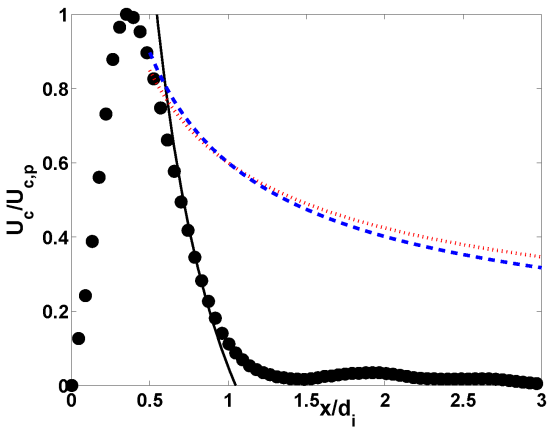

(b) $d_i = 1.27$ cm, $P_{in} = 4$ W.

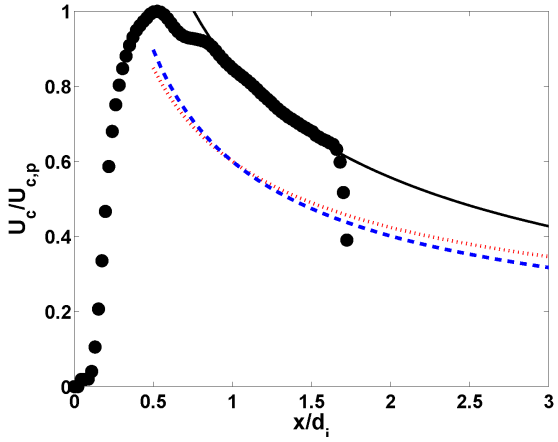

(c) $d_i = 2.54$ cm, $P_{in} = 3$ W.

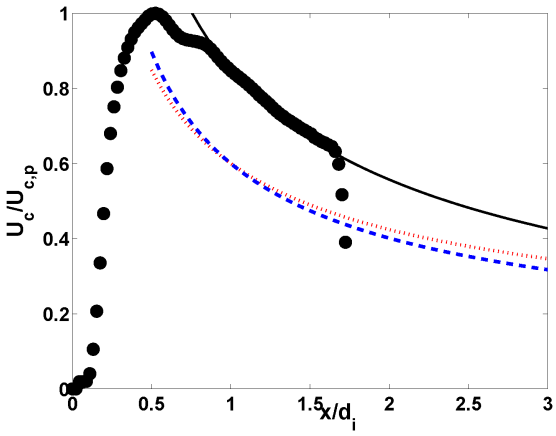

(d) $d_i = 2.54$ cm, $P_{in} = 4$ W.

Figure 8.15: Streamwise distribution of centerline axial velocity for steady operation of annular PSJA (solid circles): effect of input power and d_i variation. Solid line (in black), dashed line (in blue), and dotted line (in red) represent empirical curve fits of the plasma induced jet, conventional rectangular synthetic (zero-net-mass-flux), and conventional rectangular (with added mass flux input) jets, respectively.

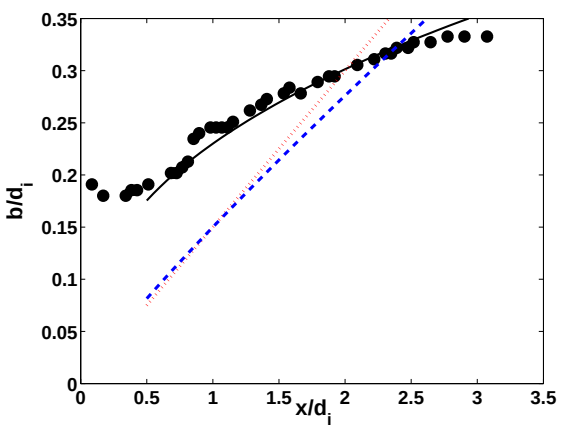

(a) $d_i = 1.27$ cm, $P_{in} = 3$ W.

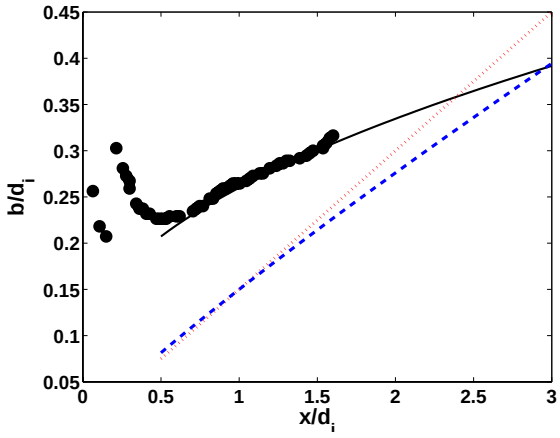

(b) $d_i = 2.54$ cm, $P_{in} = 3$ W.

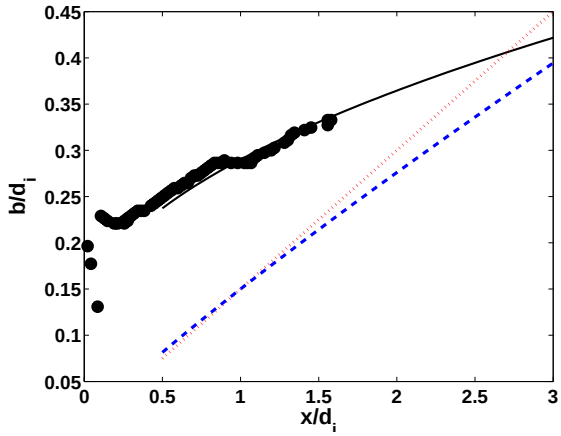

(c) $d_i = 2.54$ cm, $P_{in} = 4$ W.

Figure 8.16: Streamwise distribution of jet half-width for steady operation of annular PSJA (solid circles): effect of input power and d_i variation. Solid line (in black), dashed line (in blue), and dotted line (in red) represent empirical curve fits of the plasma induced jet, conventional rectangular synthetic (zero-net-mass-flux), and conventional rectangular (with added mass flux input) jets, respectively.

Chapter 9

CONCLUDING REMARKS

9.1 Overview

A concept for synthesizing air jets directed normal to a wall without the requirement of any external mass input employing surface based, weakly ionized, non thermal, atmospheric pressure dielectric barrier discharges was introduced. Detailed fluid dynamic characterization of the isolated jet was performed via experimentation for identifying working principles and optimum ranges of operation. Parametric dependence of the jet outputs on actuator dimensions and several operating conditions were examined. The flow field mechanisms of the plasma synthetic jet actuator in quiescent and flat plate boundary layer have been detailed. Plasma morphology based observations have been simultaneously conducted with flow field measurements to relate the plasma strength to jet characteristics. The application of these actuators for controlling the separation on a circular cylinder was examined. This concluding chapter has been organized according to the different phases of research: quiescent jet, cross flow-jet interaction, and flow control application. Directions for future work are pointed out in the last section of this chapter.

Some recent efforts in plasma flow control have employed the PSJA developed herein, such as in activating multiple arrays of these devices in synchronous/asynchronous arrangements to improve the jet performance levels (see Bolitho & Jacob [205]), and characterizing high temperature ambient conditions on PSJA characteristics with a motivation for application in microturbines (see Segawa *et al.* [206]).

9.2 Quiescent Behavior

By modifying the geometry of the electrode arrangement used for the construction of a conventional DBD plasma actuator, a novel means of tailoring the residual air surrounding the actuator in the form of a synthetic jet is introduced in this study. Similar to synthetic jets, these plasma induced jets do not require an external supply of mass input for creating the jet. The momentum imparted by the jet is non-zero, and the end application envisioned for this plasma synthetic jet actuator (PSJA) is in flow separation control through mixing enhancement. The peak velocities induced by these jets are in the order of several m/s, which limits the current domain of application of this device to low Re flows, unlike con-

ventional synthetic jets which induce higher velocities and have also been tested in a wide variety of flow scales. However, the PSJA consists of no moving parts, sufficiently low power (tens of watts), and have a definite ease of implementation over synthetic jet actuators that have a fundamental requirement of a cavity and surface modifications. In addition, plasma synthetic jets can be operated under steady conditions, thereby expanding the application envelope to areas such as micro aerial vehicle thrust generation. In a quiescent medium, the symmetric plasma region created by the PSJA (toroidal in 3-D, linear in 2-D) is found to induce near actuator entrainment of fluid on either side of the symmetry plane, and the same volume of fluid is ejected in the form of a jet normal to the actuator plane. Reversing the electrode arrangement used for the construction of the actuator results in a flow field resemblant of a suction device. However, this configuration is not pursued for the purpose of this dissertation, and only the blowing jet is examined throughout this research. Both steady and unsteady modes of operation are explored. While the global flow field features resemble those of conventional continuous and synthetic jets, many dissimilarities are also found to exist.

9.2.1 Parametric Studies

Several inputs to the system were varied to examine their relation to the jet characteristics. These included the input power, pulsing frequency, embedded electrode diameter, and plasma morphology. Increasing the input power increased the jet outputs, and no limits where the effect becomes invariant or counter-productive were identified. For the particular actuator size investigated, an optimum range of pulsing $\mathcal{O}(10$ Hz) was arrived from experimental measurements, so as to obtain maximum jet velocity for a given input power. The embedded electrode diameter controlled the available area for the plasma to expand, and hence increasing the quantity within certain bounds increased jet outputs, as expected. Time exposures of the plasma region formed in a PSJA using a CCD camera showed the existence of three different morphological regimes: a ring of plasma with a filamentary appearance at low power input, a quasi disk of plasma at moderate power input, and a full disk of plasma that formed with increasing power with plasma expansion on the dielectric surface over an area equal to that of the embedded electrode. These stages occurred in a rather discrete manner one after the other, with changing input power. For a constant size actuator, the efficiency of the actuator in imparting force onto a quiescent medium was found to be affected by both the plasma morphology and pulsing frequency, such that it was possible to operate an actuator with one of these factors outside their recommended optimum by leveraging on the other. Interestingly, the effect of plasma heating the neutral

air was found to not significantly affect the cross-stream and streamwise distribution of flow characteristics, which contributed toward clarifying an issue of major concern in the plasma flow control research community.

9.2.2 Scaling

The governing parameters to the determination of the induced flow velocity and momentum for any arbitrary plasma actuator configuration include a large set of variables that may be grouped into: system inputs of power applied across electrodes, actuator dimensions, plasma strength, pulsing frequency, and materials used for construction; operating conditions of AC voltage, frequency, waveform shape, and duty cycle; atmospheric conditions of pressure, temperature, humidity, and composition. No close-form relations between any of these factors have been proposed during the time of writing this dissertation. The effect of the first four parameters in the above set were investigated across three different values of actuator embedded electrode diameter, the characteristic dimension that dictates the amount of area available for the plasma to form and expand, in order to derive the spatial scaling behavior of isolated annular plasma synthetic jets. Two different plasma morphologies (ring and quasi disk) and input power levels (3 W and 4 W) were controlled across three different actuators. A parallel effort of analytically modeling the actuator was carried out in tandem. The model was based on a control volume that did not include the plasma induced entrainment, effects of actuator curvature, and unsteady operation. Scaling laws were arrived at, based on fundamental fluid dynamics principles. Three quantities were used to evaluate the predictive performance of this model, including the average jet axial velocity, hydrodynamic force imparted by the jet, and efficiency of the actuator in injecting non-zero momentum to the surrounding fluid. While the first two metrics were compared with experimental values and reasonable matching was observed, the efficiency of the actuator provided useful insight on the effects of these parametric variations. A summary of items of interest follow

- ring morphology—jet outputs indicate existence of an optimum actuator size
- quasi disk morphology—jet outputs increase with d_i
- increased power input—jet outputs increase with d_i
- No unique optimum pulsing frequency observed to exist across all the input conditions
- Actuator efficiency increases with decreasing d_i , and do not follow an inverse square relation with d_i

On the comparison of the plasma induced jet characteristics with conventional rectangular continuous and synthetic jets, the following are worth noting:

- Entrainment of fluid near the actuator surface is seen in both plasma induced and conventional synthetic jets, with the result that the momentum flux variation in the streamwise direction is no longer invariant
- As a result of the above reason, profiles of both plasma and conventional synthetic jets show deviation from self similarity of continuous jets
- Self similarity of PSJA occurs at very close distances to the actuator, in direct contrast to other conventional jets
- Turbulent kinetic energy contours show opposite trends in plasma induced jets as compared to conventional jets, in that the diffusion of energy decreases in the streamwise and cross-stream directions in the latter, which is the opposite to what is observed in the former
- Plasma synthetic jets, in general, exhibit a low peak velocity magnitude located very close to the actuator, an increased rate of decay of local maximum and centerline velocities, and lesser spreading than conventional continuous and synthetic jets
- Increasing actuator diameter increases the spreading of the jet and lowers the decay rate to where it is not close to a sharp decrease from the peak value

9.3 Cross Flow Interaction

The interaction of the PSJA with an external flow was documented by implementing the actuator on a flat plate placed at zero inclination to the free stream direction. Three values of blowing ratio were examined on sufficiently low speed flows. It was observed that the actuator essentially created a separated flow region that was well demarcated from the main flow. This interaction domain formed by the PSJA modified the direction of the flow, as well as the integral boundary layer characteristics. The penetration of the jet into the free stream was found to be directly affected by input power. Not only did increasing power increase the depth of jet interaction with cross flow, but it also generated standing longitudinal vorticity with a sense of rotation opposing the main flow. Within the vicinity of the plasma, the displacement thickness increased beyond its upstream value, and no return to this value was observed downstream of the actuator, within the field of view of the experiment. Depending on the construction of the actuator, different flow field

mechanisms of plasma synthetic jet-cross flow interaction were identified. For an annular PSJA, the mechanism resembled closely to a conventional jet in cross flow, where the jet penetrates the flow such that it does not completely lose its identity (unless if subject to free stream values much greater than jet velocity). For a linear PSJA, however, the mechanism resembled closely to that of a conventional linear plasma actuator in cross flow. In the latter case, the starting vortex of the plasma synthetic jet that was facing upstream of the cross flow was eradicated completely by the incoming free stream, and the formation of a spatially fixed cross-stream vortex whose strength weakens with increasing flow velocity was observed. The effectiveness of the actuator in modifying the boundary layer characteristics by penetrating the main flow was found to decrease with baseline flow Re, as expected.

9.3.1 Separation Control

The flow over a circular cylinder was considered as the problem of interest to examine the applicability of plasma synthetic jet actuators toward flow control applications. Two sufficiently low speed flow velocities were considered, and the performance of conventional linear plasma and linear plasma synthetic jet actuators were compared. The values of actuator pulsing frequency where chosen so as to effect an $\mathcal{O}(1)$ actuation relative to the wake shedding frequency. The wake deficits were marginally tightened by both actuators at the lowest Re, which effectively would increase the aerodynamic performance benefits. The input power levels employed were of such low magnitude herein that substantial performance improvement was not registered during any particular actuator/flow condition. However, these effects are expected to be scalable within certain limits, so implementation of PSJA based flow control appears very promising, especially considering the flexibility of the design that is possible with this actuator, as outlined below.

9.4 Suggestions for Future Work

9.4.1 Temporal Characterization

The measurements presented within this dissertation are obtained using digital particle image velocimetry (PIV). This technique provides excellent resolution of the whole flow field and instantaneous information necessary to describe the jet formation and evolution. However, this diagnostic method suffers from limited temporal resolution, which is important to characterize the jet. The maximum sampling rate achievable using the experimental setup herein was 15 Hz, typical capture rates used in time-averaged PIV was 10 Hz. It is clearly seen that such a time scale filters out most of the turbulent information from the

data. Hence, high time resolution measurements of PSJA characteristics in quiescent and cross flows are required. This will enable access to previously undetermined information on statistics such as the advection rates of the starting vortices, power spectrum, and response of the actuator along various phase times of periodicity in the AC input. Essentially, this will complement PIV observations and help to construct a spatio-temporal picture of actuator performance variation across several associated parameters. In addition, hot wire data can be used to obtain information on the far field of the jet (10–100 diameters downstream) to see if the scaling relations determined in this dissertation are valid throughout the jet flow field or if there is change in the behavior. The latter is a concern in PIV due to the tedious nature of setting up an experiment, and mostly having to compromise the field of observation (very small windows), for the sake of maintaining a reasonable spatial resolution.

9.4.2 Cavity-Actuator Concept

Conventional cavity based synthetic jet actuators are usually driven at the Helmholtz (resonance) frequency of the system, such that maximum amplitude of the jet driver (diaphragm, piston, etc.) can be obtained for lower power inputs. A similar idea can be used to drive a PSJA placed in a cavity such that the plasma region forms on its bottom surface. In this manner, the actuator can be operated at the resonance frequency of the cavity, thereby resulting in increased entrainment of fluid and consequent improvement in jet outputs. Arrays of such cavity driven actuators can be then arranged in a suction/blowing arrangement to create potentially limitless design space for flow control applications.

9.4.3 Application Studies

The field of plasma actuators currently abounds with numerous possibilities for its use in flow control. The prospects of operational implementation of these devices in practical applications beyond the laboratory level still largely remains to be examined. In this regard, a few potential applicability studies of these actuators are identified herein.

Forebody Vortex Control

Most conventional missiles and other slender bodies of revolution are limited in their maneuverability, particularly during high angle of attack flight. This is due to two major issues: boundary layer separation on the forebody due to incoming flow and body surface conditions, and unwanted side forces arising from the asymmetric vortex shedding occuring post separation. The inability to control missile trajectories arises primarily because of the

forces generated by the forebody vortices. In this context, some researchers have attempted to restore symmetry in the vortex shedding either passively by placing strakes (Ng [207]), or actively by means of momentum injection at specific points in the forebody and the cylinder (Williams and Papazian [208]). While stabilized flight is achieved with symmetric vortex shedding from the forebody, methods to exert control of the vortex shedding process itself has its inherent benefits in enhancing maneuverability through the introduction of desired side forces. Classic flow control approaches such as blowing [207] have been shown to be effective in vortex control, and recent results include laboratory level demonstrations of closed loop flow control at high angle of attack using active microvortex generators (see Patel *et al.* [209]). Annular plasma synthetic jet actuators can be employed to examine their applicability in forebody vortex control. An array of actuators can be located on the body such that the arrangement can be either collectively or independently actuated to stabilize the flight by restoring vortex symmetry or introducing side forces along different directions in the flow for trajectory control (Fig. 9.1).

Combustion Enhancement

The current emission standards required by federal and international aviation agencies have posed an important challenge to the gas turbine engine industry. Incomplete mixing of the fuel and oxidizer results in the emission of pollutants such as nitric oxide, carbon monoxide and unburned hydrocarbons during the combustion process (see Fric [210]). This is precipitated mostly due to the requirement for the mixing to occur within very short length and time scales in the combustor. Enhancing the fuel-oxidizer mixing process prior to combustion not only boosts the efficiency of the process, but also reduces the emission of undesirable compounds, and in addition, exerts substantial influence on the jet noise control. Traditional passive (mechanical tabs, e.g. Samimy *et al.* [211]) and active (vortex generators, e.g. Zaman *et al.* [212]) flow control device studies have been performed for axisymmetric jets. Most recently, Wang & Menon [133] conducted a numerical investigation of enhancing fuel air mixing using MEMS based synthetic jet actuators. They observed that introducing periodicity in the flow (by means of the actuators) affected mixing markedly mostly on account of additional entrainment effected by the control method. Plasma actuators offer a easily implementable, low power method of mixing enhancement. A promising direction of applicability research of plasma discharges is in the area of gas turbine combustion flow control. Figure 9.2 shows plasma actuator concepts for mixing and combustion enhancement in the flow experienced in a typical fuel injector. Steady and unsteady pulsed operation of the actuator may be used to produce varying effects on the baseline flow, with the plasma

jet forcing either in directions that are axial or normal to the main flow.

Thrust Vectoring

Modifying the characteristics of conventional jet flows by either changing the main flow direction or the spreading and mixing rates have important implications in thrust vectoring and noise control applications. Altering the direction of a primary jet flow by means of introducing a secondary flow have been previously investigated (e.g. Strykowski *et al.* [130]). Recent works have incorporated zero mass flux jets for thrust vectoring using either conventional cavity driven synthetic jet actuators (such as Smith & Glezer [128]) or a combination of steady suction and blowing (Bettridge *et al.* [213]). Similarly, plasma synthetic jet actuators can be employed for the purpose of vectoring a primary jet. Plasma synthetic jet actuators do not require to be operated in a pulsed manner like conventional synthetic jet actuators. Figure 9.3 shows a concept for using plasma actuators in jet vectoring applications. Note that the creation of "trapped" secondary vortices seen in the operation of the PSJA introduces nominally low pressure regions of interaction between the primary and plasma synthetic jet (similar to conventional synthetic jets [128]), and this eliminates the need for having extended mechanical surfaces such as diffusers or collars [130].

9.5 Summary

A new actuator employing DBD plasma, the plasma synthetic jet actuator (PSJA), has been developed in this research effort to synthesize a vertical jet from a residual air flow, with characteristics similar to conventional jets driven by mechanical elements. Such jet flows are highly interesting from an engineering standpoint due to their use in the control of fluid flows (such as to delay boundary layer separation, for example), and this serves as the underlying motivation for exploration of the actuator concept presented herein. In the PSJA, a region of DBD plasma was created by the application of high voltage, high frequency AC to the electrodes of the actuator, and a jet was induced due to the entrainment of near actuator air available in the fluidic system (thereby eliminating the need for an elaborate external air supply) and subsequent expulsion of this volume of air in the form of a jet. Depending on whether the actuator was operated in a steady or pulsed manner, vortical structures were observed to be generated in addition to the zero-net-mass-flux jet. Compared to its mechanically driven counterparts (such as a membrane motion driven synthetic jet actuator), the beneficial features of no-moving parts design, ease of construction and implementation of the PSJA on any arbitrary surface renders this actuator a highly flexible configuration for application to a wide range of aerodynamic flow control

problems. Furthermore, merely reversing the actuator design results in a suction device, and arrays of these blowing/suction actuators could thus be used in steady/unsteady modes of operation to create potentially limitless design space for the active control of fluid flows. The present study was focused on the fluid dynamic characteristics of a single PSJA in the blowing configuration with and without an external baseline cross flow. Several optimum operational parametric ranges of system inputs to the actuator were found and scaling of jet characteristics were presented in relation to conventional jets. The separation control applicability aspect of the PSJA was investigated using the low speed flow over a circular cylinder as a test problem, and the results showed promising benefits in the reduction of wake velocity deficits, albeit only over a low free stream velocity range. Some avenues for future research on design variation and application studies of plasma synthetic jet actuators were noted in this concluding chapter.

At present, whether this low speed limitation of plasma actuators can be surpassed or not appears to be the big question facing the research community. The PSJA concept presented in this dissertation provides a new method to enhance the flow control applicability of a conventional plasma actuator by leveraging on its flow field behavior. The increased flow field penetration, generation of standing vortical structures, and the capability of tailoring blowing/suction arrays essentially renders the PSJA a highly attractive device for unsteady flow control as compared to conventional plasma actuators. Techniques to push the low Reynolds number barrier further would continually have to be explored in the future, in order to transition plasma based flow control technology from the existent laboratory level to real time application in large scale fluid engineering problems. In this context, numerical modeling of plasma actuators currently appears to be an advisable direction toward achieving dual objectives of actuator design optimization as well as in elucidating the mechanisms of the plasma-neutral gas interaction. On the experimental front, a fairly large database of flow control effects of conventional plasma actuators is available. However, a lack of consensus on the metrics needed to record and report experiments in plasma flow control exists somewhat, as a result of which a fair amount of the data is not entirely useful to the modeling community. Well-controlled, focused experimental efforts seem to be the need of the hour, and a balance between investigation of underlying physical mechanisms and applicability studies is required. A detailed spatio-temporal characterization of the plasma and neutral gas characteristics (such as density, temperature, pressure, etc.) near the actuator, for example, is clearly lacking, and would be extremely useful for advancing the state-of-the-art. Experimental plasma flow control studies such as the one presented in this dissertation are necessary in order to develop newer methods to improve the actuator influ-

ence on the flow field, and also to identify areas where the existing state of this technology can be applied to result in beneficial outcomes. Given the potential engineering applicability and the wealth of scientific knowledge that yet remains to be unraveled, plasma flow control will continue to interest researchers for the years to come.

9.6 Tables and Figures

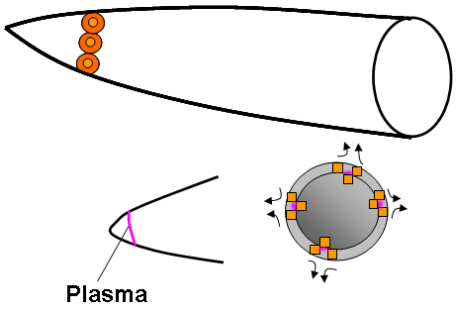

Figure 9.1: Forebody vortex control concepts using plasma actuators.

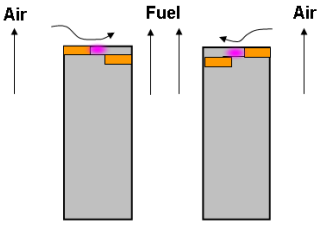

(a) Plasma jet axial to flow.

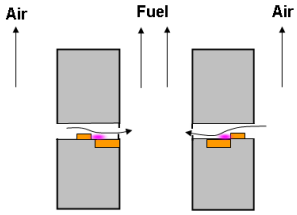

(b) Plasma jet normal to flow.

Figure 9.2: Combustion enhancement concepts using plasma actuators.

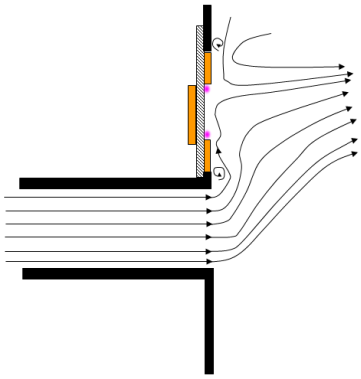

Figure 9.3: Thrust vectoring with plasma actuation.

Appendix A

TEMPORAL SCALING

The objective herein is to identify a non-dimensional time scale for the actuator induced vortex rings observed in the flow field. The inputs to the PSJA are: P_{in}, d_i, f_p, and plasma morphology. The last factor can be assumed to be somewhat coupled to the input power P_{in}, and therefore need not be treated as an independent term. The length scale of the PSJA flow field is the embedded electrode dimension d_i. The characteristic time scale is the period of the actuator pulsing f_p, as the plasma actuator AC frequency can be treated to be decoupled to the flow field effects, $f_{AC} >> f_{flow}(\sim f_p)$. Since the speed of the jet flow is $\mathcal{O}(1$ m/s), the kinematic viscosity of air ν_{air} (same units as circulation) also plays an important role in the development of near wall vorticity. It must be noted that most of these arguments are derived based on a dimensional analysis sense, and the analytical results will be compared to those of experiments for the purpose of validation. The power input per unit length of the actuator is a constant, which results in the proportionality,

$$P_{in} \propto d_i$$

The input electrical power P_{in} is directly related to the observed flow field effect of vortex structure and synthetic jet formation. This can be thought of as being similar to the stroke of a mechanical element (such as a piston, diaphragm, etc.) embedded in a cavity that serves to drive and sustain a conventional continuous or synthetic jet flow engendered in the surrounding fluid, typically formed by the advection and interaction of multiple vortex structures created at the exit of the cavity orifice. The power input directly affects the flow field momentum. Combining the above observations enables a relation for the power input in terms of other actuator system inputs as

$$\varepsilon P_{in} = \rho_{air}\, \nu_{air}\, {u_{driver}}^2\, d_i \tag{A.1}$$

where ε is a function of the efficiency of power transmission from the driving circuit to that across the plasma actuator, and u_{driver} is the characteristic velocity scale for the plasma synthetic jet driver. As no impedance matching of the transformer output was performed herein, the electrical loss is expected to be quite significant. In the above relation, the effect of buoyancy is excluded, following the results presented earlier on the quiescent plasma synthetic jet. The discharge characteristics have been shown to be affected by

the ambient conditions, which in this case is included indirectly using the density of air during actuator operation. Also, the power input is directly proportional to the driving flow momentum ($\rho {u_{driver}}^2$), which from a physical standpoint, is in agreement with experimental observations. A relation for u_{driver} of the PSJA may hence be synthesized in terms of P_{in} as follows,

$$u_{driver} = \sqrt{\frac{\varepsilon P_{in}}{\rho_{air} \nu_{air} d_i}} \tag{A.2}$$

such that a increased jet velocities can be obtained by increasing P_{in}. Thus, similar to the stroke length of a conventional mechanically driven jet representative of a non-dimensional time scale of vortex ring formation, a PSJA formation parameter may be expressed in terms of the driving velocity, length, and time scales as

$$F^* = \frac{u_{driver}}{d_i \, f_p}. \tag{A.3}$$

To check the validity of these considerations, an estimate of the starting vortex ring circulation can be formulated in terms of the above velocity and length scales as,

$$\Gamma_{model} = u_{driver} \, d_i \tag{A.4}$$

Note that there is no direct dependency of the pulsing frequency f_p on the predicted circulation value. As a result, for a fixed power input, Γ_{model} will effectively be constant, regardless of f_p. This model can thus be used to infer the vortex formation independent of pulsing. A comparison between model and experiment (time averaged PIV) based circulation strengths of the starting vortex can thus be used to construct the error involved in the above analytical model as

$$\epsilon_\Gamma = \frac{\Gamma_{model}}{\Gamma_{PIV}} \tag{A.5}$$

The main source of error in this model arises from the lack of a definition for ε across different actuators as well as input states. Such information is unavailable on account of the limitation in conducting measurement of power available across the plasma actuator electrodes. Herein, ε will be treated as a fixed term related through a power law to the actuator efficiency. Previous results showed that the operating efficiency of the plasma actuator based on input electrical power and output hydrodynamic force (and jet velocity) is extremely low $\mathcal{O}(10^{-4})$. For the results presented below, the use of $\varepsilon = \eta^2$ is attempted.

Figures A.1-A.2 show the variation of starting vortex circulation across different phases of the PSJA pulsing cycle. Both model prediction from equation A.4 and experimental measurements, and the associated error ϵ_Γ (equation A.5) are shown for 1 Hz and 10 Hz pulsing of PSJA with d_i=1.27 cm. The input power for these runs was 10.5 W per cycle,

and the efficiency η value used was $1{\cdot}10^{-4}$. In both cases, the experimental circulation (calculated using $\oint udl$) does not match the model values with any reasonable accuracy. In general, equation A.4 over predicts the value of circulation, most ostensibly due to the lack of sufficient details near the actuator, and possibly due to the assumption of incompressibility. Phase-averaged estimates of starting vortex strength is shown via dashed lines, and it is interesting to note that this value corresponds to approximately $60{\pm}5$ m^2/s for both values of pulsing. This suggests that it is the power input that controls the average circulation of the starting vortex (an implicit assumption in the model above) as compared to the pulsing frequency. The latter factor, however, affects the rate of advection of the plasma induced vortices in the flow field. The formation parameter for 1 Hz pulsing was 106.1674, while that for the 10 Hz pulsing was 10.6167.

The effect of varying input power and actuator dimension on the starting vortex circulation is shown in Fig. A.3. These were obtained from phase-locked PIV measurements at $t = 24$ ms in the 10 Hz pulsing cycle. The value of $\varepsilon = \eta^2$ was the same as that used in the previous results. It is seen that with the exception of 3 W power input, a direct relation between actuator size and vortex strength (assumed in the model) is observed in PIV. However, the actual relation between Γ and d_i departs from the linear form in equation A.4. Also, with increasing power input, the strength of the starting vortex increases, as expected from the model. The 1.27 cm actuator appears to have the most discrepancy (as much as an order of magnitude) between the model and experiment, while ϵ_Γ appears to be less than 5 for the other two larger actuators.

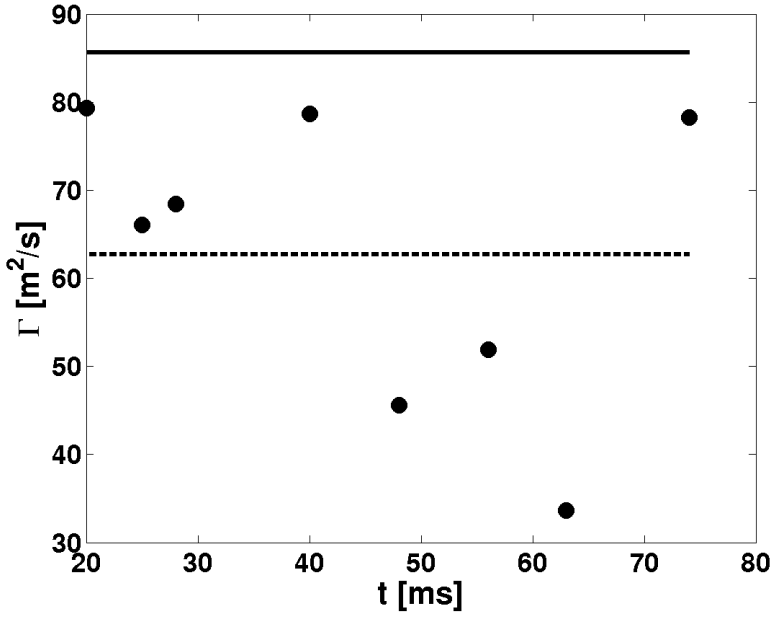

(a)

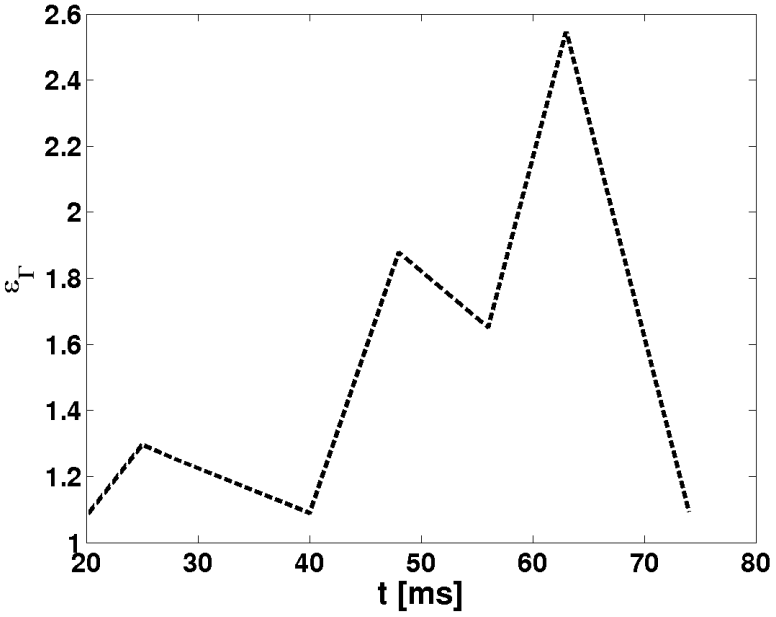

(b)

Figure A.1: (a) Starting vortex circulation of annular PSJA (d_i=1.27 cm) pulsed at 1 Hz; solid and dashed lines indicate model and experiment (phase-averaged), respectively, where the circles correspond to measurement values, and (b) error between prediction and experiment.

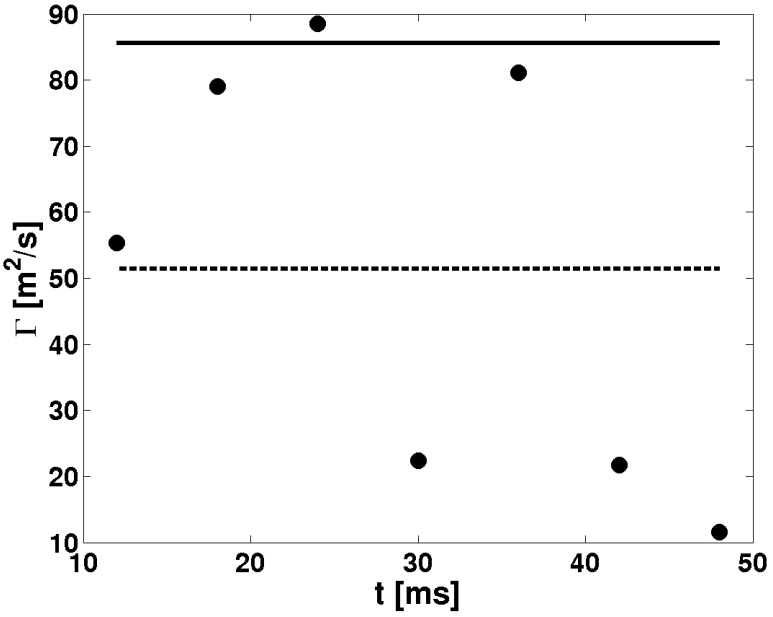

(a)

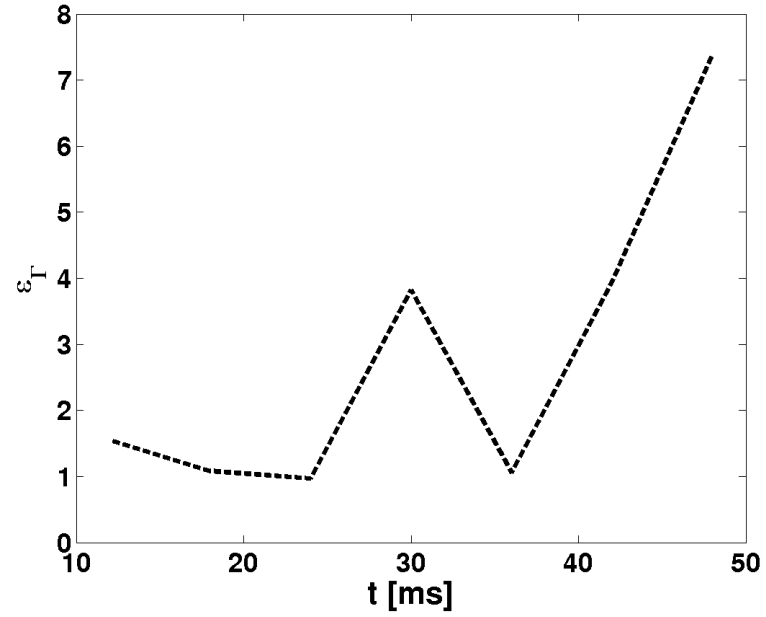

(b)

Figure A.2: (a) Starting vortex circulation of annular PSJA (d_i=1.27 cm) pulsed at 10 Hz; solid and dashed lines indicate model and experiment (phase-averaged), respectively, where the circles correspond to measurement values, and (b) error between prediction and experiment.

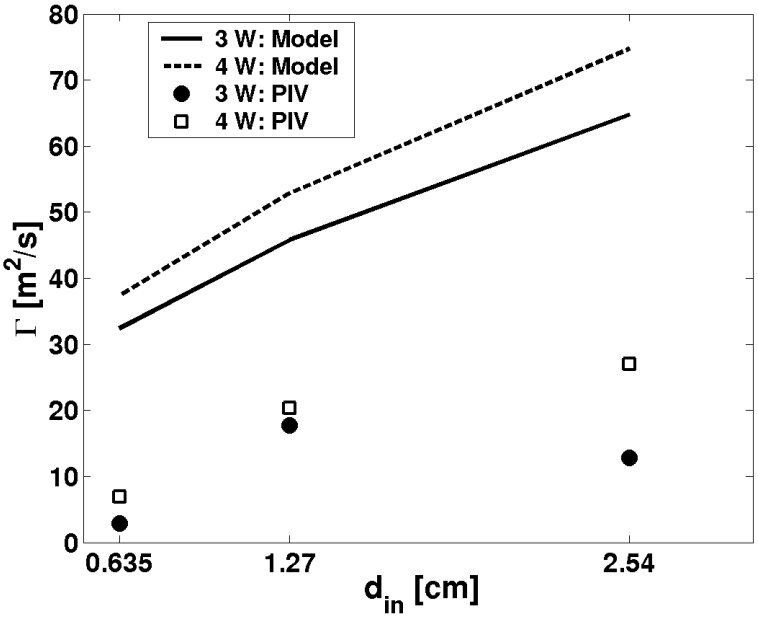

(a)

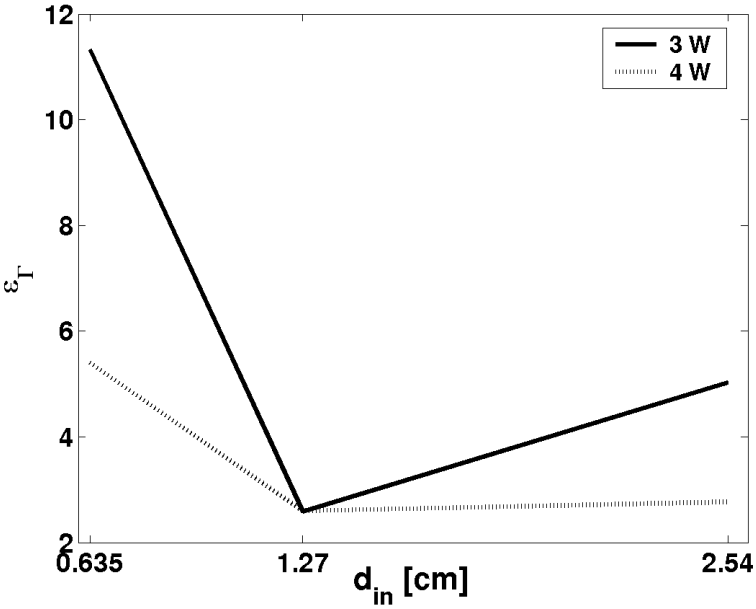

(b)

Figure A.3: Effect of actuator size and power input on the starting vortex circulation of annular PSJA pulsed at 10 Hz: (a) comparison, and (b) error between model and experiment.

BIBLIOGRAPHY

[1] M. Gad-El-Hak, A. Pollard, and J-. P. Bonnet (editors). *Flow Control: Fundamentals and Practices*. Springer–Verlag, New York, 1998.

[2] P. B. S. Lissaman. Low-Reynolds-Number Airfoils. *Annual Rev. of Fluid Mech.*, 15:223–239, 1983.

[3] T. Peacock, E. Bradley, J. Hertzberg, and Y. C. Lee. Forcing a Planar Jet Flow Using MEMS. *Experiments in Fluids*, 37:22–28, 2004.

[4] S. Sivasegaram S. R. N. De Zilwa and J.H. Whitelaw. Control of Combustion Oscillations Close to Stoichiometry. *Flow, Turbulence and Combustion*, 63:395–414, 2000.

[5] J. P. Bons, R. Sondergaard, and R. B. Rivir. The Fluid Dynamics of LPT Blade Separation Control Using Pulsed Jets. *Journal of Turbomachinery*, 124:77–85, 2002.

[6] R. B. Rivir, R. Sondergaard, J. P. Bons, and J. P. Lake. Passive and Active Control of Separation in Gas Turbines. AIAA Paper 2000–2235, Fluids 2000 Conference and Exhibit, Denver, CO, June 2000.

[7] D. E. Culley, M. M. Bright, P. S. Prahst, and A. J. Strazisar. Active Flow Separation Control of a Stator Vane Using Embedded Injection in a Multistage Compressor Experiment. *Journal of Turbomachinery*, 126:24–34, 2004.

[8] M. B. Chiekh, J. C. Béra, and M. Sunyach. Synthetic Jet Control for Flows in a Diffuser: Vectoring, Spreading and Mixing Enhancement. *Journal of Turbulence*, 32:1–12, 2003.

[9] Y. Kubo, V. J. Modi, C. Kotsubo, K. Hayashida, and K. Kato. Suppression of Wind-Induced Vibrations of Tall Structures Through Moving Surface Boundary-Layer Control. *Journal of Wind Engineering and Industrial Aerodynamics*, 61:181–194, 1996.

[10] M. Gad-El-Hak. Flow Control: The Future. *Journal of Aircraft*, 38:402–418, 2001.

[11] L. Prandtl. Über Flüssigkeitsbewegung Bei Sehr Kleiner Reibung. Proceedings of the Third International Mathematical Congress, Heidelberg, Germany, 1904.

[12] S. N. Brown and K. Stewartson. Laminar Separation. *Annual Rev. of Fluid Mech.*, 1:45–72, 1969.

[13] R. L. Panton. *Incompressible Flow*. Wiley & Sons, New York, 1984.

[14] H. Schlichting and K. Gersten. *Boundary Layer Theory*. Springer-Verlag, New York, 8th edition, 2000.

[15] J. C. Williams. Incompressible Boundary Layer Separation. *Annual Rev. of Fluid Mech.*, 9:113–144, 1977.

[16] F. T. Smith. Steady and Unsteady Boundary-Layer Separation. *Annual Rev. of Fluid Mech.*, 18:197–220, 1986.

[17] R. L. Simpson. Turbulent Boundary-Layer Separation. *Annual Rev. of Fluid Mech.*, 21:205–234, 1989.

[18] P. K. Kundu and I. M. Cohen. *Fluid Mechanics*. Academic Press, New York, 3rd edition, 2004.

[19] J. M. McDonough. Introductory Lectures on Turbulence: Physics, Mathematics, and Modeling. Lecture notes, available on the web at: *http://www.engr.uky.edu/∼acfd/* (accessed June 7, 2007), 2004.

[20] M. Gad-El-Hak. Control of Low-Speed Airfoil Aerodynamics. *AIAA Journal*, 28:1537–1552, 1990.

[21] H. P. Horton. *Laminar Separation Bubbles in Two and Three-Dimensional Incompressible Flow*. PhD thesis, University of London, 1968.

[22] A. Roshko and W. Fiszdon. *On the Persistence of Transition in the Near Wake*. Problems of Hydrodynamics and Continuum Mechanics, Society of Industrial and Applied Mathematics, Philadelphia, 1969.

[23] E. O. Tuck. A Criterion for Leading–Edge Separation. *J. Fluid Mech.*, 222:33–37, 1991.

[24] L. F. Crabtree. Effects of Leading-Edge Separation on Thin Wings in Two-Dimensional Incompressible Flow. *Journal of the Aeronautical Sciences*, 24:597–604, 1957.

[25] E. Stanewsky. Adaptive Wing and Flow Control Technology. *Progress in Aerospace Sciences*, 37:583–667, 2001.

[26] H. M. Nagib, J. W. Kiedaisch, I. J. Wygnanski, A. D. Stalker, T. Wood, and M. A. McVeigh. First-In-Flight Full-Scale Application of Active Flow Control: The XV-15 Tiltrotor Download Reduction. MAFC Program, Defense Advanced Research Projects Agency Contract (W911NF-04-1-0012) Final Report (A277724), October 2004.

[27] C. A. Lyon, M. S. Selig, and A. P. Broeren. Boundary Layer Trips on Airfoils at Low Reynolds Numbers. AIAA Paper 1997–0511, 35th AIAA Aerospace Sciences Meeting, Reno, NV, January 1997.

[28] M. F. Kerho and M. B. Bragg. Airfoil Boundary Layer Development and Transition with Large Leading-Edge Roughness. *AIAA Journal*, 35(1):75–84, 1997.

[29] M. McQuilling, B. Hollon, and J. D. Jacob. Active Separation Flow Control in a Low Pressure Turbine Blade Cascade Model. AIAA Paper 2003–0615, 41st Aerospace Sciences Meeting and Exhibit, Reno, NV, January 2003.

[30] D.S. Miklosovic, M.M. Murray, L.E. Howle, and F.E. Fish. Leading-Edge Tubercules Delay Stall on Humpback Whale (*Megaptera novaeangliae*) Flippers. *Phys. Fluids*, 16(5):39–42, May 2004.

[31] A. Santhanakrishnan and J. D. Jacob. Low *Re* Flow over an Airfoil with Regular Surface Perturbations. Oral presentation, 30th AIAA Annual Dayton-Cincinnati Aerospace Sciences Symposium, March 2005.

[32] A. Santhanakrishnan and J. D. Jacob. Effect of Regular Surface Perturbations on Flow Over an Airfoil. AIAA Paper 2005–5145, 35th AIAA Fluid Dynamics Conference and Exhibit, Toronto, Ontario, June 2005.

[33] K. B. M. Q. Zaman, A. Bar-Sever, and S. M. Mangalam. Effect of Acoustic Excitation on the Flow Over a Low Re Airfoil. *J. Fluid Mech.*, 182:127–148, 1987.

[34] A. Seifert, T. Bachar, D. Koss, M. Shepshelovich, and I. Wygnanski. Oscillatory Blowing: A Tool to Delay Boundary-Layer Separation. *AIAA Journal*, 34:2052–2060, 1993.

[35] A. Seifert, A. Darabi, and I. Wygnanski. Delay of Airfoil Stall by Periodic Excitation. *Journal of Aircraft*, 33:691–698, 1996.

[36] M. Amitay, D. R. Smith, V. Kibens, D. E. Parekh, and A. Glezer. Modification of the Aerodynamic Characteristics of an Unconventional Airfoil Using Synthetic Jet Actuators. *AIAA Journal*, 39(3):361–370, 2001.

[37] V. J. Modi. On the Moving Surface Boundary-Layer Control. AIAA Paper 2000–2238, Fluids 2000 Conference and Exhibit, Denver, CO, June 2000.

[38] T. Lee and P. Gerontakos. Investigation of Flow Over an Oscillating Airfoil. *J. Fluid Mech.*, 512:313–341, 2004.

[39] A. Santhanakrishnan, N. J. Pern, and J. D. Jacob. Optimization and Validation of a Variable Camber Airfoil. AIAA Paper 2005–1956, 13th AIAA/ASME/AHS Adaptive Structures Conference, Austin, Texas, April 2005.

[40] N. J. Pern, Jamey D. Jacob, and R. P. LeBeau. Characterization of Zero Mass Flux Flow Control for Separation Control of an Adaptive Airfoil. AIAA Paper 2006–3032, 3rd AIAA Flow Control Conference, San Francisco, CA, June 2006.

[41] M. Gad-El-Hak. *Flow Control: Passive, Active, and Reactive Flow Management*. Cambridge University Press, New York, 2000.

[42] E. B. White and W. S. Saric. Application of Variable Leading Edge Roughness for Transition Control on Swept Wings. AIAA Paper 2000–0283, 38th AIAA Aerospace Sciences Meeting, Reno, NV, January 1997.

[43] L. Löfdahl and M. Gad-El-Hak. MEMS Applications in Turbulence and Flow Control. *Progress in Aerospace Sciences*, 35:101–203, 1999.

[44] M. R. Soltani and M. B. Bragg. Measurements on an Oscillating 70-Deg Delta Wing in Subsonic Flow. *Journal of Aircraft*, 27:211–217, 1990.

[45] D. Munday and J. D. Jacob. Active Control of Separation on a Wing with Oscillating Camber. *Journal of Aircraft*, 39:187–189, 2002.

[46] J. R. Roth, D. M. Sherman, and S. P. Wilkinson. Boundary Layer Flow Control With A One Atmosphere Uniform Glow Discharge Plasma. AIAA Paper 98–0328, 36th AIAA Aerospace Sciences Meeting and Exhibit, Reno, NV, January 1998.

[47] J. R. Roth and X. Dai. Optimization of the Aerodynamic Plasma Actuator as an Electrohydrodynamic (EHD) Electrical Device. AIAA Paper 2006–1203, 44th AIAA Aerospace Sciences Meeting and Exhibit, Reno, NV, January 2006.

[48] J. List, A. Byerley, T. McLaughlin, and R. Van Dyken. Using a Plasma Actuator to Control Laminar Separation on a Linear Cascade Turbine Blade. AIAA Paper 2003–1026, 41st AIAA Aerospace Sciences Meeting and Exhibit, Reno, NV, January 2003.

[49] J. D. Jacob, R. Rivir, C. Carter, and J. Estevadeordal. Boundary Layer Flow Control Using AC Discharge Plasma Actuators. AIAA Paper 2004–2128, 2nd AIAA Flow Control Conference, Portland, OR, June 2004.

[50] F. F. Chen. *Introduction to Plasma Physics and Controlled Fusion*. Springer, 2nd edition, 2006.

[51] D. A. Gurnett and A. Bhattacharjee. *Introduction to Plasma Physics: With Space and Laboratory Applications*. Cambridge University Press, UK, 2005.

[52] M. A. Lieberman and A. J. Lichtenberg. *Principles of Plasma Discharges and Materials Processing*. Wiley & Sons, New York, 1994.

[53] C. H. Kruger, C. O. Laux, D. M. Packan, L. Yu, A. P. Yalin, R. N. Zare, M. Nagulapally, G. V. Candler, and J. D. Kelley. Nonequilibrium Discharges in Atmospheric Pressure Air. IEEE conference record, Pulsed Power Plasma Science, Las Vegas, NV, June 2001.

[54] C. L. Enloe, T. E. McLaughlin, R. D. VanDyken, K. D. Kachner, E. J. Jumper, T. C. Corke, M. Post, and O. Haddad. Mechanisms and Responses of a Single Dielectric Barrier Discharge Plasma Actuator: Geometric Effects. *AIAA Journal*, 42(3):595–604, 2004.

[55] J. Li and K. Dhali. Simulations of Microdischarges in a Dielectric-Barrier Discharge. *J. Appl. Phys.*, 82(9):4205–4210, 1997.

[56] R. Rivir, A. White, C. Carter, B. Ganguly, A. Forelines, and J. Crafton. Turbine Flow Control, Plasma Flows. AIAA Paper 2003–6055, 41st AIAA Aerospace Sciences Meeting and Exhibit, Reno, NV, January 2003.

[57] C. Suchomel, D. Van Wie, and D. Risha. Perspectives on Cataloguing Plasma Technologies Applied to Aeronautical Sciences. AIAA Paper 2003–3852, 34th AIAA Plasmadynamics and Lasers Conference, Orlando, FL, June 2003.

[58] T. C. Corke and M. L. Post. Overview of Plasma Flow Control: Concepts, Optimization, and Applications. AIAA Paper 2005–563, 43rd AIAA Aerospace Sciences Meeting and Exhibit, Reno, NV, January 2005.

[59] E. Moreau. Airflow Control with Non-Thermal Plasma Actuators. *J. Phys. D: Appl. Phys.*, 40(3):605–636, 2007.

[60] D. J. Harney. *An Aerodynamic Study of the "Electric Wind"*. Engineer's Degree thesis, California Institute of Technology, 1957.

[61] M. Malik, L. Weinstein, and M. Hussani. Ion Wind Drag Reduction. AIAA Paper 83–0231, 21st AIAA Aerospace Sciences Meeting and Exhibit, Reno, NV, January 1983.

[62] J. R. Rosendale, M. R. Malik, and M. Y. Hussaini. Ion-Wind Effects on Poiseuille and Blasius Flow. *AIAA Journal*, 26(8):1166–1172, 1988.

[63] S. El-Khabiry and G. Colver. Drag Reduction by DC Corona Discharge Along an Electrically Conductive Flat Plate for Small Reynolds Number Flow. *Phys. Fluids*, 9(3):587–599, May 1997.

[64] G. Artana, J. D'Adamo, L. Leger, E. Moreau, and G. Touchard. Flow Control with Electrohyrodynamic Actuators. *AIAA Journal*, 40(9):1773–1779, 2002.

[65] E. Moreau, L. Leger, and G. Touchard. Effect of a DC Surface-Corona Discharge on a Flat Plate Boundary Layer for Air Flow Velocity up to 25 m/s. *Journal of Electrostatics*, 64:215–225, 2006.

[66] J. R. Roth, D. M. Sherman, and S. P. Wilkinson. Electrodynamic Flow Control with a Glow-Discharge Surface Plasma. *AIAA Journal*, 38(7):1166–1172, 2000.

[67] L. Hultgren and D. Ashpis. Demonstration of Separation Delay with Glow-Discharge Plasma Actuators. AIAA Paper 2003–1025, 41st AIAA Aerospace Sciences Meeting and Exhibit, Reno, NV, January 2003.

[68] J. Huang, T. C. Corke, and F. O. Thomas. Plasma Actuators for Separation Control of Low-Pressure Turbine Blades. *AIAA Journal*, 44(1):51–57, 2006.

[69] K. Ramakumar. Active Flow Control of Low Pressure Turbine Blade Separation Using Plasma Actuators. Master's thesis, University of Kentucky, Lexington, Kentucky, May 2006.

[70] J. Huang, T. C. Corke, and F. O. Thomas. Unsteady Plasma Actuators for Separation Control of Low-Pressure Turbine Blades. *AIAA Journal*, 44(7):1477–1487, 2006.

[71] T. C. Corke, E. J. Jumper, M.L. Post, D. Orlov, and T. E. McLaughlin. Application of Weakly-Ionized Plasmas as Wing Flow-Control Devices. AIAA Paper 2002–0350, 40th AIAA Aerospace Sciences Meeting and Exhibit, Reno, NV, January 2002.

[72] M. L. Post. Phased Plasma Actuators for Unsteady Flow Control. Master's thesis, University of Notre Dame, Notre Dame, Indiana, 2001.

[73] A. Asghar and E. J. Jumper. Phase Syncrhonization of Vortex Shedding from Multiple Cylinders Using Plasma Actuators. AIAA Paper 2003–1028, 41st AIAA Aerospace Sciences Meeting and Exhibit, Reno, NV, January 2003.

[74] T. E. McLaughlin, M. D. Munska, J. P. Vaeth, T. E. Dauwalter, J. R. Goode, and S. G. Siegal. Plasma-Based Actuators for Cylinder Wake Vortex Control. AIAA Paper 2004–2129, 2nd AIAA Flow Control Conference, Portland, OR, June 2004.

[75] J. Siegenthaler, E. J. Jumper, and A. Asghar. A Preliminary Study in Regularizing the Coherent Structures in a Planar, Weakly Compressible, Free Shear Layer. AIAA Paper 2003–0680, 41st AIAA Aerospace Sciences Meeting and Exhibit, Reno, NV, January 2003.

[76] T. C. Corke, C. He, and M. P. Patel. Plasma Flaps and Slats: An Application of Weakly Ionized Plasma Actuators. AIAA Paper 2004–2127, 2nd AIAA Flow Control Conference, Portland, OR, June 2004.

[77] M. L. Post and T. C. Corke. Separation Control Using Plasma Actuators – Dynamic Stall Control on an Oscillating Airfoil. AIAA Paper 2004–2517, 2nd AIAA Flow Control Conference, Portland, OR, June 2004.

[78] F. O. Thomas, A. Kozlov, and T. C. Corke. Plasma Actuators for Landing Gear Noise Reduction. AIAA Paper 2005–3010, 11th AIAA/CEAS Aeroacoustics Conference, Monterey, CA, May 2005.

[79] T. C. Corke, B. Mertz, and M. P. Patel. Plasma Flow Control Optimized Airfoil. AIAA Paper 2006–1208, 44th AIAA Aerospace Sciences Meeting and Exhibit, Reno, NV, January 2006.

[80] B. Goksel, D. Greenblatt, I. Rechenberg, C. N. Nayeri, and C. O. Paschereit. Steady and Unsteady Plasma Wall Jets for Separation and Circulation Control. AIAA Paper 2006–3686, 3rd AIAA Flow Control Conference, San Francisco, CA, June 2006.

[81] R. Sosa and G. Artana. Steady Control of Laminar Separation over Airfoils with Plasma Sheet Actuators. *Journal of Electrostatics*, 64:604–610, 2006.

[82] M. Samimy, I. Adamovich, J. Kim, B. Webb, S. Keshav, and Y. Utkin. Active Control of High Speed Jets Using Localized Arc Filament Plasma Actuators. AIAA Paper 2004–2130, 2nd AIAA Flow Control Conference, Portland, OR, June 2004.

[83] M. Samimy, J. H. Kim, J. Kastner, I. Adamovich, and Y. Utkin. Active Control of High-Speed and High-Reynolds-Number Jets Using Plasma Actuators. *J. Fluid Mech.*, 578:305–330, 2007.

[84] C. L. Enloe, T. E. McLaughlin, R. D. VanDyken, K. D. Kachner, E. J. Jumper, and T. C. Corke. Mechanisms and Responses of a Single Dielectric Barrier Discharge Plasma Actuator: Plasma Morphology. *AIAA Journal*, 42(3):589–594, 2004.

[85] S. Leonov, V. Bityurin, N. Savischenko, A. Yuriev, and V. Gromov. Influence of Surface Electrical Discharge on Friction of Plate in Subsonic and Transonic Airfoil. AIAA Paper 2001–0640, 39th AIAA Aerospace Sciences Meeting and Exhibit, January 2001.

[86] M. Forte, L. Leger, J. Pons, E. Moreau, and G. Touchard. Plasma Actuators for Airflow Control: Measurement of the Non-stationary Induced Flow Velocity. *Journal of Electrostatics*, 63:929–936, 2005.

[87] J. W. Baughn, C. O. Porter, B. L. Peterson, T. E. McLaughlin, C. L. Enloe, G. I. Font, and C. Baird. Momentum Transfer for an Aerodynamic Plasma Actuator with an Imposed Boundary Layer. AIAA Paper 2006–168, 44th AIAA Aerospace Sciences Meeting and Exhibit, Reno, NV, January 2006.

[88] C. O. Porter, J. W. Baughn, T. E. McLaughlin, C. L. Enloe, and G. I. Font. Temporal Force Measurements on an Aerodynamic Plasma Actuator. AIAA Paper 2006–104, 44th AIAA Aerospace Sciences Meeting and Exhibit, Reno, NV, January 2006.

[89] B. E. Balcer, M. E. Franke, and R. B. Rivir. Effects of Plasma Induced Velocity on Boundary Layer Flow. AIAA Paper 2006–875, 44th AIAA Aerospace Sciences Meeting and Exhibit, Reno, NV, January 2006.

[90] R. D. VanDyken, T. E. McLaughlin, and C. L. Enloe. Parametric Investigations of a Single Dielectric Barrier Plasma Actuator. AIAA Paper 2004–846, 42nd AIAA Aerospace Sciences Meeting and Exhibit, Reno, NV, January 2004.

[91] C. L. Enloe, T. E. McLaughlin, R. D. VanDyken, and J. C. Fischer. Plasma Structure in the Aerodynamic Plasma Actuator. AIAA Paper 2004–844, 42nd AIAA Aerospace Sciences Meeting and Exhibit, Reno, NV, January 2004.

[92] R. Anderson and S. Roy. Preliminary Experiments of Barrier Discharge Plasma Actuators using Dry and Humid Air. AIAA Paper 2006–369, 44th AIAA Aerospace Sciences Meeting and Exhibit, Reno, NV, January 2006.

[93] M. Forte, J. Jolibois, E. Moreau, G. Touchard, and M. Cazalens. Optimization of a Dielectric Barrier Discharge Actuator by Stationary and Non-stationary Measurements of the Induced Flow Velocity - Application to Airflow Control. AIAA Paper 2006–2863, 3rd AIAA Flow Control Conference, San Francisco, CA, June 2006.

[94] W. Shyy, B. Jayaraman, and A. Andersson. Modeling of Glow Discharge-Induced Fluid Dynamics. *J. Appl. Phys.*, 92(11):6434–6443, December 2002.

[95] M. Visbal and D. V. Gaitonde. Control of Vortical Flows Using Simulated Plasma Actuators. AIAA Paper 2006–505, 44th AIAA Aerospace Sciences Meeting and Exhibit, Reno, NV, January 2006.

[96] K. D. Hall, E. J. Jumper, T. C. Corke, and T. E. McLaughlin. Potential Flow Model of a Plasma Actuator as a Lift Enhancement Device. AIAA Paper 2005–783, 43rd AIAA Aerospace Sciences Meeting and Exhibit, Reno, NV, January 2005.

[97] D. M. Orlov and T. C. Corke. Numerical Simulation of Aerodynamic Plasma Actuator Effects. AIAA Paper 2005–1083, 43rd AIAA Aerospace Sciences Meeting and Exhibit, Reno, NV, January 2005.

[98] D. M. Orlov, T. C. Corke, and M. P. Patel. Electric Circuit Model for Aerodynamic Plasma Actuator. AIAA Paper 2006–1206, 44th AIAA Aerospace Sciences Meeting and Exhibit, Reno, NV, January 2006.

[99] J. P. Boeuf and L. C. Pitchford. Electrohydrodynamic Force and Aerodynamic Flow Acceleration in Surface Dielectric Barrier Discharge. *J. Appl. Phys.*, 97(10):103307, May 2005.

[100] Y. B. Suzen, P. G. Huang, J. D. Jacob, and D. E. Ashpis. Numerical Simulation of Plasma Based Flow Control Applications. AIAA Paper 2005–4633, 35th AIAA Fluid Dynamics Conference and Exhibit, Toronto, Ontario, June 2005.

[101] Y. B. Suzen and P. G. Huang. Simulations of Flow Separation Control Using Plasma Actuators. AIAA Paper 2006–877, 44th AIAA Aerospace Sciences Meeting and Exhibit, Reno, NV, January 2006.

[102] J. R. Roth. *Industrial Plasma Engineering, Volume II – Applications to Non-Thermal Plasma Processing*. Institute of Physics Publishing, Bristol and Philadelphia, 2001.

[103] G. I. Font. Boundary Layer Control with Atmospheric Plasma Discharges. AIAA Paper 2004–3574, 40th AIAA/ASME/SAE/ASEE Joint Propulsion Conference and Exhibit, Fort Lauderdale, FL, July 2004.

[104] G. I. Font and W. L. Morgan. Plasma Discharges in Atmospheric Pressure Oxygen for Boundary Layer Separation Control. AIAA Paper 2005–4632, 35th Fluid Dynamics Conference and Exhibit, Toronto, Ontario, June 2005.

[105] G. I. Font, S. Jung, C. L. Enloe, T. E. McLaughlin, W. L. Morgan, and J. W. Baughn. Simulation of the Effects of Force and Heat Produced by a Plasma Actuator on Neutral Flow Evolution. AIAA Paper 2006–167, 44th AIAA Aerospace Sciences Meeting and Exhibit, Reno, NV, January 2006.

[106] S. Roy, H. Kumar, D. V. Gaitonde, and M. Visbal. Effective Discharge Dynamics for Plasma Actuators. AIAA Paper 2006–374, 44th AIAA Aerospace Sciences Meeting and Exhibit, Reno, NV, January 2006.

[107] J. S. Shang. Electromagnetic Field of Dielectric Barrier Discharge. AIAA Paper 2005–5182, 36th AIAA Plasmadynamics and Lasers Conference, Toronto, Ontario, June 2005.

[108] J. R. Roth, X. Dai, J. Rahel, and D. M. Shermann. The Physics and Phenomenology of Paraelectric One Atmosphere Uniform Glow Discharge Plasma (OAUGDP^{TM}) Actuators for Aerodynamic Flow Control. AIAA Paper 2005–781, 43rd AIAA Aerospace Sciences Meeting and Exhibit, Reno, NV, January 2005.

[109] C. L. Enloe, T. E. McLaughlin, G. I. Font, and J. W. Baughn. Parameterization of Temporal Structure in the Single Dielectric Barrier Aerodynamic Plasma Actuator.

AIAA Paper 2005–564, 43rd AIAA Aerospace Sciences Meeting and Exhibit, Reno, NV, January 2005.

[110] C. Baird, C. L. Enloe, T. E. McLaughlin, and J. W. Baughn. Acoustic Testing of the Dielectric Barrier Discharge (DBD) Plasma Actuator. AIAA Paper 2005–565, 43rd AIAA Aerospace Sciences Meeting and Exhibit, Reno, NV, January 2005.

[111] C. L. Enloe, T. E. McLaughlin, and G. I. Font. Parameterization of Temporal Structure in the Single-Dielectric-Barrier Aerodynamic Plasma Actuator. *AIAA Journal*, 44(6):1127–1136, 2006.

[112] C. L. Enloe, T. E. McLaughlin, G. I. Font, and J. W. Baughn. Frequency Effects on the Efficiency of the Aerodynamic Plasma Actuator. AIAA Paper 2006–166, 44th AIAA Aerospace Sciences Meeting and Exhibit, Reno, NV, January 2006.

[113] J. W. Gregory, C. L. Enloe, G. I. Font, and T. E. McLaughlin. Force Production Mechanisms of a Dielectric-Barrier Discharge Plasma Actuator. AIAA Paper 2007–185, 45th AIAA Aerospace Sciences Meeting and Exhibit, Reno, NV, January 2007.

[114] T. Abe, Y. Takizawa, S. Sato, and N. Kimura. A Parametric Experimental Study for Momentum Transfer by Plasma Actuator. AIAA Paper 2007–187, 45th AIAA Aerospace Sciences Meeting and Exhibit, Reno, NV, January 2007.

[115] M. Amitay, B. L. Smith, and A. Glezer. Aerodynamic Flow Control Using Synthetic Jet Technology. AIAA Paper 98–0208, 36th AIAA Aerospace Sciences Meeting and Exhibit, Reno, NV, January 1998.

[116] O . K. Rediniotis, J. Ko, X.Yue, and A.J. Kurdilla. Synthetic Jets, their Reduced Order Modeling and Applications to Flow Control. AIAA Paper 99–1000, 37th AIAA Aerospace Sciences Meeting and Exhibit, Reno, NV, January 1999.

[117] R. Mittal and P. Rampunggoon. On the Virtual Aeroshaping Effect of Synthetic Jets (Brief Communication). *Phys. Fluids*, 14(4):1533–1536, 2002.

[118] U. Ingard and S. Labate. Acoustic Circulation Effects and the Nonlinear Impedance of Orifices. *Journal of the Acoustical Society of America*, 22(2):211–218, 1950.

[119] N. Riley. The Steady Streaming Induced by a Vibrating Cylinder. *J. Fluid Mech.*, 68:801–812, 1975.

[120] N. Riley and M. F. Wybrow. The Flow Induced by the Torsional Oscillations of an Elliptic Cylinder. *J. Fluid Mech.*, 290:279–298, 1995.

[121] B. J. Davidson and N. Riley. Jets Induced by Oscillatory Motion. *J. Fluid Mech.*, 53:287–303, 1972.

[122] J. Lighthill. Acoustic Streaming. *J. Sound Vib.*, 61(3):391–418, 1978.

[123] N. Riley. Acoustic Streaming. *Theoret. Comput. Fluid Dynamics*, 10:349–356, 1998.

[124] B. L. Smith and G. W. Swift. A Comparison Between Synthetic Jets and Continuous Jets. *Experiments in Fluids*, 34:467–472, 2003.

[125] F. O. Edis, N. Erbas, O. Baysal, and A. R. Aslan. Micro Synthetic Jets and their Interaction with a Cross Flow in Slip Regime. Technical report, Proc. of International Conference on Recent Advancement in Space Technologies (RAST 2003), Istanbul, Turkey, November 2003.

[126] M. Gad-El-Hak (editor). *The MEMS Handbook*. CRC, Florida, 2nd edition, 2005.

[127] B. L. Smith and A. Glezer. Vectoring and Small-Scale Motions Effected in Free Shear Flows Using Synthetic Jet Actuators. AIAA Paper 97–0213, 35th AIAA Aerospace Sciences Meeting and Exhibit, Reno, NV, January 1997.

[128] B. L. Smith and A. Glezer. Jet Vectoring Using Synthetic Jets. *J. Fluid Mech.*, 458:1–34, 2002.

[129] D. Guo, A. W. Cary, and R. K. Agarwal. Numerical Simulation of Vectoring of a Primary Jet with a Synthetic Jet. *AIAA Journal*, 41(12):2364–2370, 2003.

[130] P. J. Strykowski, A. Krothapalli, and D. J. Forliti. Counterflow Thrust Vectoring of Supersonic Jets. *AIAA Journal*, 34:2306–2314, 1996.

[131] Z. Travnicek and V. Tesar. Annular Synthetic Jet Used for Impinging Flow Mass-Transfer. *International Journal of Heat and Mass Transfer*, 46:3291–3297, 2003.

[132] S. A. Davis and A. Glezer. Mixing Control of Fuel Jets Using Synthetic Jet Actuators. AIAA Paper 99–0447, 37th AIAA Aerospace Sciences Meeting and Exhibit, Reno, NV, January 1999.

[133] H. Wang and S. Menon. Fuel–Air Mixing Enhancement by Synthetic Microjets. *AIAA Journal*, 39(12):2308–2319, 2001.

[134] D. Parekh, S. Palaniswamy, and U. Goldberg. Numerical Simulation of Separation Control Via Synthetic Jets. AIAA Paper 2002–3167, 1st Flow Control Conference, St. Louis, MO, June 2002.

[135] J. L. Vadillo, R. K. Agarwal, A. W. Cary, and W. W. Bower. Numerical Study of Virtual Aerodynamic Shape Modification of an Airfoil Using a Synthetic Jet Actuator. AIAA Paper 2003–4158, 33rd AIAA Fluid Dynamics Conference and Exhibit, Orlando, FL, June 2003.

[136] J. Dandois, E. Garnier, and P. Sagaut. Numerical Simulation of Active Separation Control by a Synthetic Jet. *J. Fluid Mech.*, 574:25–58, 2007.

[137] M. Amitay, D. Pitt, and A. Glezer. Separation Control in Duct Flows. *Journal of Aircraft*, 39(4):616–620, 2002.

[138] M. Amitay, D. Parekh, D. Pitt, V. Kibbens, and A. Glezer. Control of Internal Flow Separation Using Synthetic Jets Actuators. AIAA Paper 2000–0903, 38th AIAA Aerospace Sciences Meeting and Exhibit, Reno, NV, January 2000.

[139] D. Tamburello and M. Amitay. Manipulation of an Axisymmetric Jet Using a Synthetic Jet Actuator. AIAA Paper 2006–0477, 44nd AIAA Aerospace Sciences Meeting and Exhibit, Reno, NV, June 2006.

[140] A. Pavlova, K. Otani, and M. Amitay. Active Control of Sprays Using Synthetic Jets. AIAA Paper 2007–0322, 45th AIAA Aerospace Sciences Meeting, Reno, NV, January 2007.

[141] J. Farnsworth, F. Cannelle, M. Ciuryla, and M. Amitay. Control of the Stingray UAV at Low Angles of Attack. AIAA Paper 2007–0321, 45th AIAA Aerospace Sciences Meeting, Reno, NV, January 2007.

[142] Y. Liu, M. Ciuryla, M. Amitay, C. Kwan, J. Myatt, and X. Zhang. Integrated Flight Control and Flow Control Using Synthetic Jet Arrays. AIAA Paper 2006–6190, AIAA Guidance, Navigation, and Control Conference and Exhibit, Keystone, CO, June 2006.

[143] M. Amitay, A. E. Washburn, S. G. Anders, and D. E. Parekh. Active Flow Control of the Stingray Uninhabited Aerial Vehicle: Transient Behavior. *AIAA Journal*, 42(11):2205–2215, 2004.

[144] A. Washburn and M. Amitay. Active Flow Control on the STINGRAY UAV: Physical Mechanisms. AIAA Paper 2004–0745, 42nd AIAA Aerospace Sciences Meeting and Exhibit, Reno, NV, January 2004.

[145] D. Parekh, S. Williams, M. Amitay, and U. Goldberg. Synthetic Jet Aerodynamic Control on a Full Scale UAV. AIAA Paper 2003–4002, 33rd AIAA Aerospace Sciences Meeting and Exhibit, Reno, NV, January 2003.

[146] J. Whitehead and I. Gursul. Interaction of Synthetic Jet Propulsion with Airfoil Aerodynamics at Low Reynolds Numbers. *AIAA Journal*, 44(8):1753–1766, 2006.

[147] A. Glezer and M. Amitay. Synthetic Jets. *Annual Rev. of Fluid Mech.*, 34:503–529, 2002.

[148] R. D. James, J. W. Jacobs, and Ari Glezer. A Round Turbulent Jet Produced By An Oscillating Diaphragm. *Phys. Fluids*, 8(9):2484–2495, 1996.

[149] B. L. Smith and Ari Glezer. The Formation and Evolution of Synthetic Jets. *Phys. Fluids*, 10(9):2281–2297, 1998.

[150] Ari Glezer. The Formation of Vortex Rings. *Phys. Fluids*, 31(12):3532–3542, 1988.

[151] A. Crook and N. J. Wood. Measurements and Visualizations of Synthetic Jets. AIAA Paper 2001–0145, 39th AIAA Aerospace Sciences Meeting and Exhibit, Reno, NV, January 2001.

[152] J. C. Béra, M. Michard, N. Grosjean, and G. Comte-Bellot. Flow Analysis of Two-Dimensional Pulsed Jets by Particle Image Velocimetry. *Experiments in Fluids*, 31:519–532, 2001.

[153] Y. Guy, T. E. McLaughlin, and J. A. Morrow. Velocity Measurements in a Synthetic Jet. AIAA Paper 2001–0118, 39th AIAA Aerospace Sciences Meeting and Exhibit, Reno, NV, January 2001.

[154] J. E. Cater and J. Soria. The Evolution of Round Zero-Net-Mass-Flux Jets. *J. Fluid Mech.*, 472:167–200, 2002.

[155] B. L. Smith and G. W. Swift. Synthetic Jets at Large Reynolds Number and Comparison to Continuous Jets. AIAA Paper 2001–3030, 31st AIAA Fluid Dynamics Conference and Exhibit, Anaheim, CA, June 2001.

[156] B. L. Smith, M. A. Trautman, and A. Glezer. Controlled Interactions of Adjacent Synthetic Jets. AIAA Paper 99–0669, 37th AIAA Aerospace Sciences Meeting and Exhibit, Reno, NV, January 1999.

[157] R. Holman, Y. Utturkar, R. Mittal, B. L. Smith, and L. Cattafesta. Formation Criterion for Synthetic Jets. *AIAA Journal*, 43(10):2110–2116, 2005.

[158] I. M. Milanovic and K. B. M. Q. Zaman. Synthetic Jets in Crossflow. Part II: Jets from Orifices of Different Geometry. AIAA Paper 2003–3715, 33rd AIAA Fluid Dynamics Conference and Exhibit, Orlando, FL, June 2003.

[159] D. P. Rizzetta, M. R. Visbal, and M. J. Stanek. Numerical Investigation of Synthetic-Jet Flowfields. *AIAA Journal*, 37(8):919–927, 1999.

[160] C. Y. Lee and D. B. Goldstein. Two Dimensional Synthetic Jet Simulation. *AIAA Journal*, 40(3):510–516, 2002.

[161] R. B. Kotapati and R. Mittal. Time-Accurate Three Dimensional Simulations of Synthetic Jets in Quiescent Air. AIAA Paper 2005–0103, 43rd AIAA Aerospace Sciences Meeting and Exhibit, Reno, NV, January 2005.

[162] L. D. Kral, J. F. Donovan, A. B. Cain, and A. W. Cary. Numerical Simulation of Synthetic Jet Actuators. AIAA Paper 97–1824, 4th AIAA Shear Flow Control Conference, Snowmass Village, CO, June 1997.

[163] J. Cui and R. K. Agarwal. Three-Dimensional Computation of a Synthetic Jet in Quiescent Air. *AIAA Journal*, 44(12):2857–2865, 2006.

[164] D. C. Wilcox. *Turbulence Modeling for CFD*. DCW Industries, California, 2nd edition, 2000.

[165] S. H. Park, Y. H. Yu, and D. Y. Byun. RANS Simulation of a Synthetic Jet in Quiescent Air. AIAA Paper 2007–1131, 45th AIAA Aerospace Sciences Meeting and Exhibit, Reno, NV, January 2007.

[166] B. L. Smith and A. Glezer. Vectoring of Adjacent Synthetic Jets. *AIAA Journal*, 43(10):2117–2124, 2005.

[167] M. Gordon and J. Soria. PIV Measurements of a Zero-Net-Mass-Flux Jet in Cross Flow. *Experiments in Fluids*, 33:863–872, 2002.

[168] D. R. Smith. Interaction of a Synthetic Jet with a Crossflow Boundary Layer. *AIAA Journal*, 40(11):2277–2288, 2002.

[169] K. B. M. Q. Zaman and I. M. Milanovic. Synthetic Jets in Crossflow. Part I: Round Jet. AIAA Paper 2003–3714, 33rd AIAA Fluid Dynamics Conference and Exhibit, Orlando, FL, June 2003.

[170] A. Bridges and D. R. Smith. Influence of Orifice Orientation on a Synthetic Jet–Boundary-Layer Interaction. *AIAA Journal*, 41(12):2394–2402, 2003.

[171] J. Dandois, E. Garnier, and P. Sagaut. Unsteady Simulation of a Synthetic Jet in Crossflow. *AIAA Journal*, 44(2):225–238, 2006.

[172] M. Amitay, A. M. Honohan, M. Trautman, and A. Glezer. Modification of the Aerodynamic Characteristics of Bluff Bodies Using Fluidic Actuators. AIAA Paper 97–2004, 4th AIAA Shear Flow Control Conference, Snowmass Village, CO, June 1997.

[173] A. M. Honohan, M. Amitay, and A. Glezer. Aerodynamic Control Using Synthetic Jets. AIAA Paper 2000–2401, AIAA Fluids 2000 Meeting, Denver, CO, June 2000.

[174] A. Glezer, M. Amitay, and A. M. Honohan. Aspects of Low- and High-Frequency Actuation for Aerodynamic Flow Control. *AIAA Journal*, 43(7):1501–1511, 2005.

[175] H. J. Hussein, S. P. Capp, and W. K. George. Velocity Measurements in a High Reynolds Number, Momentum Conserving, Axisymmetric, Turbulent Jet. *J. Fluid Mech.*, 258:31–75, 1994.

[176] A. Santhanakrishnan, K. Ramakumar, and J. D. Jacob. Characteristics of a Plasma Synthetic Jet. Oral presentation, Bulletin of the American Physical Society Fluid Dynamics Division, Annual Meeting, November 2005.

[177] A. Santhanakrishnan and J. D. Jacob. On Plasma Synthetic Jet Actuators. AIAA Paper 2006–0317, 44th AIAA Aerospace Sciences Meeting and Exhibit, Reno, NV, January 2006.

[178] U. Kogelschatz. Dielectric-barrier Discharges: Their History, Discharge Physics, and Industrial Applications. *Plasma Chemistry and Plasma Processing*, 23(1):1–46, 2003.

[179] J. D. Jacob. Time Resolved PIV Measurements of Plasma Based Flow Control. Air Force Summer Faculty Fellowship Program Final Report, AFRL, WPAFB, July 2004.

[180] T. D. Dudderar and P. G. Simpkins. Laser Speckle Photography in a Fluid Medium. *Nature*, 270:45–47, 1977.

[181] H. Li, R. Sadr, and M. Yoda. Multilayer Nano-Particle Image Velocimetry. *Experiments in Fluids*, 41(2):185–194, 2006.

[182] I. Fujita, M. Muste, and A. Kruger. Large-Scale Particle Image Velocimetry for Flow Analysis in Hydraulic Applications. *J. Hydr. Res.*, 36(3):397–414, 1998.

[183] R. J. Adrian. Twenty Years of Particle Image Velocimetry. *Experiments in Fluids*, 39:159–169, 2005.

[184] R. J. Adrian. Particle–Imaging Techniques for Experimental Fluid Mechanics. *Annual Rev. of Fluid Mech.*, 23:261–304, 1991.

[185] C. E. Willert and M. Gharib. Digital Particle Image Velocimetry. *Experiments in Fluids*, 10:181–193, 1991.

[186] M. Raffel, C. Willert, and J. Kompenhans. *Particle Image Velocimetry: A Practical Guide*. Springer-Verlag, New York, 1998.

[187] Y.-C. Cho. Digital Image Velocimetry. *Appl. Optics*, 28:740–748, 1989.

[188] S. Gogineni, L. Goss, D. Pestian, and R. Rivir. Two-Color Digital PIV Employing a Single Camera. *Experiments in Fluids*, 25:320–328, 1998.

[189] J. D. Jacob. PIV Boot Camp. Oral Presentation, University of Kentucky, Fluid Mechanics Lab Meeting, February 2004.

[190] P. Freymuth. Flow Visualization in Fluid Mechanics. *Rev. Sci. Instrum.*, 64(1):1–18, 1993.

[191] M. Gharib, D. Kremers, M. Koochesfahani, and M. Kemp. Leonardo's Vision of Flow Visualization. *Experiments in Fluids*, 33(1):219–223, 2002.

[192] M. Van Dyke. *An Album of Fluid Motion*. Parabolic Press, Stanford, California, 1992.

[193] J. C. Agui and J. Jiménez. On the Performance of Particle Tracking. *J. Fluid Mech.*, 185:447–468, 1987.

[194] J. D. Jacob. *Experimental Investigation of the Trailing Vortex Wake of Rectangular Airfoils*. PhD thesis, University of California at Berkeley, Berkeley, California, 1995.

[195] M. Sholl and Ö. Savaş. A Fast Lagrangian PIV Method for Study of General High-Gradient Flows. AIAA Paper 1997–0493, 35th AIAA Aerospace Sciences Meeting, Reno, NV, January 1997.

[196] D. Fabris. *Combined Experimental and Numerical Investigations of a Vortex Ring Impinging Normally on a Wall*. PhD thesis, University of California at Berkeley, Berkeley, California, 1996.

[197] L. Tsuei and Ö. Savaş. Treatment of Interfaces in Particle Image Velocimetry. *Experiments in Fluids*, 29:203–214, 1999.

[198] A. Bejan. *Convection Heat Transfer*. Wiley & Sons, New Jersey, 3rd edition, 2004.

[199] J. D. Jacob, K. Ramakumar, R. Anthony, and R. B. Rivir. Control of Laminar and Turbulent Shear Flows Using Plasma Actuators. TSFP 4-225, 4th International Symposium on Turbulence and Shear Flow Phenomena, Williamsburg, VA, June 2005.

[200] K. Ramakumar and J. D. Jacob. Flow Control and Lift Enhancement Using Plasma Actuators. AIAA Paper 2005–4635, 35th AIAA Fluid Dynamics Conference and Exhibit, Toronto, Ontario, June 2005.

[201] A. Santhanakrishnan and J. D. Jacob. Formation and Scaling of Plasma Synthetic Jet Actuators. AIAA Paper 2007–0940, 45th AIAA Aerospace Sciences Meeting and Exhibit, Reno, NV, January 2007.

[202] A. Santhanakrishnan and J. D. Jacob. Flow Control with Plasma Synthetic Jet Actuators. *J. Phys. D: Appl. Phys.*, 40(3):637–651, 2007.

[203] A. Santhanakrishnan and J. D. Jacob. Effect of Plasma Morphology on Flow Control Using Plasma Synthetic Jet Actuators. AIAA Paper 2007–0783, 45th AIAA Aerospace Sciences Meeting and Exhibit, Reno, NV, January 2007.

[204] D. A. Reasor. Numerical Simulation of Two Flow Control Approaches for Low Reynolds Number Applications. Master's thesis, University of Kentucky, Lexington, Kentucky, 2007.

[205] M. Bolitho and J. D. Jacob. Use of Aggregate Plasma Synthetic Jet Actuators for Flow Control. AIAA Paper 2007–637, 45th AIAA Aerospace Sciences Meeting and Exhibit, Reno, NV, January 2007.

[206] T. Segawa, H. Furutani, H. Yoshida, T. Jukes, and K. Choi. Wall Normal Jet under Elevated Temperatures Produced by Surface Plasma Actuator. AIAA Paper 2007–784, 45th AIAA Aerospace Sciences Meeting and Exhibit, Reno, NV, January 2007.

[207] T. T. Ng. Effect of a Single Strake on the Forebody Vortex Asymmetry. *Journal of Aircraft*, 27(9):161184, 1990.

[208] D. R. Williams and H. Papazian. Forebody Vortex Control with the Unsteady Bleed Technique. *AIAA Journal*, 29:853–855, 1991.

[209] M. P. Patel, C. P. Tilmann, and T. T. Ng. Closed-Loop Missile Yaw Control via Manipulation of Forebody Flow Asymmetries. *Journal of Spacecraft and Rockets*, 41(3):436–443, 2004.

[210] T. F. Fric. Effects of Fuel-Air Unmixedness on NO_x Emissions. *Journal of Propulsion and Power*, 9(5):708–713, 1993.

[211] M. Samimy, K. B. M. Q. Zaman, and M. F. Reeder. Effect of Tabs on the Flow and Noise Control of an Axisymmetric Jet. *AIAA Journal*, 31:609–619, 1993.

[212] K. B. M. Q. Zaman, M. F. Reeder, and M. Samimy. Control of an Axisymmetric Jet Using Vortex Generators. *Phys. Fluids*, 6(2):778–796, 1994.

[213] M. W. Bettridge, R. E. Spall, and B. L. Smith. Aerodynamic Jet Vectoring Using Steady Blowing and Suction. AIAA Paper 2004–0921, 42nd AIAA Aerospace Sciences Meeting and Exhibit, Reno, NV, January 2004.

VITA

Arvind Santhanakrishnan was born on March 12, 1981 in Chennai (formerly Madras), India. He completed his secondary school education in 1998 from Vidya Mandir (Adyar), Madras, India. He obtained his Bachelors degree in Mechanical Engineering in first class with distinction from Bharathidasan University, Tiruchirapalli, India in 2002. He began his graduate studies at the University of Kentucky in August 2002. As a graduate student, he served as a Research Assistant at the Fluid Mechanics Laboratory and as a Teaching Assistant for the Department of Mechanical Engineering. He has instructed several semesters of undergraduate courses for the Department of Mechanical Engineering. He has presented numerous talks on his research at international level conferences, and published several peer-reviewed conference and journal articles.

Awards

- Best Presentation, *Quiescent and Crossflow Characteristics of Linear Plasma Synthetic Jet Actuators*, 2007 AIAA 32nd Annual Dayton-Cincinnati Aerospace Science Symposium
- Best Presentation, *Flow Control Using Plasma Synthetic Jet Actuators*, 2006 AIAA 31st Annual Dayton-Cincinnati Aerospace Science Symposium
- Recipient of Kentucky Graduate Scholarship 2002-2007

Publications

Journal Articles

A. Santhanakrishnan and J. D. Jacob. Flow Control with Plasma Synthetic Jet Actuators. *J. Phys. D: Appl. Phys.*, 40(3):637-651, 2007.

A. Santhanakrishnan and J. D. Jacob. Experimental Characterization of Plasma Synthetic Jet Actuators. Submitted to *Experiments in Fluids*, in review.

A. Santhanakrishnan and J. D. Jacob. Effect of Plasma Morphology on the Characteristics of Isolated Plasma Synthetic Jets. To be submitted.

Conference Proceedings

Santhanakrishnan, A., and Jacob, J. D., "Formation and Scaling of Plasma Synthetic Jet Actuators," AIAA 2007-0940, *45th AIAA Aerospace Sciences Meeting and Exhibit*, Reno, NV, January, 2007.

Santhanakrishnan, A., and Jacob, J. D., "Effect of Plasma Morphology on Flow Control Using Plasma Synthetic Jet Actuators," AIAA 2007-0783, *45th AIAA Aerospace Sciences Meeting and Exhibit*, Reno, NV, January, 2007.

Santhanakrishnan, A., Jacob, J. D., and Suzen, Y. B., "Flow Control Using Plasma and Linear/Annular Plasma Synthetic Jet Actuators," AIAA 2006-3033, *3rd AIAA Flow Control Conference*, San Francisco, CA, June, 2006.

Santhanakrishnan, A., and Jacob, J. D., "On Plasma Synthetic Jet Actuators," AIAA 2006-0317, *44th AIAA Aerospace Sciences Meeting and Exhibit*, Reno, NV, January, 2006.

Santhanakrishnan, A., Pern, N. J., Ramakumar, K., Simpson, A. D., and Jacob, J. D., "Enabling Flow Control Technology for Low Speed UAVs," AIAA 2005-6960, *AIAA Infotech@Aerospace*, Arlington, VA, September, 2005.

Santhanakrishnan, A., and Jacob, J. D., "Effect of Regular Surface Perturbations on Flow Over an Airfoil," AIAA 2005-5145, *35th AIAA Fluid Dynamics Conference and Exhibit*, Toronto, Ontario, June, 2005.

Santhanakrishnan, A., Pern, N. J., and Jacob, J. D., "Optimization and Validation of a Variable Camber Airfoil," AIAA 2005-1956, *13th AIAA/ASME/AHS Adaptive Structures Conference*, Austin, TX, April, 2005.

Simpson, A. D., Santhanakrishnan, A., Jacob, J. D., Smith, S., Lumpp, J., and Cadogan, D. "Flying on Air: UAV Flight Testing with Inflatable Wing Technology," AIAA 2004-6570, *AIAA 3rd "Unmanned Unlimited" Technical Conference, Workshop and Exhibit*, Chicago, IL, September, 2004.

Santhanakrishnan, A., and Jacob, J. D., "Shape Optimization and Flight Testing of Wing with Oscillating Camber," *AIAA Region III Student Conference*, Purdue University, West Lafayette, IN, 2004.

Presentations (without papers)

Characterization and Flow Physics of Plasma Synthetic Jet Actuators. A. Santhanakrishnan. Presented to the faculty of the Department of Mathematics, University of North Carolina, Chapel Hill, NC, June 21, 2007.

Plasma Actuators for the Control of Aerodynamic Flows. A. Santhanakrishnan. University of Kentucky AIAA Student Chapter Seminar, Lexington, KY, April 19, 2007.

Quiescent and Crossflow Characteristics of Linear Plasma Synthetic Jet Actuators. A. San-

thanakrishnan and J. D. Jacob. 32nd AIAA Annual Dayton-Cincinnati Aerospace Sciences Symposium, Dayton, OH, March 7, 2007.

Scaling of Plasma Synthetic Jet Actuators. J. D. Jacob and A. Santhanakrishnan. 59th Annual Meeting of the American Physical Society, Division of Fluid Dynamics, Tampa, FL, November 21, 2006.

Characteristics of Plasma Synthetic Jet Actuators in Crossflow. A. Santhanakrishnan and J. D. Jacob. 59th Annual Meeting of the American Physical Society, Division of Fluid Dynamics, Tampa, FL, November 19, 2006.

Flow Control Using Plasma Synthetic Jet Actuators. A. Santhanakrishnan and J. D. Jacob. 31st AIAA Annual Dayton-Cincinnati Aerospace Sciences Symposium, Dayton, OH, March 7, 2006.

Characterization of a Plasma Synthetic Jet. A. Santhanakrishnan, K. Ramakumar and J. D. Jacob. 58th Annual Meeting of the American Physical Society, Division of Fluid Dynamics, Chicago, IL, November 20, 2005.

Flow Control in Low Pressure Turbine Blades Using Plasma Actuators. K. Ramakumar, A. Santhanakrishnan and J. D. Jacob. 58th Annual Meeting of the American Physical Society, Division of Fluid Dynamics, Chicago, IL, November 20, 2005.

Low Re Flow over an Airfoil with Regular Surface Perturbations. A. Santhanakrishnan and J. D. Jacob. 30th AIAA Annual Dayton-Cincinnati Aerospace Sciences Symposium, Dayton, OH, March 8, 2005.

Shape Optimization and Flight Testing of Wing with Oscillating Camber. A. Santhanakrishnan and J. D. Jacob. 29th AIAA Annual Dayton-Cincinnati Aerospace Sciences Symposium, Dayton, OH, March 9, 2004.